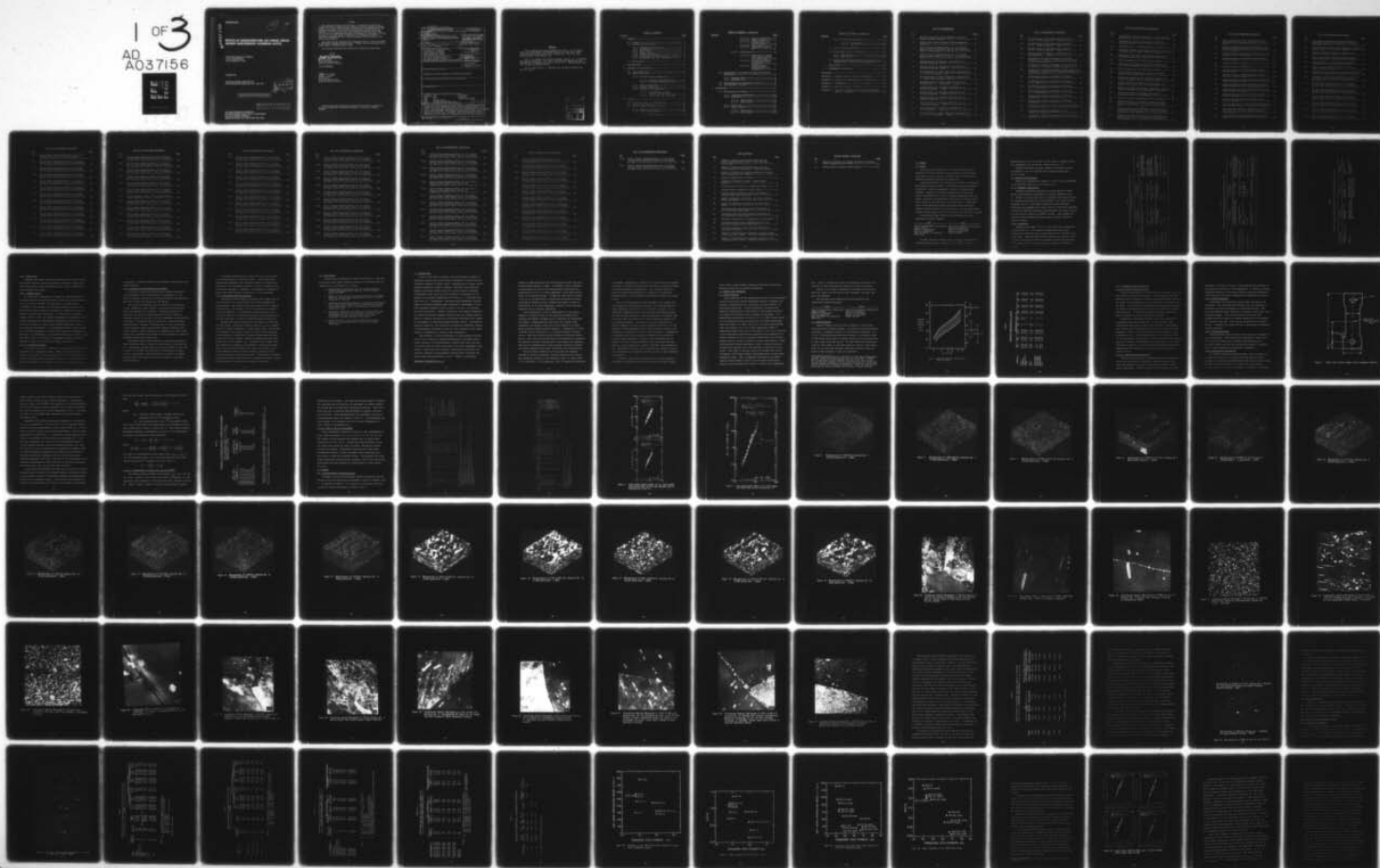


AD-A037 156

ALUMINUM CO OF AMERICA ALCOA CENTER PA ALCOA LABS  
EFFECTS OF MICROSTRUCTURE ON FATIGUE CRACK GROWTH OF HIGH-STRENGTH (U)  
AUG 76 W G TRUCKNER, J T STALEY, R J BUCCI F33615-74-C-5079  
56-76-AF5 AFML-TR-76-169 NL

UNCLASSIFIED

1 OF 3  
AD  
A037156  
1



AD A 037156

AFML-TR-76-169

(12) J

## EFFECTS OF MICROSTRUCTURE ON FATIGUE CRACK GROWTH HIGH-STRENGTH ALUMINUM ALLOYS

ALUMINUM COMPANY OF AMERICA  
ALCOA LABORATORIES  
ALCOA CENTER, PA 15069

OCTOBER 1976

TECHNICAL REPORT AFML-TR-76-169  
FINAL REPORT FOR PERIOD MAY 1974 - MAY 1976

DDC  
RECEIVED  
MAR 21 1977  
A

Approved for public release; distribution unlimited

COPY AVAILABLE TO DDC DOES NOT  
PERMIT FULLY LEGIBLE PRODUCTION

AIR FORCE MATERIALS LABORATORY  
AIR FORCE WRIGHT AERONAUTICAL LABORATORIES  
AIR FORCE SYSTEMS COMMAND  
WRIGHT-PATTERSON AIR FORCE BASE, OHIO 45433




• NOTICE

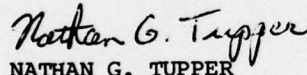
When Government drawings, specifications, or other data are used for any purpose other than in connection with a definitely related Government procurement operation, the United States Government thereby incurs no responsibility nor any obligation whatsoever; and the fact that the government may have formulated, furnished, or in any way supplied the said drawings, specifications, or other data, is not to be regarded by implication or otherwise as in any manner licensing the holder or any other person or corporation, or conveying any rights or permission to manufacture, use, or sell any patented invention that may in any way be related thereto.

This report has been reviewed by the Information Office (IO) and is releasable to the National Information Service (NTIS). At NTIS, it will be available to the general public, including foreign nations.

This technical report has been reviewed and is approved for publication.

  
JOSEPH S. SANTNER, 1/Lt, USAF  
Project Engineer  
Structural Metals Branch  
Metals and Ceramics Division

FOR THE COMMANDER

  
NATHAN G. TUPPER  
Acting Chief  
Structural Metals Branch  
Metals and Ceramics Division

Copies of this report should not be returned unless return is required by security considerations, contractual obligations, or notice on a specific document.

UNCLASSIFIED

SECURITY CLASSIFICATION OF THIS PAGE (When Data Entered)

REPORT DOCUMENTATION PAGE		READ INSTRUCTIONS BEFORE COMPLETING FORM
1. REPORT NUMBER AFML-TR-76-169	2. GOVT ACCESSION NO.	3. REPORT'S CATALOG NUMBER
4. TITLE (and Subtitle) EFFECTS OF MICROSTRUCTURE ON FATIGUE CRACK GROWTH OF HIGH-STRENGTH ALUMINUM ALLOYS		5. DATE OF REPORT & PERIOD COVERED Final Technical Report, May 1974 - May 1976
7. AUTHOR(s) W. G. Truckner, J. T. Staley, R. J. Bucci, A. B. Thakker		6. PERFORMING ORG. REPORT NUMBER 56-76-AF5
9. PERFORMING ORGANIZATION NAME AND ADDRESS Aluminum Co. of America Alcoa Technical Center Alcoa Center, PA 15069		8. CONTRACT OR GRANT NUMBER(s) F33615-74-C-5079 new
11. CONTROLLING OFFICE NAME AND ADDRESS Air Force Materials Laboratory Air Force Systems Command Wright-Patterson Air Force Base, OH 45433		10. PROGRAM ELEMENT, PROJECT, TASK, AREA & WORK UNIT NUMBERS Project No. 7351
14. MONITORING AGENCY NAME & ADDRESS (if different from Controlling Office)		12. REPORT DATE August 1976
		13. NUMBER OF PAGES 276p
		15. SECURITY CLASS. (of this report) Unclassified
		15a. DECLASSIFICATION/DOWNGRADING SCHEDULE
16. DISTRIBUTION STATEMENT (of this Report)  Approved for Public Release; distribution unlimited.		
17. DISTRIBUTION STATEMENT (of the abstract entered in Block 20, if different from Report)		
18. SUPPLEMENTARY NOTES		
19. KEY WORDS (Continue on reverse side if necessary and identify by block number) aluminum 7075 environment alloy 7475 frequency 2024 7050 constant amplitude 2124 microstructure 2048 fatigue crack growth rate		
20. ABSTRACT (Continue on reverse side if necessary and identify by block number) Effects of microstructure and composition on resistance to fatigue crack growth were determined using constant amplitude loading conditions in low and high humidity air at test frequencies of 2 and 20 Hz. Strengthening precipitate had the largest effect at $\Delta K$ delta K above about 4 ksi/in., while solute composition had the largest effect at $\Delta K$ below about 3 ksi/in. Large intermetallic particles affected growth at high and intermediate levels of $\Delta K$ delta K.		

DD FORM 1 JAN 73 1473

EDITION OF 1 NOV 65 IS OBSOLETE

UNCLASSIFIED

SECURITY CLASSIFICATION OF THIS PAGE (When Data Entered)

4 KSI sq. root g (in.)

3 KSI sq. root g (in.)

log

### PREFACE

This investigation was conducted for the U. S. Air Force Materials Laboratory, Wright-Patterson Air Force Base, Ohio, under Contract F33615-74-C-5079, Project No. 7351, by Alcoa Laboratories, Alcoa Center, Pa.

Mr. J. T. Staley was project manager, and Dr. W. G. Truckner was project engineer. Drs. Bucci and Thakker supervised the fatigue crack propagation tests, and Mr. D. A. Mauney supervised the fatigue initiation tests.

Lt. P. Blau and Lt. J. Santner were project monitors for the Air Force.

RECEIVED	
WTS	DATE
DTG	EXT
BY	
APPROVED	
SPECIAL AGENT	
A	



## TABLE OF CONTENTS

<u>Section</u>	<u>Page</u>
1. SUMMARY-----	1
1.1 Scope-----	1
1.2 Results and Discussion-----	2
1.2.1 Insoluble Constituents-----	2
1.2.2 Dispersoids-----	2
1.2.3 Grain Size-----	6
1.2.4 Copper Content-----	6
1.2.5 Dislocation Density-----	6
1.2.6 Strengthening Precipitate Type (Temper)---	7
1.2.7 Environment and Test Frequency-----	8
1.3 Conclusions-----	9
2. INTRODUCTION-----	10
3. MATERIAL AND PROCEDURES-----	13
3.1 Alloy Selection-----	13
3.2 Experimentation-----	14
3.2.1 Microstructural Examination-----	17
3.2.1.1 Pre-Test Characterization-----	17
3.2.1.2 Post-Test Characterization-----	18
3.2.2 Static Properties-----	18
3.2.3 Fatigue Initiation-----	18
3.2.4 Fatigue Crack Propagation-----	18
3.2.4.1 Intermediate $\Delta K$ Tests ( $\Delta K$ 4 to 20 ksi $\sqrt{\text{in.}}$ )-----	21
3.2.4.2 Low $\Delta K$ ( $\Delta K$ 2 to 8 ksi $\sqrt{\text{in.}}$ )-----	23
4. RESULTS-----	23
4.1 Microstructural Characterization-----	23
4.2 Static Properties-----	60
4.3 Fatigue Crack Propagation Tests-----	60
4.3.1 Methods of Analysis-----	60
4.3.2 Crack Growth Results-----	76
4.3.2.1 7XXX Alloys-----	76



# TABLE OF CONTENTS - Continued

<u>Section</u>	<u>Page</u>
4.3.2.1.1 Type of Dispersoid---	76
4.3.2.1.2 Copper Content-----	77
4.3.2.1.3 Strengthening Pre- cipitate Type-----	78
4.3.2.1.4 Grain Size-----	79
4.3.2.1.5 Dispersoid-Constitu- ent-----	81
4.3.2.2 2XXX Alloys-----	82
4.3.2.2.1 Constituent, Disper- soid, and Strengthen- ing Precipitate-----	83
4.3.2.2.2 Dislocation Density- Strengthening Pre- cipitate-----	86
4.3.2.2.3 Copper Content- Strengthening Pre- cipitate-----	87
4.4 Supplementary Structures to Study Precipitate Morphology-----	88
4.4.1 Overaged 2024-----	89
4.4.2 Underaged 7050-----	89
4.5 Lab-Fabricated vs Commercial 7075-T6-----	90
4.6 Fractographic Studies-----	91
5. DISCUSSION-----	113
5.1 Microstructural Effects-----	113
5.1.1 Insoluble Constituent-----	113
5.1.2 Dispersoid-----	116
5.1.2.1 7XXX Alloys-----	116
5.1.2.2 2XXX Alloys-----	117
5.1.3 Grain Size-----	117
5.1.4 Copper Content-----	118
5.1.4.1 7XXX Alloys-----	118
5.1.4.2 2XXX Alloys-----	119

# TABLE OF CONTENTS - Continued

<u>Section</u>	<u>Page</u>
5.1.5 Precipitate Morphology-----	120
5.1.5.1 Intermediate $\Delta K$ -----	120
5.1.5.2 Low $\Delta K$ -----	130
5.1.6 Dislocation Density-----	132
5.2 Environment and Test Frequency-----	133
5.2.1 2XXX Alloys-----	135
5.2.2 7XXX Alloys-----	137
5.3 Relationship Between Mechanical Properties and Fatigue Crack Propagation Performance-----	141
6. CONCLUSIONS-----	144
7. RECOMMENDED FUTURE WORK-----	149
REFERENCES-----	152
APPENDIX A - Fatigue Crack Initiation Resistance-----	158
APPENDIX B - Effects of Microstructure on Toughness-----	164
APPENDIX C - Intermediate $\Delta K$ , $\Delta a/\Delta N$ vs $\Delta K$ Plots-----	169
APPENDIX D - Low $\Delta K$ , $\Delta a/\Delta N$ vs $\Delta K$ Plots-----	232
APPENDIX E - $\Delta a/\Delta N$ vs $\Delta K$ Plots for Combined Intermediate and Low $K$ Results-----	244

# LIST OF ILLUSTRATIONS

<u>No.</u>		<u>Page</u>
1.	Relates Incremental Crack Advance to Size of Microstructural Feature-----	15
2.	Center Crack Tension Fatigue Crack Propagation Specimen-----	19
3.	Cyclic Stress Intensity Range, $\Delta K$ , Vs. Cyclic Fatigue Crack Growth Rate, $\Delta a/\Delta N$ , from Replicate Tests of Structures No. 9 and 12-----	26
4.	Cyclic Stress Intensity Range, $\Delta K$ , Vs. Cyclic Fatigue Crack Growth Rate, $\Delta a/\Delta N$ , of Structure No. 12-----	27
5.	Microstructure of 7050-T76, Structure No. 1. 240,000 grains/mm <sup>3</sup> (100X)-----	28
6.	Microstructure of 7050+Mn-T76, Structure No. 2. 110,000 grains/mm <sup>3</sup> . (100X)-----	29
7.	Microstructure of X7080 (hiCu)-T76, Structure No. 3. 20,000 grains/mm <sup>3</sup> . (100X)-----	30
8.	Microstructure of X7080 (hiCu)-T76, Structure No. 4. Mixed Grain Structure (100X)-----	31
9.	Microstructure of X7080 (hiCu)-T76 (lg.g.s.), Structure No. 8. 5 grains/mm <sup>3</sup> . (100X)-----	32
10.	Microstructure of 7075-T61, Structure No. 9. 65,000 grains/mm <sup>3</sup> . (100X)-----	33
11.	Microstructure of 7075-T6, Structure No. 10. 65,000 grains/mm <sup>3</sup> . (100X)-----	34
12.	Microstructure of 7475-T61, Structure No. 11. 135,000 grains/mm <sup>3</sup> -----	35
13.	Microstructure of 7475-T6, Structure No. 12. 130,000 grains/mm <sup>3</sup> . (100X)-----	36
14.	Microstructure of 7075-T61, Structure No. 13. 5000 grains/mm <sup>3</sup> . (100X)-----	37
15.	Microstructure of 2024 (hiMn)-T31, Structure No. 14. 13,000 grains/mm <sup>3</sup> . (100X)-----	38



# LIST OF ILLUSTRATIONS (CONTINUED)

<u>No.</u>		<u>Page</u>
16.	Microstructure of 2124 (hiMn)-T31, Structure No. 15. 11,000 grains/mm <sup>3</sup> . (100X)-----	39
17.	Microstructure of 2024 (loMn)-T31, Structure No. 16. 20,000 grains/mm <sup>3</sup> . (100X)-----	40
18.	Microstructure of 2124 (loMn)-T31, Structure No. 17. 13,000 grains/mm <sup>3</sup> . (100X)-----	41
19.	Microstructure of 2048-T31, Structure No. 24. 5000 grains/mm <sup>3</sup> . (100X)-----	42
20.	Transmission Electron Micrograph of 7050-T76, Structure No. 1, Showing the Continuous Precipitate on the Grain Boundary-----	43
21.	Transmission Electron Micrograph of 7050 (+Mn)-T76, Structure No. 2 Showing Al <sub>20</sub> CuMn <sub>3</sub> Dispersoid-----	44
22.	Transmission Electron Micrograph of X7080 (hiCu)-T76, Structure No. 3 Showing Grain Boundary Precipitate of Strengthening Phase-----	45
23.	Transmission Electron Micrograph of Structure No. 5, 7050-TX1-----	46
24.	Transmission Electron Micrograph of Structure No. 6, 7050-TX2-----	47
25.	Transmission Electron Micrograph of Structure No. 7, (7050-TX3)-----	48
26.	Transmission Electron Micrograph of Structure No. 7, (7050-TX3)-----	49
27.	Transmission Electron Micrograph of 7475-T61, Structure No. 11-----	50
28.	Transmission Electron Micrograph of 7475-T6, Structure No. 12-----	51
29.	Transmission Electron of 2124 (loMn)-T31, Structure No. 17-----	52
30.	Transmission Electron Micrograph of 2124 (hiMn)-T86, Structure No. 19-----	53
31.	Transmission Electron Micrograph of 2024 (loMn)-T36, Structure No. 22-----	54



# LIST OF ILLUSTRATIONS (CONTINUED)

<u>No.</u>		<u>Page</u>
32	Transmission Electron Micrograph of 2024(10Mn)-T81, Structure No. 23-----	55
33.	Transmission Electron Micrograph of 2024-T8X, Structure No. 26-----	56
34.	Microstructures of X7080(hiCu)-T76 and 7050-T76---	59
35.	Micrograph Showing Constituent Particles in (a) 2024, (b) 2124, and (c) 2048. (100X)-----	61
36.	Toughness of the 7XXX Series Alloys Measured by Unit Crack Propagation Energy-----	67
37.	Notch Toughness of the 7XXX Series Alloys-----	68
38.	Toughness of the 2XXX Series Alloys Measured by Unit Crack Propagation Energy-----	69
39.	Notch Toughness of the 2XXX Series Alloys-----	70
40.	Cyclic Stress Intensity Range, $\Delta K$ , Vs. Cyclic Fatigue Crack Growth Rate, $\Delta a/\Delta N$ -----	72
41.	Effects of Microstructure and Test Variables on Crack Propagation Life of 2024 Type Sheet-----	84
42.	Effects of Volume % Constituent and Temper in Fatigue Crack Growth Rate of 2024 Sheet-----	85
43.	Scanning Electron Fractograph Illustrating Ductile Rupture Associated with Constituent Particles-----	92
44.	Scanning Electron Fractograph Illustrating Constituent Effect at Intermediate $\Delta K$ -----	93
45.	Scanning Electron Fractograph of 2024 (hiMn)-T31--	94
46.	Fracture Surface of 7050-T76 Illustrating Small Effect of Constituent Particles on Crack Growth Rate-----	95
47.	Fracture Surface of X7080(hiCu)-T76 Showing that Constituent Particles are only a Local, Temporary Obstacle to Crack Growth-----	96
48.	Scanning Electron Fractograph of X7080 (hiCu)-T76 Showing Small Effect of $Al_2O_3Cu_2Mn_3$ Dispersoid on Crack Growth-----	97

# LIST OF ILLUSTRATIONS (CONTINUED)

<u>No.</u>		<u>Page</u>
49.	Fracture Surface of X7080 (hiCu)-T76 Showing Small Effect of Al <sub>20</sub> Cu <sub>2</sub> Mn <sub>3</sub> Dispersoid on Crack Growth-----	98
50.	Scanning Electron Fractograph of 7080(hiCu)-T76 Having Two Different Grain Sizes Showing Similar Fracture Appearance-----	99
51.	Scanning Electron Micrograph of X7080 (hiCu)-T76 Having Ductile Fracture Surface-----	101
52.	Scanning Electron of X7080-T76 Showing Faceted Fracture Surface-----	102
53.	Fracture Surface of 2048-T31-----	103
54.	Fracture Surface of 2048-T86-----	104
55.	Fracture Surface of 2048-T86 Showing Dimpled Fracture Area-----	105
56.	Fracture Surface of 2048-T31 Showing Plateau and Ridge Fracture Appearance-----	106
57.	Fracture Surface of X7080-T76 Showing Plateau and Ridge Fracture Appearance-----	107
58.	Fracture Surface of 7050-T76 Showing in Greater Detail Plateau and Ridge Fracture Appearance-----	108
59.	Fracture Surface of 7050-T76 Showing Plateau and Ridge Fracture Appearance-----	109
60.	Fracture Surface of 2024-T31 Showing Rimped Fracture Appearance-----	110
61.	Fracture Surface of 2048-T31 Showing Rimped Fracture Appearance-----	111
62.	Fracture Appearance of 7050-T76 Showing "Cleavage-Like" Regions Present on the Fracture Surface----	112
63.	Mean Calculated Fatigue Propagation Life (both 2 and 20 Hz) for 6050 with Various Degrees of Precipitation-----	122
64.	Mean Calculated Fatigue Propagation Life (both frequencies and environments) for Alloy 2024-----	123

# LIST OF ILLUSTRATIONS (CONTINUED)

<u>No.</u>		<u>Page</u>
65.	Relationship Between Fatigue Crack Propagation Performance and Fracture Toughness for 2XXX and 7XXX Sheet Alloys-----	127
66.	Fully Reversed Constant Strain Amplitude Controlled Fatigue Tests of 2024 in Three Tempers-----	129
67.	Effects of Moisture Content on Fatigue Crack Growth of Aluminum Alloys (Ref. 63)-----	134
68.	Effect of Frequency and Environment on Fatigue Crack Growth Rate of 2X24-T31 and T86 Tempers-----	136
69.	Yield Strength Vs. Fatigue Crack Propagation Performance of 2XXX and 7XXX Alloy Sheet-----	141
A-1	Compact Tension Keyhole Specimen for Fatigue Crack Initiation Testing-----	159
B-1	Comparison of the Toughness of the 25 2XXX and 7XXX Alloys with Commercially Established Al Alloys----	167
B-2	Comparison of the Notch Toughness of the 25 2XXX and 7XXX Alloys with Commercially Established Al Alloys-----	168
C-1	Cyclic Stress Intensity Range, $\Delta K$ , Vs. Cyclic Fatigue Crack Growth Rate, $\Delta a/\Delta N$ , of Structure No. 1-----	170
C-2	Cyclic Stress Intensity Range, $\Delta K$ , Vs. Cyclic Fatigue Crack Growth Rate, $\Delta a/\Delta N$ , of Structure No. 1-----	171
C-3	Cyclic Stress Intensity Range, $\Delta K$ , Vs. Cyclic Fatigue Crack Growth Rate, $\Delta a/\Delta N$ , of Structure No. 2-----	172
C-4	Cyclic Stress Intensity Range, $\Delta K$ , Vs. Cyclic Fatigue Crack Growth Rate, $\Delta a/\Delta N$ , of Structure No. 2-----	173
C-5	Cyclic Stress Intensity Range, $\Delta K$ , Vs. Cyclic Fatigue Crack Growth Rate, $\Delta a/\Delta N$ , of Structure No. 3-----	174
C-6	Cyclic Stress Intensity Range, $\Delta K$ , Vs. Cyclic Fatigue Crack Growth Pate, $\Delta a/\Delta N$ , of Structure No. 3-----	175

# LIST OF ILLUSTRATIONS (CONTINUED)

<u>No.</u>		<u>Page</u>
C-7	Cyclic Stress Intensity Range, $\Delta K$ , Vs. Cyclic Fatigue Crack Rate, $\Delta a/\Delta N$ , of Structure No. 4-----	176
C-8	Cyclic Stress Intensity Range, $\Delta K$ , Vs. Cyclic Fatigue Crack Growth Rate, $\Delta a/\Delta N$ , of Structure No. 4-----	177
C-9	Cyclic Stress Intensity Range, $\Delta K$ , Vs. Cyclic Fatigue Crack Growth Rate $\Delta a/\Delta N$ , of Structure No. 5-----	178
C-10	Cyclic Stress Intensity Range, $\Delta K$ , Vs. Cyclic Fatigue Crack Growth Rate, $\Delta a/\Delta N$ , of Structure No. 5-----	179
C-11	Cyclic Stress Intensity Range, $\Delta K$ , Vs. Cyclic Fatigue Crack Growth Rate $\Delta a/\Delta N$ , of Structure No. 6-----	180
C-12	Cyclic Stress Intensity Range, $\Delta K$ , Vs. Cyclic Fatigue Crack Growth Rate, $\Delta a/\Delta N$ , of Structure No. 6-----	181
C-13	Cyclic Stress Intensity Range, $\Delta K$ , Vs. Cyclic Fatigue Crack Growth Rate $\Delta a/\Delta N$ , of Structure No. 7-----	182
C-14	Cyclic Stress Intensity Range, $\Delta K$ , Vs. Cyclic Fatigue Crack Growth Rate, $\Delta a/\Delta N$ , of Structure No. 7-----	183
C-15	Cyclic Stress Intensity Range, $\Delta K$ , Vs. Cyclic Fatigue Crack Growth Rate, $\Delta a/\Delta N$ , of Structure No. 8-----	184
C-16	Cyclic Stress Intensity Range, $\Delta K$ , Vs. Cyclic Fatigue Crack Growth Rate, $\Delta a/\Delta N$ , of Structure No. 8-----	185
C-17	Cyclic Stress Intensity Range, $\Delta K$ , Vs. Cyclic Fatigue Crack Growth Rate, $\Delta a/\Delta N$ , of Structure No. 9-----	186
C-18	Cyclic Stress Intensity Range, $\Delta K$ , Vs. Cyclic Fatigue Crack Growth Rate, $\Delta a/\Delta N$ , of Structure No. 9-----	187
C-19	Cyclic Stress Intensity Range, $\Delta K$ , Vs. Cyclic Fatigue Crack Growth Rate $\Delta a/\Delta N$ , of Structure No. 9-----	188



# LIST OF ILLUSTRATIONS (CONTINUED)

<u>No.</u>		<u>Page</u>
C-20	Cyclic Stress Intensity Range, $\Delta K$ , Vs. Cyclic Fatigue Crack Growth Rate, $\Delta a/\Delta N$ , of Structure No. 10-----	189
C-21	Cyclic Stress Intensity Range, $\Delta K$ , Vs. Cyclic Fatigue Crack Growth Rate, $\Delta a/\Delta N$ , of Structure No. 10-----	190
C-22	Cyclic Stress Intensity Range, $\Delta K$ , Vs. Cyclic Fatigue Crack Growth Rate, $\Delta a/\Delta N$ , of Structure No. 11-----	191
C-23	Cyclic Stress Intensity Range, $\Delta K$ , Vs. Cyclic Fatigue Crack Growth Rate $\Delta a/\Delta N$ , of Structure No. 11-----	192
C-24	Cyclic Stress Intensity Range, $\Delta K$ , Vs. Cyclic Fatigue Crack Growth Rate, $\Delta a/\Delta N$ , of Structure No. 12-----	193
C-25	Cyclic Stress Intensity Range, $\Delta K$ , Vs. Cyclic Fatigue Crack Growth Rate, $\Delta a/\Delta N$ , of Structure No. 12-----	194
C-26	Stress Intensity Range, $\Delta K$ , Vs. Cyclic Fatigue Crack Growth Rate, $\Delta a/\Delta N$ , of Structure No. 12----	195
C-27	Cyclic Stress Intensity Range, $\Delta K$ , Vs. Cyclic Fatigue Crack Growth Rate, $\Delta a/\Delta N$ , of Structure No. 12-----	196
C-28	Cyclic Stress Intensity Range, $\Delta K$ , Vs. Cyclic Fatigue Crack Growth Rate, $\Delta a/\Delta N$ , of Structure No. 13-----	197
C-29	Cyclic Stress Intensity Range, $\Delta K$ , Vs. Cyclic Fatigue Crack Growth Rate, $\Delta a/\Delta N$ , of Structure No. 13-----	198
C-30	Cyclic Stress Intensity Range, $\Delta K$ , Vs. Cyclic Fatigue Crack Growth Rate $\Delta a/\Delta N$ , of Structure No. 14-----	199
C-31	Cyclic Stress Intensity Range, $\Delta K$ , Vs. Cyclic Fatigue Crack Growth Rate, $\Delta a/\Delta N$ , of Structure No. 14-----	200
C-32	Cyclic Stress Intensity Range, $\Delta K$ , Vs. Cyclic Fatigue Crack Growth Rate, $\Delta a/\Delta N$ , of Structure No. 15-----	201

# LIST OF ILLUSTRATIONS (CONTINUED)

<u>No.</u>		<u>Page</u>
C-33	Cyclic Stress Intensity Range, $\Delta K$ , Vs. Cyclic Fatigue Crack Growth Rate, $\Delta a/\Delta N$ , of Structure No. 15-----	202
C-34	Cyclic Stress Intensity Range, $\Delta K$ , Vs. Cyclic Fatigue Crack Growth Rate, $\Delta a/\Delta N$ , of Structure No. 16-----	203
C-35	Cyclic Stress Intensity Range, $\Delta K$ , Vs. Cyclic Fatigue Crack Growth Rate, $\Delta a/\Delta N$ , of Structure No. 16-----	204
C-36	Cyclic Stress Intensity Range, $\Delta K$ , Vs. Cyclic Fatigue Crack Growth Rate, $\Delta a/\Delta N$ , of Structure No. 17-----	205
C-37	Cyclic Stress Intensity Range, $\Delta K$ , Vs. Cyclic Fatigue Crack Growth Rate, $\Delta a/\Delta N$ , of Structure No. 17-----	206
C-38	Cyclic Stress Intensity Range, $\Delta K$ , Vs. Cyclic Fatigue Crack Growth Rate, $\Delta a/\Delta N$ , of Structure No. 18-----	207
C-39	Cyclic Stress Intensity Range, $\Delta K$ , Vs. Cyclic Fatigue Crack Growth Rate, $\Delta a/\Delta N$ , of Structure No. 18-----	208
C-40	Cyclic Stress Intensity Range, $\Delta K$ , Vs. Cyclic Fatigue Crack Growth Rate, $\Delta a/\Delta N$ , of Structure No. 19-----	209
C-41	Cyclic Stress Intensity Range, $\Delta K$ , Vs. Cyclic Fatigue Crack Growth Rate, $\Delta a/\Delta N$ , of Structure No. 19-----	210
C-42	Cyclic Stress Intensity Range, $\Delta K$ , Vs. Cyclic Fatigue Crack Growth Rate $\Delta a/\Delta N$ , of Structure No. 20-----	211
C-43	Cyclic Stress Intensity Range, $\Delta K$ , Vs. Cyclic Fatigue Crack Growth Rate, $\Delta a/\Delta N$ , of Structure No. 20-----	212
C-44	Cyclic Stress Intensity Range, $\Delta K$ , Vs. Cyclic Fatigue Crack Growth Rate, $\Delta a/\Delta N$ , of Structure No. 21-----	213

# LIST OF ILLUSTRATIONS (CONTINUED)

<u>No.</u>		<u>Page</u>
C-45	Cyclic Stress Intensity Range, $\Delta K$ , Vs. Cyclic Fatigue Crack Growth Rate, $\Delta a/\Delta N$ , of Structure No. 21 -----	214
C-46	Cyclic Stress Intensity Range, $\Delta K$ , Vs. Cyclic Fatigue Crack Growth Rate $\Delta a/\Delta N$ , of Structure No. 22-----	215
C-47	Cyclic Stress Intensity Range, $\Delta K$ , Vs. Cyclic Fatigue Crack Growth Rate, $\Delta a/\Delta N$ , of Structure No. 22-----	216
C-48	Cyclic Stress Intensity Range, $\Delta K$ , Vs. Cyclic Fatigue Crack Growth Rate, $\Delta a/\Delta N$ , of Structure No. 23-----	217
C-49	Cyclic Stress Intensity Range, $\Delta K$ , Vs. Cyclic Fatigue Crack Growth Rate, $\Delta a/\Delta N$ , of Structure No. 23-----	218
C-50	Cyclic Stress Intensity Range, $\Delta K$ , Vs. Cyclic Fatigue Crack Growth Rate, $\Delta a/\Delta N$ , of Structure No. 24-----	219
C-51	Cyclic Stress Intensity Range, $\Delta K$ , Vs. Cyclic Fatigue Crack Growth Rate, $\Delta a/\Delta N$ , of Structure No. 24-----	220
C-52	Cyclic Stress Intensity Range, $\Delta K$ , Vs. Cyclic Fatigue Crack Growth Rate, $\Delta a/\Delta N$ , of Structure No. 24-----	221
C-53	Cyclic Stress Intensity Range, $\Delta K$ , Vs. Cyclic Fatigue Crack Growth Rate, $\Delta a/\Delta N$ , of Structure No. 25-----	222
C-54	Cyclic Stress Intensity Range, $\Delta K$ , Vs. Cyclic Fatigue Crack Growth Rate, $\Delta a/\Delta N$ , of Structure No. 25-----	223
C-55	Cyclic Stress Intensity Range, $\Delta K$ , Vs. Cyclic Fatigue Crack Growth Rate, $\Delta a/\Delta N$ , of Structure No. 26-----	224
C-56	Cyclic Stress Intensity Range, $\Delta K$ , Vs. Cyclic Fatigue Crack Growth Rate, $\Delta a/\Delta N$ , of Structure No. 26-----	225



# LIST OF ILLUSTRATIONS (CONTINUED)

<u>No.</u>		<u>Page</u>
C-57	Cyclic Stress Intensity Range, $\Delta K$ , Vs. Cyclic Fatigue Crack Growth Rate, $\Delta a/\Delta N$ , of Structure No. 27-----	226
C-58	Cyclic Stress Intensity Range, $\Delta K$ , Vs. Cyclic Fatigue Crack Growth Rate, $\Delta a/\Delta N$ , of Structure No. 27-----	227
C-59	Cyclic Stress Intensity Range, $\Delta K$ , Vs. Cyclic Fatigue Crack Growth Rate, $\Delta a/\Delta N$ , of Structure No. 28-----	228
C-60	Cyclic Stress Intensity Range, $\Delta K$ , Vs. Cyclic Fatigue Crack Growth Rate, $\Delta a/\Delta N$ , of Structure No. 28-----	229
C-61	Cyclic Stress Intensity Range, $\Delta K$ , Vs. Cyclic Fatigue Crack Growth Rate, $\Delta a/\Delta N$ , for Commercial 7075-T6-----	230
C-62	Cyclic Stress Intensity Range, $\Delta K$ , Vs. Cyclic Fatigue Crack Growth Rate, $\Delta a/\Delta N$ , for Commercial 7075-T6-----	231
D-1	Cyclic Stress Intensity Range, $\Delta K$ , Vs. Cyclic Fatigue Crack Growth Rate, $\Delta a/\Delta N$ , of Structure No. 1-----	233
D-2	Cyclic Stress Intensity Range, $\Delta K$ , Vs. Cyclic Fatigue Crack Growth Rate, $\Delta a/\Delta N$ , of Structure No. 3-----	234
D-3	Cyclic Stress Intensity Range, $\Delta K$ , Vs. Cyclic Fatigue Crack Growth Rate, $\Delta a/\Delta N$ , of Structure No. 4-----	235
D-4	Cyclic Stress Intensity Range, $\Delta K$ , Vs. Cyclic Fatigue Crack Growth Rate, $\Delta a/\Delta N$ , of Structure No. 9-----	236
D-5	Cyclic Stress Intensity Range, $\Delta K$ , Vs. Cyclic Fatigue Crack Growth Rate $\Delta a/\Delta N$ , of Structure No. 10-----	237
D-6	Cyclic Stress Intensity Range, $\Delta K$ , Vs. Cyclic Fatigue Crack Growth Rate, $\Delta a/\Delta N$ , of Structure No. 11-----	238
D-7	Cyclic Stress Intensity Range, $\Delta K$ , Vs. Cyclic Fatigue Crack Growth Rate, $\Delta a/\Delta N$ , of Structure No. 13-----	239



# LIST OF ILLUSTRATIONS (CONTINUED)

<u>No.</u>		<u>Page</u>
D-8	Cyclic Stress Intensity Range, $\Delta K$ , Vs. Cyclic Fatigue Crack Growth Rate, $\Delta a/\Delta N$ , of Structure No. 16-----	240
D-9	Cyclic Stress Intensity Range, $\Delta K$ , Vs. Cyclic Fatigue Crack Growth Rate, $\Delta a/\Delta N$ , of Structure No. 17-----	241
D-10	Cyclic Stress Intensity Range, $\Delta K$ , Vs. Cyclic Fatigue Crack Growth Rate, $\Delta a/\Delta N$ , of Structure No. 21-----	242
D-11	Cyclic Stress Intensity Range, $\Delta K$ , Vs. Cyclic Fatigue Crack Growth Rate, $\Delta a/\Delta N$ , of Structure No. 24-----	243
E-1	Cyclic Stress Intensity Range, $\Delta K$ , Vs. Cyclic Fatigue Crack Growth Rate, $\Delta a/\Delta N$ , of Structure No. 1-----	245
E-2	Cyclic Stress Intensity Range, $\Delta K$ , Vs. Cyclic Fatigue Crack Growth Rate $\Delta a/\Delta N$ , of Structure No. 3-----	246
E-3	Cyclic Stress Intensity Range, $\Delta K$ , Vs. Cyclic Fatigue Crack Growth Rate, $\Delta a/\Delta N$ , of Structure No. 4-----	247
E-4	Cyclic Stress Intensity Range, $\Delta K$ , Vs. Cyclic Fatigue Crack Growth Rate, $\Delta a/\Delta N$ , of Structure No. 9-----	248
E-5	Cyclic Stress Intensity Range, $\Delta K$ , Vs. Cyclic Fatigue Crack Growth Rate $\Delta a/\Delta N$ , of Structure No. 10-----	249
E-6	Cyclic Stress Intensity Range, $\Delta K$ , Vs. Cyclic Fatigue Crack Growth Rate, $\Delta a/\Delta N$ , of Structure No. 11-----	250
E-7	Cyclic Stress Intensity Range, $\Delta K$ , Vs. Cyclic Fatigue Crack Growth Rate, $\Delta a/\Delta N$ , of Structure No. 13-----	251
E-8	Cyclic Stress Intensity Range, $\Delta K$ , Vs. Cyclic Fatigue Crack Growth Rate, $\Delta a/\Delta N$ , of Structure No. 16-----	252
E-9	Cyclic Stress Intensity Range, $\Delta K$ , Vs. Cyclic Fatigue Crack Growth Rate, $\Delta a/\Delta N$ , of Structure No. 17-----	253

LIST OF ILLUSTRATIONS (CONTINUED)

<u>No.</u>		<u>Page</u>
E-10	Cyclic Stress Intensity Range, $\Delta K$ , Vs. Cyclic Fatigue Crack Growth Rate $\Delta a/\Delta N$ , of Structure No. 21-----	254
E-11	Cyclic Stress Intensity Range, $\Delta K$ , Vs. Cyclic Fatigue Crack Growth Rate, $\Delta a/\Delta N$ , of Structure No. 24-----	255

# LIST OF TABLES

<u>No.</u>		<u>Page</u>
1.	Summary of Microstructural Effects on Fatigue Crack Propagation Rate (FCPR) - 7075 and 7050-Type Alloys-----	3
2.	Summary of Microstructural Effects on Fatigue Crack Propagation Rate (FCPR) - 2024-Type Alloys----	4
3.	Summary of Effects of Testing Variables on Fatigue Crack Propagation Rate (FCPR)-----	5
4.	Chemical Composition of Alloys-----	16
5.	Schedule of Specimen Loading - Center Notch Specimen-----	22
6.	Microstructural Features of 7XXX-Type Alloys-----	24
7.	Microstructural Features of 2XXX Alloys-----	25
8.	Volume Percent Constituent Particles Present in Selected 2XXX and 7XXX Alloys-----	57
9.	Temper, Mechanical Properties, and Grain Sizes of 7XXX Alloy Sheet-----	62
10.	Temper and Mechanical Properties of 2XXX Alloy Sheet-----	63
11.	Transverse Tear and Notch Tensile Properties of the 7XXX Series Alloy Sheet-----	64
12.	Transverse Tear and Notch Tensile Properties of the 2XXX Series Alloy Sheet-----	65
13.	Mechanical Properties of Supplementary Structures---	66
14.	Estimated Fatigue Crack Propagation Lives from Replicate Fatigue Crack Growth Tests-----	75
15.	Microprobe Analysis of The Fracture Surface of Selected Structures-----	115
16.	Summary of Microstructural Effects on Fatigue Crack Propagation Rate (FCPR) - 7075 and 7050-Type Alloys-	145
17.	Summary of Microstructural Effects on Fatigue Crack Propagation Rate (FCPR) - 2024-Type Alloys-----	146

LIST OF TABLES - Continued

<u>No.</u>		<u>Page</u>
18.	Summary of Effects of Testing Variables on Fatigue Crack Propagation Rate (FCPR)-----	147
A-1	Fatigue Crack Initiation Test Results-----	162



## 1. SUMMARY

### 1.1 Scope

The goal of this program was to provide guidance for development of optimum metallurgical structures to retard fatigue crack growth in high-strength aluminum alloys, yet maintaining essential mechanical and physical properties.

Alloys selected for this program were variants of commercial high-strength aluminum alloys. By employing various processing techniques, a large and systematic variety of structures was produced. Twenty-five different structures which fulfilled initial requirements for a set of designed experiments were produced; 13 based on the 7XXX series (Al-Zn-Mg-Cu) aluminum alloys and 12 based on the 2XXX series (Al-Cu-Mg) alloys. Three additional structures were produced and tested after preliminary analysis of test results of the original 25. All structures were tested in sheet gauges (0.085 inch for 7XXX and 0.065 inch for 2XXX).

The following table summarizes the microstructural and composition variants examined:

<u>7XXX</u>	<u>2XXX</u>
Type of Strengthening Precipitate	Type of Strengthening Precipitate
Copper Content	Dislocation Density
Amount of Constituent	Amount of Constituent
Size of Dispersoid	Amount of Dispersoid
Type and Amount of Dispersoid	Copper Content
Grain Size	

Constant amplitude fatigue crack propagation tests were conducted over the  $\Delta K$  range of about 4 to 20  $\text{ksi}\sqrt{\text{in.}}$  in room

temperature air at 94 to 99% and 5 to 10% relative humidity and at test frequencies of 2 and 20 Hz. Stress ratio was 1/3.

Selected structures were also tested in the higher humidity environment at  $\Delta K$  2 to 8 ksi $\sqrt{\text{in.}}$  and at nominal frequencies of 20 or 50 Hz.

## 1.2 Results and Discussion

Results are summarized in Tables 1, 2, and 3 and are discussed in the following sections, 1.2.1 through 1.2.7.

### 1.2.1 Insoluble Constituents

Insoluble constituent particles are those particles formed during solidification by separation of impurity elements Fe and Si. Effects on crack growth rate of decreasing the volume fraction of insoluble constituent particles depended on the levels of both toughness and  $\Delta K$ . Alloy-temper combinations which developed relatively low toughness with normal levels of constituent particles (7075-T6 and 2024-T86) benefited from decreasing the volume fraction at levels of  $\Delta K$  of about 15 ksi $\sqrt{\text{in.}}$  or higher. Alloy-temper combinations which developed relatively high toughness (2024-T31) showed no effect.

### 1.2.2 Dispersoids

Dispersoids are small (.01 to .5  $\mu\text{m}$ ) solid state precipitates containing Mn, Cr, or Zr formed at temperatures above 750°F. Changing the amount and type of dispersoid did not influence crack growth rate. Increasing the size and interparticle spacing of the  $\text{Al}_{12}\text{Mg}_2\text{Cr}$  dispersoid in 7075-T6 increased toughness and decreased crack growth rates at higher  $\Delta K$  levels of about 15 ksi $\sqrt{\text{in.}}$  and greater.

TABLE 1

SUMMARY OF MICROSTRUCTURAL EFFECTS ON FATIGUE CRACK PROPAGATION RATE (FCPR)  
7075 AND 7050 TYPE ALLOYS

Microstructural Variant	Low Humidity Air $\Delta K > 5 \text{ ksi}\sqrt{\text{in.}}$	High Humidity Air $\Delta K > 2 \text{ ksi}\sqrt{\text{in.}}$	Comments
Precipitate type and morphology by increasing degree of precipitation in 7050.	Increasing degree of precipitation decreased FCPR.	Larger effect than in low humidity.	With increased degree of precipitation, precipitate changed from GP to $\eta'$ to mixtures of S, S', $\eta$ , and $\eta'$ .
Cu Content 1% vs. 2.3%	High Cu gave slightly lower FCPR.	High Cu gave lower FCPR, $\Delta K > 5 \text{ ksi}\sqrt{\text{in.}}$	Low Cu gave lower FCPR $\Delta K < 4 \text{ ksi}\sqrt{\text{in.}}$ . Confirmation of low $\Delta K$ result needed.
Volume % insoluble Constituent 0.5% vs. 1.2%	Low vol. % constituent gave lower FCPR $\Delta K > 15 \text{ ksi}\sqrt{\text{in.}}$	Low vol. % constituent gave lower FCPR $\Delta K > 15 \text{ ksi}\sqrt{\text{in.}}$	No effect when toughness already high by modifying Cr dispersoid.
$\text{Al}_{12}\text{Mg}_2\text{Cr}$ dispersoid size and distribution	Large, widely spaced dispersoids gave lower FCPR in 7075 $\Delta K > 15 \text{ ksi}\sqrt{\text{in.}}$	Large, widely spaced dispersoids gave lower FCPR $\Delta K > 15 \text{ ksi}\sqrt{\text{in.}}$	No effect in 7475 where toughness already high by reducing vol. % constituent.
Type of Dispersoid Zr, Mn, and Zr plus Mn	No effect.	No effect.	Varied in 7050 type alloy base.
Grain Size 5 to 65,000 grains/mm <sup>3</sup>	No effect.	No effect.	Varied in 7050 and 7075 type alloys.

TABLE 2

SUMMARY OF MICROSTRUCTURAL EFFECTS ON FATIGUE CRACK PROPAGATION RATE (FCPR)  
2024 TYPE ALLOYS

Microstructural Variant	Low Humidity Air $\Delta K > 5$ ksi in.	High Humidity Air $\Delta K > 2$ ksi/in.	Comments
Type of precipitate GP vs. S	GP zones gave lower FCPR. Disparity between FCPR of both precipitate types larger than in higher humidity.	GP zones gave lower FCPR when $\Delta K > 3$ ksi/in.	With decreasing $\Delta K$ FCPR converge for both types of precipitate. No effect of precipitate when $\Delta K < 3$ ksi/in.
Dislocation density 1% vs. 5% stretch after quenching.	1% Stretch gave lower FCPR $\Delta K > 15$ ksi/in.	1% Stretch gave lower FCPR $\Delta K > 15$ ksi/in.	Effect of stretch greater in T8 than in T3 temper.
Vol. % insoluble Constituent 1.4 vs. 2.28	Low Vol. % gave lower FCPR in T86 temper $\Delta K > 15$ ksi/in.	Low vol. % gave lower FCPR in T86 temper $\Delta K > 15$ ksi/in.	No effect in T31 temper.
Vol. % Mn dispersoid 1.1 vs. 2.6%	No effect.	No effect.	No tests at $\Delta K < 5$ ksi/in.
Cu Content 3.25 vs. 4.25%	Low Cu gave lower FCPR in both T86 and T31 tempers.	Low Cu gave lower FCPR in both T86 and T31 tempers.	Only T31 tested $\Delta K < 5$ ksi/in. Additional tests needed to confirm and explain Cu effect.



TABLE 3

## SUMMARY OF EFFECTS OF TESTING VARIABLES ON FATIGUE CRACK PROPAGATION RATE (FCPR)

Testing Variant	2024-Type	7075-Type	7050-Type
Environment Low vs. high humidity air.	Low humidity air gave lower FCPR.	Low humidity air gave lower FCPR.	5% RH gave lower FCPR.
Frequency 2 vs. 20 Hz.	Little effect in high humidity air. 20 Hz gave lower FCPR in low humidity air.	Generally smaller effects than in 2024-T31. 2 Hz gave lower FCPR than 20 Hz in high humidity and gave higher FCPR in low humidity.	2 Hz gave lower FCPR in high humidity in T76 temper.

### 1.2.3 Grain Size

Although the larger grain sizes studied in this work extended well beyond the size range encountered in commercial sheet fabricated from ingots, crack propagation rates were not affected in high-strength 7XXX alloys.

### 1.2.4 Copper Content

In 7XXX alloys increasing Cu content in X7080-type alloys decreased fatigue crack growth rates in both high and low humidity air at  $\Delta K$  above  $5 \text{ ksi}\sqrt{\text{in.}}$ . Limited data at  $\Delta K$  levels below  $4 \text{ ksi}\sqrt{\text{in.}}$  in high humidity air indicated that the lower Cu alloy had slightly better fatigue resistance, but additional tests are needed to confirm this indication. In 2XXX alloys, reducing Cu content (2048 vs 2X24) was generally beneficial in improving crack growth resistance with the greatest improvement noted at low  $\Delta K$ . The role of copper on fatigue crack growth mechanisms of both is not completely understood. It is hypothesized that copper content has a strong relationship on crack growth kinetics in presence of moisture. At intermediate  $\Delta K$ , improved performance of 2048 alloys over 2X24 alloys is attributed to increased fracture toughness because of lower volume fraction of  $\text{CuAl}_2$  and  $\text{Al}_2\text{CuMg}$ .

### 1.2.5 Dislocation Density

Increasing the amount of stretch in alloy 2024 after quenching increased crack propagation rates. Based on life prediction analysis, an increase in percent stretch from 1 to 5% increased the crack propagation rate and reduced fatigue life. This decrease in life is attributed to a decrease in ductility or toughness and,

consequently, a smaller capability to accommodate strain during the fatigue process.

#### 1.2.6 Strengthening Precipitate Type (Temper)

The type of precipitate significantly affected the fatigue crack propagation rate in 2XXX alloys at intermediate  $\Delta K$ . GP zones (T3 tempers) provided a more fatigue-resistant microstructure than did S' transition precipitate (T8 tempers).

The effect of precipitate type was related to material ductility, response to cyclic loading in strain-controlled fatigue tests, and sensitivity to moisture. Structures containing GP zones were more ductile (higher tensile elongation, energy to propagate a crack in tear test, and notch toughness) than structures containing S' precipitate aged to equivalent or higher monotonic strength levels. Moreover, structures with GP zones can develop higher stabilized cyclic strength after repeated reversed cyclic plastic strains. These results are in agreement with models which predict that increasing the product of cyclic strength and ductility decreases fatigue crack growth rate.

Precipitate type in 2X24 alloys had no significant effect on crack propagation rate at lowest  $\Delta K$  levels tested in high humidity air. Convergence of growth rate for T3 and T8 tempers at very low  $\Delta K$  levels ( $<3 \text{ ksi}\sqrt{\text{in.}}$ ) was attributed to similarities in sensitivity to environment. Above the very low  $\Delta K$  levels, T3 tempers produced lower crack growth rates than T8 tempers in both high and low humidity.

Precipitate morphology also affected fatigue crack propagation characteristics in 7050-type alloys. Crack growth rates progressively decreased with increasing degree of precipitation. Magnitude of the improvement depended on moisture content of the surrounding atmosphere. Therefore, the phenomenon is believed to result from modifications in sensitivity to the environment.

#### 1.2.7 Environment and Test Frequency

Increasing relative humidity increased crack growth rates in all structures, but the magnitude of the effect depended upon microstructure, the inherent mechanical properties (viz, strength and ductility), and kinetics of the crack growth rate process in hostile environments. Environmentally-enhanced fatigue crack growth was noted in low humidity environments where moisture content was sufficient to cause environment-frequency interaction.

Frequency-environment interaction was observed in both 2XXX and 7XXX alloys. Decreasing frequency from 20 to 2 Hz in general resulted in either comparable or higher growth rates. This effect is attributed to the greater amount of time per cycle available for environment to interact with freshly created metal surfaces. In some 7XXX alloys, however, lowering frequency decreased crack growth rate in high humidity air. Decreasing cyclic growth rate with reduction in frequency is attributed to increased corrosion activity per cycle which blunts the crack and/or builds up corrosion residue on mating fracture surfaces, increasing crack closure forces which retard crack growth. Differences in frequency response to different microstructures is therefore related to crack growth kinetics of the material-environment interaction.



### 1.3 Conclusions

Conclusions are presented in detail in Section 6. The most significant conclusions regarding effects of microstructure and composition are summarized as follows.

1. Strengthening precipitate had the largest effect on fatigue crack propagation rate at  $\Delta K$  levels above about 4 ksi $\sqrt{\text{in}}$ .
2. Amounts of the major alloying elements had the largest effect on fatigue crack propagation rate at  $\Delta K$  levels below about 3 ksi $\sqrt{\text{in}}$ .
3. Increasing dislocation density as modified by stretching 2XXX alloys after quenching had a lesser but statistically significant effect on increasing fatigue crack propagation rate.
4. Insoluble constituent particles had little effect and dispersoid particles had no effect on fatigue crack propagation rate at  $\Delta K$  levels much below about 15 ksi $\sqrt{\text{in}}$  for both 2XXX and 7XXX alloys.
5. Grain size from 5 to 65,000 grains per mm<sup>3</sup> had no effect on crack growth rate in peak and overaged 7XXX alloys.

## 2. INTRODUCTION

Prior to the 1960's, aircraft structure designers tended to emphasize tensile yield and ultimate strengths to provide the most favorable strength to weight ratio. Introduction of linear elastic fracture mechanics concepts, however, indicated that structural members containing cracks could fail at gross section stresses considerably lower than the yield strength if resistance of the material to unstable propagation of a crack (i.e., fracture toughness) was low. Consequently, designers began requesting improvements in fracture toughness which resulted in development of such high toughness aluminum alloys as 2124, 7475, etc., to increase aircraft reliability. However, analysis of the failure mechanisms in aircraft structural members indicates that any further improvements in aircraft reliability or structural efficiency will depend on development of improved fatigue-resistant alloys. Consequently, need has arisen for more definitive information concerning effects of metallurgical structure as well as alloy composition and temper effects on resistance to fatigue crack propagation.

Improvements in fatigue resistance to high-strength aluminum alloys lie in ability to produce metallurgical structures which resist formation of microstructural instabilities which can lead to fatigue crack initiation and which also resist subsequent crack growth. Toward this goal numerous investigations have been conducted to identify microstructural features which influence and control the fatigue process[1 to 21].\* However, conclusions

---

\*Brackets indicate references.

reached in these studies are far from complete and have left many microstructural effects in doubt. For example, little information is known about the role of both strengthening precipitates and dispersoids (0.01 to 0.5  $\mu\text{m}$  high temperature, solid state precipitates) in the fatigue process. In addition, the effect of larger ( $\sim 2$  to 50  $\mu\text{m}$ ) solidification or constituent particles on fatigue properties of aluminum alloys, although the subject of many investigations, is not well understood. Effects of grain size and shape are also not entirely understood.

Also contributing to lack of understanding of the fatigue behavior of aluminum alloys is the interaction between microstructure and testing variables such as frequency and environment. For example, investigators[22] have shown that fatigue crack propagation of aluminum alloys can be quite sensitive to atmospheric moisture content and test frequency. Consequently, if these variables are not controlled, e.g., moisture content of ambient lab air, conflicting results may be obtained by different investigators. Thus, not only must effects of microstructure be considered, but effects of testing variables such as environment and frequency must also be considered since these variables certainly influence the fatigue process through their interaction with microstructure.

The alloy design selected for this program was purposely intended to avoid the necessity of making comparison with fatigue data presently available in the literature since, as stated above, it is a difficult, if not impossible, task to compare data generated

in different laboratories. Therefore, all comparisons were internal and subject to highly controlled test procedures to assure as nearly as possible identical circumstances. This procedure provided a means to evaluate statistically the interaction of mechanical, microstructural, and environmental variables on fatigue crack propagation.

Alloys and microstructures were selected on the premise that other mechanical and physical requirements must be maintained if a viable commercial aluminum alloy is to become a reality. It is important to emphasize these latter material requirements because any loss in yield strength or fracture toughness, for example, must not be such that the material will fail by monotonic loading, yet be "fatigue resistant." In addition, any major alteration of alloying elements to improve fatigue properties must not be at the expense of other properties such as stress-corrosion cracking (SCC) resistance or resistance to fatigue crack initiation. Consequently, the approach used in this program in developing aluminum alloys having improved resistance to fatigue crack propagation was to restrict the major alloying elements to the range which has been shown to be near optimal for strength, toughness, and resistance to SCC. Resistance to fatigue crack initiation was checked to ensure that improvements in propagation behavior would not lower resistance to initiation.

In summary, this program was designed to provide guidance on development of optimum microstructures required to resist fatigue



crack growth in high-strength aluminum alloys while maintaining essential mechanical and physical properties.

### 3. MATERIAL AND PROCEDURES

#### 3.1 Alloy Selection

Alloys selected for this program were variants of high-strength aluminum alloys which develop acceptable strength, toughness, and corrosion characteristics by controlling the type and amount of second-phase particles. In the high-strength, precipitation-hardening aluminum alloys, three types of second-phase particles are present which control static strength and toughness: (a) strengthening precipitates ( $\sim 0.001$  to  $0.5 \mu\text{m}$ ) formed during natural or room temperature aging and artificial or elevated temperature aging below  $400^\circ\text{F}$ , (b) small ( $0.01$  to  $0.5 \mu\text{m}$ ) solid state precipitates containing Mn, Cr, or Zr called dispersoids formed at temperatures above  $750^\circ\text{F}$ , and (c) the larger ( $\sim 2$  to  $50 \mu\text{m}$ ) particles called constituents formed during solidification by separation of impurity elements Fe and Si (insoluble constituents) and alloying elements such as Cu and Mg (partially soluble constituents). These microstructural features encompass a range in particle sizes and interparticle spacings from a few Angstroms to thousands of Angstroms. This range in particle sizes also includes the range of incremental crack growth normally encountered during fatigue crack propagation tests. Thus, by employing the proper alloy design program, effectiveness of each of the particular second-phase particles can be assessed with regard to fatigue crack propagation

rate. Figure 1 compares the range of incremental crack growth with the size\* of the microstructural features in these structures.

Effects of Cu content, dislocations introduced by stretching after the quench from the solution heat treatment, and grain size were also examined.

The following table summarizes the microstructural and composition variants evaluated:

7XXX	2XXX
Type of Strengthening Precipitate	Type of Strengthening Precipitate
Copper Content	Dislocation Density
Amount of Constituent	Amount of Constituent
Size of Dispersoid	Amount of Dispersoid
Type and Amount of Dispersoid	Copper Content
Grain Size	

### 3.2 Experimentation

Listed in Table 4 are the alloys selected for this program along with their chemical analyses. By employing various processing techniques, a systematic variety of structures was produced. Initially, 25 different structures were produced; 13 structures based on 7XXX series (Al-Zn-Mg-Cu) aluminum alloys and 12 structures based on 2XXX series (Al-Cu-Mg) alloys. The 7XXX series were produced as 0.085-in. thick sheet and the 2XXX series as 0.065-in. thick sheet. After initial data were analyzed, additional structures were produced by heat treatment to test new hypotheses.

\*It would be more correct and meaningful to have used interparticle spacing rather than particle size for this comparison. However, due to segregation of the elements such as Fe, Si, Mn, Cr, and Zr, during solidification and their slow diffusion rate during subsequent thermal treatments, the interparticle spacing is nonuniform and is impossible to estimate meaningfully. Thus, the size of the particles was used as indicator of the scale of these features.

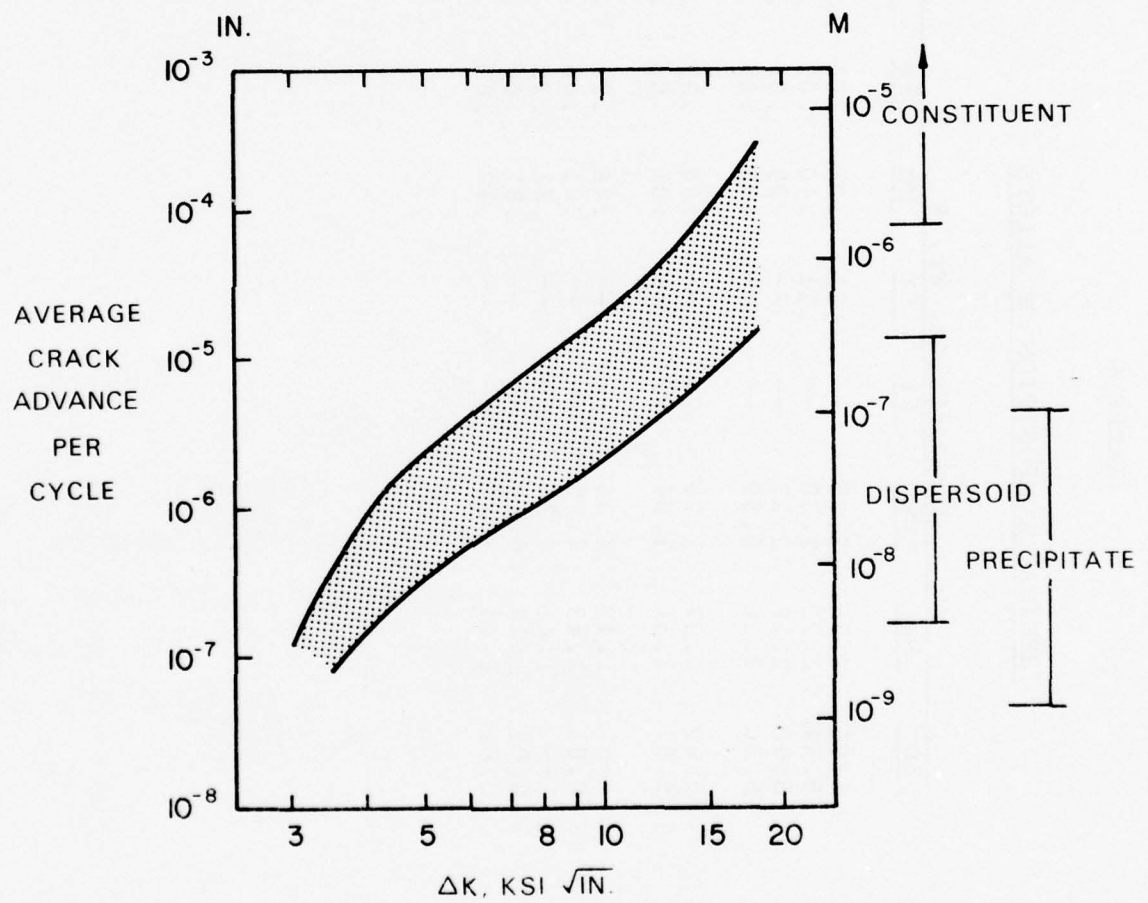


Figure 1 Relates Incremental Crack Advance to Size of Microstructural Feature

TABLE 4

## CHEMICAL COMPOSITION OF ALLOYS

Alloy	Composition, Wt. %							
	Zn	Mg	Cu	Cr	Zr	Mn	Fe	Ti
7050	6.06	2.38	2.35	--	.11	.01	.04	.02
7050+Mn	5.54	2.22	2.30	--	.11	.40	.05	.02
X7080 (hiCu)	5.90	2.18	2.27	--	--	.39	.06	.02
X7080	5.96	2.26	0.99	--	--	.38	.05	.01
7075	5.89	2.57	1.70	.20	--	.04	.28	.04
7475	5.57	2.31	1.64	.23	--	.01	.06	.02
2024 (loMn)	--	1.43	4.36	--	--	.46	.22	.02
2124 (loMn)	0.01	1.43	4.10	--	--	.41	.06	.01
2024 (hiMn)	--	1.41	4.34	--	--	.81	.21	.03
2124 (HiMn)	0.01	1.46	4.15	--	--	.81	.06	.02
2048	0.01	1.44	3.25	--	--	.38	.06	.02



### 3.2.1 Microstructural Examination

#### 3.2.1.1 Pre-Test Characterization

Initial microstructural characterization was carried out using both optical and electron microscopy. These techniques provided qualitative and quantitative information concerning these structures from grain size measurements to the strengthening precipitate size and shape. X-ray diffraction techniques were employed to determine the degree of recrystallization as well as to identify the second-phase particles. In addition, electron microprobe analysis was used to identify the larger constituent particles.

Quantitative information concerning the volume fraction of second-phase particles greater than 1  $\mu\text{m}$  was obtained using Quantitative Metallurgical System (QMS) equipment. Measurements were carried out at the highest magnification available with this instrument,  $\sim 700\times$ . At this magnification, the resolution of the instrument is 1  $\mu\text{m}$ . Seventy applications of the field,  $\sim 10,000 \mu\text{m}^2$  per application, were applied to each structure in each spatial direction; surface, cross-sectional and longitudinal. All measurements were carried out on lightly etched metallographic specimens. Measurements were conducted on the automatic mode to minimize operator errors.

#### 3.2.1.2 Post-Test Characterization

Analysis of fatigue crack propagation fracture surfaces was carried out using optical microscopy, scanning electron microscopy, and electron microscopy using two-stage, plastic-carbon replica techniques. Selected specimens were examined with these

techniques at various  $\Delta K$  levels to help establish the influence of metallurgical structure on crack propagation. In addition, electron microprobe analysis of the fatigue fracture surface was employed to study the role of the large constituent and dispersoid particles.

#### 3.2.2 Static Properties

Longitudinal and transverse tensile tests were made on all structures. Tear tests and notch-tensile tests were employed as indicators of fracture toughness for these materials[23]. The tear test measures energy required to propagate a crack (unit crack propagation energy - UPE) while the notch yield ratio (NYR) measures ability of material to deform plastically in the presence of a stress raiser (NYR = notch tensile strength/yield strength = NTS/YS). Increasing UPE and/or NYR can be correlated to increasing fracture toughness.

#### 3.2.3 Fatigue Initiation

Limited fatigue crack initiation tests were also conducted on the 25 structures. This evaluation was performed to ensure that any of the 25 microstructural variants considered would not seriously detract from fatigue initiation resistance. Procedure, results, and conclusions are presented in Appendix A.

#### 3.2.4 Fatigue Crack Propagation

All fatigue testing was conducted under a set of highly controlled test conditions in constant amplitude tension-tension loading on a closed loop electrohydraulic MTS materials test system. The test configuration was a 3-in. wide center crack tension specimen (Figure 2) of the T-L orientation (direction of principal

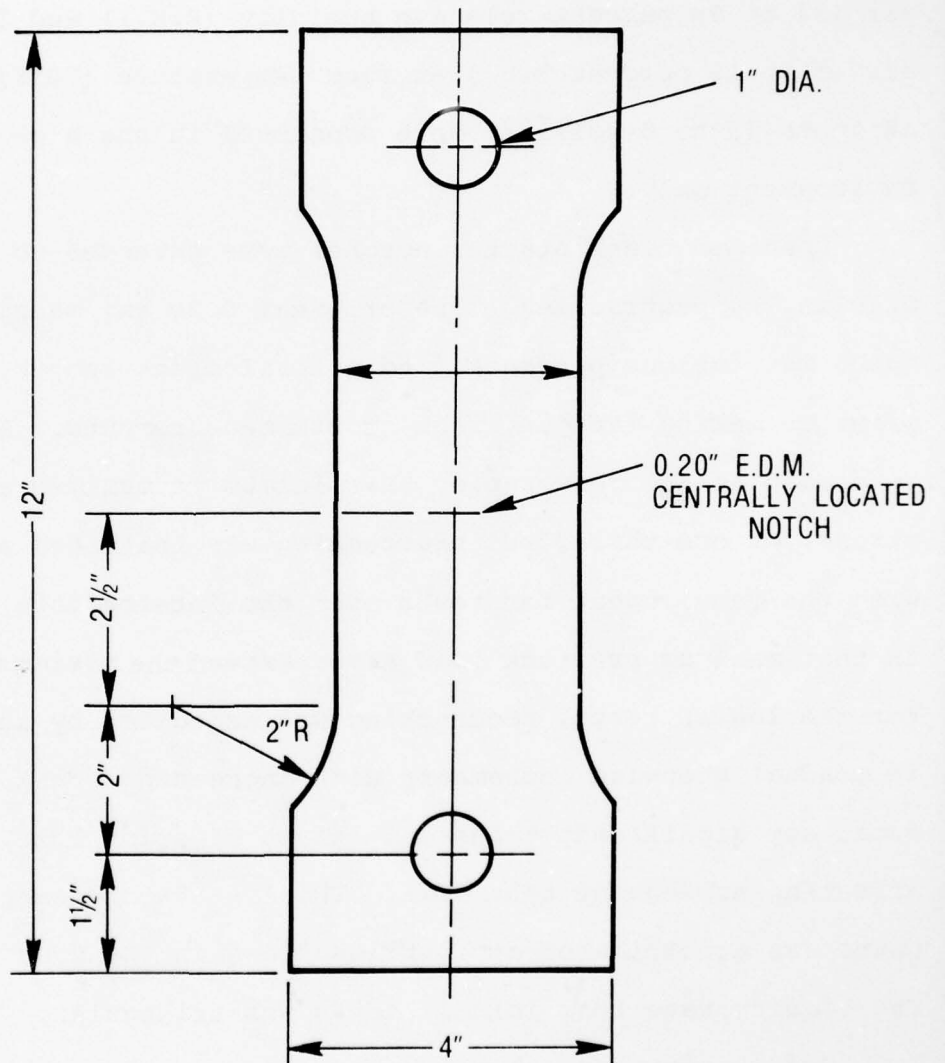


Figure 2 Center Crack Tension Fatigue Crack Propagation Specimen

loading normal to the sheet rolling direction and direction of crack travel parallel to the rolling direction). Intermediate level  $\Delta K$  tests ( $\Delta K > 4 \text{ ksi}\sqrt{\text{in.}}$ ) were conducted in both high humidity air (94 to 99 percent relative humidity (R.H.)) and low humidity air (5 to 10 percent R.H.) at room temperature (70°F). Low level  $\Delta K$  tests (2 to 8  $\text{ksi}\sqrt{\text{in.}}$ ) were conducted in the high humidity environment only.

Specimen crack starter notches were extended to a minimum of 0.10 in. by precracking. The original 0.20 in. machined starter notch was fatigue precracked to a total crack length,  $2a = 0.4 \text{ in.}$ , prior to making fatigue crack growth measurements. All data were generated at a stress ratio,  $R$ , minimum to maximum applied cyclic stress, of one-third, but precracking was initiated at  $R = 0.05$  with the requirement for tests over the intermediate levels of  $\Delta K$  that maximum precrack load never exceed the maximum test load. For the low  $\Delta K$  tests, precracking was expedited by shedding loads in gradual stepwise increments with increasing crack length to avoid any significant transient effect of prior load history affecting subsequent test data. The last 5% of precracking in all cases was accomplished at test loads and in the test environment. The loading wave form for all tests was triangular.

Crack growth measurements were made using an optical gridline technique where the crack was followed visually (5X magnification) as it traversed a series of reference gridlines photographically printed on the specimen surface. Crack travel was measured as a function of elapsed cycles and cyclic crack growth rate averaged



over the total crack length according to the following relationship:

$$\left(\frac{\Delta a}{\Delta N}\right)_i = \frac{1}{2} \left(\frac{\Delta 2a}{\Delta N}\right)_i = \frac{1}{2} \left(\frac{2a_i - 2a_{i-1}}{N_i - N_{i-1}}\right), i = 1, 2, 3,$$

where:

$2a_i$  = the total crack length (averaged through the thickness) at the  $i^{\text{th}}$  measurement point,

$N_i$  = the elapsed cycles at the  $i^{\text{th}}$  measurement point.

For a valid crack growth rate measurement, the increment of total crack travel had to equal or exceed 0.02 in. The stress intensity expression employed in determining the  $\Delta a/\Delta N$  vs  $\Delta K$  relationship is given by the following relationship[24]:

$$\Delta K = \Delta \sigma \sqrt{\pi \ell_i} \cdot Y \left( 2\ell_i/W \right), i = 1, 2, 3, \dots,$$

where:

$$Y \left( 2\ell_i/W \right) = 1 + 0.128 \left( \frac{2\ell_i}{W} \right) - 0.288 \left( \frac{2\ell_i}{W} \right)^2 + 1.525 \left( \frac{2\ell_i}{W} \right)^3,$$

and where  $\Delta \sigma$  is the applied gross stress range  $(\sigma_{\max} - \sigma_{\min})$ ,  $W$  the total specimen width, and  $2\ell_i$  the intermediate total crack length within the  $i^{\text{th}}$  increment of growth; that is,

$$2\ell_i = 1/2 (2a_i + 2a_{i-1}).$$

#### 3.2.4.1 Intermediate $\Delta K$ Tests ( $\Delta K$ 4 to 20 ksi $\sqrt{\text{in.}}$ )

The nominal applied maximum gross stress,  $\sigma_{\max}$ , was 8 ksi for all tests. Within a single test, the effect of frequency of load application was assessed by "frequency switching" between 2 and 20 Hz. Table 5 gives a schedule of center notch specimen loading

TABLE 5

SCHEDULE OF SPECIMEN LOADING - CENTER NOTCH SPECIMEN

Total Specimen Width,  $W = 3$  inch  
 Applied Stress Range,  $\Delta\sigma = 5.3$  ksi  
 Stress Ratio,  $R = 1/3$

Half Crack Length (a), * inches	Increment of Growth ( $\Delta a$ ), ** inches	Approx $\Delta K$ ksi $\sqrt{\text{in.}}$	Frequency, Hz
From 0.1 to 0.2	(Precrack)	-	20(+)
From 0.2 to 0.32	0.12	4.0	20
From 0.32 to 0.4	0.08	5.4	2
From 0.4 to 0.5	0.10	6.7	20
From 0.5 to 0.6	0.10	8.2	2
From 0.6 to 0.7	0.10	9.0	20
From 0.7 to 0.8	0.10	9.7	2
From 0.8 to 0.94	0.14	12.0	20
From 0.94 to 1.12(+)	0.18(+)	12.0(+)	2

\*Center notch panel total crack length is commonly referred to as 2a.  
 Original total starter notch length - 0.2 inch (or half length = 0.1 inch).

\*\*Each crack tip, assuming symmetrical growth.

conditions for all tests. Over the crack growth range of interest, this procedure was followed for all specimens to achieve maximum and uniform data for meaningful statistical analysis. Some pilot tests were run on selected 7XXX structures to observe reproducibility of data. Good reproducibility was confirmed using two or three replicate tests (for example, Figure 3). Good agreement was also observed in overlapping data for low and intermediate  $\Delta K$  tests (Figure 4 and Appendix E).

#### 3.2.4.2 Low $\Delta K$ ( $\Delta K$ 2 to 8 ksi $\sqrt{\text{in.}}$ )

After preliminary analysis of results of the intermediate  $\Delta K$  tests, some structures (1, 3, 4, 9, 10, 11, 13, 16, 17, 21, 24) were tested in high humidity environment only at nominal test frequencies of 20 or 50 Hz. Limited data were obtained at 2 Hz. The growth rate range was chosen to ensure overlapping between high and low ranges. Precracking loads and load ranges were successively reduced in small increments when approaching the test loads to avoid any transient effect. Once desired low crack growth rates were achieved during precrack, cyclic test loads were established and held constant for accumulation of crack growth rate data.

### 4. RESULTS

#### 4.1 Microstructural Characterization

A summary of the microstructural features resulting from the selected alloy and fabrication procedures is given in Tables 6 and 7. In Addition, Figures 5 to 33 serve to illustrate the microstructural features described in Tables 6 and 7.

TABLE 6  
MICROSTRUCTURAL FEATURES OF 7XXX TYPE ALLOYS

Structure Number	Alloy	Grain Size, $\mu\text{m}$ (1)			Figure Number	Constituent Phase Type	Amount	Dispersoid Phase (2) Type	Strengthening Phase (3)	Figure Number	Other Features
		Long-Transverse	Transverse	Longitudinal							
1	7050-T76	.0185	.0122	.0185	5	$\text{Al}_7\text{Cu}_2\text{Fe}$ , $\text{Al}_2\text{CuMg}$ , $\text{Mg}_2\text{Si}$	1.00%	ZrAl <sub>3</sub>	n'	20	Continuous $\eta$ precipitate on grain boundary no significant ppt.
2	7050-4461-T76	.0265	.0115	.0315	6	$\text{Mg}_2\text{Si}$ , $\text{Al}_{12}(\text{Fe,Mn})_{13}\text{Si}$	0.25%	ZrAl <sub>3</sub> , $\text{Al}_{20}\text{Mg}_{13}\text{Mn}_3$	n'	21	Similar to 7050 except for presence of $\eta$ dispersoid
3	X7080-41001-T76	.0550	.0170	.0550	7	$\text{Mg}_2\text{Si}$ , $\text{Al}_{12}(\text{Fe,Mn})_{13}\text{Si}$	0.25%	$\text{Al}_{20}\text{Cu}_2\text{Mn}_3$	n'	22	Continuous grain boundary precipitate, no ppt.
4	X7080-T6	Mixed Grain Size			8	$\text{Mg}_2\text{Si}$ , $\text{Al}_{12}(\text{Fe,Mn})_{13}\text{Si}$	0.25%	$\text{Al}_{20}\text{Cu}_2\text{Mn}_3$	n'	23	Small needle-like S' precipitate plus $\eta$ precipitate
5	7050-T71 (4)	.0185	.0122	.0185	*	$\text{Al}_7\text{Cu}_2\text{Fe}$ , $\text{Al}_2\text{CuMg}$ , $\text{Mg}_2\text{Si}$	1.00%	ZrAl <sub>3</sub>	S', n, n'	24	Larger lath S' plus $\eta$ larger.
6	7050-T72 (4)	.0185	.0122	.0185	*	$\text{Al}_7\text{Cu}_2\text{Fe}$ , $\text{Al}_2\text{CuMg}$ , $\text{Mg}_2\text{Si}$	1.00%	ZrAl <sub>3</sub>	S', S, n	25, 26	Discontinuous precipitate at grain boundary. Non-uniform precipitate in matrix.
7	7050-T73 (4)	.0185	.0122	.0185	*	$\text{Al}_7\text{Cu}_2\text{Fe}$ , $\text{Al}_2\text{CuMg}$ , $\text{Mg}_2\text{Si}$	1.00%	ZrAl <sub>3</sub>	S, n, n'	25, 26	Continuous grain boundary precipitate, no ppt.
8	X7080-41001-T76	1.0	0.20	1.0	9	$\text{Mg}_2\text{Si}$ , $\text{Al}_{12}(\text{Fe,Mn})_{13}\text{Si}$	0.25%	$\text{Al}_{20}\text{Cu}_2\text{Mn}_3$	GP		Similar dispersoid as #11
9	7075-T71	.013	0.011	.039	10	$\text{Al}_7\text{Cu}_2\text{Fe}$ , $\text{Al}_{12}(\text{Fe,Mn})_{13}\text{Si}$ , $\text{FeAl}_6$ , $\text{Mg}_2\text{Si}$	1.20%	$\text{Al}_{12}\text{Mg}_2\text{Cr}$	GP		Similar dispersoid as #12
10	7075-T6	.032	0.019	.095	11	$\text{Al}_7\text{Cu}_2\text{Fe}$ , $\text{Al}_{12}(\text{Fe,Mn})_{13}\text{Si}$ , $\text{FeAl}_6$ , $\text{Mg}_2\text{Si}$	1.20%	$\text{Al}_{12}\text{Mg}_2\text{Cr}$	GP, n'		Larger, more widely spaced dispersoid, discontinuous grain boundary precipitate, narrow ppt.
11	7475-T71	.0260	0.0130	0.0280	12	$\text{Al}_7\text{Cu}_2\text{Fe}$ , $\text{Al}_2\text{CuMg}$ , $\text{Mg}_2\text{Si}$	0.50%	$\text{Al}_{12}\text{Mg}_2\text{Cr}$	GP, n'		Smaller, closer spaced dispersoid, discontinuous precipitate at grain boundary, narrow ppt.
12	7475-T6	.0250	0.0195	0.030	13	$\text{Al}_7\text{Cu}_2\text{Fe}$ , $\text{Al}_2\text{CuMg}$ , $\text{Mg}_2\text{Si}$	0.50%	$\text{Al}_{12}\text{Mg}_2\text{Cr}$	GP, n'	28	Similar dispersoid as 9.
13	7075-T71	0.125	0.0155	0.100	14	$\text{Al}_7\text{Cu}_2\text{Fe}$ , $\text{Al}_{12}(\text{Fe,Mn})_{13}\text{Si}$ , $\text{FeAl}_6$ , $\text{Mg}_2\text{Si}$	1.20%	$\text{Al}_{12}\text{Mg}_2\text{Cr}$	GP, n'		

- (1) All structures were recrystallized.
- (2) The ZrAl<sub>3</sub> dispersoid is a spherical precipitate approximately 200-300 Å in diameter and can be coherent with the matrix. The  $\text{Al}_{12}\text{Mg}_2\text{Cr}$  dispersoid is a somewhat larger precipitate ranging from 0.05 to 0.3  $\mu\text{m}$  in diameter, depending on the thermal treatment. The  $\text{Al}_{20}\text{Mg}_{13}\text{Mn}_3$  is a larger, rod-like precipitate that ranges in size from 0.1 to 0.6  $\mu\text{m}$  in the long direction.
- (3) In 7XXX (Al-Zn-Mg-Cu) alloys the precipitate sequence is usually:  
solid solution  $\rightarrow \eta \rightarrow \eta' \rightarrow \eta''$   
GP = clusters of Zn and Mg atoms. Structure variable depending on Zn and Mg contents.  
n' = transition phase of  $\eta$ , partially coherent on {111} Al planes.  
n =  $\eta$  (ZnAl<sub>6</sub>) equilibrium phase.
- (4) The following nonconventional precipitation heat treatments were employed which produced S' and S:  
Structure #1 - Quenched directly from solution heat treatment temperature to 5000° molten salt, hold one minute, cold water quench.  
Structure #2 - Same as #1 but hold 5 minutes at 5000°.  
Structure #3 - Same as #2 plus 2 hours at 350° after cold water quench.
- (5) Structures 27 and 28 had some grain structure, constituent, and dispersoid as Structure 1, 7050-T76. Strengthening precipitate in Structure 27 was GP zone and in Structure 28 was a mixture of GP zone and  $\eta$ .
- \* See Note 3 on Table 1.



TABLE 7  
MICROSTRUCTURAL FEATURES OF ZYXX ALLOYS

Structure Number	Alloy	Grain Size, $\mu\text{m}$ (1)			Figure Number	Constituent Phase Type	Amount	Dispersoid Phase (2)		Strengthening Phase (3)	Amount of Cold Work	Figure Number	Other Features
		Long-Transverse	Transverse	Longitudinal				Type	Amount				
14	2024(T12)-T31	0.061	0.020	0.061	15	$\text{Al}_{12}(\text{Fe,Mn})_{13}\text{Si}$ , $\text{Al}_7\text{Cu}_2\text{Fe}$ , $\text{Mg}_2\text{Si}$	2.2%	$\text{Al}_2\text{O}_3\text{MgMg}_3$	2.6%	GP	1%	14	Low dislocation density
15	2124(T12)-T31	0.059	0.020	0.061	16	$\text{Al}_7\text{Cu}_2\text{Fe}$ , $\text{Al}_2\text{CuMg}$ , $\text{CuAl}_2$	1.4%	$\text{Al}_2\text{O}_3\text{MgMg}_3$	2.6%	GP	1%	15	Low dislocation density
16	2024(T12)-T31	0.039	0.025	0.050	17	$\text{Al}_{12}(\text{Fe,Mn})_{13}\text{Si}$ , $\text{Al}_7\text{Cu}_2\text{Fe}$ , $\text{Mg}_2\text{Si}$	2.2%	$\text{Al}_2\text{O}_3\text{MgMg}_3$	1.1%	GP	1%	16	Low dislocation density
17	2124(T12)-T31	0.055	0.021	0.059	18	$\text{Al}_7\text{Cu}_2\text{Fe}$ , $\text{Al}_2\text{CuMg}$ , $\text{CuAl}_2$	1.40%	$\text{Al}_2\text{O}_3\text{MgMg}_3$	1.1%	GP	1%	17	Low dislocation density
18	2024(T12)-T36	0.061	0.020	0.061	+	$\text{Al}_{12}(\text{Fe,Mn})_{13}\text{Si}$ , $\text{Al}_7\text{Cu}_2\text{Fe}$ , $\text{Mg}_2\text{Si}$	2.2%	$\text{Al}_2\text{O}_3\text{MgMg}_3$	2.6%	S'	5%	18	Narrow pfz, relatively high dislocation density
19	2124(T12)-T36	0.059	0.020	0.061	+	$\text{Al}_7\text{Cu}_2\text{Fe}$ , $\text{Al}_2\text{CuMg}$ , $\text{CuAl}_2$	1.40%	$\text{Al}_2\text{O}_3\text{MgMg}_3$	2.6%	S'	5%	19	Narrow pfz, relatively high dislocation density
20	2024(T12)-T36	0.039	0.025	0.050	+	$\text{Al}_{12}(\text{Fe,Mn})_{13}\text{Si}$ , $\text{Al}_7\text{Cu}_2\text{Fe}$ , $\text{Mg}_2\text{Si}$	2.2%	$\text{Al}_2\text{O}_3\text{MgMg}_3$	1.1%	S'	5%	20	Narrow pfz, relatively high dislocation density
21	2124(T12)-T36	0.055	0.021	0.059	+	$\text{Al}_7\text{Cu}_2\text{Fe}$ , $\text{Al}_2\text{CuMg}$ , $\text{CuAl}_2$	1.40%	$\text{Al}_2\text{O}_3\text{MgMg}_3$	1.1%	S'	5%	21	Narrow pfz, relatively high dislocation density
22	2024(T12)-T36	0.039	0.025	0.050	+	$\text{Al}_{12}(\text{Fe,Mn})_{13}\text{Si}$ , $\text{Al}_7\text{Cu}_2\text{Fe}$ , $\text{Mg}_2\text{Si}$	2.2%	$\text{Al}_2\text{O}_3\text{MgMg}_3$	1.1%	GP	5%	22	Narrow pfz, relatively high dislocation density
23	2024(T12)-T31	0.039	0.025	0.050	+	$\text{Al}_{12}(\text{Fe,Mn})_{13}\text{Si}$ , $\text{Al}_7\text{Cu}_2\text{Fe}$ , $\text{Mg}_2\text{Si}$	2.2%	$\text{Al}_2\text{O}_3\text{MgMg}_3$	1.1%	S'	1%	23	Low dislocation density continuous S on grain boundary, narrow pfz.
24	2048-T31	0.070	0.025	0.082	19	$\text{Al}_7\text{Cu}_2\text{Fe}$ , $\text{Al}_2\text{CuMg}$ , $\text{CuAl}_2$	0.50%	$\text{Al}_2\text{O}_3\text{MgMg}_3$	1.1%	GP	1%	24	Low dislocation on density
25	2048-T36	0.070	0.025	0.082	+	$\text{Al}_7\text{Cu}_2\text{Fe}$ , $\text{Al}_2\text{CuMg}$ , $\text{CuAl}_2$	0.50%	$\text{Al}_2\text{O}_3\text{MgMg}_3$	1.1%	S'	5%	25	High dislocation density
26	2024-T3X	.	.	.	+	.	.	.	.	S'	1%	26	no pfz.

\* Microstructure features similar to structure No. 16.

\* Grain structure of 19-23 and 25 similar to Structure Nos. 14-18 and 24.

(1) All recrystallized.

(2) The  $\text{Al}_2\text{O}_3\text{MgMg}_3$  dispersoids are rod-like precipitate that range in size from 0.1 to 0.6  $\mu\text{m}$  in the long direction.

(3) In 20XX alloys the precipitation sequence is:

Solid solution of  $\text{Fe}$ ,  $\text{Si}$ ,  $\text{S}$

GP = Guinier-Preston Zones; consists of groups of  $\text{Fe}$  and  $\text{Cu}$  atoms that cluster on  $\{110\}\text{Al}$  planes.

S' = transition phase of S, coherent on  $\{021\}\text{Al}$  planes.

S = equilibrium  $\text{Al}_2\text{CuMg}$ .

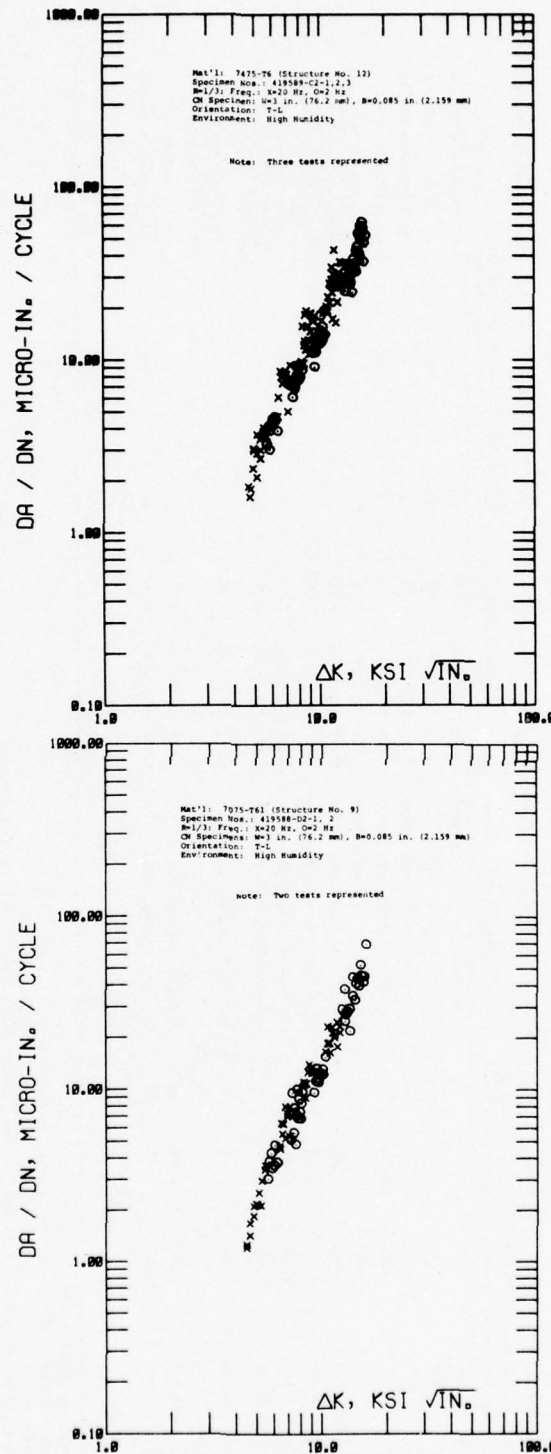


Figure 3 Cyclic Stress Intensity Range,  $\Delta K$ , Vs. Cyclic Fatigue Crack Growth Rate,  $\Delta a / \Delta N$ , from Replicate Tests of Structures No. 9 and 12.

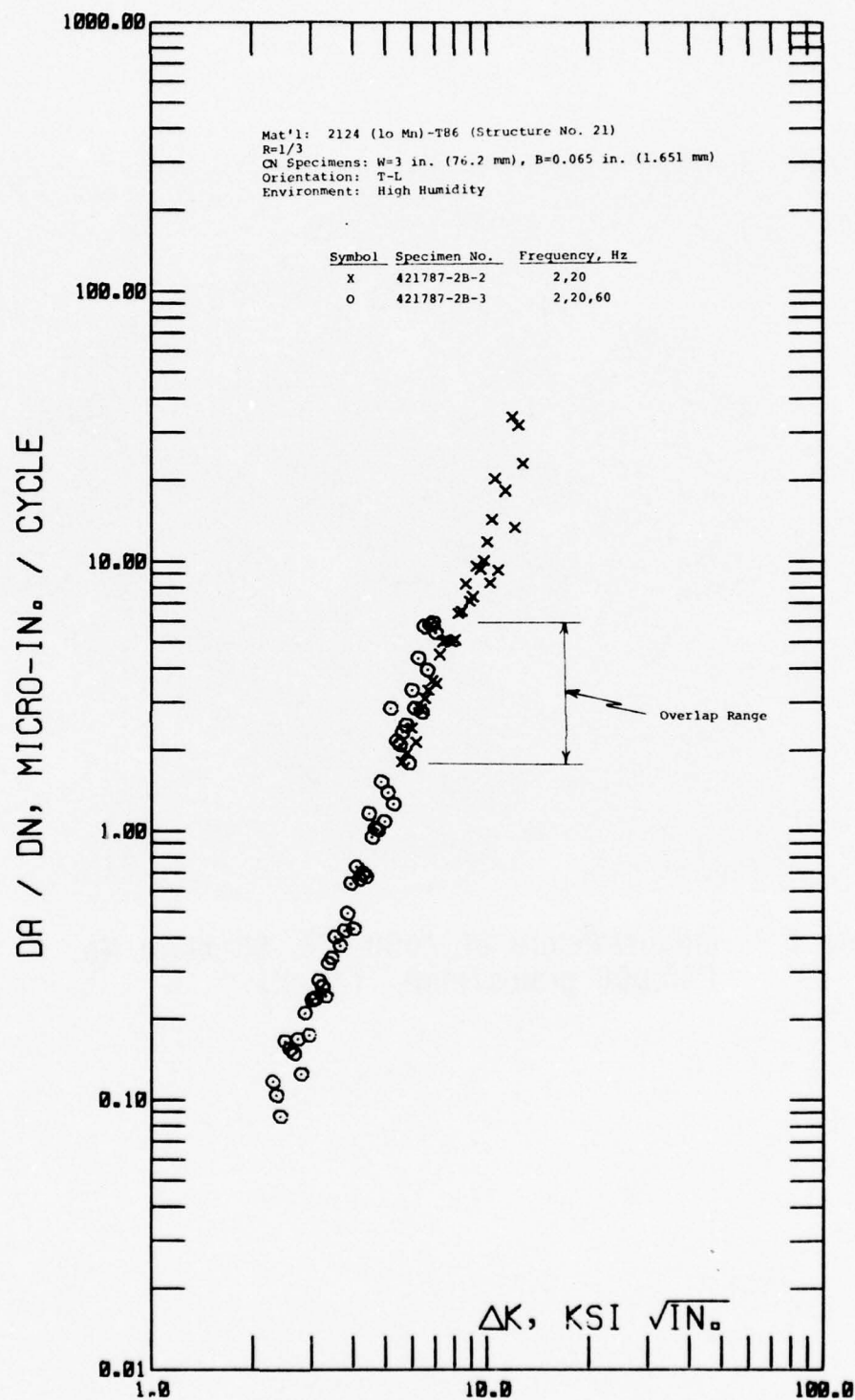


Figure 4 Cyclic Stress Intensity Range,  $\Delta K$ , Vs. Cyclic Fatigue Crack Growth Rate,  $\Delta a / \Delta N$ , of Structure No. 21

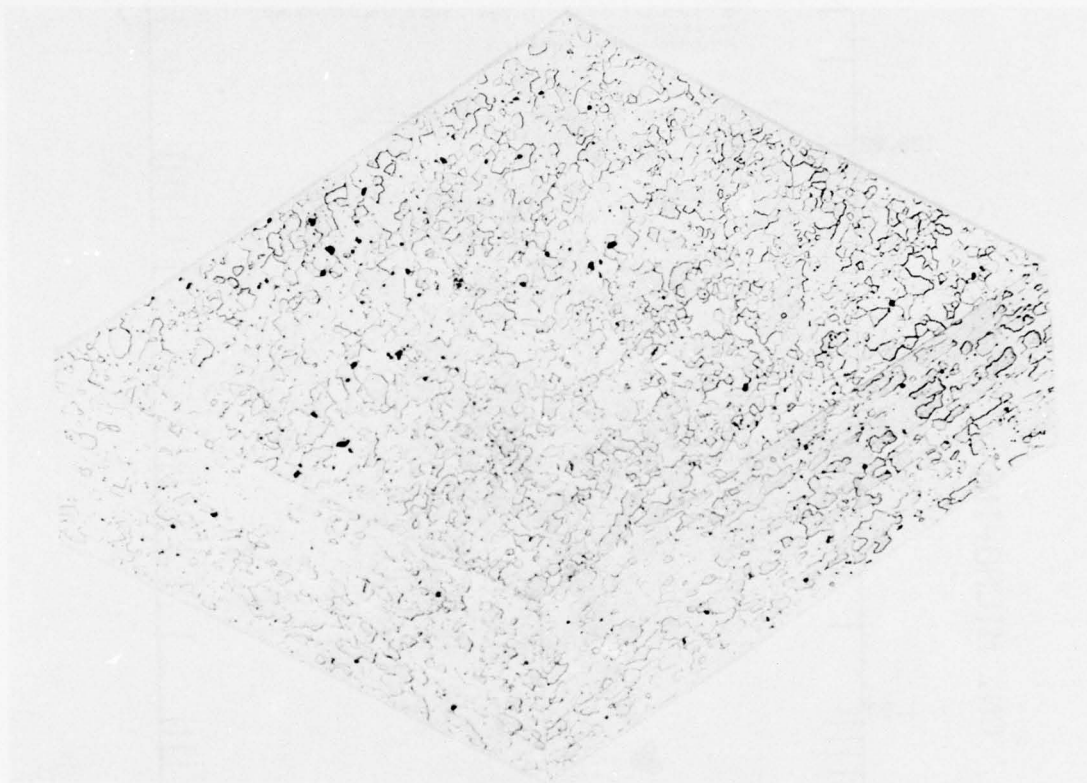


Figure 5    Microstructure of 7050-T76, Structure No. 1  
240,000 grains/mm<sup>3</sup>. (100X)



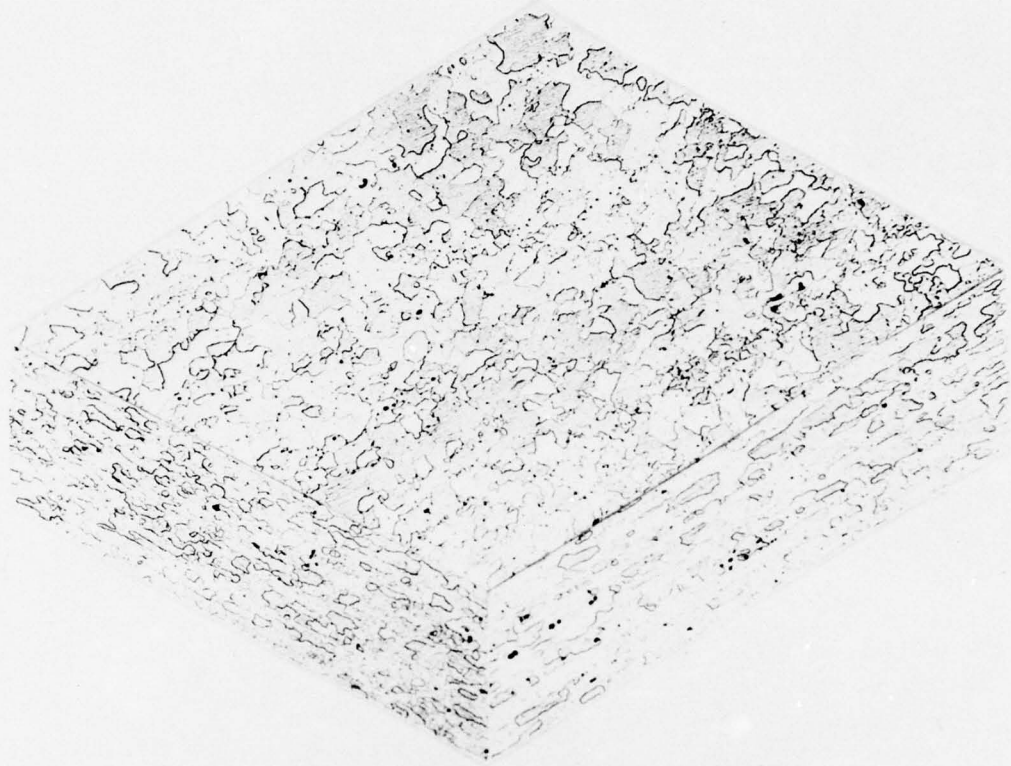


Figure 6      Microstructure of 7050+Mn-T76, Structure No. 2  
110,000 grains/mm<sup>3</sup>. (100X)

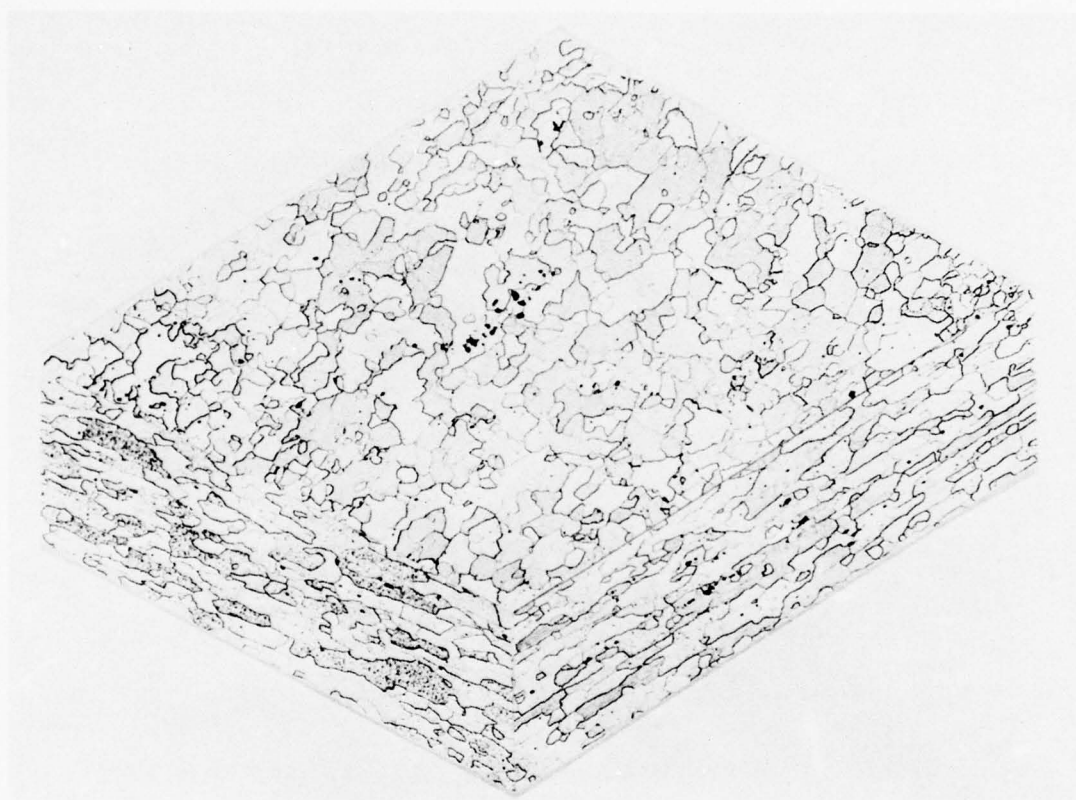


Figure 7    Microstructure of X7080 (hi Cu)-T76, Structure No. 3.  
20,000 grains/mm<sup>3</sup>. (100X)

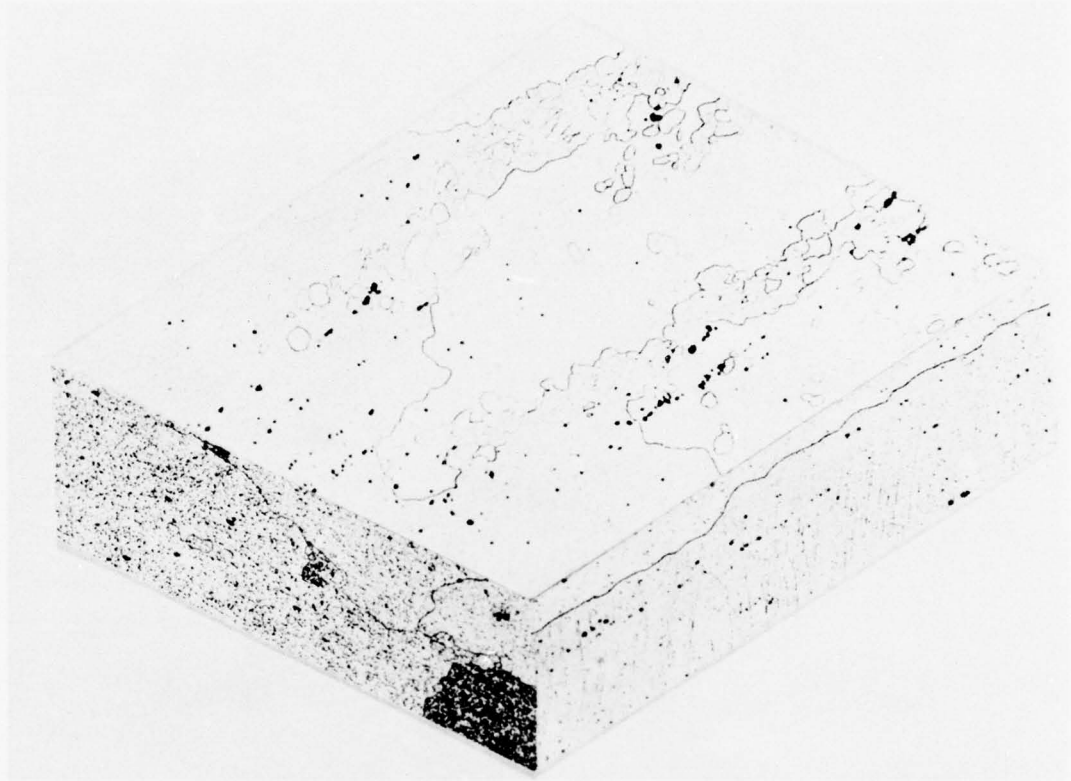


Figure 8 Microstructure of X7080 (hi Cu)-T76, Structure No. 4  
Mixed Grain Structure. (100X)



Figure 9      Microstructure of X7080 (hi Cu)-T76 (lg. g.s.),  
Structure No. 8.    5 grains/mm<sup>3</sup>. (100X)



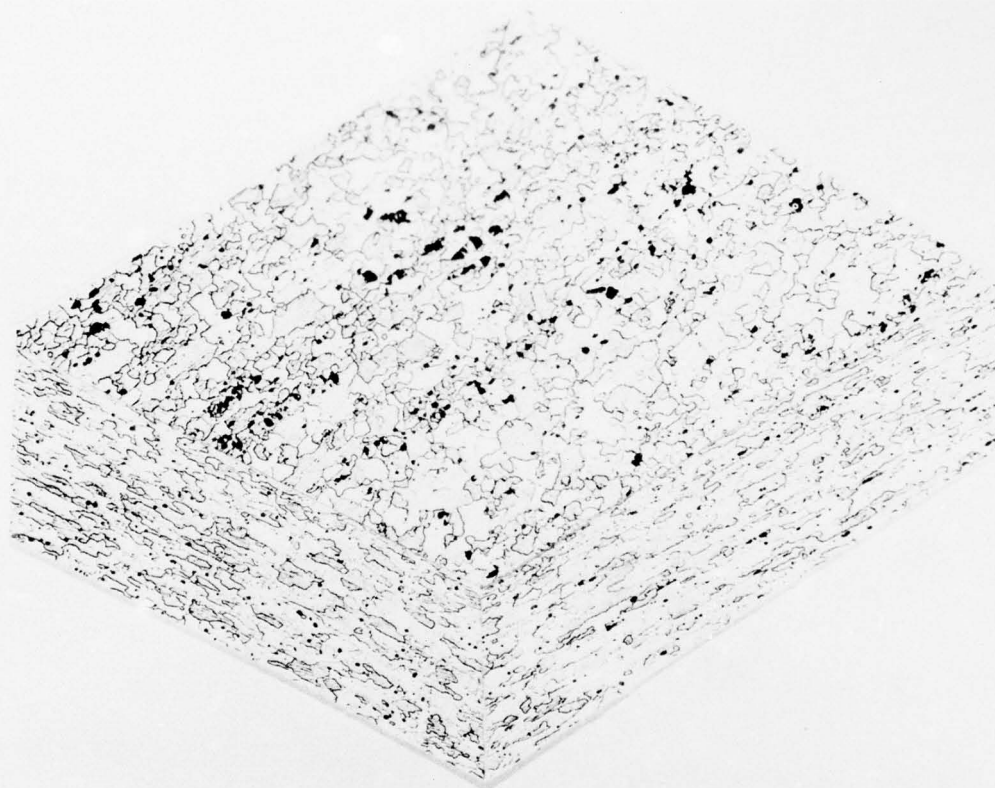


Figure 10 Microstructure of 7075-T61, Structure No. 9,  
65,000 grains/mm<sup>3</sup>. (100X)

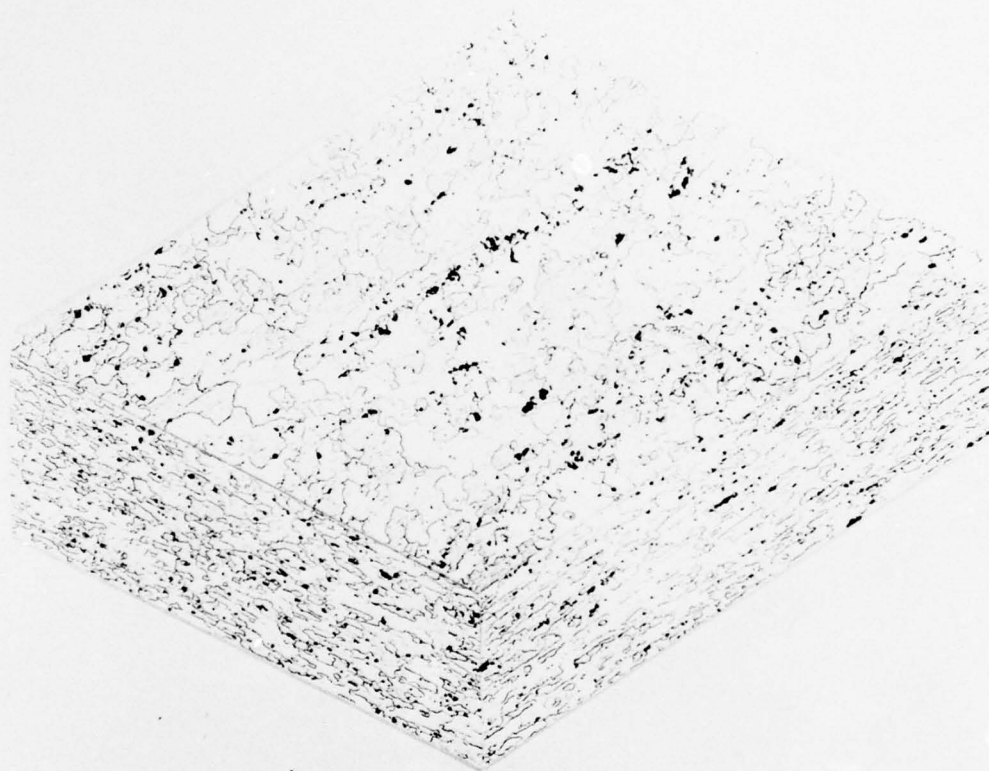


Figure 11 Microstructure of 7075-T6, Structure No. 10.  
65,000 grains/mm<sup>3</sup>. (100X)

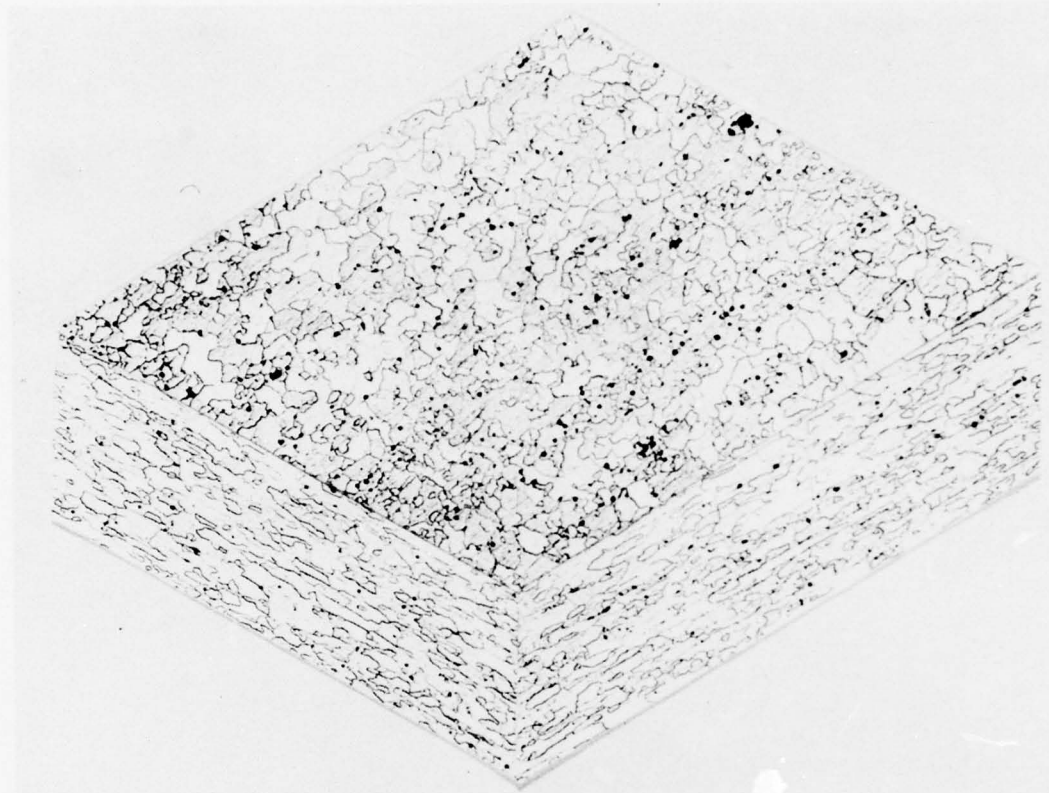
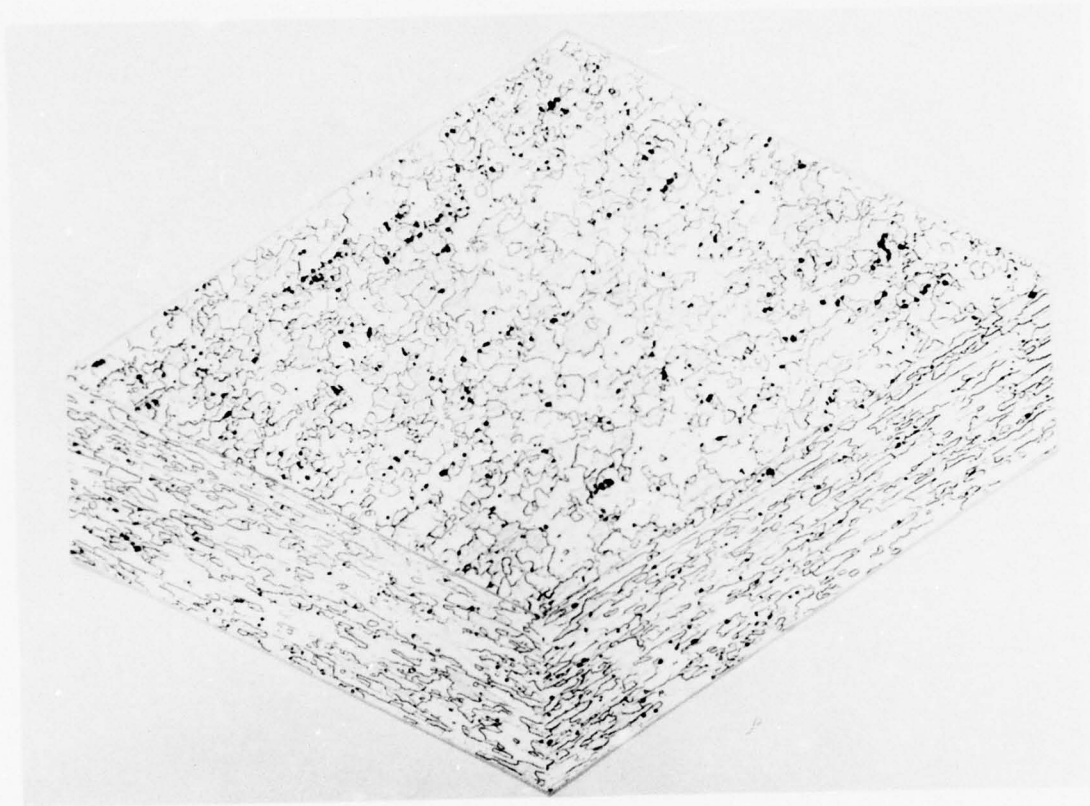


Figure 12 Microstructure of 7475-T61, Structure No. 11.  
135,000 grains/mm<sup>3</sup>. (100X)



**Figure 13 Microstructure of 7475-T6, Structure No. 12**  
**130,000 grains/mm<sup>3</sup>. (100X)**



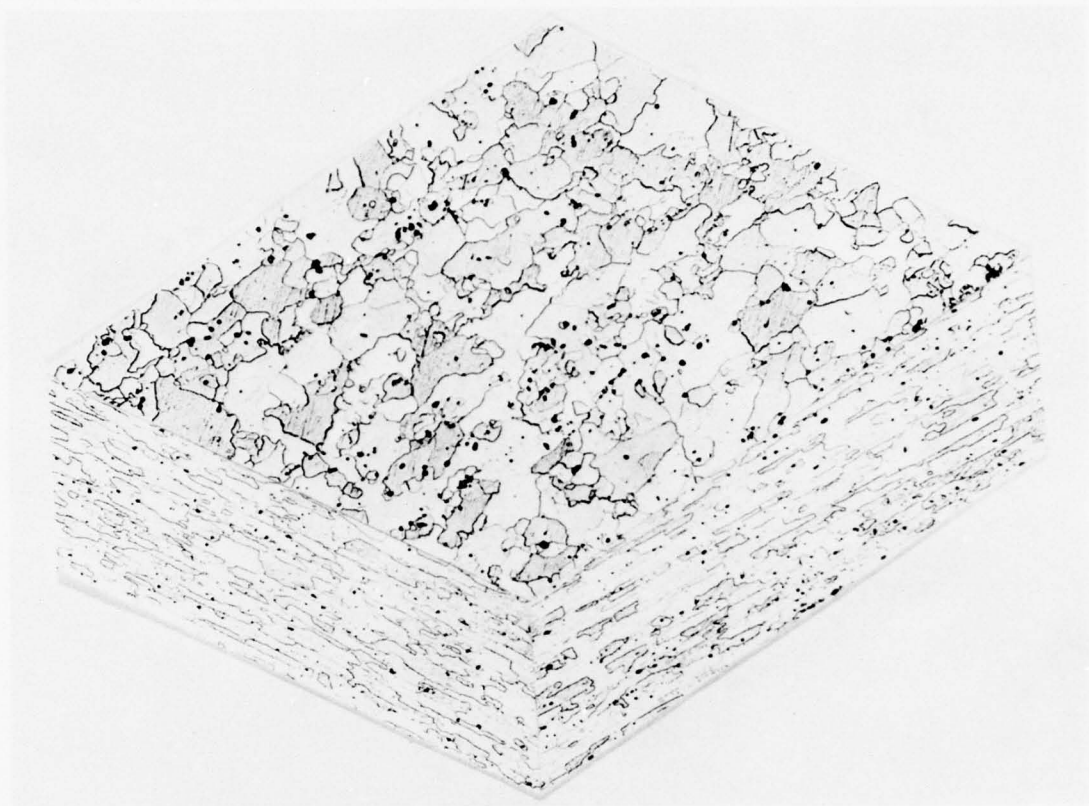


Figure 14 Microstructure of 7075-T61, Structure No. 13.  
5000 grains/mm<sup>3</sup>. (100X)

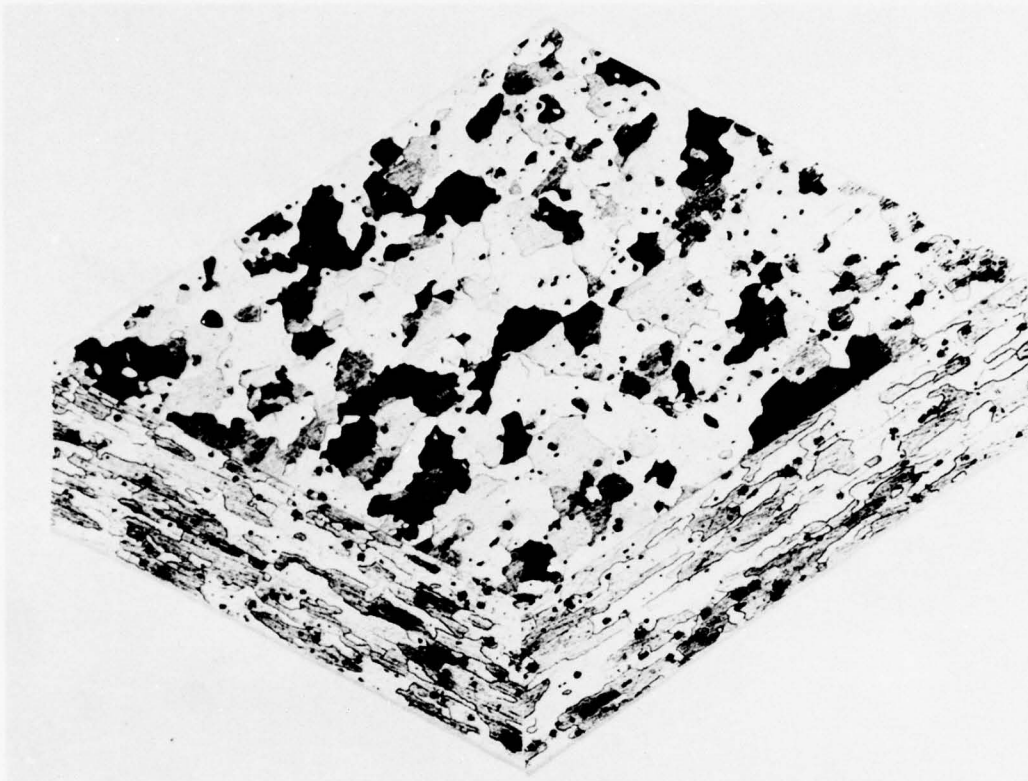


Figure 15 Microstructure of 2024 (hi Mn)-T31, Structure No. 14.  
13,000 grains/mm<sup>3</sup>. (100X)

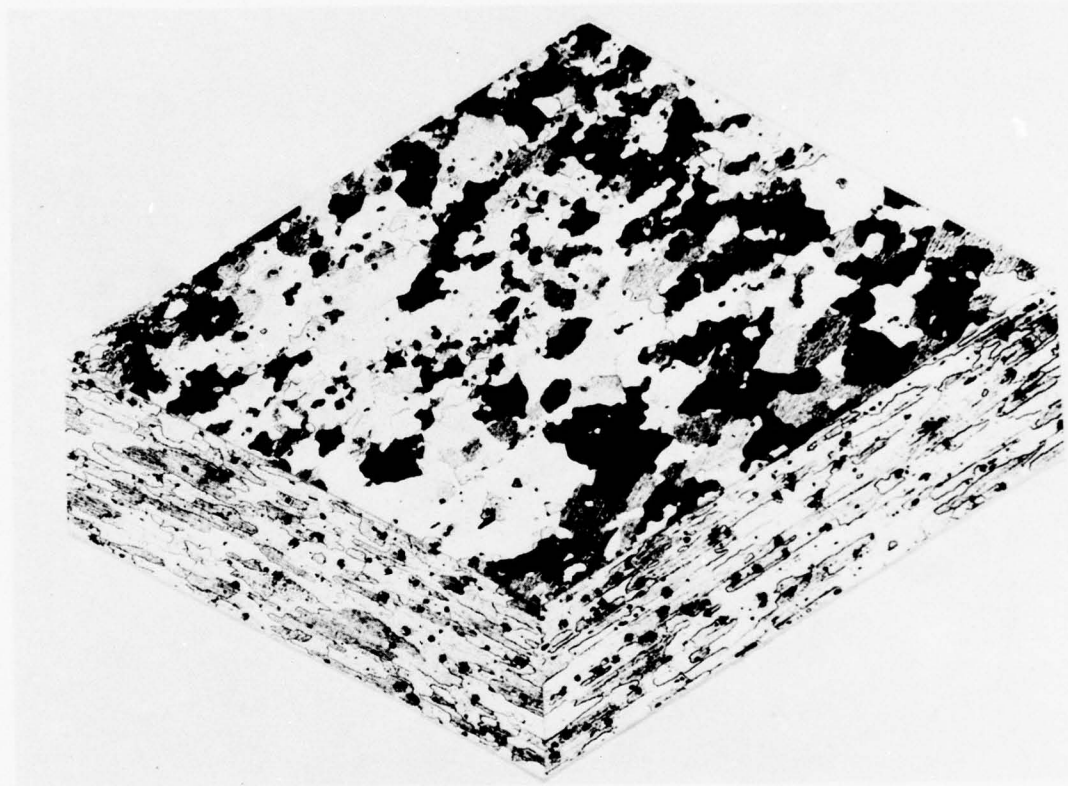


Figure 16 Microstructure of 2124 (hi Mn)-T31, Structure No. 15.  
11,000 grains/mm<sup>3</sup>. (100X)

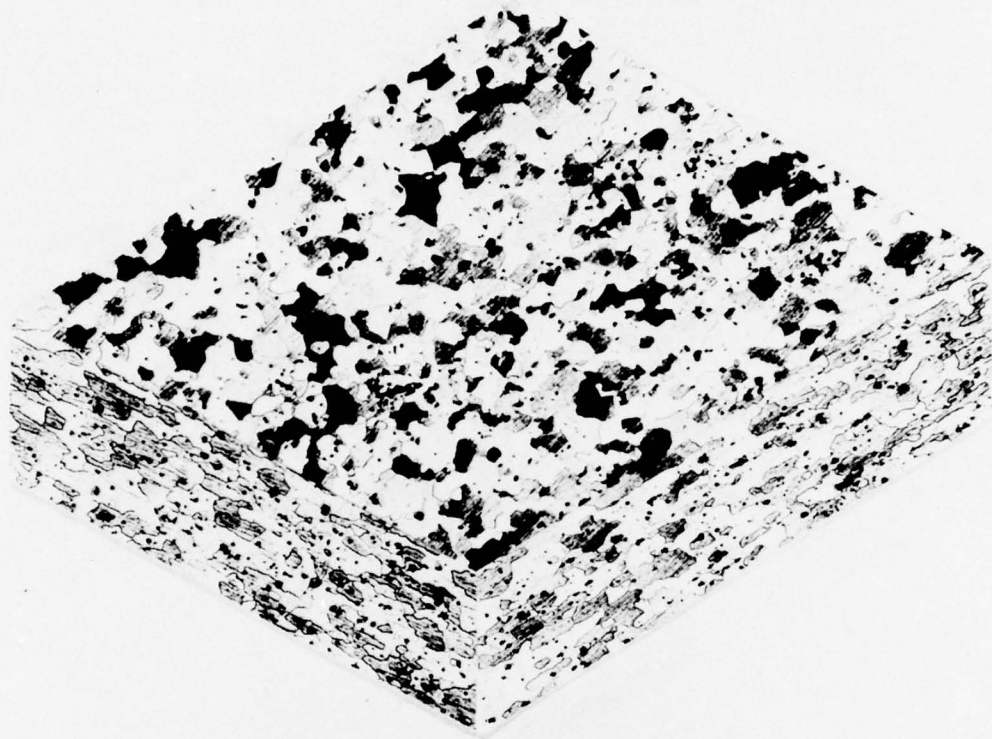


Figure 17 Microstructure of 2024 (lo Mn)-T31, Structure No. 16  
20,000 grains/mm<sup>3</sup>. (100X)



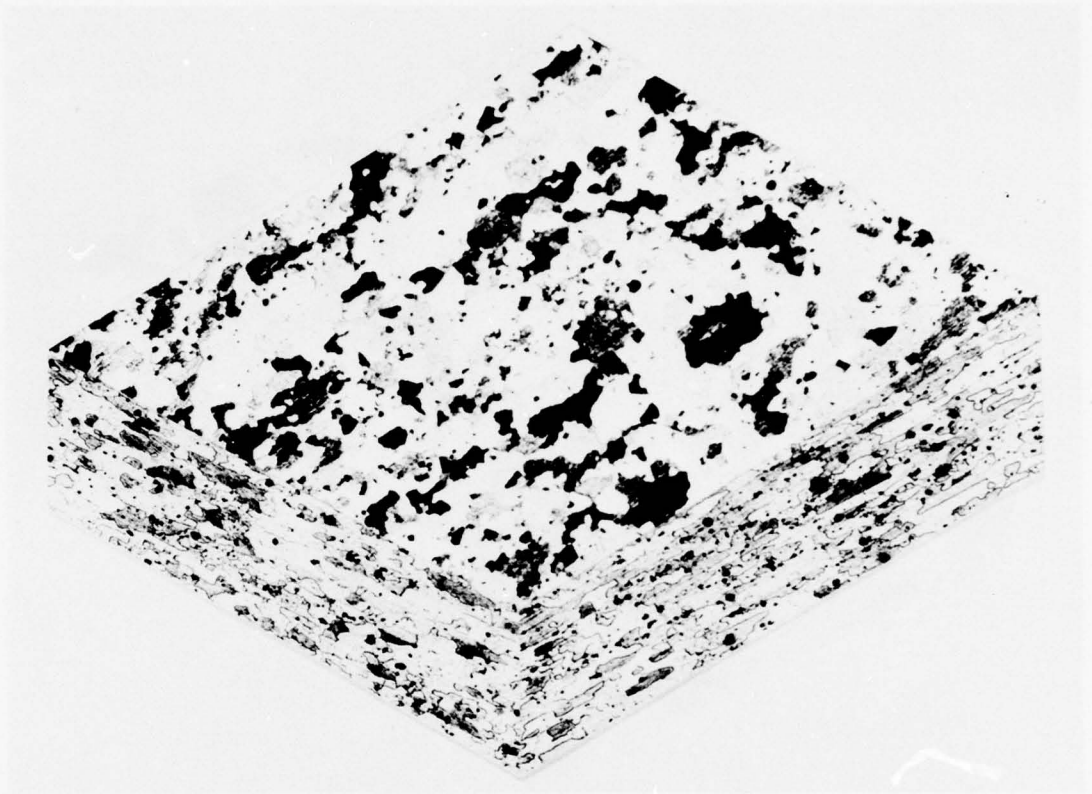


Figure 18 Microstructure of 2124 (lo Mn)-T31, Structure No. 17.  
13,000 grains/mm<sup>3</sup>. (100X)

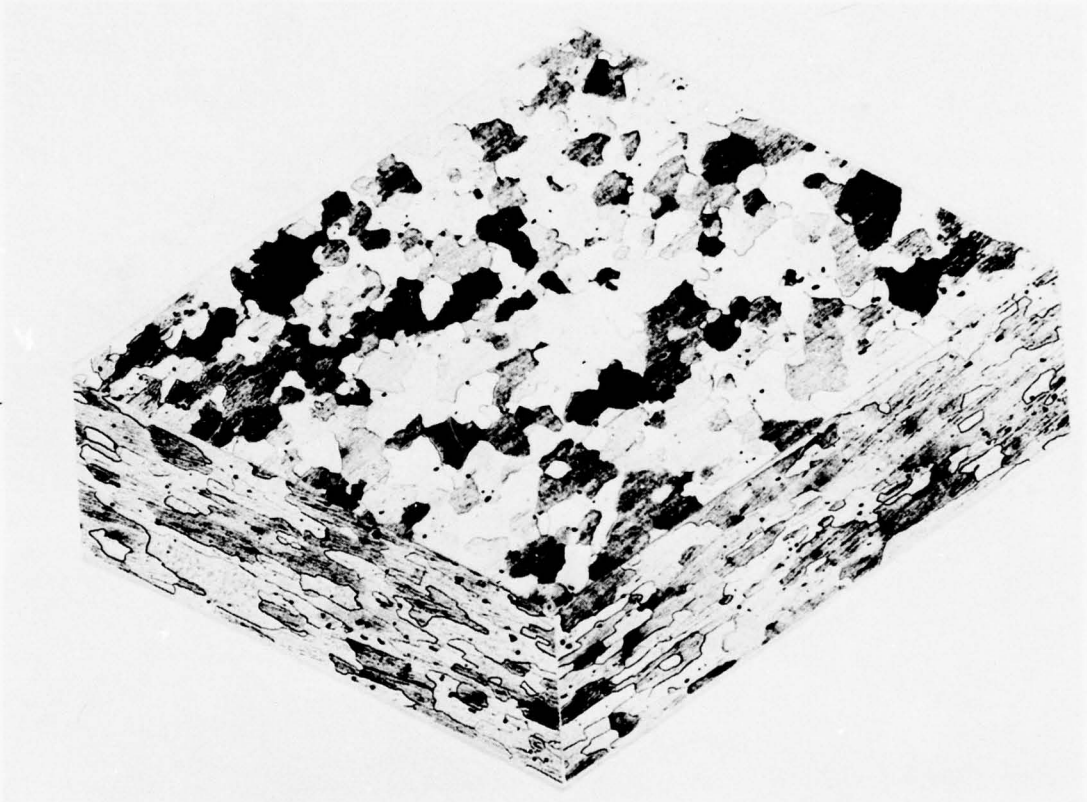


Figure 19 Microstructure of 2048-T31, Structure No. 24  
5000 grains/mm<sup>3</sup>. (100X)

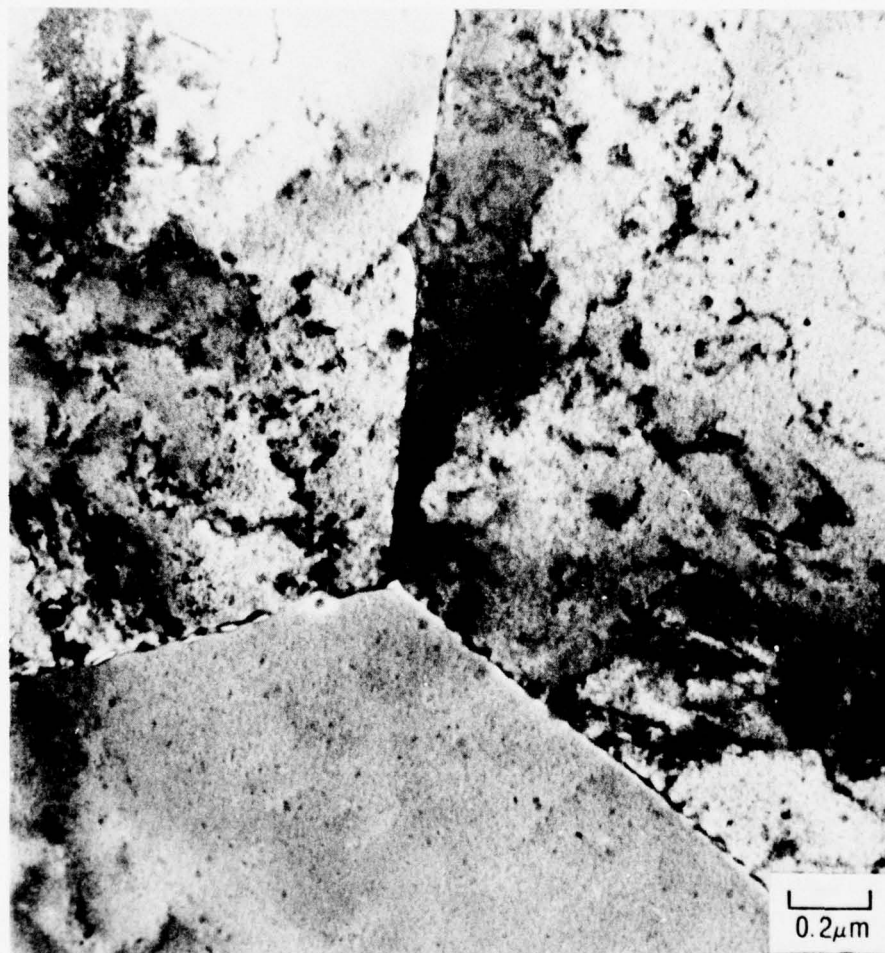


Figure 20 Transmission Electron Micrograph of 7050-T76, Structure No. 1, Showing the Continuous Precipitate on the Grain Boundary. Note the "Pinning" Action of  $\text{ZrAl}_3$  Particle on Grain Boundary Mobility.

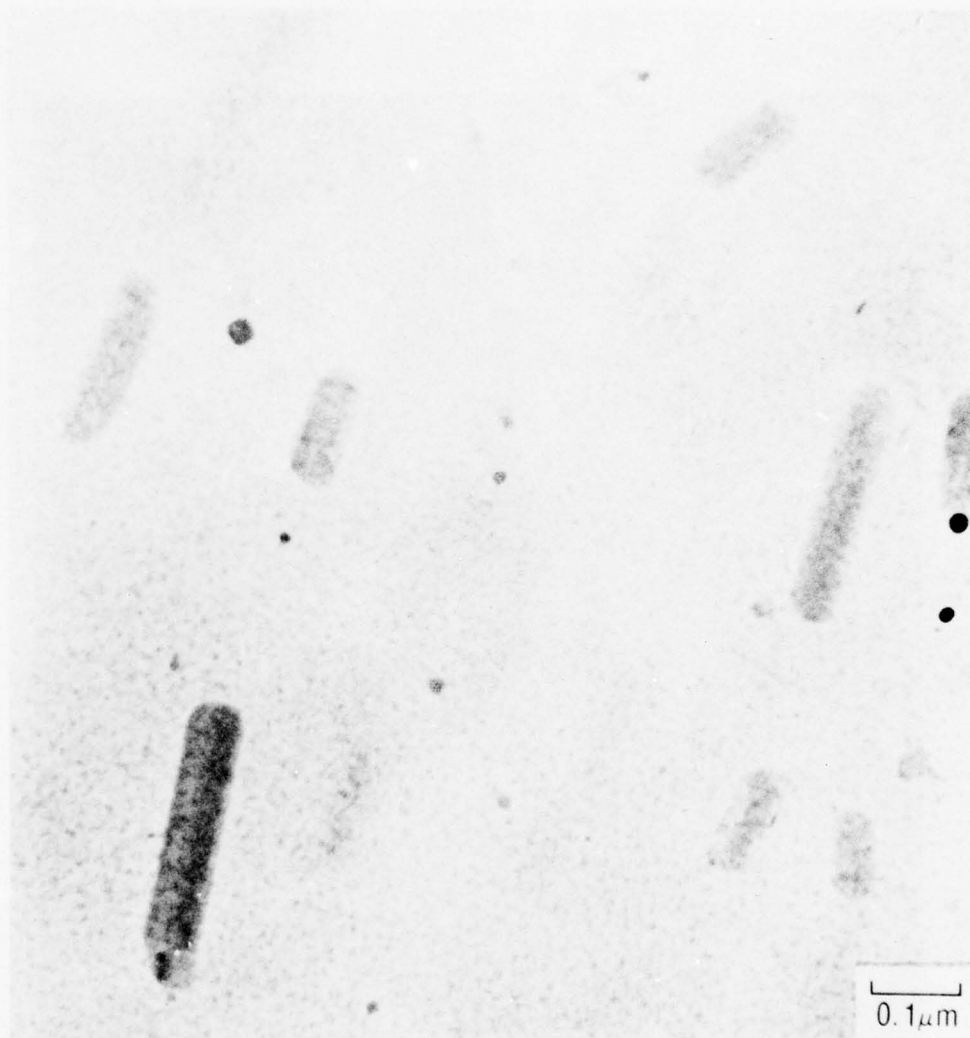


Figure 21 Transmission Electron Micrograph of 7050 (+Mn)-T76, Structure No. 2 Showing  $\text{Al}_{20}\text{CuMn}_3$  Dispersoid.



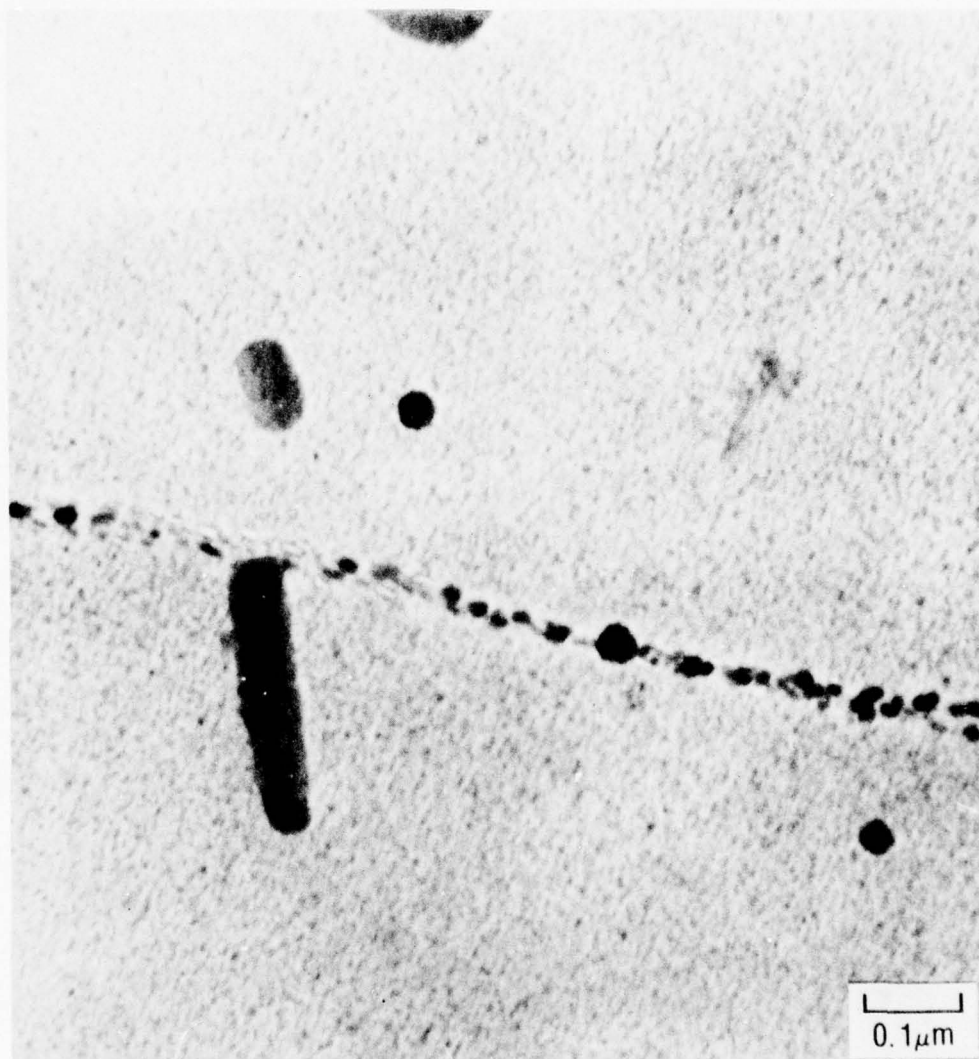


Figure 22 Transmission Electron Micrograph of X7080 (hi Cu)-T76, Structure No. 3 Showing Grain Boundary Precipitate of Strengthening Phase.

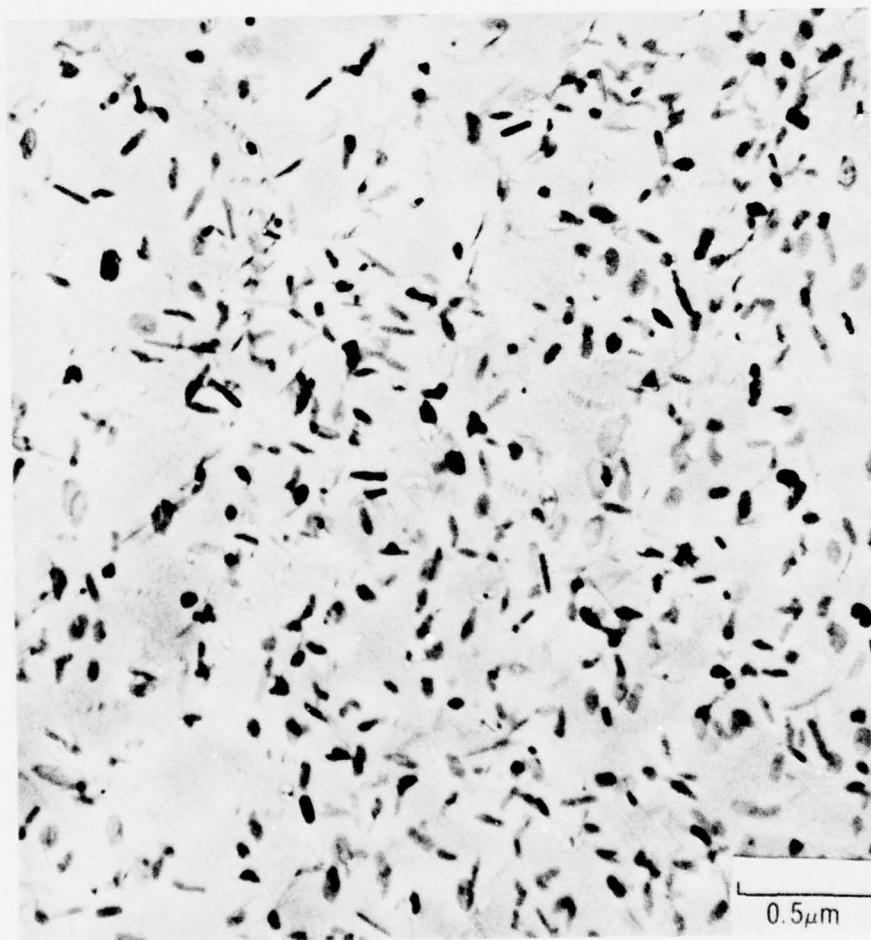


Figure 23 Transmission Electron Micrograph of Structure No. 5, 7050-TX1 Showing Small Needle-Like S' Strengthening Precipitate and Coarser  $\eta$  Precipitate.



Figure 24 Transmission Electron Micrograph of Structure No. 6, 7050-TX2, Showing the Large, Lath-Type S' Precipitate and the Coarser, More Widely Spaced  $\eta$  Precipitate.

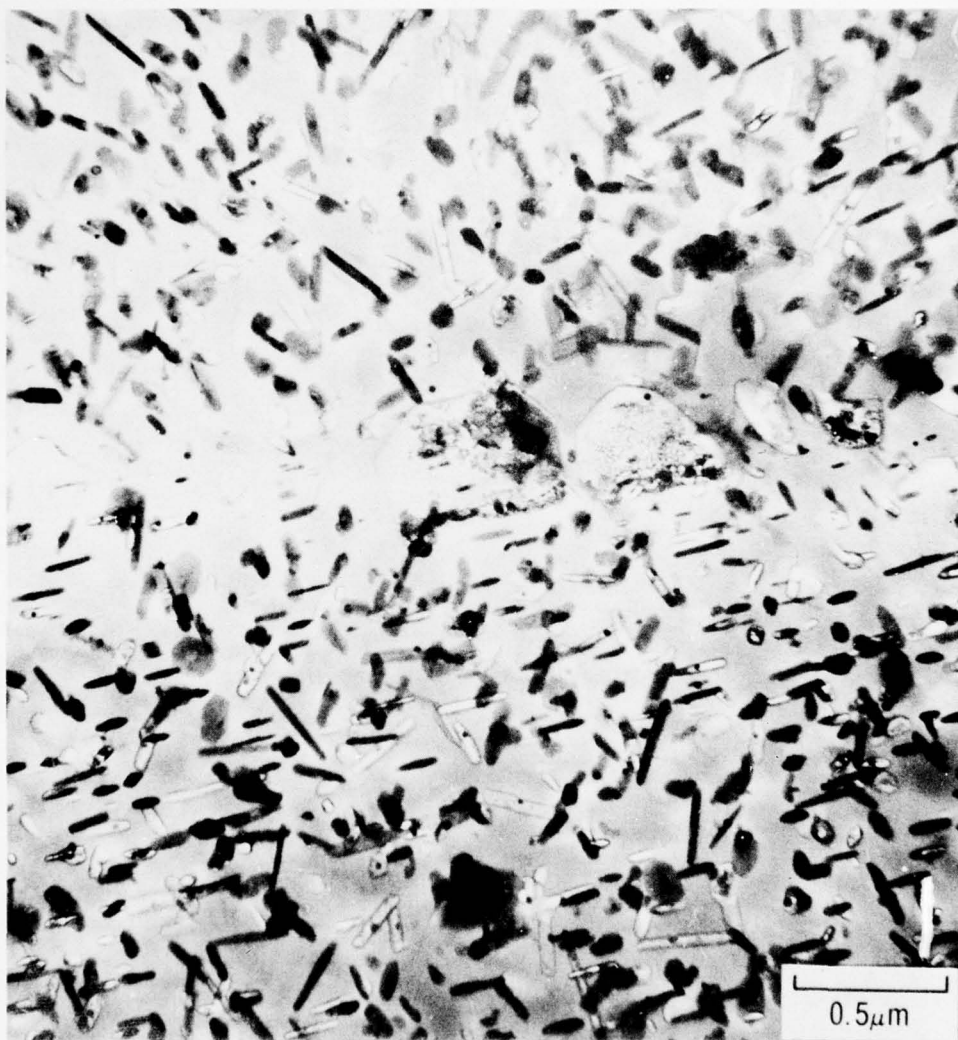


Figure 25 Transmission Electron Micrograph of Structure No. 7 (7050-TX3). Both Elongated S' and Globular  $\eta$  Precipitates are Shown.





Figure 26 Transmission Electron Micrograph of Structure No. 7 (7050-TX3). This Region is Completely Free of S and  $\eta$  and Contains Only  $\eta'$ .

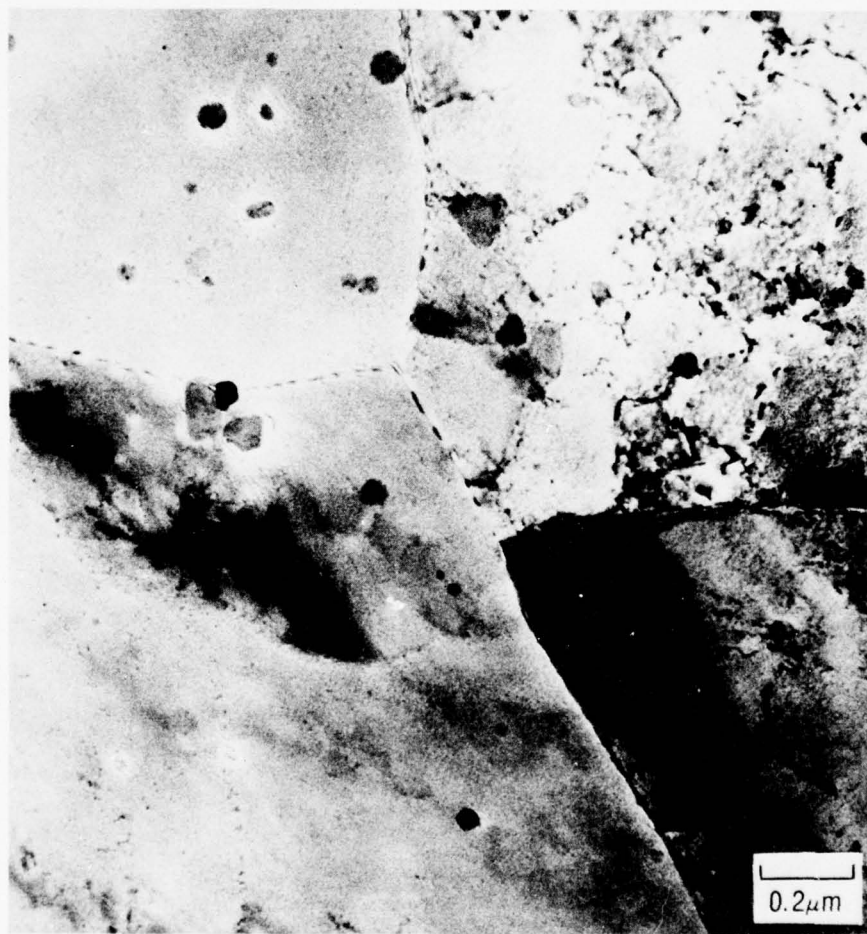


Figure 27 Transmission Electron Micrograph of 7475-T61, Structure No. 11, Illustrating the Larger, More Widely Spaced  $\text{Al}_{12}\text{Mg}_2\text{Cr}$  Dispersoid. Compare with Structure No. 12, 7475-T6, Figure 28.

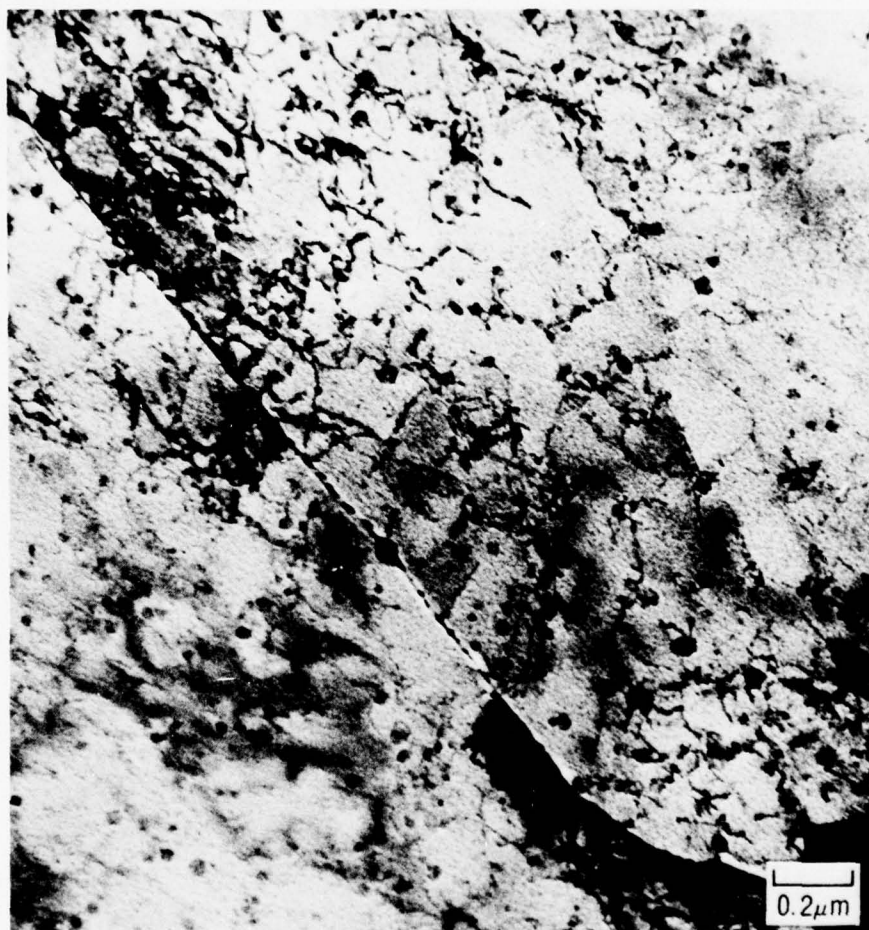


Figure 28 Transmission Electron Micrograph of 7475-T6, Structure No. 12, Showing Smaller, More Closely Spaced  $\text{Al}_{12}\text{Mg}_2\text{Cr}$  Dispersoid.

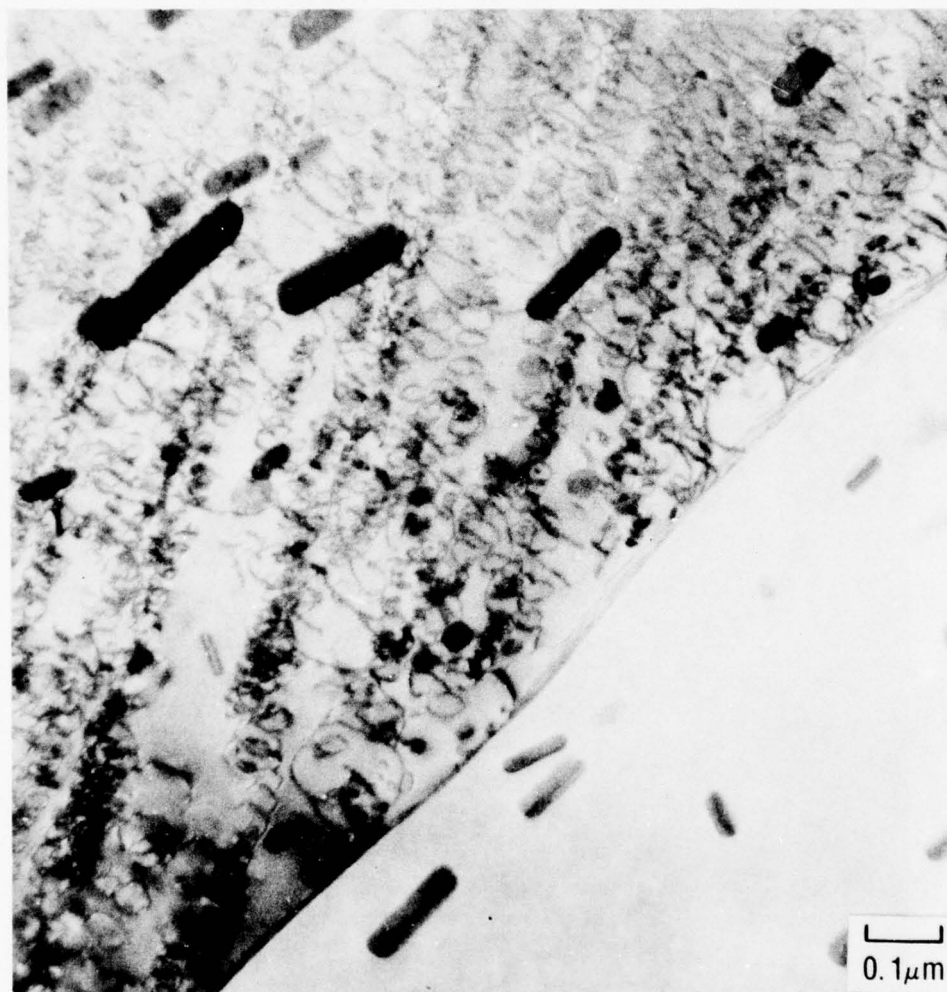


Figure 29 Transmission Electron Micrograph of 2124 (10 Mn)-T31, Structure No. 17. Strengthening GP Zones are not Visible. Top Grain Oriented to Show Dislocation Structure.





Figure 30 Transmission Electron Micrograph of 2124 (hi Mn)-T86, Structure No. 19. Needle-Like S' Strengthening Precipitate Visible in Right Grain. Left Grain Oriented to Show Dislocation Structure.

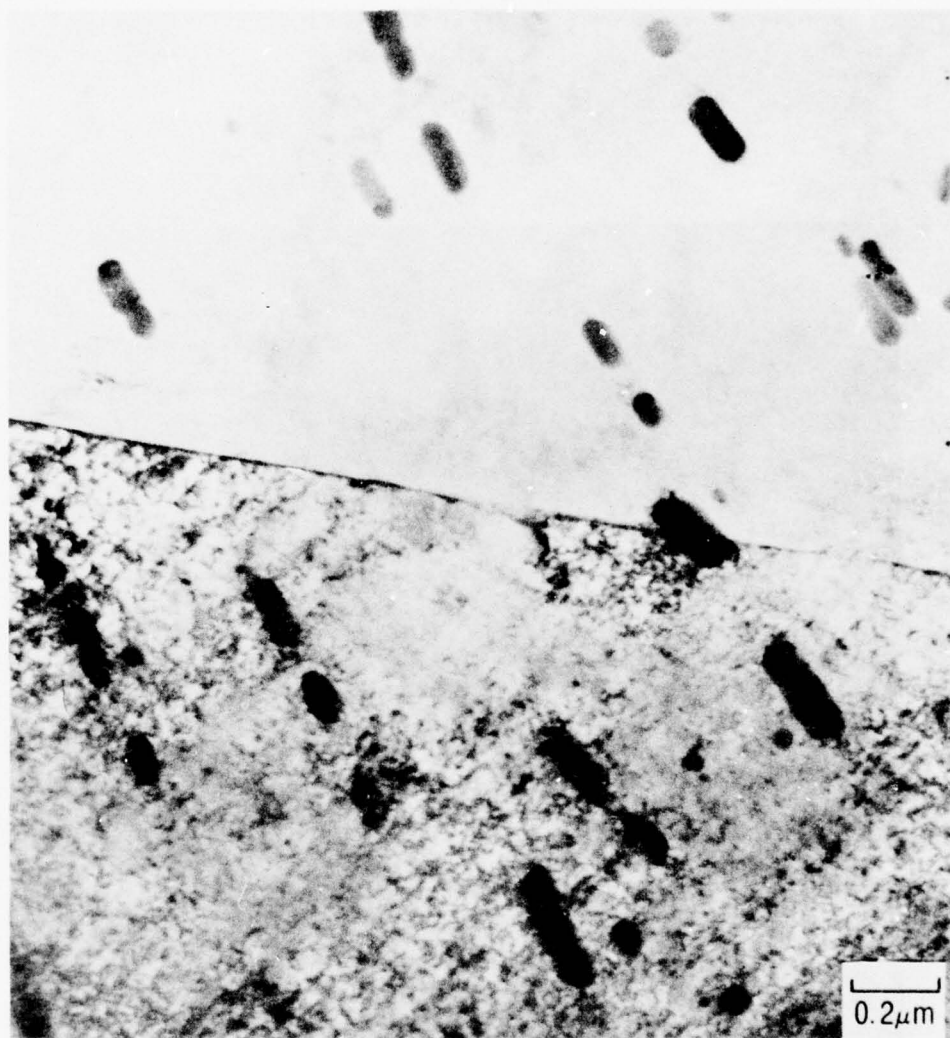


Figure 31 Transmission Electron Micrograph of 2024 (10 Mn)-T36, Structure No. 22. The Strengthening Phase is the GP Zone Formed by Room Temperature Aging (not visible in the micrograph, top grain). Lower Grain Oriented to Show Dislocation Structure.

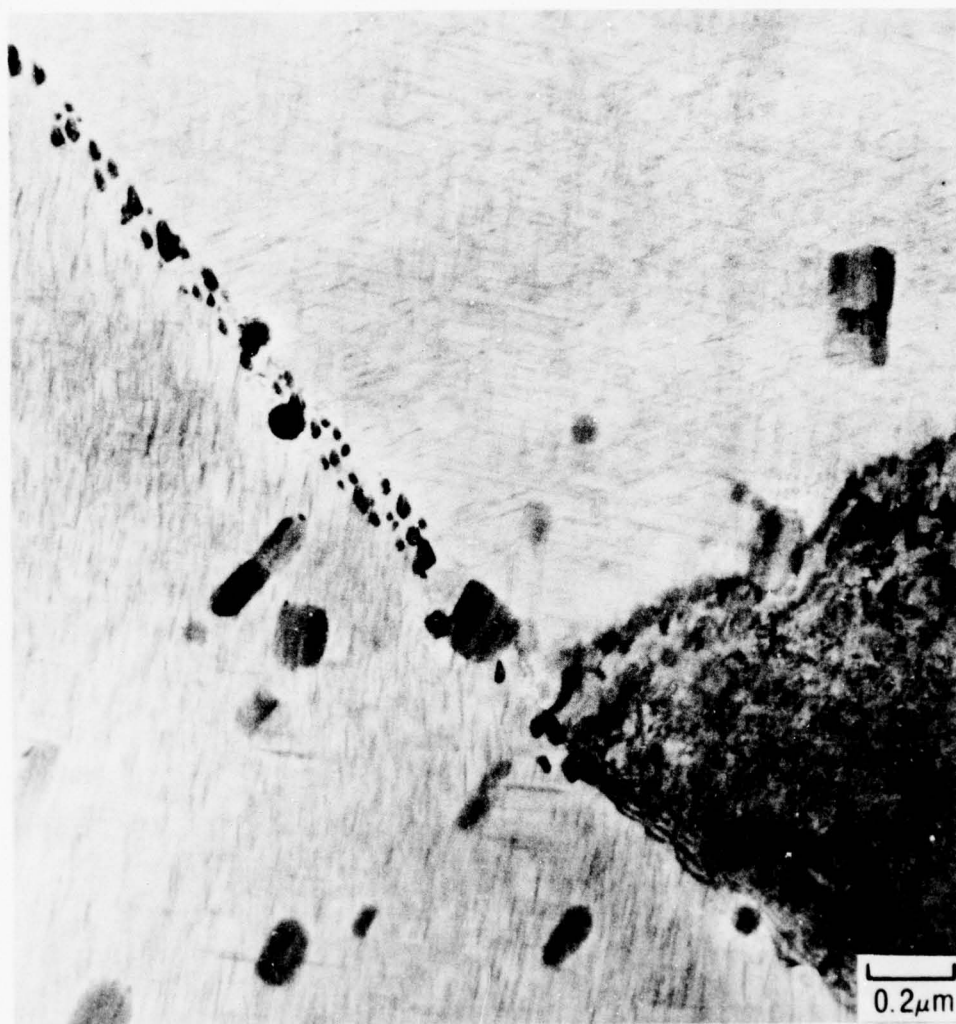


Figure 32 Transmission Electron Micrograph of 2024 (10 Mn)-T81, Structure No. 23, Showing the Transition Strengthening Needle-Like Precipitate, S', and the Grain Boundary Precipitate, S (Al<sub>2</sub>CuMg). Bottom Right Grain Oriented to Illustrate Dislocation Density.

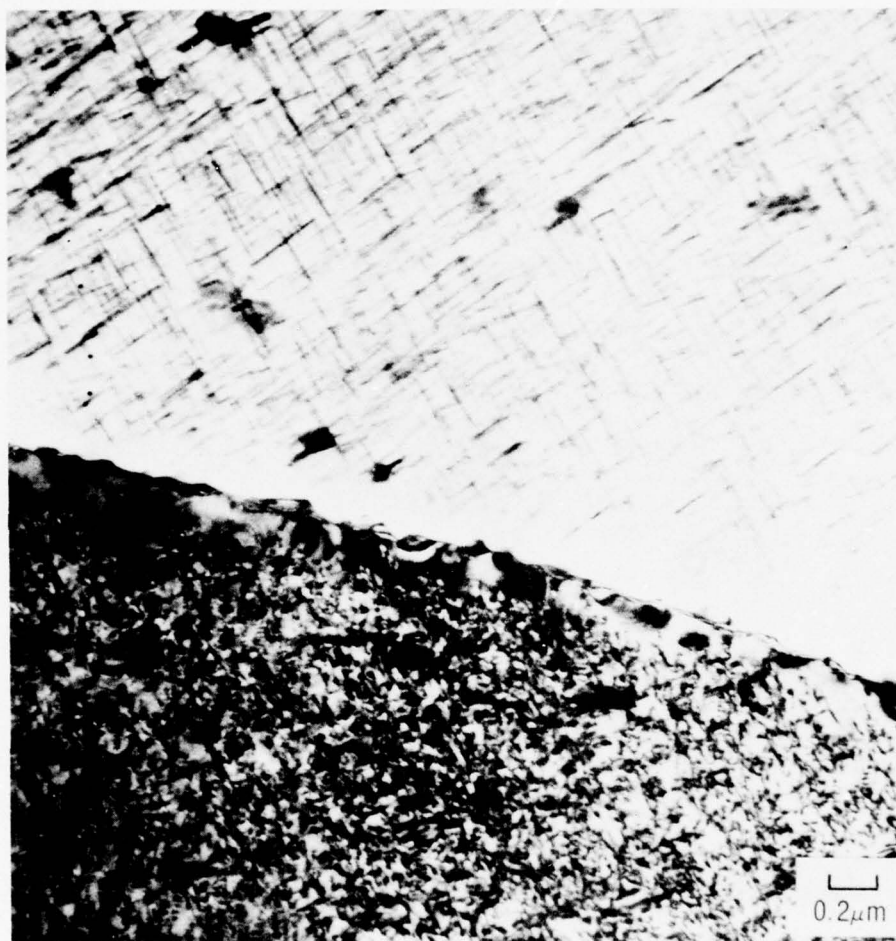


Figure 33 Transmission Electron Micrograph of 2024-T8X, Structure No. 26  
Showing Large Needle-Like S' Strengthening Precipitate.  
Bottom Grain Oriented to Show Dislocation Density.



More detailed volume fraction measurements than those given in Tables 6 and 7 of both insoluble and soluble constituent particles greater than  $1\ \mu$  are given in Table 8. For the 2XXX alloys,  $\text{Al}_7\text{Cu}_2\text{Fe}$ ,  $\text{Al}_{12}(\text{Fe},\text{Mn})_3\text{Si}$ ,  $\text{Al}_2\text{CuMg}$ ,  $\text{CuAl}_2$ , and possibly minor amounts of  $\text{Mg}_2\text{Si}$  were included in the volume fraction measurements. The volume fraction measurements from the cross-section and the longitudinal sections agree reasonably well while the volume fraction measured from the surface gave a higher result. This behavior is consistent with results reported by El-Soudani and Pelloux[25] who found that when total number of grid applications was less than the number required for the volume fraction to converge in all three spatial directions, the volume fraction measured from the surface gave a higher value. Although convergence of the volume percent on the cross-section and longitudinal planes does not necessarily indicate the true volume fraction, it is believed that this does represent a value which is sufficient to characterize the volume fraction of large constituent particles in this alloy. Thus, a 2.2 volume percent of constituent greater than  $1\ \mu\text{m}$  in 2024 should represent a reasonable estimate. By decreasing the amount of Fe and Si (and Cu by 0.2 wt.%), the volume percent constituent was reduced to approximately 1.40 (2124). By reducing the Cu another one percent (2048), the volume percent of constituent particles was decreased fourfold to 0.50.

In addition to reducing the volume percent of particles by decreasing the amount of Fe, Si, and Cu, the range in total constituent particle area (a measure of the size of particles) was

TABLE 8

VOLUME PERCENT CONSTITUENT PARTICLES PRESENT IN SELECTED  
2XXX AND 7XXX ALLOYS

Alloy	Vol. %		Range of Total Particle Area, $\mu^2$ , per Application of One Field*	
	Surface	Cross- Section	Surface	Longitudinal
2024	3.21	2.18	47-1262	92-464
2124	1.99	1.38	14-660	37-277
2048	0.79	0.48	8-402	5-172
7050	1.18	0.78	37-315	2-197
X7080	0.38	0.18	20-143	7-146
7075	1.18	1.07	1-692	33-311
7475	0.59	0.41	1-362	12-203

\*1 Field = 10,000  $\mu^2$  (0.01 mm<sup>2</sup>)

also reduced significantly, particularly in the large particle range. For example, particles in 2024 having a total area of 200-300  $\mu\text{m}^2$  were not uncommon, while in 2048 the number of these large size particles was reduced.

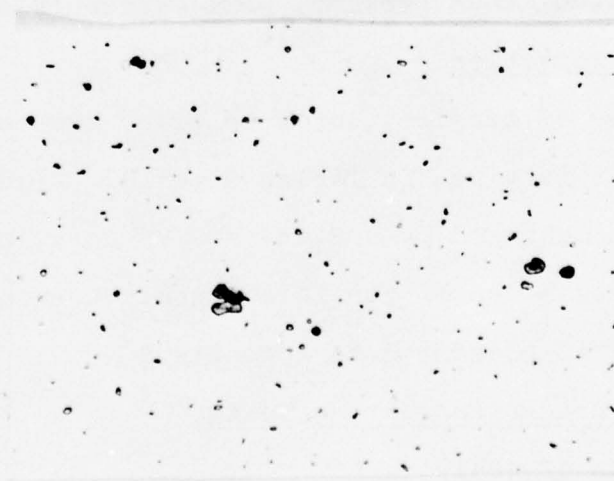
Although the only nominal difference in composition between alloy X7080(hiCu) and 7050 is the Mn substitution for the Zr, the volume percent of constituent particles greater than 1  $\mu\text{m}$  was significantly different (Figure 34). Alloy 7050 had a volume percent near 1.0 while in X7080(hiCu) the volume percent constituent particles was between 0.2-0.4. The lower volume fraction of constituent particles in X7080(hiCu) can be attributed to the presence of  $\text{Al}_{20}\text{Mn}_3\text{Cu}_2$  dispersoid and the lower Mg content which precluded the formation of  $\text{Al}_2\text{CuMg}$  particles (S-phase). In 7050 (no Cu-containing dispersoid), the amount of free Cu was greater than in X7080(hiCu) and this resulted in the formation of the S-phase ( $\text{Al}_2\text{CuMg}$ ), and thus contributed to a higher volume fraction of constituent. The remaining constituents present in these materials are  $\text{Al}_7\text{Cu}_2\text{Fe}$  and  $\text{Mg}_2\text{Si}$  particles.

A comparison of the volume fraction of constituents ( $\text{Al}_7\text{Cu}_2\text{Fe}$ ,  $\text{Al}_{12}(\text{Fe,Mn})_3\text{Si}$ ,  $\text{FeAl}_6$ , and  $\text{Mg}_2\text{Si}$ ) in the 7075 and the high purity version, 7475 (no  $\text{Al}_{12}(\text{Fe,Mn})_3\text{Si}$  and  $\text{FeAl}_6$ ), reflects the lower Fe and Si content present in 7475 (Table 8). Not only is volume fraction reduced, but the range of total particle area (a measure of size of the particles) is also smaller in the 7475. The volume percent of constituents in 7075 of 1.20-1.30 is in agreement with the work of El-Soudani and Pelloux[25] who reported a volume



a

Microstructure of X7080 (hi Cu)-T76, Structure No. 8, Revealing the Large Constituent Particles and Smaller  $\text{Al}_{20}\text{Cu}_2\text{Mn}_3$  Dispersoid Particles (500X)



b

Microstructure of 7050-T76, Structure No. 1, Revealing the Large Constituent Particles. (500X)

Figure 34 Microstructure of X7080 (hi Cu)-T76 and 7050-T76



percent of constituents for 7075 of similar Fe and Si content of 1.30-1.40.

One point worth noting concerning these measurements is that the automated system measures all areas that appear dark in the structure. Thus, voids and cracks, if present, will register and be included in the measurement of the volume percent. Alloys 7475-T6 and 7075-T6 had a slightly higher number of voids present than usually found in commercially produced material; however, comparison of test results with those for commercial 7475 and 7075 indicates that these voids did not affect the static or cyclic mechanical properties. Alloys 2024-T3, 2124-T3, and 2048-T3 had voids or cracks associated with large constituent particles, Figure 35. Alloys X7080-T76(hiCu) and 7050-T76 contained very few voids, which, when present, were extremely small.

#### 4.2 Static Properties

A summary of tensile, notch-tensile, and tear properties of all structures is given in Tables 9 to 13. Figures 36 to 39 show the toughness measured by UPE and NTS/YS as a function of yield strength. Discussion of the relationship between microstructure and toughness is presented in Appendix B.

#### 4.3 Fatigue Crack Propagation Tests

##### 4.3.1 Methods of Analysis

In many instances inherent scatter of crack growth rate information, generally plotted as  $\log \Delta a / \Delta N$  vs  $\log \Delta K$ , is sufficient to confound ranking of fatigue crack growth rate performance of different alloy microstructures possessing subtle differences in

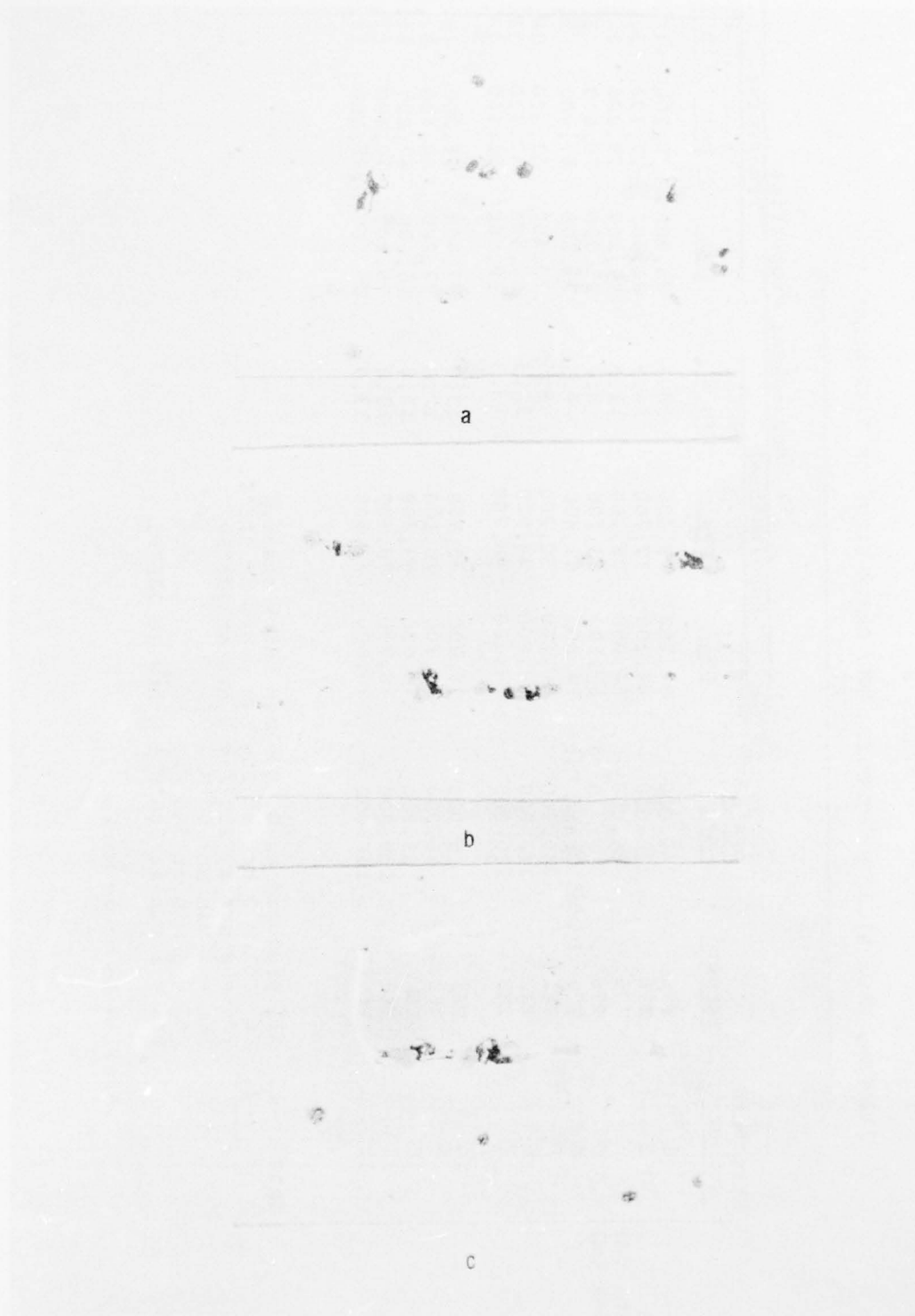


Figure 35 Micrograph Showing Constituent Particles in (a) 2024, (b) 2124, and (c) 2048. (1000X)

TABLE 9

## TEMPER, MECHANICAL PROPERTIES, AND GRAIN SIZES OF 7XXX ALLOY SHEET

Alloy <sup>1</sup>	Structure Number	Temper <sup>2</sup>	Grains mm <sup>3</sup>	Mechanical Properties					
				Longitudinal			Transverse		
				T.S. psi	Y.S. psi	% El. in 2"	T.S. psi	Y.S. psi	% El. in 2"
7050	1	T76	240,000	84,700	79,400	10.5	85,900	80,100	10.5
7050+Mn	2	T76	110,000	84,100	77,700	10.5	84,400	77,700	12.0
X7080 (hi Cu)	3	T76	20,000	84,900	78,700	11.5	84,100	79,200	11.5
X7080 (hi Cu)	8	T76	5	87,600	83,100	8.0	85,000	79,600	7.0
X7080	4	T76	Mixed Grain Size	74,800	69,800	9.5	71,200	67,400	5.0
7050	5	TX1	240,000	70,800	52,200	8.5*	72,400	51,800	17.0
7050	6	TX2	240,000	63,800	44,900	11.5	66,500	47,400	12.0
7050	7	TX3	240,000	67,100	48,700	13.0	69,500	51,400	14.5
7075	13	T61	5,000	78,000	70,900	13.0	77,400	68,200	14.0
	9	T61	65,000	77,700	70,100	12.0	77,200	68,400	12.0
	10	T6	65,000	76,500	69,400	12.0	76,600	67,600	11.5
7475	11	T61	135,000	78,700	70,700	13.0	79,200	70,400	11.0
	12	T6	130,000	78,600	70,600	13.0	78,100	68,300	13.5

Notes: 1. All produced as 0.090-inch thick sheet.

2. T6, T61 = 3 hrs at 250°F + 3 hrs at 315°F.

T76 = 3 hrs at 250°F + 9 hrs at 325°F.

TX1 = 1 min at 500°F.

TX2 = 5 min at 500°F.

TX3 = 1 min at 500°F + 2 hrs at 325°F.

\*Failed in gauge mark.

TABLE 10

## TEMPER AND MECHANICAL PROPERTIES OF 2XXX ALLOY

## SHEET

Alloy <sup>1</sup>	Structure Number	Temper <sup>2</sup>	Mechanical Properties					
			Longitudinal			Transverse		
			T.S. psi	Y.S. psi	% El. in 2"	T.S. psi	Y.S. psi	% El. in 2"
2024 (low Mn)	16	T31	67,800	48,400	21.0	64,500	43,700	20.0
	22	T36	67,700	56,600	15.5	64,000	47,400	15.0
	23	T81	67,300	60,900	6.5	68,000	62,200	6.5
	20	T86	74,000	71,000	6.5	71,000	67,100	6.5
2124 (low Mn)	17	T31	65,700	47,000	21.5	64,200	41,700	23.0
	21	T86	74,500	71,500	7.0	70,700	65,200	7.0
2024 (high Mn)	14	T31	67,200	48,400	---	66,400	43,700	20.0
	18	T86	75,300	71,800	7.0	74,000	69,400	6.0
2124 (high Mn)	15	T31	67,700	47,900	20.0	65,900	43,100	22.0
	19	T86	74,600	71,300	7.0	73,200	69,000	7.0
2048	24	T31	60,400	43,900	20.0	59,000	40,000	23.0
	25	T86	70,400	68,500	7.0	69,700	67,800	7.0

## Notes:

1. All produced as 0.063-inch thick sheet.
2. T31 = 1% stretch + 4 days minimum age at room temperature.  
T36 = 5% stretch + 4 days minimum age at room temperature.  
T81 = 1% stretch + 12 hrs. at 375°F  
T86 = 5% stretch + 8 hrs. at 375°F



TABLE 11

TRANSVERSE TEAR AND NOTCH TENSILE PROPERTIES  
OF THE 7XXX SERIES ALLOY SHEET

Alloy-Temper <sup>1,2</sup>	Structure Number	Tear Properties			Notch Tensile Properties	
		Strength, ksi	TRS/YS	UPE, <sup>3</sup> in.lb/in. <sup>2</sup>	Strength, ksi	NTS/YS
7050-T76	1	69.5	0.87	280	73.9	0.92
7050+Mn-T76	2	89.1	1.15	445	79.8	1.04
X7080(hi Cu)-T76	3	85.6	1.08	4	69.5	0.88
X7080(hi Cu)-T76	8	93.4	1.17	325	77.1	0.97
X7080-T76	4	98.1	1.46	550	71.9	1.07
7050-TX1	5	73.5	1.42	545	72.4	1.40
7050-TX2	6	70.7	1.49	490	66.5	1.40
7050-TX3	7	71.0	1.30	560	69.5	1.36
7075-T61	13	91.9	1.35	570	73.9	1.08
7075-T61	9	84.9	1.24	465	72.5	1.06
7075-T6	10	77.3	1.14	300	67.2	0.99
7475-T61	11	97.5	1.38	785	78.7	1.12
7475-T6	12	85.5	1.25	530	70.2	1.03

Notes: 1. T6, T61 = 3 hrs at 250°F + 3 hrs at 315°F.

T76 = 3 hrs at 250°F + 9 hrs at 325°F.

TX1 = 1 min at 500°F.

TX2 = 5 min at 500°F.

TX3 = 1 min at 500°F + 2 hrs at 325°F.

2. All produced as 0.090-inch thick sheet.

3. UPE is average of three specimens.

4. Curve not reliable due to rapid fracture and diagonal fracture.

TABLE 12

TRANSVERSE TEAR AND NOTCH TENSILE PROPERTIES  
OF THE 2XXX SERIES ALLOY SHEET

Alloy-Temper <sup>1,2</sup>	Structure Number	Tear Properties			Notch Tensile Properties	
		Strength, ksi	TS/YS	UPE, in.lb/in.	Strength, ksi	NTS/YS
2024(lo Mn)-T31	16	74.7	1.71	635	52.6	1.20
2024(lo Mn)-T36	22	73.8	1.56	485	56.2	1.19
2024(lo Mn)-T81	23	62.6	1.01	150	58.9	0.95
2024(lo Mn)-T86	20	60.5	0.90	105	56.4	0.84
2124(lo Mn)-T31	17	79.6	1.91	945	54.3	1.30
2124(lo Mn)-T86	21	73.6	1.13	230	66.8	1.02
2024(hi Mn)-T31	14	73.7	1.68	640	53.2	1.22
2024(hi Mn)-T86	18	62.7	0.90	120	57.0	0.82
2124(hi Mn)-T31	15	78.4	1.82	845	53.2	1.23
2124(hi Mn)-T86	19	69.0	1.00	180	65.9	0.96
2048-T31	24	78.8	1.97	1300	53.0	1.33
2048-T86	25	83.1	1.23	405	71.0	1.05

- Notes: 1. All produced as 0.063-inch thick sheet.  
2. T31 = 1% stretch + 4 days minimum age at room temperature.  
T36 = 5% stretch + 4 days minimum age at room temperature.  
T81 = 1% stretch + 12 hrs at 375°F.  
T86 = 5% stretch + 8 hrs at 375°F.

TABLE 13

MECHANICAL PROPERTIES OF SUPPLEMENTARY STRUCTURES

<u>Structure</u>	<u>Alloy- Temper</u>	<u>T.S., ksi</u>	<u>Y.S., ksi</u>	<u>%El in 2 in.</u>	<u>NTS/YS</u>	<u>Tear Str YS</u>	<u>U.P.E. in.-lb/in<sup>2</sup></u>
26	2024-T8X	58.6	47.3	7.5	-	1.23	200
27	7050-W	79.2	54.5	24.0	1.26	-	-
28	7050-T6	84.9	77.4	15.5	1.07	-	-

All tests in long-transverse direction

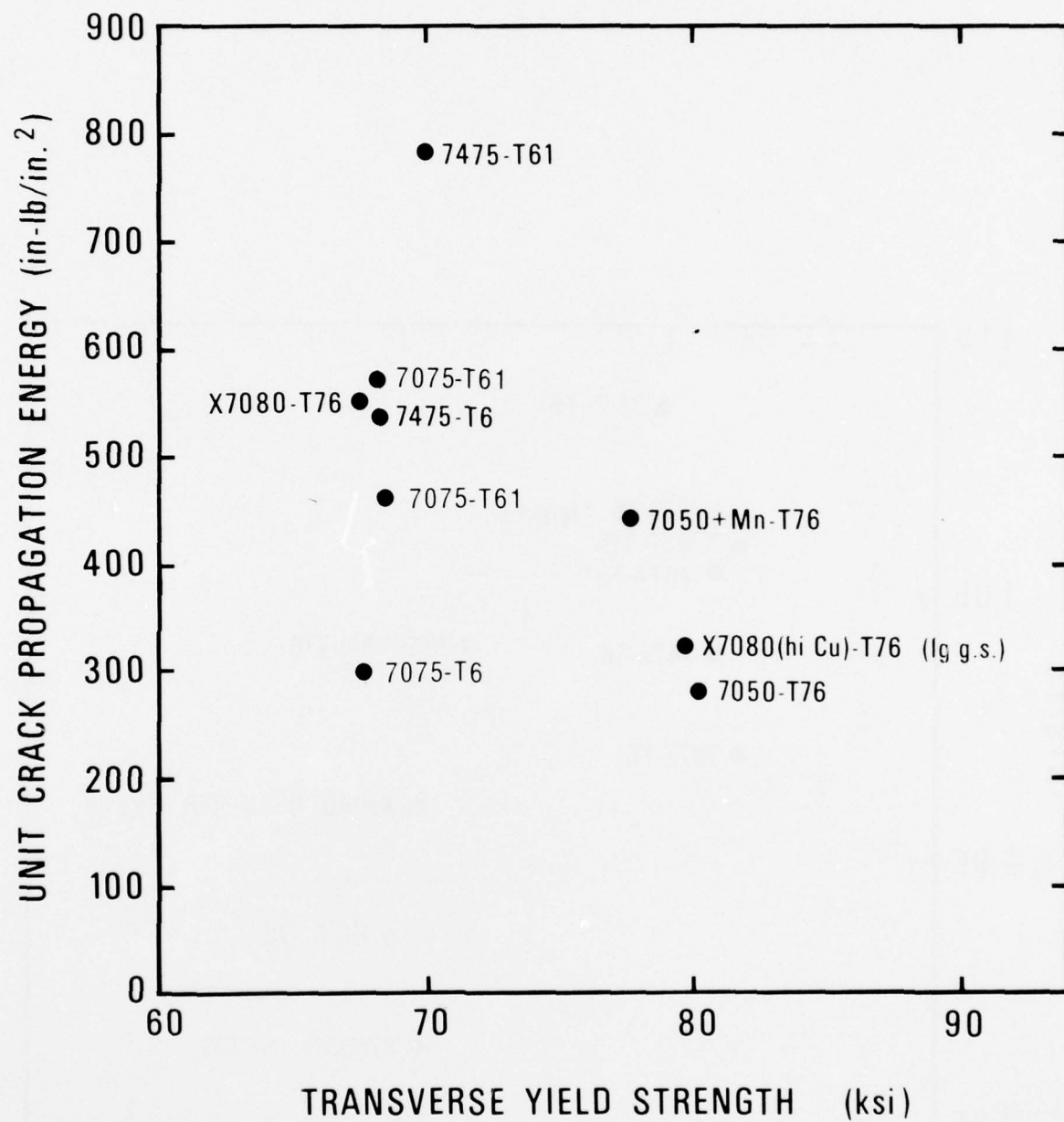


Figure 36 Toughness of the 7XXX Series Alloys Measured by Unit Crack Propagation Energy.



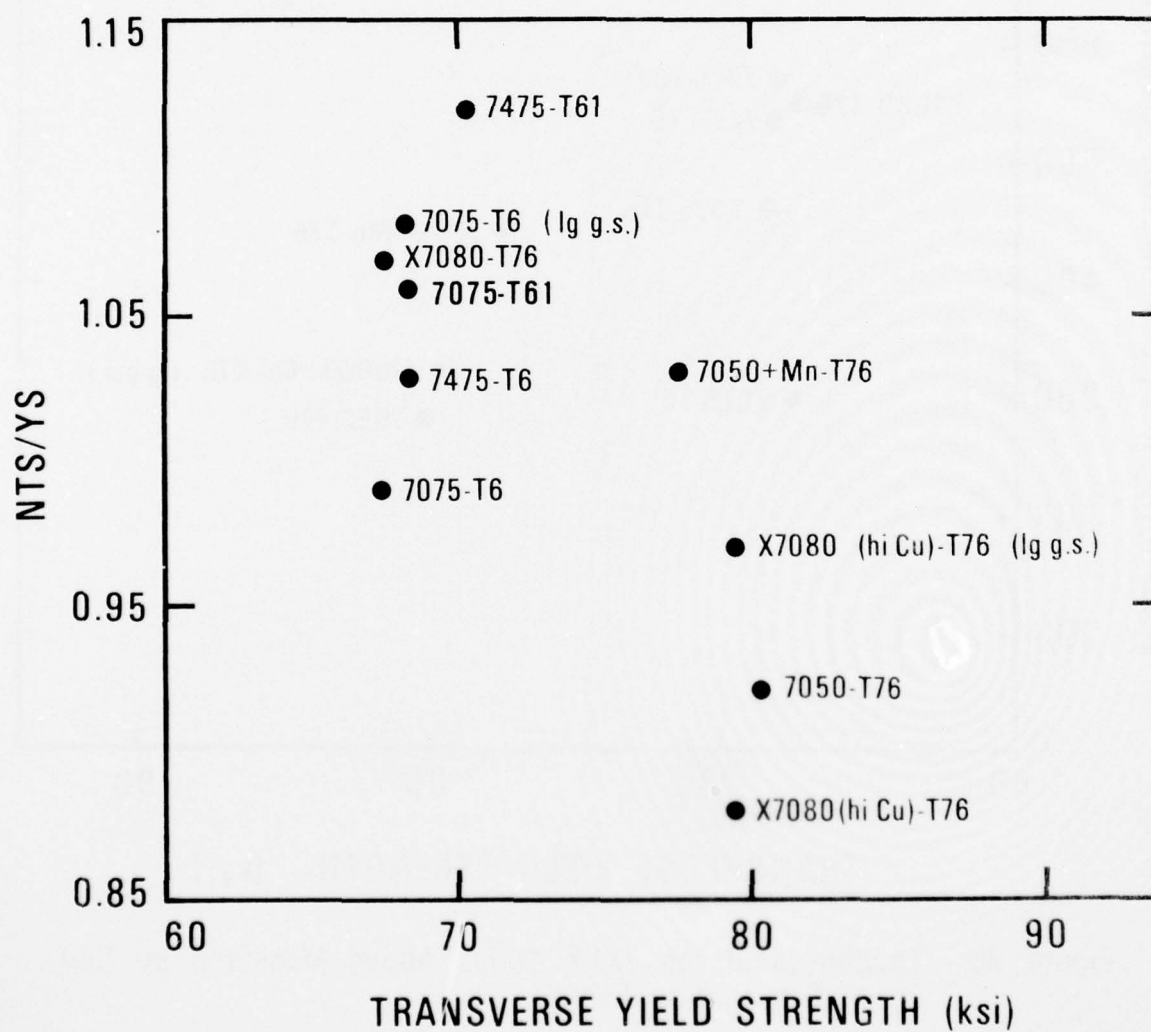


Figure 37 Notch Toughness of the 7XXX Series Alloys.

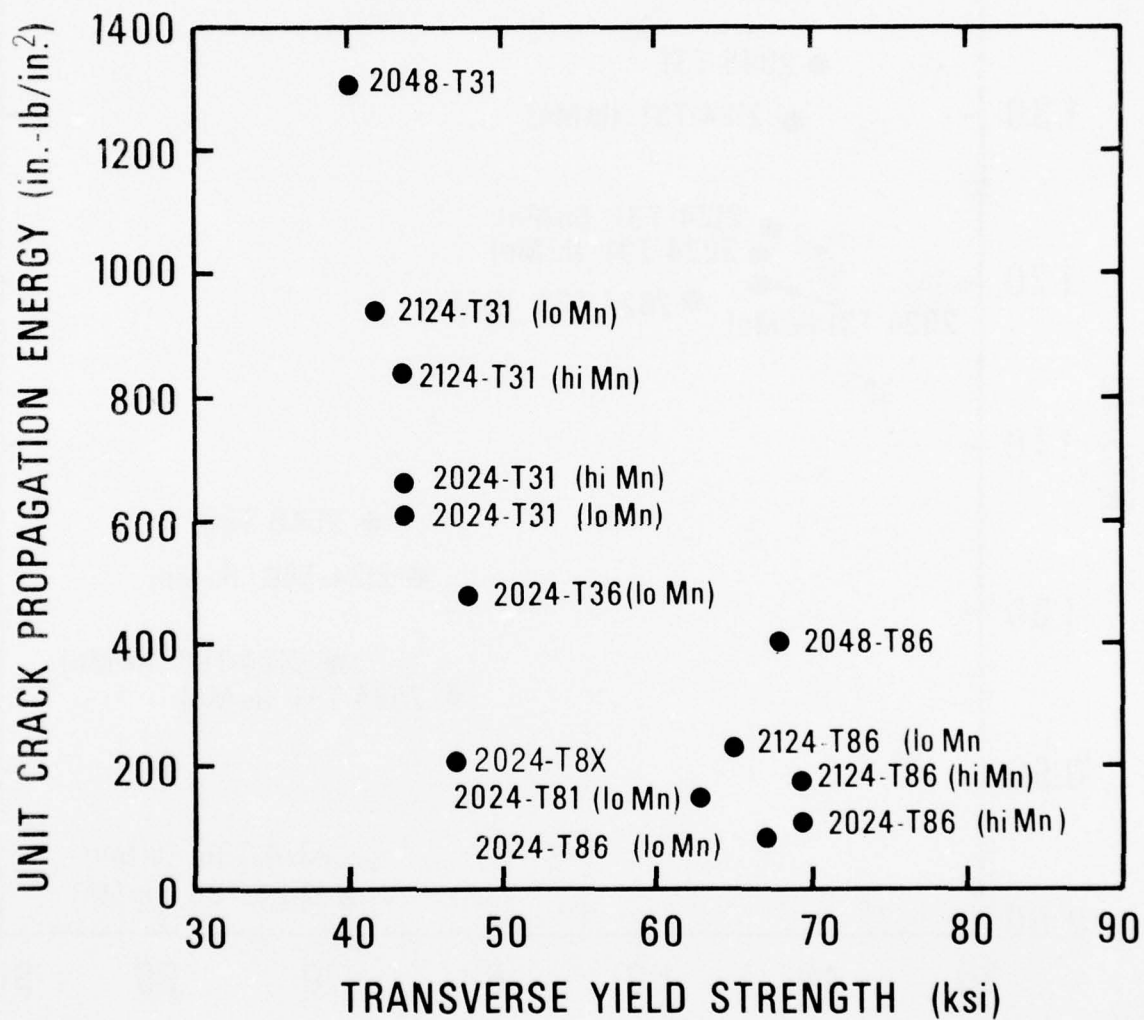


Figure 38 Toughness of the 2XXX Series Alloys Measured by Unit Crack Propagation Energy.

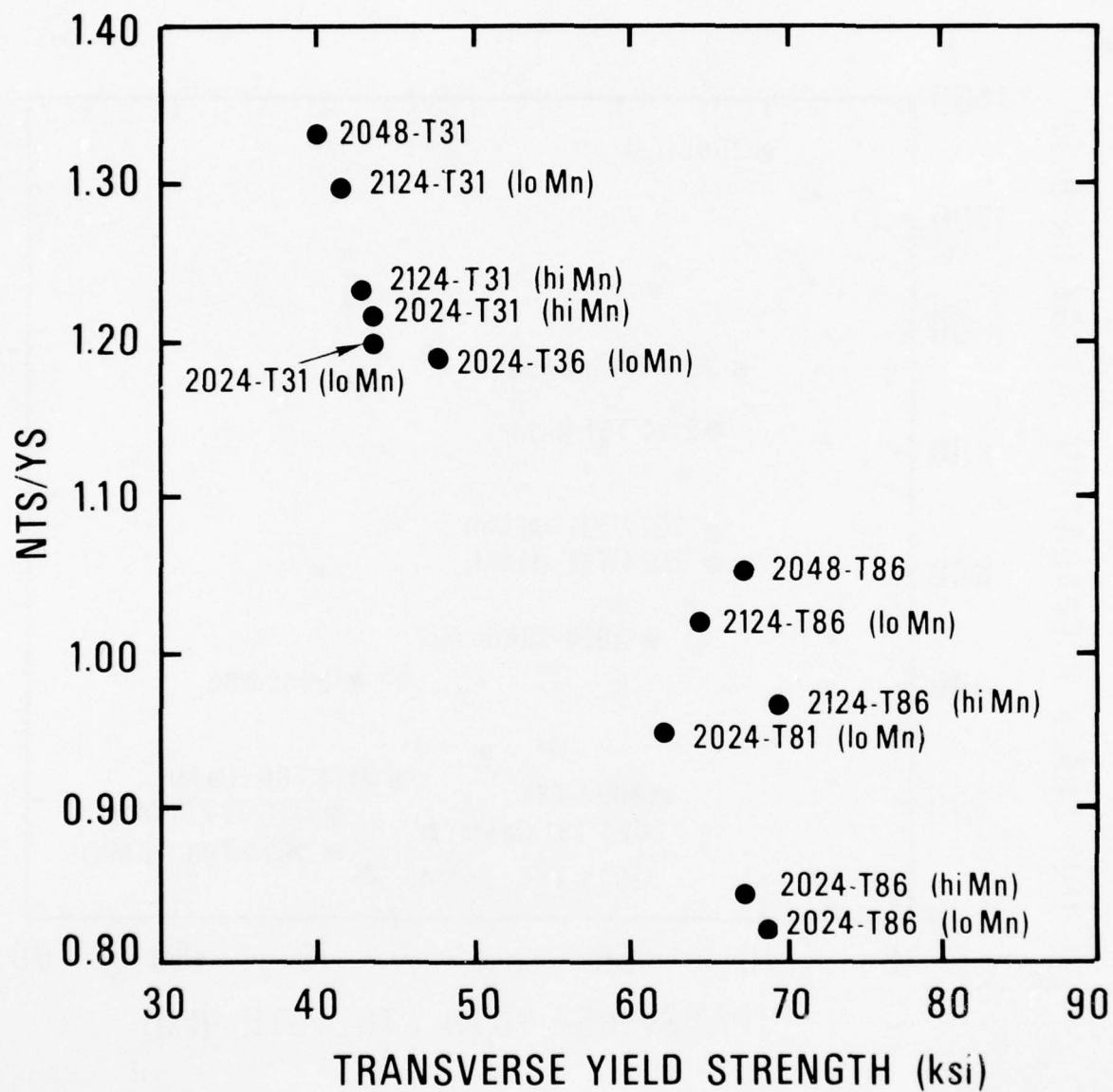


Figure 39 Notch Toughness of the 2XXX Series Alloys.

fatigue crack propagation characteristics. Much of the variability may be attributed to test technique, thereby justifying the concern for tight experimental controls maintained throughout this program.

Crack growth rate data were analyzed using different approaches. Visual side by side comparison of  $\Delta a/\Delta N$  vs  $\Delta K$  data points for different microstructures were made to ascertain qualitative differences. This method affords assessment of main effects on crack growth rate but evaluation of interaction effects of microstructure, environment, and test frequency becomes difficult.

Analysis of variance was used to estimate the main effects and interactions of microstructural and testing variables on fatigue crack growth rate at discrete levels of  $\Delta K$ . Since a two-level factorial design was used, the Yates algorithm[26] provided a convenient method to estimate effects.\*

For one approach using the Yates analysis, crack growth rate,  $\Delta a/\Delta N$ , was considered as a dependent variable at distinct levels of stress intensity range,  $\Delta K$ , of 6 and 16  $\text{ksi}\sqrt{\text{in.}}$ . Growth rate information to  $\Delta K$  levels as high as 16  $\text{ksi}\sqrt{\text{in.}}$  was not obtained for all structures and conditions. However, sufficient growth rate data was available at lower  $\Delta K$  in all cases to make reasonable extrapolation to  $\Delta K = 16 \text{ ksi}\sqrt{\text{in.}}$ . The method of extrapolation was typical of that shown in Figure 40 used for cyclic life estimations discussed in the following paragraph.

---

\*A 95% confidence level was used to assess whether effects were significant.



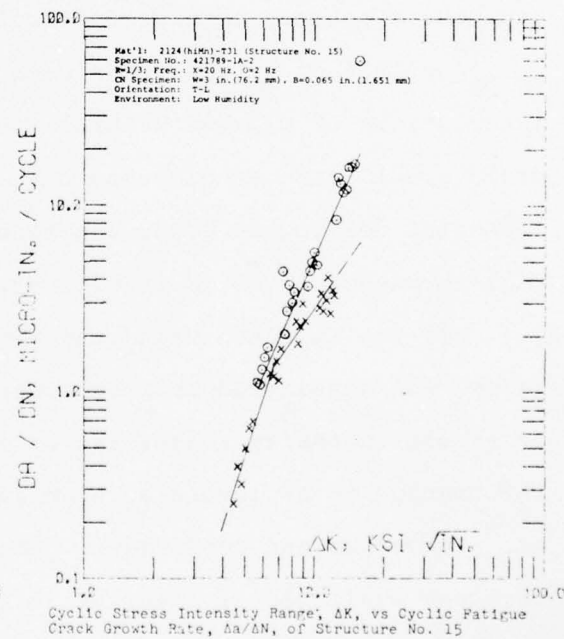
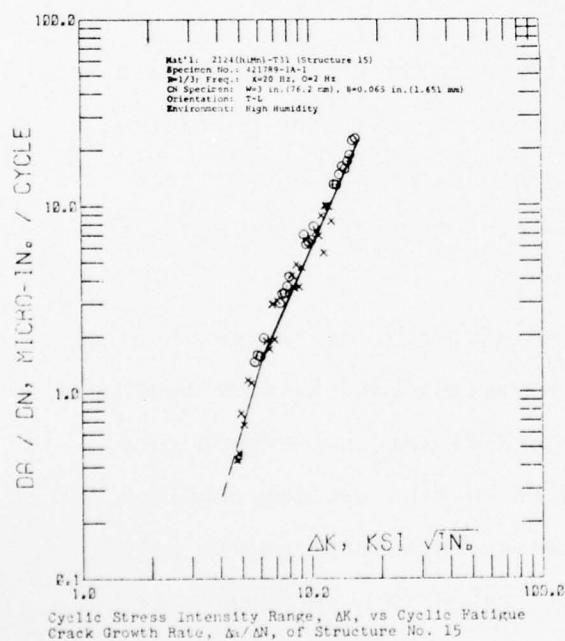
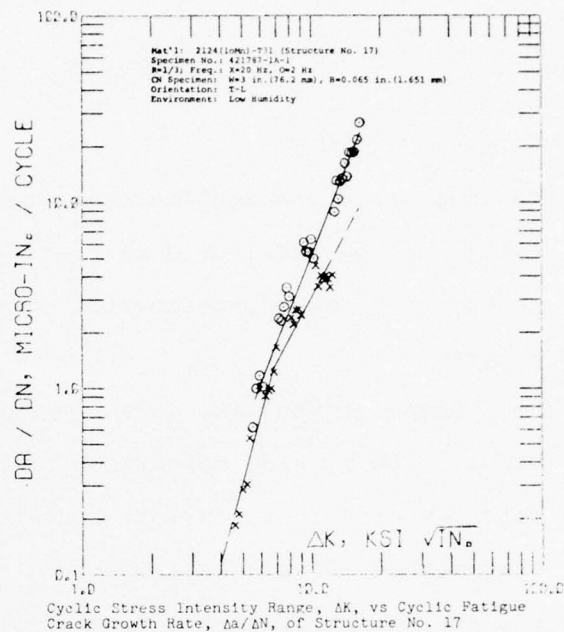
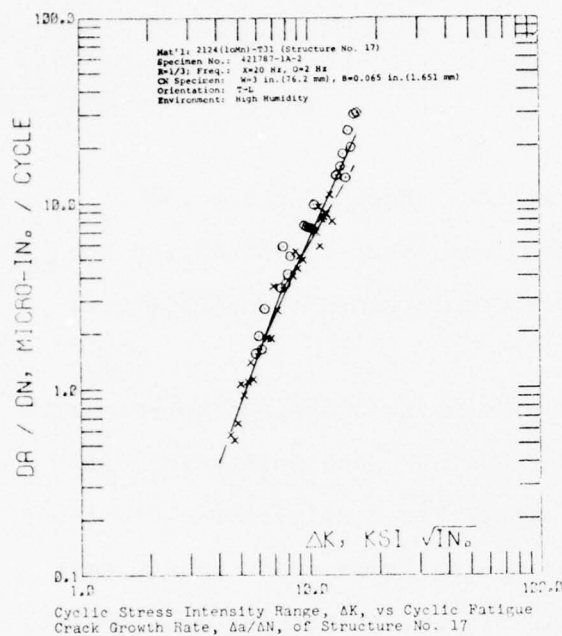


Figure 40 Cyclic Stress Intensity Range,  $\Delta K$ , Vs. Cyclic Fatigue Crack Growth Rate,  $da/dN$

Another approach was to analyze influence of different variables on cyclic life. Cyclic life is a meaningful parameter directly related to end product use. Using cyclic life rather than growth rate afforded an alternate means of ranking fatigue crack propagation performance by which alloy differences can be viewed more sensitively. To maximize amount of information per test, intermediate  $\Delta K$  data was generated at two levels of test frequency per specimen. Therefore, straight comparison of crack length vs cycles ( $a$  vs  $N$ ) information of each test would be impractical, since all specimens did not undergo identical load histories. However, cyclic life estimates derived from fracture mechanics analysis of fatigue crack growth rate data, two frequencies per test, provided two estimated  $a$  vs  $N$  curves per test, one for each frequency (2 and 20 Hz). This method was used to both supplement and verify conclusions drawn from comparison of crack growth rate at specific  $\Delta K$  values. Like crack growth rate, predicted fatigue life was employed as a dependent variable in the Yates analysis.

Cyclic life (number of stress cycles) required to grow a crack from a given initial to final size in the 3-inch wide center crack tension configuration was computed employing a linear damage approach and crack growth rate information generated for each of the microstructures, environments, and frequencies. The computations performed assumed initial half crack length, " $a$ ," of .373 inch and a final " $a$ " value of 1.1 inch. The assumed applied stresses were constant amplitude and set at  $\sigma_{\max} = 8$  ksi and  $R = \sigma_{\min}/\sigma_{\max} = 1/3$ . At this stress level,  $\Delta K$  equaled 6 and

15 ksi $\sqrt{\text{in.}}$ , respectively, for each of the above "a" values. These bounds on crack length and intermediate  $\Delta K$  levels were selected since all structures had meaningful data generated at two frequencies within the stated ranges. Moreover, the range in crack growth rates and  $\Delta K$  traversed in this study are representative of values encountered in actual service. Critical levels of fracture toughness,  $K_{IC}$ , developed for 7XXX and 2XXX alloys in nominal .063 inch gauges would typically be well above 22.5 ksi $\sqrt{\text{in.}}$ , the maximum cyclic stress intensity,  $K_{max}$ , at  $\Delta K = 15$  for  $R = 1/3$ . Therefore, the  $\Delta K = 15$  ksi $\sqrt{\text{in.}}$  upper bound chosen for life comparisons was considered to be low enough such that results over the stated  $\Delta K$  range would not be unfairly biased by differences in  $K_{IC}$ . To facilitate crack growth computation, a series of piecewise continuous "best fit" straight lines were selected to best represent the crack growth rate information for each set of conditions. Typical fits to actual data are shown in plots in Figure 40.

Fracture mechanics life predictions established in the above manner from data of replicate intermediate  $\Delta K$  crack growth tests of four 7XXX alloys were demonstrated to be highly reproducible (Table 14). A total of ten crack growth specimens were identically tested in high humidity air at two frequencies per test for a total of 20 replications on estimated life. The maximum deviation of predicted life from individual tests was in all cases within 7% of the mean predicted life for each 7XXX alloy. One exception to this high degree of reproducibility was noted for two replicate 2XXX alloy tests conducted in low humidity air (calculated lives

AD-A037 156

ALUMINUM CO OF AMERICA ALCOA CENTER PA ALCOA LABS F/G 11/6  
EFFECTS OF MICROSTRUCTURE ON FATIGUE CRACK GROWTH OF HIGH-STREN--ETC(U)  
AUG 76 W 6 TRUCKNER, J T STALEY, R J BUCCI F33615-74-C-5079  
56-76-AF5 AFML-TR-76-169 NL

UNCLASSIFIED

2 OF 3  
AD  
A037156





TABLE 14

ESTIMATED FATIGUE CRACK PROPAGATION LIVES FROM REPLICATE  
FATIGUE CRACK GROWTH TESTS

Alloy	Structure No.	Specimen No.	Environment	Estimated Life, Cycles $\Delta K=6$ to 15 ksi/in.	
				2 Hz	20 Hz
7075-T61	9	419588-D2-1	H.H.A. <sup>†</sup>	70951	62598
		419588-D2-2	H.H.A.	73593	64532
				<u>72272</u>	<u>63565</u> (mean)
7475-T6	12	419589-C2-1	H.H.A.	69443	53328
		419589-C2-2	H.H.A.	77305	58765
		419589-C2-3	H.H.A.	70959	60586
				<u>72569</u>	<u>57559</u> (mean)
A*	--	A-1	H.H.A.	89937	67504
		A-2	H.H.A.	90112	67543
				<u>90024</u>	<u>67523</u> (mean)
B*	--	B-1	H.H.A.	59761	60283
		B-2	H.H.A.	57152	59741
		B-3	H.H.A.	54134	54281
				<u>57015</u>	<u>58080</u> (mean)
2048-T31	24	421790-1A-1	L.H.A. <sup>†</sup>	258362	422061
		421790-1A-4	L.H.A.	200556	323638
				<u>229459</u>	<u>382849</u> (mean)

<sup>†</sup>H.H.A. (high humidity air), L.H.A. (low humidity air).

\*Alloys A and B were nonstandard 7XXX microstructures tested under identical conditions as those involved in this program.

differed by approximately 30%); refer to Table 14 and also to section 4.3.2.2.3. The greater degree of variability noted under these circumstances was tentatively attributed to the high sensitivity of fatigue crack growth rate to small changes in moisture content for Al-Cu-Mg alloys tested in low humidity air and at high frequencies. See section 5.2.1 and Figure 67.

Efficiency of the full-factorial design can be appreciated by considering the experimental module containing Structures 14 through 21 (refer to section 4.3.2.2.1). The  $2^5$  full-factorial design of three microstructural features (constituent, dispersoid, and precipitate) and two testing variants (frequency and environment) required 16 specimens (two frequencies per specimen). The information provided on any one of the effects was the same as that which would be available had all 16 specimens been tested to study one of the effects.

In summary, conclusions developed in this investigation for intermediate levels of  $\Delta K$  (4 to 20 ksi $\sqrt{\text{in.}}$ ) were based upon both visual and statistical examination of crack growth rate data and estimated cyclic life. Because low  $\Delta K$  tests were limited, it was not possible to employ statistical methods. Consequently, all conclusions concerning these low  $\Delta K$  tests were made using visual comparisons of generated data.

#### 4.3.2 Crack Growth Results

##### 4.3.2.1 7XXX Alloys

###### 4.3.2.1.1 Type of Dispersoid

This module was designed to provide information regarding relative merits of  $ZrAl_3$  and  $Al_{20}Cu_2Mn_3$  dispersoids separately and in combination:

<u>Alloy-Temper</u>	<u>Structure</u>	<u>Weight, %</u>	
		<u>Zr</u>	<u>Mn</u>
7050-T76	1	0.11	0.01
7050+Mn-T76	2	0.11	0.40
X7080 (hiCu)-T76	3	0.01	0.39

Intermediate  $\Delta K$  (Figures C-1 to C-6)\*

<u>Structure</u>	<u>Life, Cycles</u>		<u><math>\frac{\Delta a}{\Delta N}</math> (<math>10^{-6}</math> in./cycle)</u>		<u><math>\Delta K = 16 \text{ ksi}/\sqrt{\text{in.}}</math></u>	
	<u><math>\Delta K = 6 \text{ to } 15 \text{ ksi}/\sqrt{\text{in.}}</math></u>		<u><math>\Delta K = 6 \text{ ksi}/\sqrt{\text{in.}}</math></u>		<u>High Humidity</u>	
	<u>High Humidity</u>	<u>Low Humidity</u>	<u>High Humidity</u>	<u>Low Humidity</u>	<u>2/20 Hz</u>	<u>Low Humidity</u>
	<u>2/20 Hz</u>	<u>2/20 Hz</u>	<u>2/20 Hz</u>	<u>2/20 Hz</u>	<u>2/20 Hz</u>	<u>2/20 Hz</u>
1	62056/47620	97590/98108	3.8/4.8	2.7/2.7	47/65*	36/36*
2	82572/69100	103668/119574	3.0/3.5	2.4/1.8	46/69*	40/32*
3	77378/52051	112513/120935	2.8/4.4	2.0/1.7	68/106*	45/29*

\* Value determined by extrapolation.

Since this module was not a complete factorial design (0.0% Zr with 0.0% Mn is absent), Yates analysis was performed by comparing results for each structure against one another. Predicted lives and crack propagation rates for the three structures were not significantly different.

Increasing the moisture content of the test environment from 5 to 95% R.H. significantly increased crack propagation rates, while decreasing the frequency in high humidity air decreased rates.

Low  $\Delta K$  (Figures D-1 and D-2)

No difference in crack growth rate was observed between Structures 1 (7050-T76) and 3 (X7080(hiCu)-T76).

4.3.2.1.2 Copper Content

\*Figure prefixes C, D, or E refer to Appendix C, D, or E, respectively.



Comparison of these structures permitted determination of the effect of Cu content on crack propagation rate in 7050-type alloys:

<u>Alloy-Temper</u>	<u>Structure</u>	<u>Weight, % Cu</u>
X7080 (hiCu)-T76	3	2.3
X7080-T76	4	0.99

#### Intermediate $\Delta K$ (Figures C-5 to C-8)

<u>Structure</u>	<u>Life, Cycles</u>		<u><math>\frac{\Delta a}{\Delta N}</math> (<math>10^{-6}</math> in./cycle)</u>			
	<u><math>\Delta K = 6</math> to <math>15</math> ksi<math>\sqrt{\text{in.}}</math></u>		<u><math>\Delta K = 6</math> ksi<math>\sqrt{\text{in.}}</math></u>		<u><math>\Delta K = 16</math> ksi<math>\sqrt{\text{in.}}</math></u>	
	<u>High Humidity 2/20 Hz</u>	<u>Low Humidity 2/20 Hz</u>	<u>High Humidity 2/20 Hz</u>	<u>Low Humidity 2/20 Hz</u>	<u>High Humidity 2/20 Hz</u>	<u>Low Humidity 2/20 Hz</u>
3	77378/52051	112513/120935	2.8/4.4	2.0/1.7	68/106*	45/29*
4	35404/26852	90679/91410	7.0/8.4	2.7/2.7	80/87*	35/35*

\* Value determined by extrapolation.

Magnitude of the effect of Cu depended on humidity level. In low humidity air, Structure 4 had slightly shorter life and somewhat higher crack growth rate. In high humidity air, however, Structure 4 had significantly shorter predicted life and higher crack growth rates. Frequency effects were not changed by copper.

Low  $\Delta K$  (Figures D-2 and D-3)

In high humidity air, growth rates of Structure 4 (X7080-T76) and Structure 3 (X7080(hiCu)-T76) converged at  $\Delta K$  of about 4 to 5 ksi $\sqrt{\text{in.}}$ . At  $\Delta K$  levels below 4 ksi $\sqrt{\text{in.}}$ , the lower Cu structure had lower crack growth rate.

#### 4.3.2.1.3 Strengthening Precipitate Type

Structures 5, 6, and 7 were experimental tempers designed to provide information concerning influence of precipitate type in alloy 7050. These structures were produced using non-conventional precipitation heat treatments at temperatures well above that used



in commercial practice. After employing these aging practices, different amounts of S-phase, S',  $\eta$ , and  $\eta'$  precipitates were produced. Results are compared with those of 7050-T76, Structure 1.

<u>Alloy-Temper</u>	<u>Structure</u>	<u>Amount and Type of Precipitate</u>
7050-T76	1	$\eta'$
7050-TX1	5	(S', $\eta$ , $\eta'$ )
7050-TX2	6	Small S with large (S', $\eta$ , $\eta'$ )
7050-TX3	7	Medium S with ( $\eta$ , $\eta'$ )

Intermediate  $\Delta K$  (Figures C-1, 2, 9 to 14)

<u>Structure</u>	<u>Life, Cycles</u>		<u><math>\frac{\Delta a}{\Delta N}</math> (<math>10^{-6}</math> in./cycle)</u>			
	<u><math>\Delta K = 6</math> to <math>15</math> ksi/in.</u>		<u><math>\Delta K = 6</math> ksi/in.</u>		<u><math>\Delta K = 16</math> ksi/in.</u>	
	<u>High Humidity</u>	<u>Low Humidity</u>	<u>High Humidity</u>	<u>Low Humidity</u>	<u>High Humidity</u>	<u>Low Humidity</u>
	<u>2/20 Hz</u>	<u>2/20 Hz</u>	<u>2/20 Hz</u>	<u>2/20 Hz</u>	<u>2/20 Hz</u>	<u>2/20 Hz</u>
1	62056/47620	97590/98108	3.8/4.8	2.7/2.7	47/69*	36/36*
5	62155/62730	103528/103350	4.9/4.9	2.7/2.7	40/40*	30/30*
6	76783/77663	144871/148269	3.4/3.4	1.6/1.6	47/47*	35/35*
7	84945/83909	109033/129900	3.2/3.2	2.2/2.1	40*/40*	40/25*

\* Value determined by extrapolation.

The degree of precipitation increased progressively in Structures 1, 5, 7, and 6, respectively. In low humidity air, crack growth life showed progressive improvement with degree of precipitation. Structure 6 showed significantly longer life than Structures 1, 5, or 7. In high humidity air, life was shortest for Structures 1 and 5, while lives of Structures 6 and 7 were approximately the same. No frequency effects were observed in the experimental tempers.

4.3.2.1.4 Grain Size

These structures were designed to evaluate the effect of grain size in the hiCu 7XXX alloys (7050-type):

Alloy-Temper	Structure	Grain Size, mm			grains/mm <sup>3</sup>
		LT	T	Long.	
X7080 (hiCu)-T76	3	0.055	0.017	0.055	20,000
X7080 (hiCu)-T76	8	1.00	0.20	1.0	5

Intermediate  $\Delta K$  (Figures C-5, 6, 15, and 16)

Structure	Life, Cycles		$\frac{\Delta a}{\Delta N}$ (10 <sup>-6</sup> in./cycle)			
	$\Delta K = 6$ to $15$ ksi/in.		$\Delta K = 6$ ksi/in.		$\Delta K = 16$ ksi/in.	
	High Humidity	Low Humidity	High Humidity	Low Humidity	High Humidity	Low Humidity
	2/20 Hz	2/20 Hz	2/20 Hz	2/20 Hz	2/20 Hz	2/20 Hz
3	77378/52051	112513/120935	2.8/4.4	2.0/1.7	68/106*	45/29*
8	84201/54155	100356/107631	3.0/4.0	2.4/2.0	47/70*	45/36*

\* Value determined by extrapolation.

Although the grain size differed by more than one order of magnitude, the predicted fatigue lives and crack propagation rates were not significantly different. Increasing relative humidity decreased life for both structures. Frequency effects of both structures were comparable.

The effects of grain size were also established in a 7075-type alloy:

Alloy-Temper	Structure	Grain Size, mm			grains/mm <sup>3</sup>
		LT	T	L	
7075-T61	9	0.033	0.011	0.039	65,000
7075-T61	13	0.125	0.015	0.10	5,000

Intermediate  $\Delta K$  (Figures C-17 to 19 and C-28, 29)

Structure	Life, Cycles		$\frac{\Delta a}{\Delta N}$ (10 <sup>-6</sup> in./cycle)			
	$\Delta K = 6$ to $15$ ksi/in.		$\Delta K = 6$ ksi/in.		$\Delta K = 16$ ksi/in.	
	High Humidity	Low Humidity	High Humidity	Low Humidity	High Humidity	Low Humidity
	2/20 Hz	2/20 Hz	2/20 Hz	2/20 Hz	2/20 Hz	2/20 Hz
9	72272 <sup>†</sup> /63565 <sup>†</sup>	107888/142228	3.7 <sup>†</sup> /3.9 <sup>†</sup>	2.2/1.6	46 <sup>†</sup> /44 <sup>†</sup> *	46/23*
13	65614/55818	102823/105246	4.2/4.6	2.4/2.2	46/65*	39/39*

<sup>†</sup>Value represents the average of two tests.  
\*Value determined by extrapolation.

The lower performance of Structure 13 with coarse grain size was not statistically significant.

Grain size did not alter the frequency-environment effects previously noted for 7X75-T6 structure.

#### Low $\Delta K$ (Figures D-4, D-7)

Structures 9 and 13 had similar crack propagation rates at low  $\Delta K$  in high humidity air.

#### 4.3.2.1.5 Dispersoid-Constituent

These structures were designed to evaluate individual and combined effects of increasing the  $Al_{12}Mg_2Cr$  dispersoid size and spacing and of decreasing volume fraction of  $Al_7Cu_2Fe$ ,  $Al_{12}(Fe,Mn)_3Si$ ,  $FeAl_6$ , and  $Mg_2Si$  insoluble constituents:

<u>Alloy-Temper</u>	<u>Structure</u>	<u>Vol % of Constituents; <math>Al_7Cu_2Fe</math>, <math>Mg_2Si</math>, etc.</u>	<u>Size and Spacing <math>Al_{12}Mg_2Cr^*</math> Dispersoid</u>
7075-T61	9	1.20	Large
7075-T6	10	1.20	Normal
7475-T61	11	0.50	Large
7475-T6	12	0.50	Normal

\*See Figures 27 and 28 for comparison of size and spacing of  $Al_{12}Mg_2Cr$  dispersoid.

#### Intermediate $\Delta K$ (Figures C-17 to C-27)

<u>Structure</u>	<u>Life, Cycles</u>		<u><math>\frac{\Delta a}{\Delta N}</math> (<math>10^{-6}</math> in./cycle)</u>			
	<u><math>\Delta K = 6</math> to <math>15</math> ksi/in.</u>		<u><math>\Delta K = 6</math> ksi/in.</u>		<u><math>\Delta K = 16</math> ksi/in.</u>	
	<u>High Humidity</u>	<u>Low Humidity</u>	<u>High Humidity</u>	<u>Low Humidity</u>	<u>High Humidity</u>	<u>Low Humidity</u>
	<u>2/20 Hz</u>	<u>2/20 Hz</u>	<u>2/20 Hz</u>	<u>2/20 Hz</u>	<u>2/20 Hz</u>	<u>2/20 Hz</u>
9	72272 <sup>†</sup> /63565 <sup>†</sup>	107888/142228	3.7 <sup>†</sup> /3.9 <sup>†</sup>	2.2/1.6	46 <sup>†</sup> /44 <sup>†</sup> **	46/23**
10	63353/55993	88442/107824	4.0/4.5	2.4/2.0	88/54**	88/50**
11	73407/55989	102968/107391	4.0/4.5	2.6/2.5	36/54**	32/34**
12	72569/57560	96624/116511	3.8 <sup>‡</sup> /4.4 <sup>‡</sup>	2.7**/2.2	42 <sup>‡</sup> /56 <sup>‡</sup> **	37/18**

\*\* Value determined by extrapolation.

<sup>†</sup> Value represents the average of two tests.

<sup>‡</sup> Value represents the average of three tests.



Predicted lives of standard alloy 7075-T6 (normal size Cr dispersoids and higher volume fraction of constituents) were shorter than lives of the other structures, and crack growth rate analysis indicated that the difference was due to the faster crack growth rate at the higher levels of  $\Delta K$ .

Increasing the moisture content decreased life and increased crack growth rate. Main frequency effects were not statistically significant, but a frequency-environment interaction was noted. Increasing frequency in high humidity air and decreasing frequency in low humidity air both increased crack growth rate.

#### Low $\Delta K$ (Figures D-4 to D-6)

At these low  $\Delta K$  levels in high humidity air, no difference in crack growth rates was observed for Structures 9 (7075-T61), 10 (7075-T6), and 11 (7475-T61).

#### 4.3.2.2 2XXX Alloys

##### 4.3.2.2.1 Constituent, Dispersoid, and Strengthening Precipitate

These structures were designed to provide a complete factorial design experiment of main effects and interactions of volume fraction of  $Al_2O_3Cu_2Mn_3$  dispersoid, volume fraction insoluble constituents (vis;  $Al_7Cu_2Fe$ ,  $Al_{12}(Fe,Mn)_3Si$ ,  $Al_2CuMg$ , and  $Mg_2Si$ ), and temper (initial dislocation density and precipitate).

<u>Alloy-Temper</u>	<u>Structure</u>	<u>Volume Fraction <math>Al_2O_3Cu_2Mn_3</math> Dispersoid</u>	<u>Volume Fraction Insoluble Constituent</u>
2024 (hiMn)-T31	14	0.026	0.022
2124 (hiMn)-T31	15	0.026	0.014
2024 (loMn)-T31	16	0.011	0.022
2124 (loMn)-T31	17	0.011	0.014
2024 (hiMn)-T86	18	0.026	0.022
2124 (hiMn)-T86	19	0.026	0.014
2024 (loMn)-T86	20	0.011	0.022
2124 (loMn)-T86	21	0.011	0.014



# Intermediate $\Delta K$ (Figures C-30 to C-45)

Structure	Life, Cycles		$\frac{\Delta a}{\Delta N}$ ( $10^{-6}$ in./cycle)			
	$\Delta K = 6 \text{ to } 15 \text{ ksi}/\sqrt{\text{in.}}$		$\Delta K = 6 \text{ ksi}/\sqrt{\text{in.}}$		$\Delta K = 16 \text{ ksi}/\sqrt{\text{in.}}$	
	High Humidity	Low Humidity	High Humidity	Low Humidity	High Humidity	Low Humidity
	2/20 Hz	2/20 Hz	2/20 Hz	2/20 Hz	2/20 Hz	2/20 Hz
14	105981/125743	183385/382188	2.6/2.4	1.3/0.64	40/22**	24/6.5**
15	167239/173333	198266/312773	1.6/1.6	1.3/0.89	22/22**	19/6.4**
16	162256/159102	171427/398000	1.4/1.4	1.3/0.78	31/25**	21/5.6**
17	157168/157310	215177/318270	1.6/1.6	1.1/0.70	23/16**	22/9.0**
18	90998/99453	103920/126121	2.1/2.1	1.8/1.8	120/62**	127/45**
19	96484/100867	125747/220731	2.2/2.2	1.7/1.1	61/52**	66/30**
20	87225/86745	118900/165298	2.4/2.4	1.6/1.5	145/145**	144/27**
21	107846/111187	120575/161659	2.1/2.1	1.7/1.5	44**/44**	64/19**

\*\*Value determined by extrapolation.

Key results of analyses are presented graphically in Figures 41 and 42.

Analysis indicated that Mn dispersoid had no main effect and did not interact with other microstructural features or with test conditions to influence results.

Volume fraction of insoluble constituent had no effect in the T31 temper. In the T86 temper, mean (averaged on both frequencies and environments) predicted lives of alloys with the lower volume fraction averaged about 35% longer. T86 temper structures containing low volume fraction of constituent had lower crack propagation rates at  $\Delta K$  of  $16 \text{ ksi}/\sqrt{\text{in.}}$ , and visual analysis of data indicated that magnitude of the difference increased with increasing  $\Delta K$ . Mean crack propagation rates of the lower volume constituent material at  $\Delta K$  of  $6 \text{ ksi}/\sqrt{\text{in.}}$  were also lower, but this difference was not found to be statistically significant at the 95% confidence level.

Temper produced the largest microstructural effect. Mean predicted lives of the T31 temper structures (GP zones, 1%

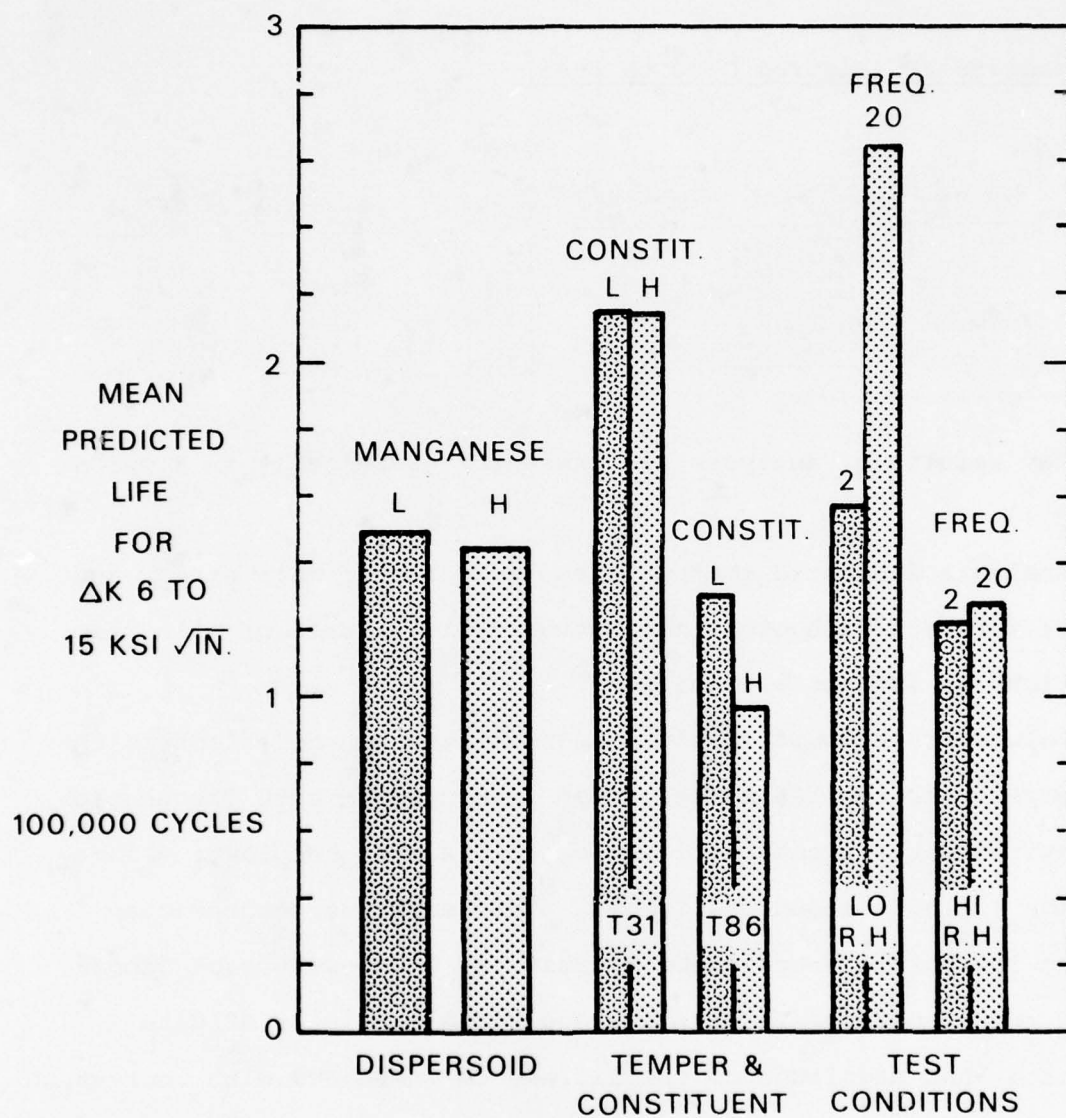


Figure 41 Effects of Microstructure and Test Variables on Crack Propagation Life of 2024 Type Sheet.

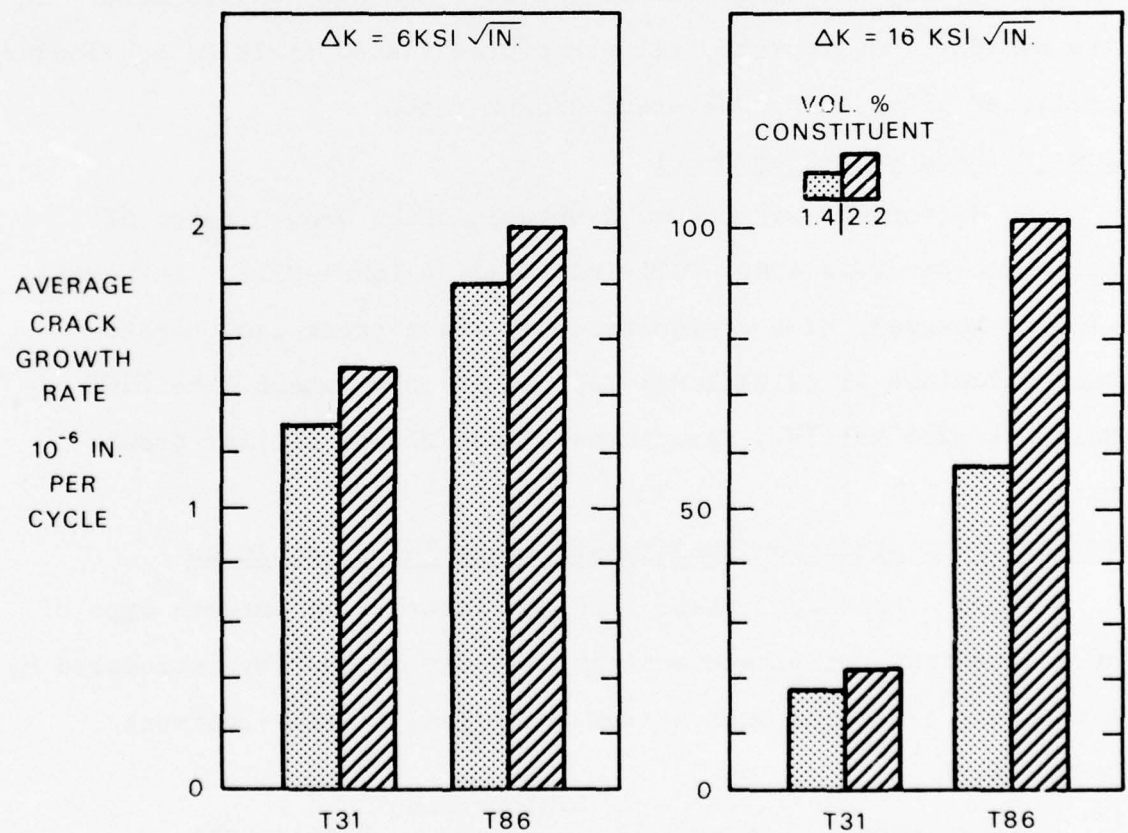


Figure 42 Effects of Volume % Constituent and Temper in Fatigue Crack Growth Rate of 2024 Sheet.

stretch) were about 75% longer than those of the T86 temper structures (S' precipitate, 5% stretch) and crack growth rates were lower, particularly at the higher levels of  $\Delta K$ .

Test frequency and environment both influenced results. Structures tested in the high humidity environment had shorter predicted lives and higher crack growth rates at both levels of  $\Delta K$ . Frequency had no effect in the high humidity environment. In low humidity environment, all structures tested at 20 Hz had longer predicted lives and lower crack growth rates.

#### Low $\Delta K$ (Figures D-8 to D-10)

No difference was observed between crack growth rates of Structure 16 (2024(10Mn)-T31) and 17 (2124(10Mn)-T31). Structure 17 did, however, have a significantly lower crack growth rate than Structure 21 (2124(10Mn)-T86) at  $\Delta K$  above about  $3 \text{ ksi}\sqrt{\text{in.}}$ . Below  $\Delta K \sim 2.5 \text{ ksi}\sqrt{\text{in.}}$ , Structures 17 and 21 had similar growth rates.

#### 4.3.2.2.2 Dislocation Density-Strengthening Precipitate

These structures established the interaction between type of strengthening precipitate and the dislocation density introduced by stretching after the quench from the solution heat treatment temperature.

<u>Alloy-Temper</u>	<u>Structure</u>	<u>Dislocation Density</u>	<u>Precipitate</u>
2024(10Mn)-T31	16	Low	GP
2024(10Mn)-T36	22	High	GP
2024(10Mn)-T81	23	Low	S'
2024(10Mn)-T86	20	High	S'



Intermediate  $\Delta K$  (Figures C-34, 35, 42, 43, 46 to 49)

Structure	Life, Cycles		$\frac{\Delta a}{\Delta N}$ ( $10^{-6}$ in./cycle)			
	$\Delta K = 6$ to $15 \text{ ksi}/\sqrt{\text{in.}}$		$\Delta K = 6 \text{ ksi}/\sqrt{\text{in.}}$		$\Delta K = 16 \text{ ksi}/\sqrt{\text{in.}}$	
	High Humidity 2/20 Hz	Low Humidity 2/20 Hz	High Humidity 2/20 Hz	Low Humidity 2/20 Hz	High Humidity 2/20 Hz	Low Humidity 2/20 Hz
16	162256/159102	171427/398000	1.4/1.4	1.3/0.78	31/25*	21/5.6*
22	111106/125593	180364/363196	2.2/1.7	1.3/0.70	37/37*	26/6.2*
23	94871/110231	141220/193256	2.2/2.2	1.6/1.3	65/48*	54/20*
20	87225/86745	118900/165298	2.2/2.2	1.7/1.1	61/52*	66/30*

\* Value determined by extrapolation.

Increasing the amount of stretch decreased life, particularly in T8 tempers. Growth rate analysis indicated that the propagation rates of the T86 temper sheet were significantly higher than those of the T81 temper sheet at  $\Delta K = 16 \text{ ksi}/\sqrt{\text{in.}}$

Stretching had no effect on the interactions of frequency and environment.

4.3.2.2.3 Copper Content-Strengthening Precipitate

These structures provided information on the effects of decreasing the Cu content in 2XXX alloys aged to two different tempers.

<u>Alloy-Temper</u>	<u>Structure</u>	<u>Cu Content</u>
2124 (10Mn)-T31	17	4.10
2048-T31	24	3.25
2124 (10Mn)-T86	21	4.10
2048-T86	25	3.25

### Intermediate $\Delta K$ (Figures C-36, 37, 44, 45, 50 to 54)

Structure	Life, Cycles		$\frac{\Delta a}{\Delta N}$ ( $10^{-6}$ in./cycle)			
	$\Delta K = 6$ to $15 \text{ ksi}/\sqrt{\text{in.}}$		$\Delta K = 6 \text{ ksi}/\sqrt{\text{in.}}$		$\Delta K = 16 \text{ ksi}/\sqrt{\text{in.}}$	
	High Humidity	Low Humidity	High Humidity	Low Humidity	High Humidity	Low Humidity
	2/20 Hz	2/20 Hz	2/20 Hz	2/20 Hz	2/20 Hz	2/20 Hz
17	157168/157310	215177/318270	1.6/1.6	1.1/0.70	23/16*	22/9.0*
24	183598/196000	229459 <sup>†</sup> /372850	1.5/1.3	0.88 <sup>†</sup> /0.57 <sup>†</sup>	18/16*	25 <sup>†</sup> /20 <sup>†</sup> *
		(258362/422061) <sup>†</sup>		(0.71/0.44) <sup>†</sup>		(34/22*) <sup>†</sup>
		200556/323638		1.1 / 0.70		15/17*
21	107846/111187	120575/161659	2.1/2.1	1.7/1.5	44*/44*	64/19*
25	130420/125242	186757/197441	1.8/1.8	1.2*/1.1	34/27*	26/17*

\* Value determined by extrapolation.

<sup>†</sup> Value represents the average of two tests.

Values from individual tests. Two hr. discussion of this variability.  
Refer to Sections 4.3.1 and 5.2.1.

In high humidity air, 2048 had longer life and lower crack growth rate than 2124 in both tempers. Alloy 2048-T86 also had longer life and lower crack growth rate than 2124-T86 in low humidity air.

The initial test of 2048-T31 in low humidity air indicated that fatigue life of 2048-T31 was far superior to that of 2124-T31 at a frequency of 20 Hz. A retest was run on 2048-T31 in low humidity air to verify this outstanding result, but estimated life from the second test was no different from that of 2124-T31.

Cu content had no effect on the environment-frequency interaction.

### Low $\Delta K$ (Figures D-9 to D-11)

In the low  $\Delta K$  range and in high humidity, crack growth resistance of 2048-T31 was better than that of 2124-T31.

### 4.4 Supplementary Structures to Study Precipitate Morphology

Preliminary analysis indicated that precipitate morphology had the largest effect on fatigue crack propagation rate. To provide supplementary information, one additional 2024 temper (Structure 26) and two additional 7050 tempers (Structures 27 and 28) were produced and tested.

#### 4.4.1 Overaged 2024

Structure 26, 2024-T8X, was prepared by solution heat treating, quenching, stretching to flatten, and aging 7 hours at 475°F. The precipitate structure was S' platelets (Table 7) and the yield strength (Table 13) was similar to that of 2024-T36. Toughness as measured by UPE was comparable to that of 2024-T86 (Table 13).  
Figures C-55, 56)

Structure	Life, Cycles		$\frac{da}{dN}$ ( $10^{-6}$ in./cycle)			
	$\Delta K = 6 \text{ to } 15 \text{ ksi}\sqrt{\text{in.}}$		$\Delta K = 6 \text{ ksi}\sqrt{\text{in.}}$		$\Delta K = 16 \text{ ksi}\sqrt{\text{in.}}$	
	High Humidity	Low Humidity	High Humidity	Low Humidity	High Humidity	Low Humidity
	2/20 Hz	2/20 Hz	2/20 Hz	2/20 Hz	2/20 Hz	2/20 Hz
26	94789/94727	130841/179396	2.5/2.5	1.7/1.6	48/48*	38/16*

\* Value determined by extrapolation.

Calculated lives of this material were not significantly different from those of 2024-T86 (Structures 18 and 20), but fatigue crack propagation rates at high  $\Delta K$  were lower.

#### 4.4.2 Underaged 7050

To prepare Structures 27 and 28, alloy 7050 panels were solution treated, quenched in cold water, and stretched to flatten. One was aged several months at room temperature (7050-W, Structure 27). The structure contained GP zones (Table 6), and yield strength (Table 13) was comparable to that of the drastically

"overaged" TX Structures 5, 6, and 7. The other panel was slightly underaged by precipitation heat treating it for 24 hours at 250°F (7050-T6, Structure 28). Yield strength was close to that of the slightly overaged 7050-T76 (Structure 1). Precipitate structure consisted of GP zones and  $\eta'$ .

Figures C-57 to 60)

Structure	Life, Cycles		$\frac{\Delta a}{\Delta N}$ ( $10^{-6}$ in./cycle)			
	$\Delta K = 6 \text{ to } 15 \text{ ksi}/\sqrt{\text{in.}}$		$\Delta K = 6 \text{ ksi}/\sqrt{\text{in.}}$		$\Delta K = 16 \text{ ksi}/\sqrt{\text{in.}}$	
	High Humidity	Low Humidity	High Humidity	Low Humidity	High Humidity	Low Humidity
	2/20 Hz	2/20 Hz	2/20 Hz	2/20 Hz	2/20 Hz	2/20 Hz
27	32599/32692	94413/93763	8.6/8.6	2.9/2.9	98/98*	34/34*
28	36761/37392	93447/96147	7.0/7.0	2.9/2.9	102/102*	36/36*

\* Value determined by extrapolation.

Fatigue crack propagation characteristics of 7050-W were the least attractive of all of the 7050 tempers, especially in the high humidity environment. Fatigue crack propagation characteristics of both 7050-W and T6 approached those of 7050-T76 in the low humidity air, but the mean lives (averaging 2 and 20 Hz data) were significantly below those of 7050-T76 in high humidity air. No frequency effects were observed.

#### 4.5 Lab Fabricated vs Commercial 7075-T6

For comparative purposes, fatigue crack growth rate tests in the intermediate region of  $\Delta K$  were conducted for commercially fabricated 7075-T6 sheet.

Figures C-20, 21, 61, 62

Structure	Life, Cycles		$\frac{\Delta a}{\Delta N}$ ( $10^{-6}$ in./cycle)			
	$\Delta K = 6 \text{ to } 15 \text{ ksi}/\sqrt{\text{in.}}$		$\Delta K = 6 \text{ ksi}/\sqrt{\text{in.}}$		$\Delta K = 16 \text{ ksi}/\sqrt{\text{in.}}$	
	High Humidity	Low Humidity	High Humidity	Low Humidity	High Humidity	Low Humidity
	2/20 Hz	2/20 Hz	2/20 Hz	2/20 Hz	2/20 Hz	2/20 Hz
Commercial 7075-T6	71466/53497	83815/88814	3.6/4.6	2.5/2.3	107/76*	81/48*
10	63353/55793	88442/107824	4.0/4.5	2.4/2.0	88/54*	88/50*

\* Value determined by extrapolation.



#### 4.6 Fractographic Studies

##### High $\Delta K$ ( $\geq 15$ ksi/in.)

At high levels of  $\Delta K$ , fractography studies revealed that fatigue failure occurred primarily by the ductile rupture mode (e.g., Figure 43).

##### Intermediate $\Delta K$

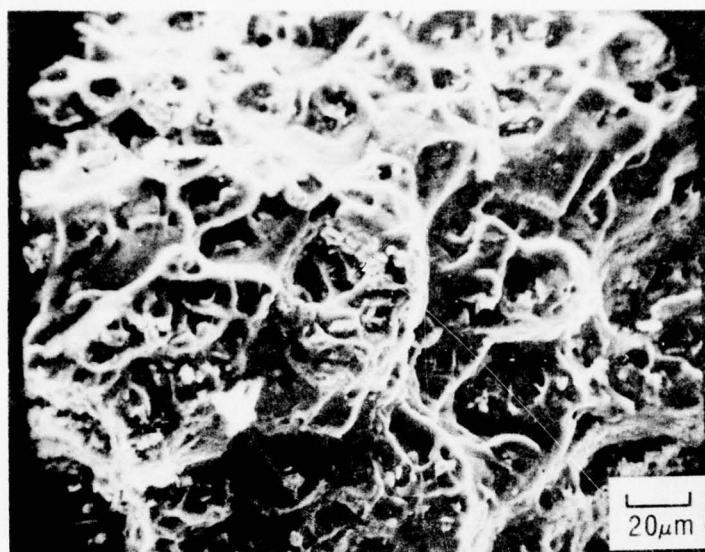
Fractographs of selected specimens showing the interaction of particular microstructural features and the propagating fatigue crack are illustrated in Figures 44 to 55.

Figure 44 shows that the constituent particles had an effect on the crack propagation path which was unlike that at high  $\Delta K$ . These particles appeared to have initiated cracks (Figure 45) and offered local resistance to the advancing crack front (Figures 46 and 47).

Dispersoid particles did not initiate cracks and did not appear to interact to a large extent with the advancing crack (Figures 48 and 49).

Fractographs of X7080-T6 in Figure 50 show that grain size did not change the overall crack propagation mode. This observation is consistent with the results of the crack growth rate and predicted life analysis which indicated that grain size had no influence on macroscopic growth rate.

In the 7XXX alloys, crack growth rate analysis indicated that in high humidity air the fatigue crack propagation rate was substantially increased by decreasing the Cu content from 2.3 to 1% (Structures 3 and 4). Micrographs of the fracture surface of



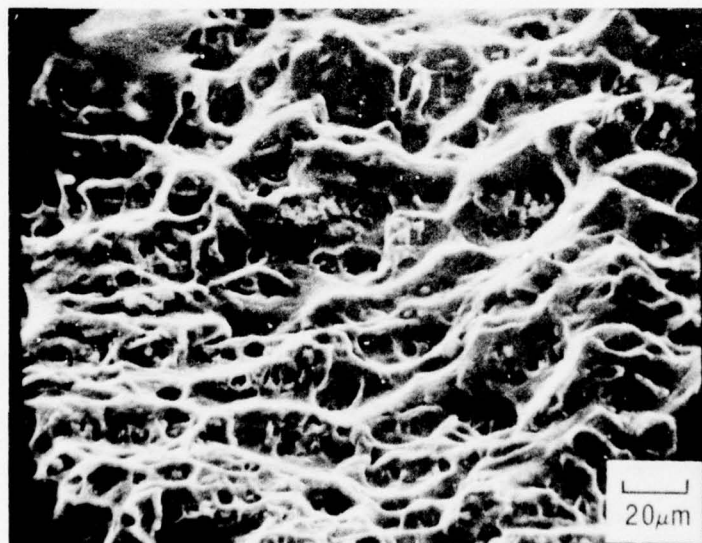
DIRECTION OF  
CRACK PROPAGATION



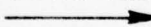
$\Delta K = 15 \text{ ksi}\sqrt{\text{in.}}$

LOW HUMIDITY  
AIR

2124 (hi Mn)-T86



DIRECTION OF  
CRACK PROPAGATION

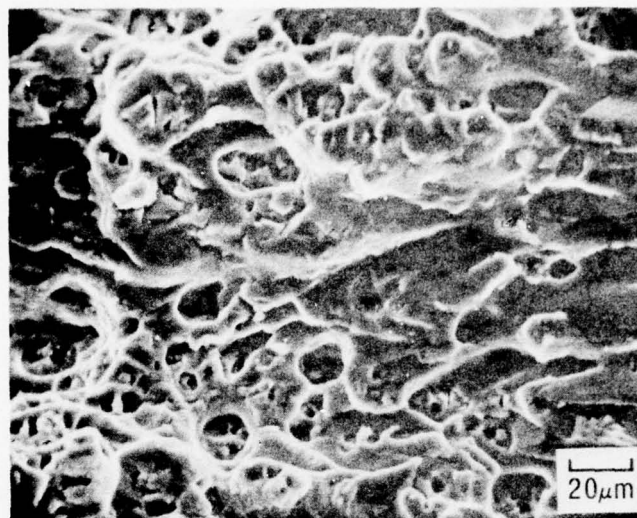


$\Delta K = 15 \text{ ksi}\sqrt{\text{in.}}$

LOW HUMIDITY  
AIR

2024 (hi Mn)-T86

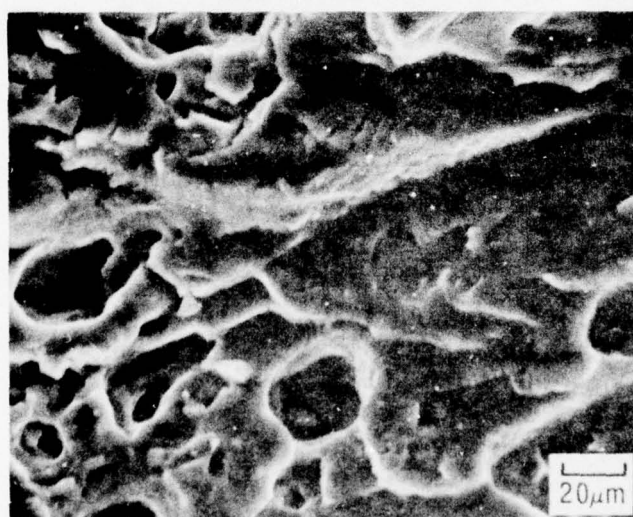
Figure 43 Scanning Electron Fractograph Illustrating Ductile Rupture Associated with Constituent Particles.



$\Delta K = 10 \text{ ksi}\sqrt{\text{in.}}$

LOW HUMIDITY  
AIR

2024 (hi Mn)-T86

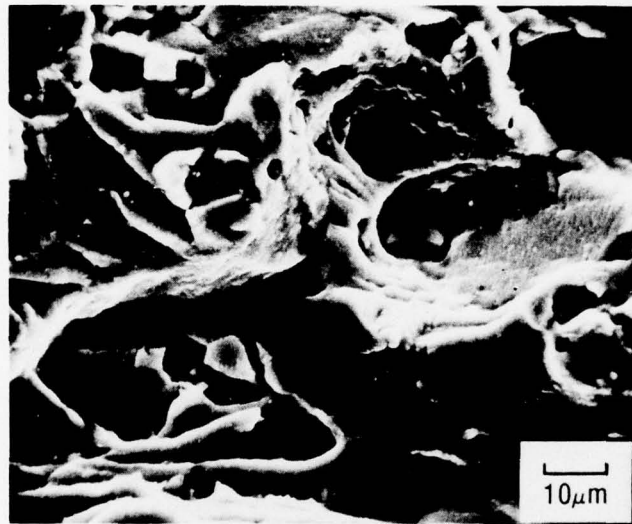


$\Delta K = 10 \text{ ksi}\sqrt{\text{in.}}$

LOW HUMIDITY  
AIR

2024 (hi Mn)-T86

Figure 44 Scanning Electron Fractograph Illustrating Constituent Effect at Intermediate  $\Delta K$ . Compare with Figure 43.

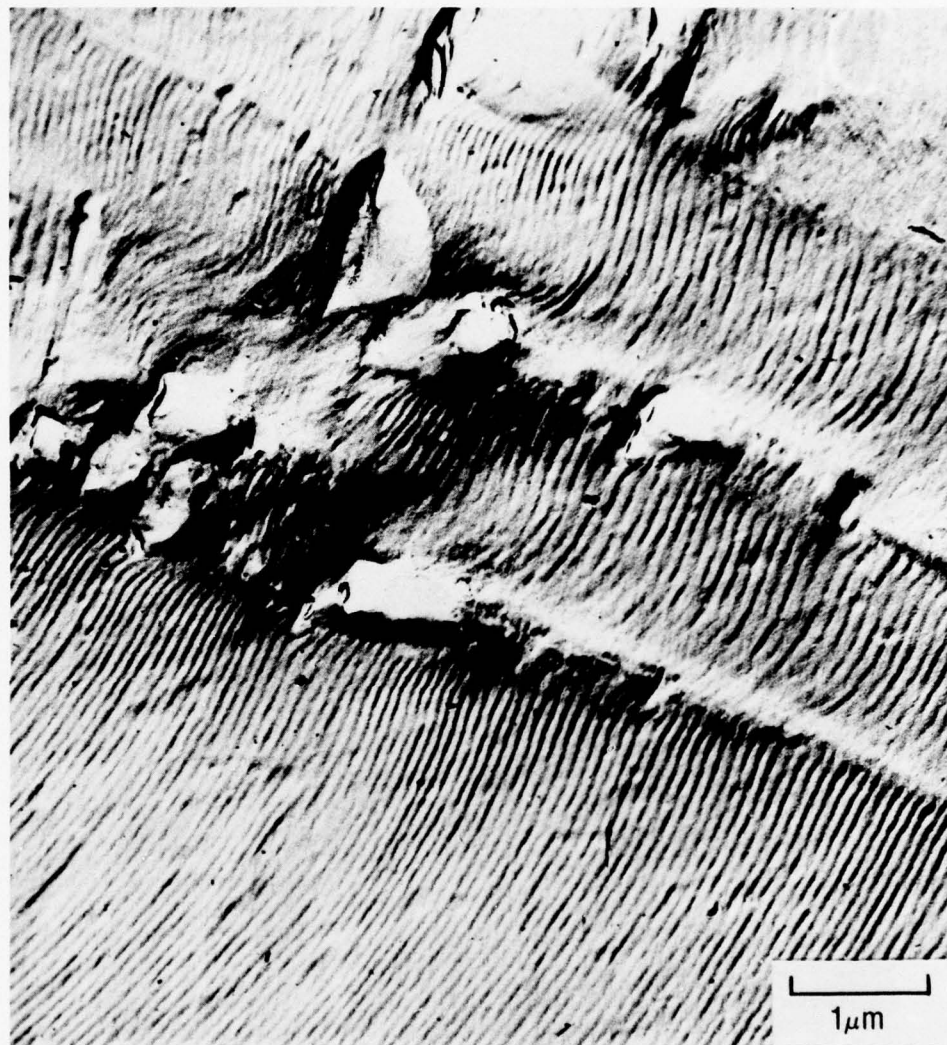


$\Delta K = 7.0 \text{ ksi}\sqrt{\text{in.}}$

LOW HUMIDITY  
AIR  
20 Hz

Figure 45 Scanning Electron Fractograph of 2024 (hi Mn)-T31.  
Note that Striations Appear to have been Initiated  
at Large Constituent Particle.





$\Delta K=9.0 \text{ ksi}\sqrt{\text{in.}}$

LOW HUMIDITY  
AIR  
20 Hz

Figure 46 Fracture Surface of 7050-T76 Illustrating Small Effect of Constituent Particles on Crack Growth Rate.



$\Delta K = 8.7 \text{ ksi}\sqrt{\text{in.}}$

LOW HUMIDITY  
AIR  
20 Hz

Figure 47 Fracture Surface of X7080 (hi Cu)-T76 Showing that Constituent Particles are only a Local, Temporary Obstacle To Crack Growth.



$\Delta K = 7.5 \text{ ksi}\sqrt{\text{in.}}$

LOW HUMIDITY  
AIR  
20 Hz

Figure 48 Scanning Electron Fractograph of X7080 (hi Cu)-T76 Showing Small Effect of Al<sub>20</sub>Cu<sub>2</sub>Mn<sub>3</sub> Dispersoid on Crack Growth.

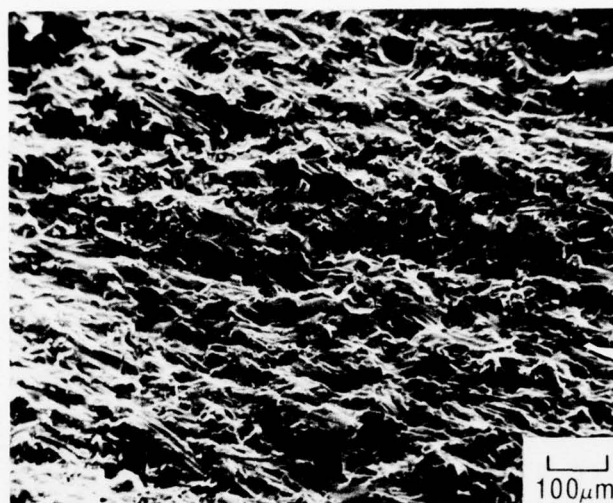


$\Delta K = 8.7 \text{ ksi}\sqrt{\text{in.}}$

LOW HUMIDITY  
AIR  
20 Hz

Figure 49 Fracture Surface of X7080 (hi Cu)-T76 Showing Small Effect of  $\text{Al}_{20}\text{Cu}_2\text{Mn}_3$  Dispersoid on Crack Growth.

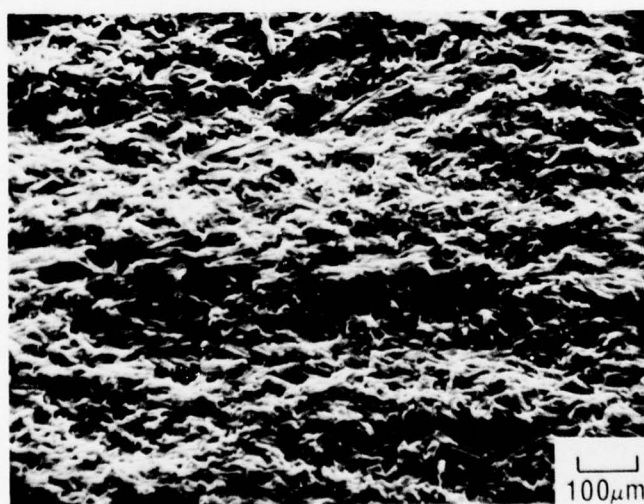




$\Delta K = 8.0 \text{ ksi}\sqrt{\text{in.}}$

LOW HUMIDITY  
AIR

X7080 (hi Cu)-T76  
(a)



$\Delta K = 8.0 \text{ ksi}\sqrt{\text{in.}}$

LOW HUMIDITY  
AIR

X7080 (hi Cu)-T76 (ig. g.s.)  
(b)

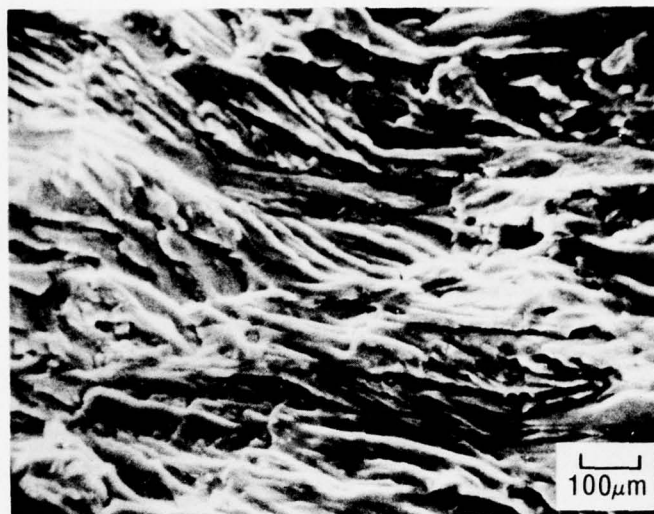
Figure 50 Scanning Electron Fractograph of 7080 (hi Cu)-T76 Having Two Different Grain Sizes Showing Similar Fracture Appearance.

these alloys show that the fracture mode was different in these structures. In the 2.3% Cu alloy (X7080(hiCu)-T76), the fracture surface had a ductile fracture appearance (Figure 51) while the 1% Cu alloy (X7080-T76) had a brittle-like, more faceted appearance (Figure 52).

Figures 53 to 55 illustrate the difference in the fracture appearance of the T31 and T86 tempers in the 2XXX alloys. The fracture surface of the T31 temper had striations which were not sharp and readily visible (Figure 53). On the other hand, the fracture surface of the T86 alloys contained sharp, well-defined fatigue striations as well as areas that appeared to contain small microcracks (Figure 54). In addition, isolated areas on the fracture surface (Figure 55) contained dimpled regions similar to that found on the fracture surface of tensile specimens. Examination of these areas revealed that particles were not associated with all of these dimpled regions.

#### Low $\Delta K$

In general, the fracture surfaces were much flatter in appearance than those tested at higher  $\Delta K$  levels (Figures 56 to 62). No evidence of fatigue striations were observed. Using the nomenclature established by Weber and Hertzberg[27], the fracture surfaces could be characterized as consisting primarily of plateau and ridges (Figures 56 to 59) and some rumpled surfaces (Figures 60 and 61). Areas were also observed that might be classified as "cleavage-like" (Figure 62). Feeney, et al.[28], who studied the fracture surface of 2024-T3 and 7075-T6 tested at low  $\Delta K$  levels



DIRECTION OF  
CRACK PROPAGATION

$\Delta K = 10 \text{ ksi}\sqrt{\text{in.}}$

HIGH HUMIDITY  
AIR

X7080 (hi Cu)-T76



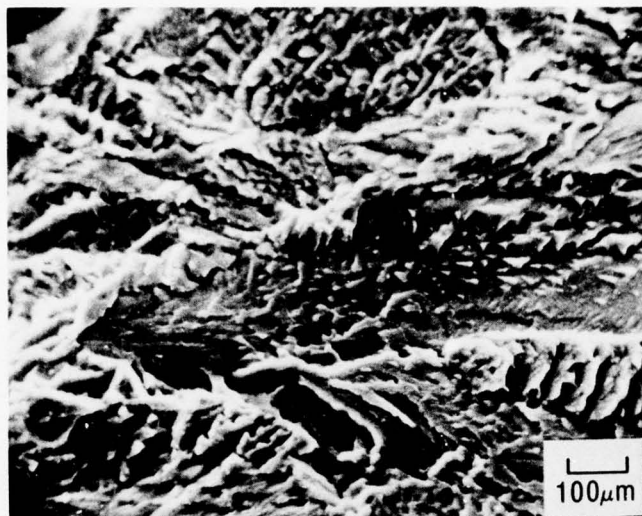
DIRECTION OF  
CRACK PROPAGATION

$\Delta K = 10 \text{ ksi}\sqrt{\text{in.}}$

HIGH HUMIDITY  
AIR

X7080 (hi Cu)-T76

Figure 51 Scanning Electron Micrograph of X7080 (hi Cu)-T76 Having Ductile Fracture Surface.

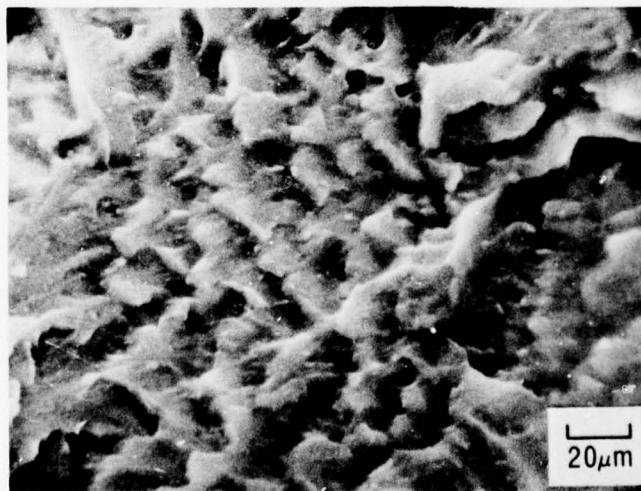


DIRECTION OF  
CRACK PROPAGATION  
→

$\Delta K = 10 \text{ ksi}\sqrt{\text{in.}}$

HIGH HUMIDITY  
AIR

X7080-T76



DIRECTION OF  
CRACK PROPAGATION  
→

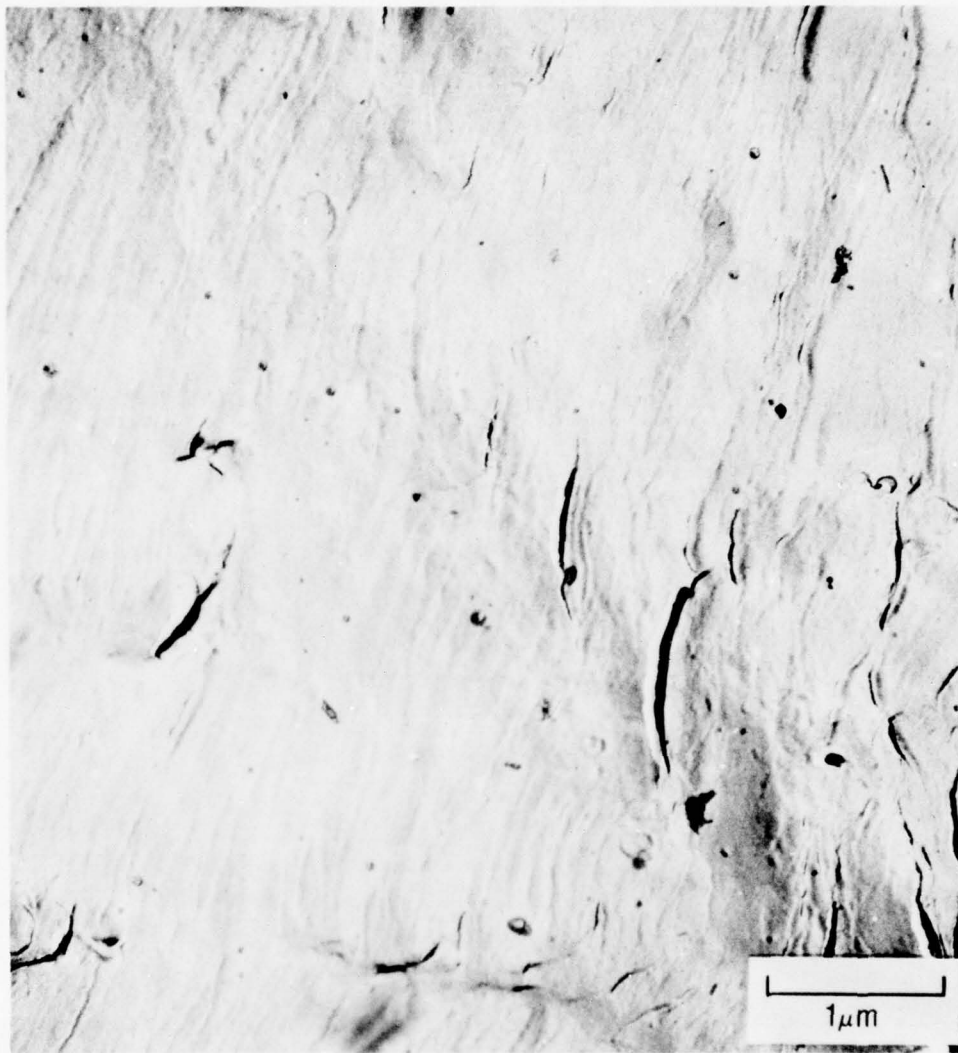
$\Delta K = 10 \text{ ksi}\sqrt{\text{in.}}$

HIGH HUMIDITY  
AIR

X7000-T76

Figure 52 Scanning Electron of X7080-T76 Showing  
Faceted Fracture Surface





$\Delta K = 11.0 \text{ ksi}\sqrt{\text{in.}}$

LOW HUMIDITY  
AIR  
2 Hz

Figure 53 Fracture Surface of 2048-T31.



$\Delta K = 11.0 \text{ ksi}\sqrt{\text{in.}}$

LOW HUMIDITY  
AIR  
20 Hz

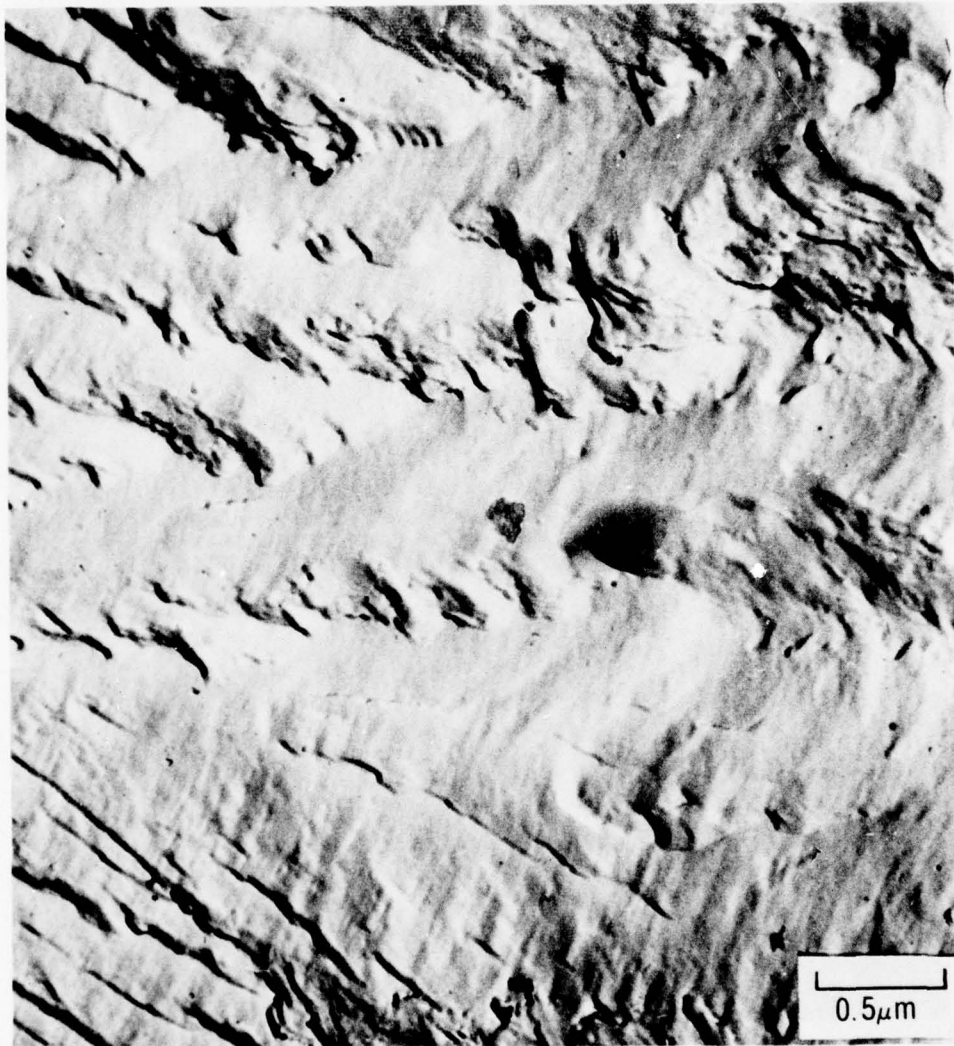
Figure 54 Fracture Surface of 2048-T86. Note Striations as well as Microcracks (upper right).



$\Delta K = 11.0 \text{ ksi}\sqrt{\text{in.}}$

LOW HUMIDITY  
AIR  
20 Hz

Figure 55 Fracture Surface of 2048-T86 Showing Dimpled Fracture Area

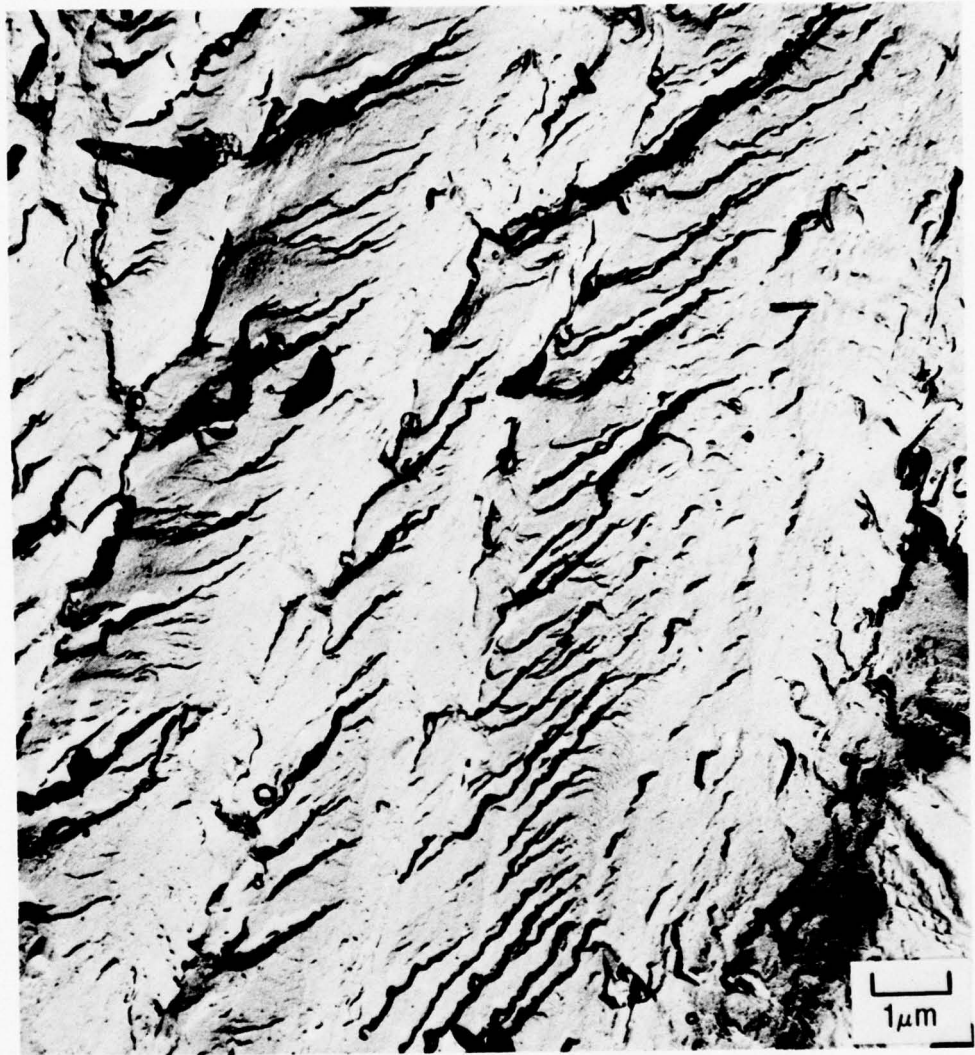


$\Delta K = 3.0 \text{ ksi}\sqrt{\text{in.}}$

HIGH HUMIDITY  
AIR  
50 Hz

Figure 56 Fracture Surface of 2048-T31 Showing Plateau and Ridge Fracture Appearance.

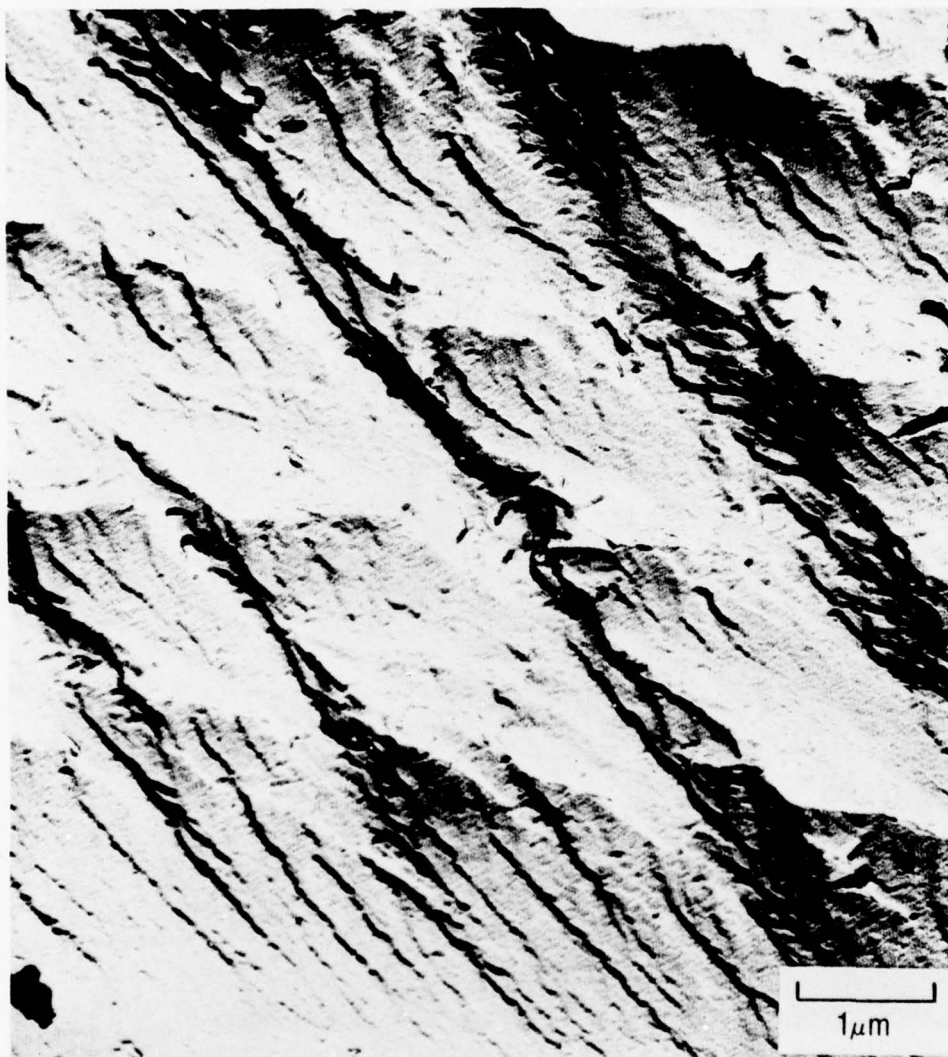




$\Delta K = 3.0 \text{ ksi}\sqrt{\text{in.}}$

HIGH HUMIDITY  
AIR  
50 Hz

Figure 57 Fracture Surface of X7080-T76 Showing Plateau and Ridge Fracture Appearance



$\Delta K = 3.0 \text{ ksi}\sqrt{\text{in.}}$

HIGH HUMIDITY  
AIR  
50 Hz

Figure 58 Fracture Surface of 7050-T76 Showing in Greater Detail Plateau and Ridge Fracture Appearance.



$\Delta K = 3.0 \text{ ksi}\sqrt{\text{in.}}$

HIGH HUMIDITY  
AIR  
50 Hz

Figure 59 Fracture Surface of 7050-T76 Showing Plateau and Ridge Fracture Appearance.



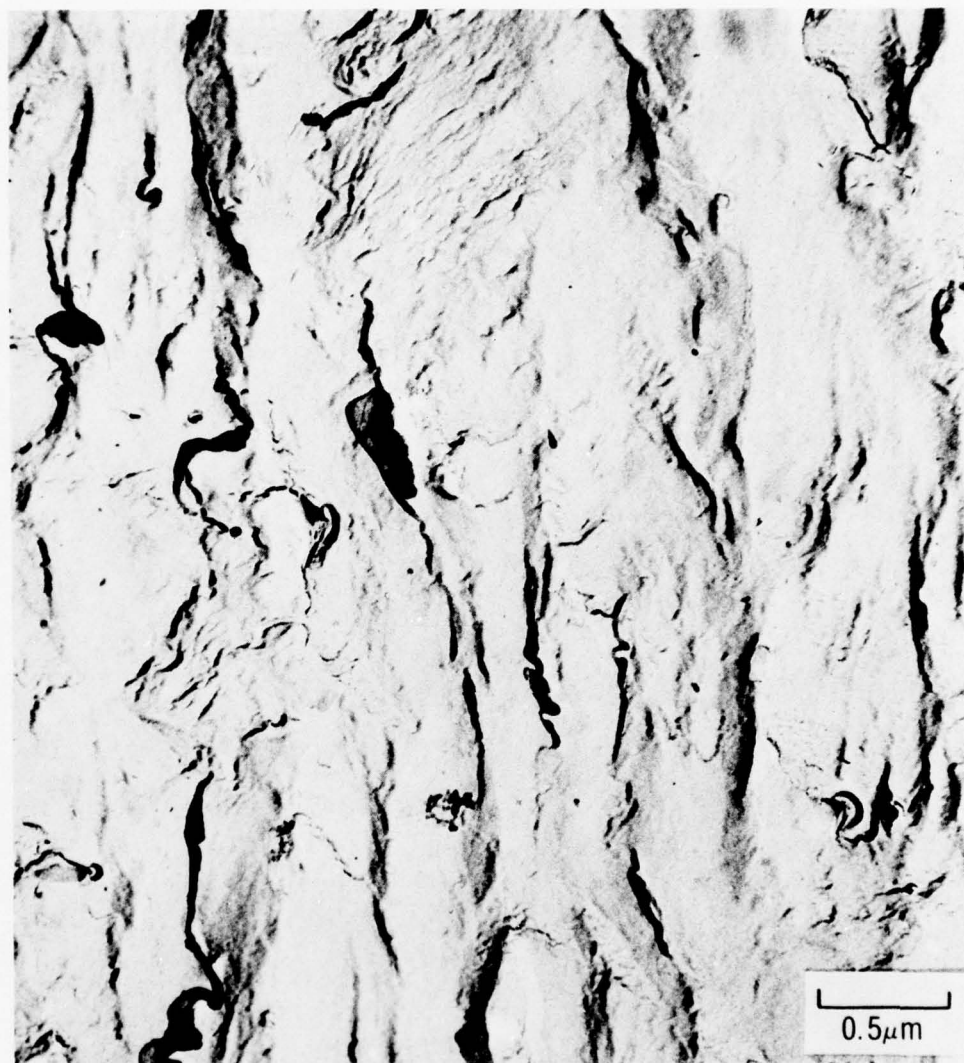


$\Delta K = 2.8 \text{ ksi}\sqrt{\text{in.}}$

LOW HUMIDITY  
AIR  
50 Hz

Figure 60 Fracture Surface of 2024-T31 Showing Rumpled Fracture Appearance.





$\Delta K = 3.0 \text{ ksi}\sqrt{\text{in.}}$

HIGH HUMIDITY  
AIR  
50 Hz

Figure 61 Fracture Surface of 2048-T31 Showing Rumpled Fracture Appearance.



$\Delta K = 2.8 \text{ ksi}\sqrt{\text{in.}}$

HIGH HUMIDITY  
AIR  
50 Hz

Figure 62 Fracture Appearance of 7050-T76 Showing "Cleavage-Like" Regions Present on the Fracture Surface.

found that the most common fracture mode was "stepwise" growth. This term appears to be synonymous with the term plateau and ridges used by Weber and Hertzberg. Feeney, et al., also observed "cleavage-like" fracture areas on the fracture surface of these alloys.

## 5. DISCUSSION

### 5.1 Microstructural Effects

#### 5.1.1 Insoluble Constituent (Contains Fe and Si)

Decreasing volume fraction of insoluble constituent particles increased energy required to propagate a crack (UPE) in tear tests of all materials. However, the tabulation below indicates that for increases in UPE less than about 300 in.-lb/in.<sup>2</sup>, absolute level of toughness attained, not the magnitude of increase, correlated with fatigue performance.

Alloy Type and Temper	Structure Nos.	Unit Crack Propagation energy ( $\frac{\text{in.-lb}}{\text{in.}^2}$ ) in tear test (UPE)			
		High Vol.Frac. Const.	Low Vol.Frac. Const.	Effect on Life†	Effect on $\Delta a/\Delta N$ High $\Delta K$ †
2X24-T31	14 & 16 vs 15 & 17	640*	900*	None	None
7X75-T61	9 vs 11	465	785	None	Possible
7X75-T6	10 vs 12	300	530	Small	Large
2X24-T86	18 & 20 vs 19 & 21	110*	200*	Large	Large

\*Average for both Mn contents.

Decreasing volume fraction of insoluble constituent for materials which had UPE values below about 500 in.-lb/in.<sup>2</sup>

provided a decrease in mean fatigue crack growth rate at high levels of  $\Delta K$ . Decreasing volume fraction of insoluble constituent for materials which already had values of UPE above this level, however, provided no further improvement in average crack growth rate. Apparently, UPE above 500 in.-lb/in.<sup>2</sup> indicates a level of fracture toughness high enough where benefits of decreasing volume fraction of insoluble constituent containing Fe and Si could not be detected at intermediate  $\Delta K$  levels. Relationships between UPE and fatigue crack propagation performance are discussed more fully in section 5.3.

Fractography indicated that failure at  $\Delta K$  of 15 ksi $\sqrt{\text{in.}}$  and higher occurred largely by a ductile rupture mode (Figure 43), and that constituent particles were associated with the dimples. At  $\Delta K$  values from 8 to 10 ksi $\sqrt{\text{in.}}$ , however, constituent particles had a smaller effect on advancement of the crack front. In Figures 46 and 47, note that striations are locally curved near the particle, but their spacing remains essentially the same. The large constituent particles may also initiate new "crack fronts" since striations in Figure 45 appear to emanate from the particle, but because the crack is advancing on various levels within the material, the overall effect of constituent particles on macroscopic growth rate is smaller than it is when they initiate dimple rupture. In addition, chemical analyses along the fracture surface ( $\Delta K$  ranging from 8 to 10 ksi $\sqrt{\text{in.}}$ , Table 15) showed a concentration of constituent-forming elements smaller than has been found for tensile failures[29]. This result indicates that the tendency was not as great for the



TABLE 15  
MICROPROBE ANALYSIS OF THE FRACTURE SURFACE OF SELECTED STRUCTURES  
 $\Delta K = 8 \text{ to } 10 \text{ ksi}\sqrt{\text{in.}}$

Structure	Alloy	Air Test	Location	Si	Fe	Cu	Mn	Mg	Cr	Zn	Zr
#3	X7080(high Cu)-T76	Dry	Fracture Center Random Section	0.10 0.03	0.15 0.07	2.17 2.32	0.38 0.39	2.28 2.29	0.03 0.02	5.60 6.03	-- --
#24	2048-T3	Dry	Fracture Center Random Section	0.10 0.04	0.12 0.06	3.53 3.58	0.39 0.42	1.63 1.66	0.01 0.02	0.03 0.01	-- --
#14	2024(high Mn)-T3	Dry	Fracture Center Random Section	0.27 0.18	0.31 0.17	5.07 4.90	0.82 0.85	1.56 1.51	0.02 0.01	0.03 --	-- --
#1	7050-T76	Dry	Fracture Center Random Section	0.08 0.04	0.08 0.06	2.11 2.35	0.05 0.05	2.37 2.50	0.02 0.02	5.99 6.18	0.14 0.12
#1	7050-T76	Moist	Fracture Center Random Section	0.08 0.03	0.08 0.06	2.27 2.32	0.05 0.04	2.42 2.49	0.02 0.02	5.84 6.32	0.14 0.12

fatigue crack to seek these particles during its advancement at this level of  $\Delta K$ .

### 5.1.2 Dispersoid

#### 5.1.2.1 7XXX Alloys

In 7050-T76-type alloys (Structures 1 to 3), presence of either the low volume fraction, very small, coherent  $ZrAl_3$  dispersoids or the greater volume fraction, larger, incoherent  $Al_{20}Cu_2Mn_3$  dispersoids did not change fatigue crack propagation rate. In fact, combining both dispersoids (Structure 2) did not change fatigue crack growth rate. Moreover, although this investigation did not compare Zr and Cr dispersoids for a given alloy, Selines and Pelloux[30] have found that substituting Zr for Cr in a 7075 alloy also did not influence the crack propagation rate.

Micrographs of the fracture surface indicate that  $Al_{20}Cu_2Mn_3$  dispersoid acts as a very small, temporary obstacle to the advancing crack front (Figures 48 and 49). Striation spacing is only locally affected by presence of dispersoid, and thus overall macroscopic crack propagation rate would not change.

Changing size and spacing of  $Al_{12}Mg_2Cr$  dispersoid did not significantly affect predicted fatigue life. However, statistical analysis using  $\Delta a/\Delta N$  as the dependent variable in the Yates algorithm indicated that there was an interaction among morphology of Cr dispersoid, volume fraction constituent, and  $\Delta K$ . At high levels of  $\Delta K$ , 7075-T6 (Structure 10, higher volume fraction constituent, normal  $Al_{12}Mg_2Cr$  dispersoid) gave higher crack growth

rates than 7075-T61 (Structure 9, same high volume fraction constituent but with large, widely spaced dispersoid particles). However, 7475-T6 and T61 (Structures 12 and 11 with low volume fraction constituent) showed no effect of dispersoid. Since modifying these dispersoids has no effect on strength, these observations suggest that size and spacing of Cr dispersoids alter fatigue resistance in 7XXX alloys by their effect on toughness. Only where toughness was low (high volume fraction constituent) was the effect of modifying dispersoid morphology found to be apparent (Figures 36 and 37).

#### 5.1.2.2 2XXX Alloys

In 2XXX alloys, increasing volume percent of  $\text{Al}_{20}\text{Cu}_2\text{Mn}_3$  dispersoid from 1.1 to 2.6 did not change mean crack growth rate at any level of  $\Delta K$  (Structures 16, 17, 20, 21 vs 14, 15, 18, 19). This is not surprising at higher  $\Delta K$  levels because changes in volume fraction of these dispersoids did not affect fracture toughness (Figures 38 and 39). At lower  $\Delta K$  levels, fractographic studies on these 2XXX alloys showed that the Mn dispersoid behaves in a manner similar to that observed in 7XXX alloys by arresting crack advancement, i.e., only local, temporary obstacle to the crack front.

#### 5.1.3 Grain Size

Although the larger grain size studied in this work extended well beyond size encountered in commercial sheet fabricated from ingots, crack propagation rates were not significantly changed. Fracture appearance of Structures 3 and 8 (X7080(hiCu)-T76) are

in general identical (Figure 50) even though grain size varied by a factor of 20 in the longitudinal direction (direction of crack growth), Figures 7 and 8. Similar observations were made for Structures 9 and 13 (7075-T61).

Investigators[3, 31 and 32] have shown that in materials that deform by wavy-type slip, e.g., pure aluminum, crack growth rate is independent of grain size. In materials which deform by planar slip such as low stacking fault energy alloys (Cu-Al), fatigue crack growth is grain size dependent. Laird[31] suggests that this grain size independence in wavy slip materials is due to the formation of subgrains in slip bands near the crack tip which help transmit the slip across the grain boundaries. In planar slip alloys, Laird indicates that these subgrains will not form, and, consequently, grain boundaries can be effective barriers to slip, i.e., dislocations pile up in planar arrays at the boundary. Direct observation of the structure adjacent to the crack tip in 2024-T3 and 7075-T6 by Grosskreutz and Shaw[33] shows that subgrains do form in these materials and thus lend support for Laird's model and the results found in this current study. Although these results show no effect of grain size, the smallest grain size evaluated was orders of magnitude greater than those produced in powder metallurgy 7XXX alloys found to have outstanding fatigue crack propagation resistance[34].

#### 5.1.4 Copper Content

##### 5.1.4.1 7XXX Alloys



Increasing Cu content from 1.0 to 2.3% in X7080-T76-type alloys slightly decreased fatigue crack growth rate in low humidity at intermediate  $\Delta K$ . However, increasing the Cu content significantly decreased crack growth rate in high humidity air at intermediate  $\Delta K$ . Crack growth rates in high humidity converged at  $\Delta K$  of about  $5 \text{ ksi}\sqrt{\text{in.}}$ , and below  $4 \text{ ksi}\sqrt{\text{in.}}$  the rates of the low Cu alloy were lower.

Micrographs of fracture surfaces of X7080-T76 tested in low and high humidity air at intermediate  $\Delta K$  indicate that in moist environment this low Cu alloy shows signs of brittle-like fracture facets in the fracture surface (Figures 51 and 52), whereas in low humidity air no signs of these facets were visible. Alloy X7080 (hiCu)-T76, tested in both dry and moist air, exhibited fracture surfaces similar to X7080-T76 tested in low humidity air. Hyatt and Quist[35] also found evidence of brittle fracture in low Cu 7XXX alloys tested in distilled  $\text{H}_2\text{O}$ . Furthermore, they found that, for a given Zn/Mg ratio in 7XXX alloys, Cu content of 2.00% (the highest studied) was optimum for resistance to fatigue crack growth.

Additional tests are needed to confirm the indication that low Cu may decrease fatigue crack growth rate at low  $\Delta K$ .

#### 5.1.4.2 2XXX Alloys

At intermediate levels of  $\Delta K$ , decreasing Cu content from 4.2 to 3.2% (2124 to 2048) increased propagation life and lowered crack growth rates in high humidity air for both T31 and T86 tempers (Structures 17, 21, 24,25). In low humidity air, decreasing Cu increased life in the T86 temper, but results of low

humidity test for the T31 temper were variable.\* Because of this anomalous behavior, additional tests are required to confirm effects of Cu in low humidity air. The high performance of alloy 2048 at intermediate  $\Delta K$  is attributed to the effect of reducing volume fraction constituent of  $\text{CuAl}_2$  and  $\text{Al}_2\text{CuMg}$  constituent particles which increases fracture toughness to a greater extent than reducing volume fraction of insoluble constituent containing Fe and Si (section 4.1). See section 5.3 for further discussion on relationship of fatigue crack growth performance to toughness.

At low  $\Delta K$ , the single high humidity test of 2048-T31 indicated that growth rate was lower than rates of 2124-T31, 2024-T31, and 2124-T86. Insensitivity of the 2024 alloy base (Cu and Mg) to differences in volume fraction of constituent (Structure 16 vs 17) and in precipitate morphology (Structure 17 vs 21) suggests that the advantage of 2048-T31 (assuming confirmation in additional tests) is due to differences in the Cu and Mg remaining in solid solution after aging. These differences in composition of solid solution could affect low  $\Delta K$  crack growth kinetics in the presence of moisture.

#### 5.1.5 Precipitate Morphology

##### 5.1.5.1 Intermediate $\Delta K$

Observations on alloy 7050 structures showed that fatigue performances of drastically overaged TX tempers (Structures 5, 6, and 7) were generally superior to those of slightly overaged T76

---

\*The variability is tentatively attributed to the large effect of small differences in moisture content of air at low humidity levels at high frequencies observed in Al-Cu-Mg alloys. See section 5.2.1 and Figure 67.

temper (Structure 1) possessing higher strength. However, comparing fatigue crack propagation performance of 7050 alloy structures possessing comparable strength, namely, 7050-W (Structure 27) with TX tempers (Structures 5, 6, and 7) and 7050-T6 (Structure 28) with 7050-T76 (Structures 1 and 2) indicates that fatigue crack growth resistance cannot be wholly correlated with monotonic yield strength (Figure 63).

Relative effects of precipitate morphology on fatigue crack growth characteristics of 7050 were strongly influenced by relative humidity. Additional discussion of interactions of precipitate structure with environment for 7XXX alloys is made in section 5.2.2.

Observations on alloy 2024 structures showed that T3 tempers (GP zones) in 2024-type alloys provided lower fatigue crack propagation rates than did T8 tempers ( $S'$  precipitates). However, supplementary tests of overaged 2024-T8X (Structure 26,  $S'$  precipitate) again demonstrated that higher crack propagation of 2024 structures containing  $S'$  precipitate cannot be correlated solely with monotonic strength (Figure 64).

The following discussion attempts to rationalize better fatigue crack propagation behavior of 2X24-T3 (GP zones) relative to that of 2X24-T8 ( $S'$  precipitates) in terms of strength and ductility parameters local to the crack tip. For the time being, effects of environment are ignored but, as will be indicated by subsequent discussion, environment-enhanced fatigue crack growth is accentuated when ductility is low. In section 5.2.1, effects

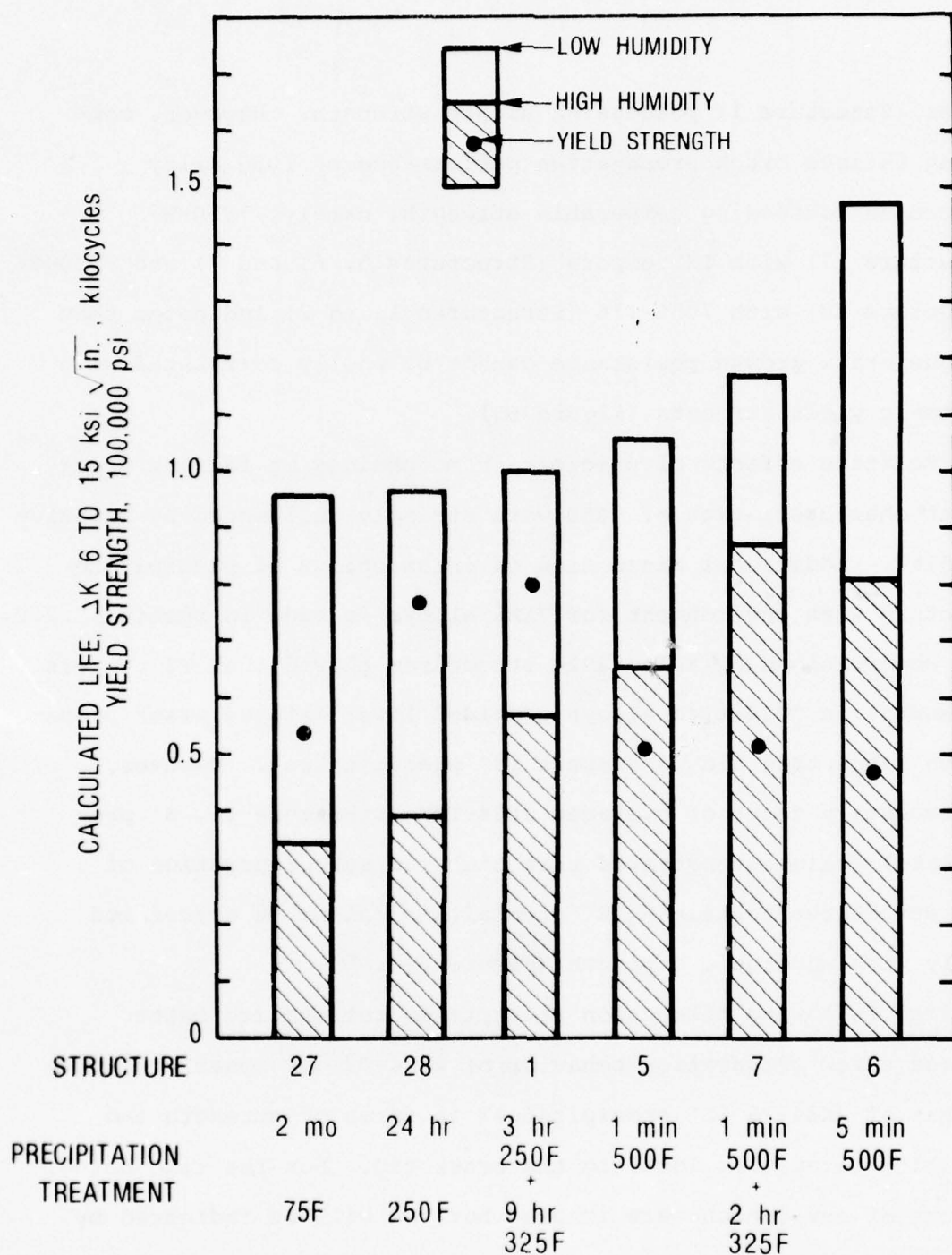


Figure 63 Mean Calculated Fatigue Propagation Life (both 2 and 20 Hz) for 7050 with Various Degrees of Precipitation.



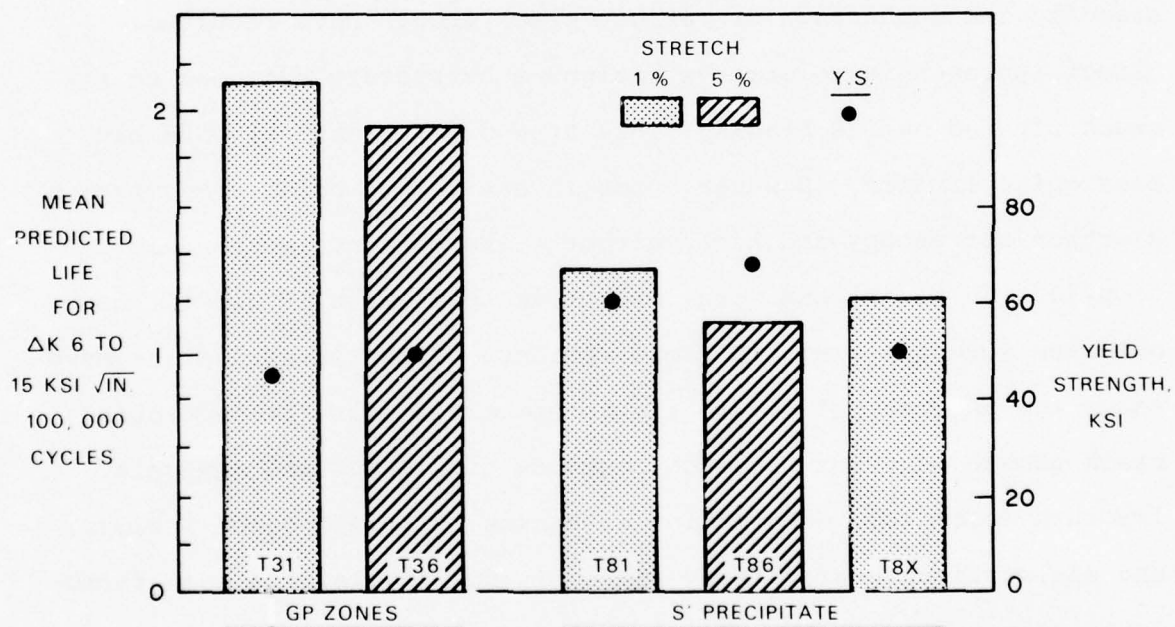


Figure 64 Mean Calculated Fatigue Propagation Life (both frequencies and environments) for Alloy 2024

of environment will be discussed in greater depth, and interaction with precipitate morphology will be addressed.

Microdeformation mechanisms occurring at the tip of a fatigue crack are not well known nor understood because of experimental difficulties in observing microstructure in the extremely localized deformation region at the crack tip (cyclic plastic zone) and the relatively larger monotonic plastic zone extending beyond the cyclic plastic zone. Consequently, different approaches to understanding the mechanisms of fatigue crack growth have resulted. A direct approach is to observe fatigue substructure adjacent to the crack tip and on its flanks. This type of experimental work has been quite limited. However, some investigators using transmission electron microscopy and high voltage transmission electron microscopy[33, 36 to 39] and X-ray microbeam techniques[40 and 41] have observed structures within these regions. Other investigators have taken the approach of developing mathematic models for predicting crack growth behavior based on concepts of dimensional analysis, fracture mechanics, deformation mechanics, strain control fatigue, and dislocation theory. Many semiempirical models have been formulated using test data to derive theoretical relationships. A number of fatigue crack propagation theories are summarized in the following references[42 to 45].

Although several of the approaches generally ignored other disciplines, common threads are apparent. First, and most important, is that microstructure must influence crack propagation. This has been established through direct observations of dislocation

substructure as well as through mathematical and empirical models showing the dependence of macroscopic mechanical properties characterizing a material, e.g., strength, fracture toughness, strain hardening coefficient, etc. Second, there is a region local to the crack tip which has undergone plastic strain, the magnitude of which increases with decreasing distance from the crack tip. Adjacent to the crack and totally embedded within a larger zone of permanent tensile plastic deformation, there is a much smaller volume of material which experiences fully reversed plastic strains of considerable intensity[46]. Third, cyclic strain history at further distances from the crack tip may be important (even though substructure produced at these low strains may be unstable in the high damage region adjacent to the crack tip) because rate of cyclic strengthening is a function of microstructure and plastic strain amplitude[47 and 48]. Fourth, magnitude and characteristics of plastic deformation at the tip of a notch root control residual stresses near the tip (e.g., crack closure[49]) and, moreover, in an aggressive environment can accelerate localized dissolution or hydrogen embrittlement leading to acceleration of crack growth[50].

Two parameters appear to characterize the foregoing observations. They are:  $\sigma$ , some measure of the material strength and  $\epsilon^*$ , some ductility parameter(s) which reflect ability of the structure to distribute high strains in the crack tip region. Pelloux[42] and others[50] have used these parameters to predict crack growth rate in terms of the crack tip opening displacement

(CTOD) and ductility. The CTOD models are generally expressed in the form[42]:

$$\frac{da}{dN} = \frac{1}{2} \cdot \text{CTOD} \cdot \frac{1}{\text{ductility}} = \frac{1}{8\pi E} \frac{(\Delta K)^2}{\sigma \cdot \epsilon^*}$$

Donahue, et al.[51], use a modified  $\Delta K$  term to account for the existence of a threshold,  $\Delta K_{th}$ , and others[52] have included a fracture toughness term ( $K_{IC}$  or  $K_C$ ) as part of the ductility parameter. In Weertman's model[53 and 54], the exponent on  $\Delta K$  is equal to four, the  $\sigma$  term is squared, and  $\epsilon^*$  is replaced by  $U$ , the energy to propagate a fatigue crack per unit area. Regardless of modifications by various investigators, however, all models of this type predict that product of strength ( $\sigma$ ) and ductility or toughness ( $\epsilon^*$ ) must be maximized to minimize crack growth.

Mean calculated fatigue lives of 2XXX-type alloy structures were found to correlate well with log UPE (a measure of fracture toughness, refer to section 5.3 and Figure 65). However, as noted earlier (Figure 63), crack propagation performance cannot be solely correlated with monotonic yield strength though fracture toughness increase is generally accompanied by strength decrease. Pelloux [42] has suggested that strength of the material ( $\sigma$ ) in the above expression should be the flow stress of material near the cyclically work-hardened plastic zone rather than monotonic or cyclic yield strength. Use of flow stress ( $\sigma$ ) in the above expression is important since fully reversed constant strain amplitude controlled fatigue tests on naturally aged 2024 indicate that this material



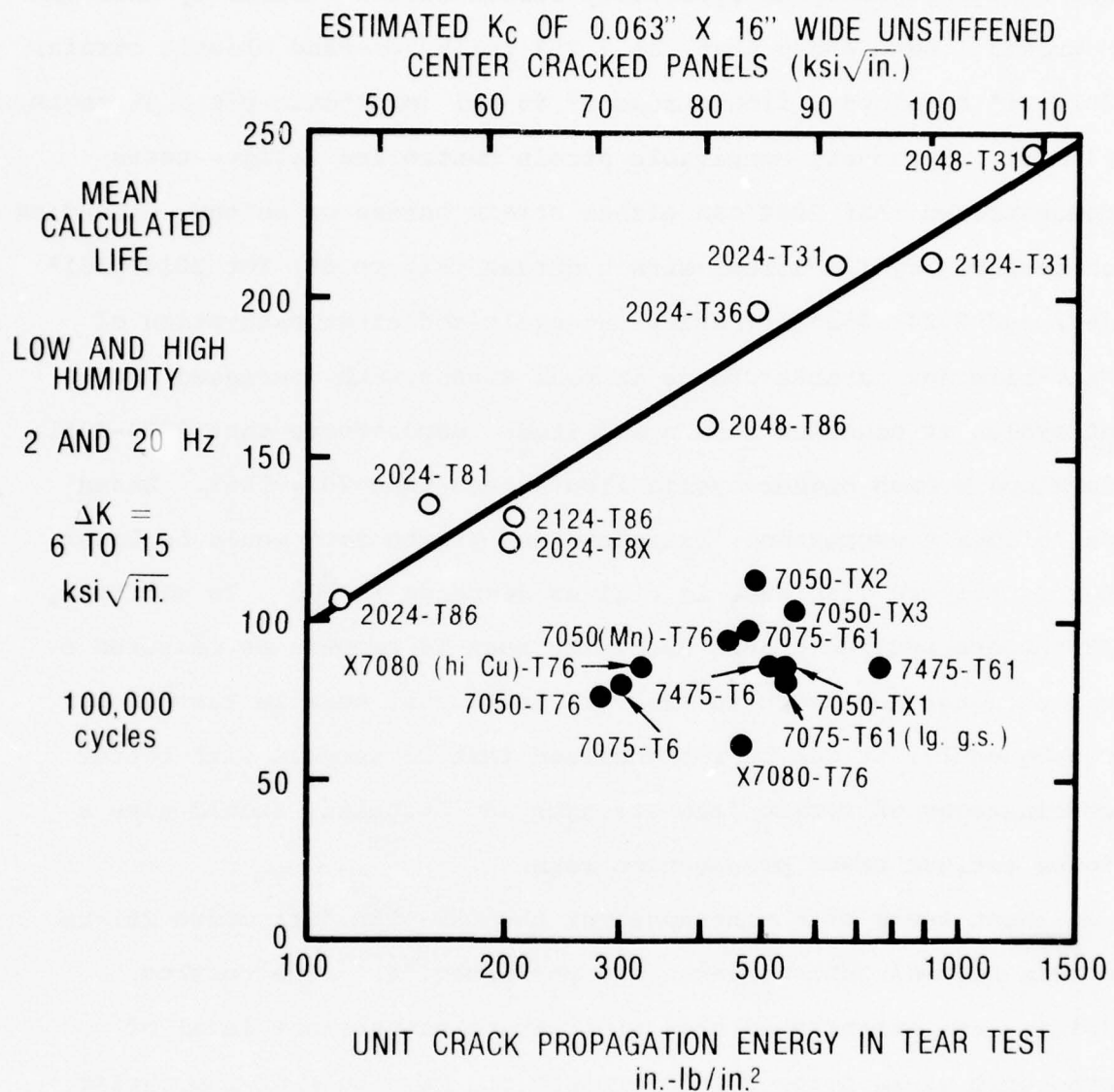
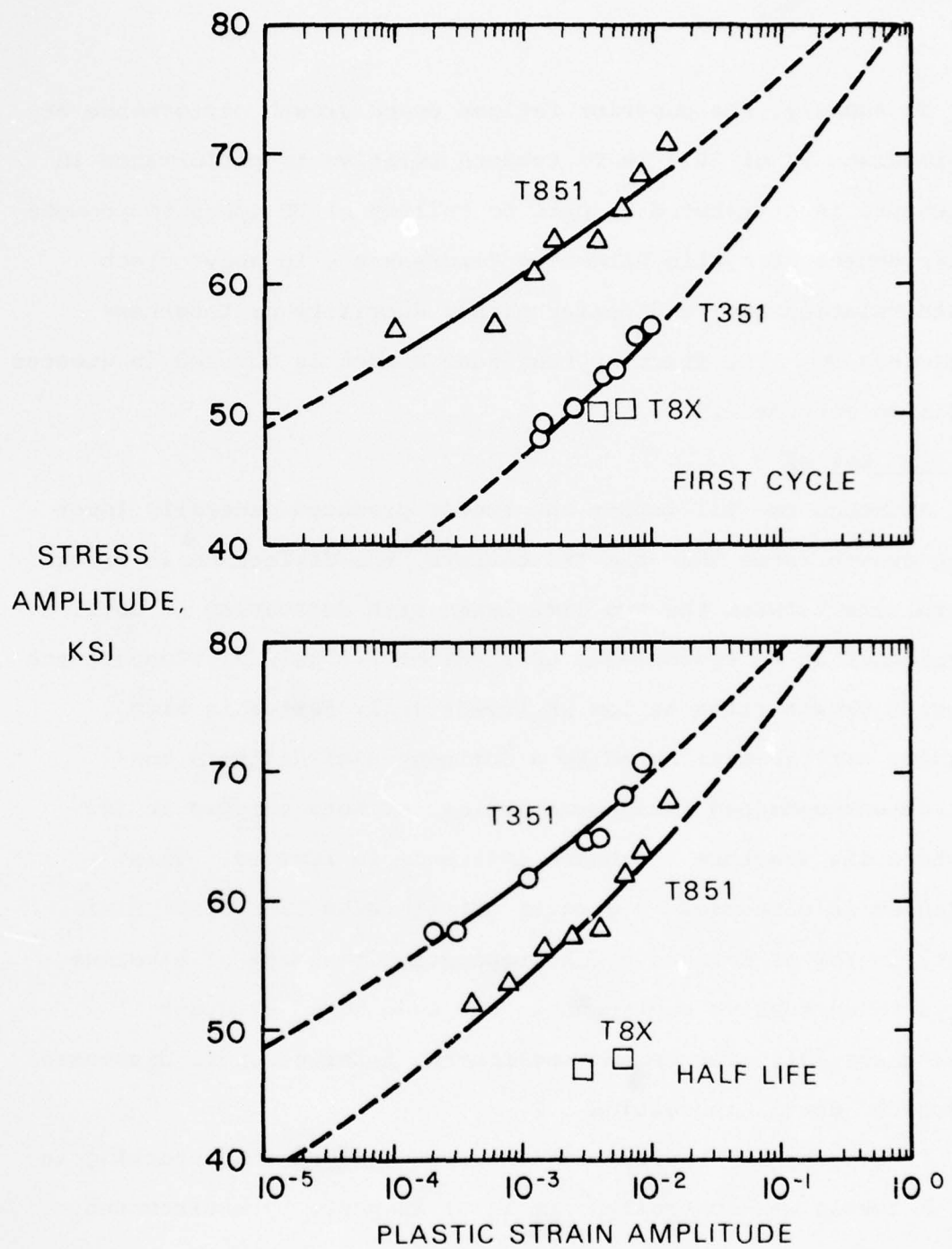


Figure 65 Relationship Between Fatigue Crack Propagation Performance and Fracture Toughness for 2XXX and 7XXX Sheet Alloys.

has a high capacity to cyclically strain harden. Tests by Endo and Morrow[55] have shown that, at 7.25% fully reversed plastic strain, 2024-T4\* develops a flow stress of 95 ksi (monotonic yield strength, 44 ksi). Moreover, comparable strain controlled fatigue tests demonstrated that 2024 can either strain harden or soften, depending on temper. Cyclic stress-strain curves (Figure 66) for 2024-T351\* [47] and 2024-T851\*[56] after one cycle and after saturation of half-life (no further change in peak stress with increased number of cycles at constant strain amplitude) demonstrate that 2024-T351 develops a much higher cyclic flow stress than 2024-T851. Based on Pelloux's expression, fatigue crack growth rate would be lower for T3 tempers (increase in  $\sigma$  gives decrease in  $\frac{da}{dN}$ ). In addition, T3 tempers provide higher ductility than T8 tempers as measured by conventional tests such as fracture toughness, tensile tests, etc. Consequently, it can be rationalized that T3 tempers with better combinations of cyclic flow strength and ductility should give a lower fatigue crack propagation rate.

Spot tests of the response of the 2024-T8X (Structure 26) to strain-control fatigue were also performed[56]. The results (Figure 66) established that precipitate nature, not level of monotonic yield strength, determined the magnitude of the cyclic response. Alloy 2024 aged to develop S' precipitate and a low level of monotonic yield strength cyclically hardened to a much lesser extent than did 2024 aged to develop GP zones.

\*The differences among 2024-T4, T31, and T351 are in the amount of stretch after quenching. The amounts are 0, 1%, and 1-1/2 to 3%, respectively. 2024-T851 is obtained by aging 2024-T351 eight hours at 375°F.



### CYCLIC STRESS STRAIN CURVES, 2024

Figure 66 Fully Reversed Constant Strain Amplitude Controlled Fatigue Tests of 2024 in Three Tempers.

In summary, the superior fatigue crack growth performance at intermediate  $\Delta K$  of 2024 in T3 tempers relative to performance in T8 tempers is attributed in part to ability of GP zones to promote higher degree of cyclic hardening (increases  $\sigma$  in above crack growth relationship) and confer higher ductility or toughness (increases  $\epsilon^*$ ). The fracture toughness aspect is covered in greater detail in section 5.3.

#### 5.1.5.2 Low $\Delta K$

Although the T31 temper (GP zones) produced generally lower crack growth rates than the T86 tempers, the difference in crack growth rate between the two diminished with decreasing  $\Delta K$  until convergence at an approximate  $\Delta K$  level of  $2.5 \text{ ksi}\sqrt{\text{in.}}$ . Convergence of crack growth rates at low  $\Delta K$  levels (only tested in high humidity air) is attributed to a dominant similarity in the environment-enhanced fatigue mechanisms of both tempers at low  $\Delta K$  where the fracture toughness influence is removed. This mechanism is discussed in greater detail in section 5.2. Similarity in low  $\Delta K$  fatigue crack propagation response of aluminum alloys in aggressive environments has been noted by other researchers[28]. The temper-environment interaction is discussed in greater detail in section 5.2.

Fractographic studies provide some evidence that cracking in low  $\Delta K$  levels was controlled, at least in part, by environment (Figures 56 to 62). The fracture surface appearance of these alloys consisted of ridges and plateaus, areas containing rumpled surfaces, and "cleavage-like" fracture regions. The exact nature of the



formation of these complex fracture surfaces is not well understood. Due to the variety of fracture modes compared to the striation mode that is present on the fracture surface at higher  $\Delta K$  levels, modeling the fatigue process is extremely difficult. For example, with the plateau and ridge morphology, the individual steps do not represent the local increments of crack growth per cycle since the spacing of these plateaus is much larger than the local extension per cycle. Because average crack growth per cycle at  $\Delta K$  below about  $3 \text{ ksi}\sqrt{\text{in.}}$  is less than the distance between atomic planes, crack growth must be a discontinuous process.

Areas referred to as rumpled surfaces are apparent on some of the fracture surfaces (Figures 60 and 61). These areas were relatively flat and do not have any unique characteristics, although they appeared to be more prevalent in the 2XXX-T3 structures. The origin of these fracture areas is not known.

"Cleavage-like" regions on the fatigue fracture surfaces have been reported by Forsyth[57] and others[58] in smooth fatigue test specimens. These cleavage regions occurred in the transition region from Stage I to Stage II crack growth and were associated with the crack changing from a shearing mode to a tensile mode during which the crack propagates along crystallographic planes. When the tensile component becomes predominant, the general fracture plane becomes normal to this tensile stress and Stage II (non-crystallographic) growth occurs. Feeney, et al.[28], suggest that the fracture surfaces of 2024-T3 and 7075-T6 tested at low  $\Delta K$  levels were similar to these fracture features observed in this

transition region between Stages I and II. In addition, using etch pitting techniques, Feeney, et al., found that these cleavage-like regions were of the (001) orientation.

Hertzberg and Mills[59] support a theory of slip plane decohesion for the cleavage-like regions. Beachem and Meyn[60] suggested this theory to account for the fracture appearance of Stage I growth. With this mechanism, reversed slip on a limited number of slip planes in front of the crack tip lowers cohesion strength of the material and, since some tensile component of the stress is always present, the material can fail by local tensile separation. This process would give a crystallographic appearance showing no signs of deformation and would also be similar to that of cleavage failure found by Feeney, et al.[28] and Santner and Fine[61]. Of course, the fracture plane in this case would be the (111).

In summary, for low  $\Delta K$  crack growth, the exact mechanism of formation of cleavage-like regions is not known, but appears to be associated with Stage I and/or the transition from Stage I to Stage II crack growth. The exact role of environment is unknown but appears to play an important role in fatigue process.

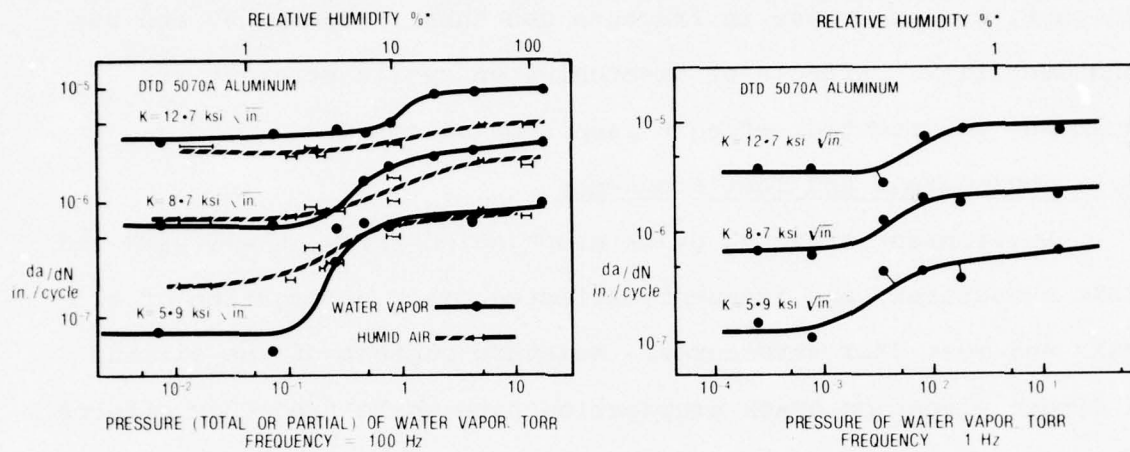
#### 5.1.6 Dislocation Density

Increasing the initial dislocation density by increasing the amount of stretch after quenching from 1 to 5% decreased the predicted life of 2024 in T8 tempers. Crack growth analysis indicated that the decrease in life was due to an increase in crack propagation rate at high levels of  $\Delta K$ . The decrease in crack growth

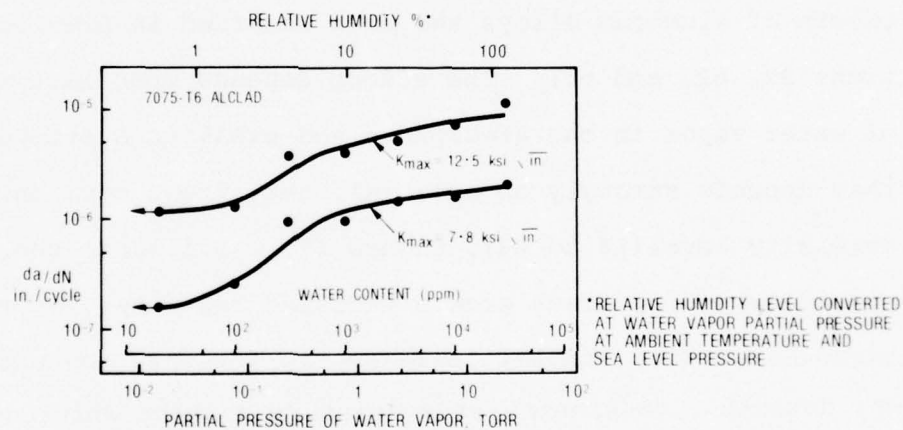
rate with an increase in percent stretch is attributed, at least in part, to a decrease in fracture toughness (Figures 38 and 39) and ductility. Effects of stretching on cyclic strength are unknown, so potential effects cannot be assessed.

## 5.2 Environment and Test Frequency

Environment affected crack propagation rates in all 2XXX and 7XXX structures, and frequency affected crack propagation of all 2XXX and most 7XXX structures. Moisture content of the air had a direct effect on crack propagation rate while frequency effects were observed through interaction with the test environment. The significant influence of water or water vapor on fatigue crack growth of aluminum alloys has been recorded in previous investigations[22, 62, and 63]. The effect depends upon partial pressure of water vapor in the atmosphere and exhibits a stepped transition that depends strongly on material, test frequency, and stress intensity level[64 to 68], Figure 67. As illustrated, the relationship between log crack growth rate and log water vapor was sigmoidal. With initial increases in moisture content, no effect was detected. Beginning at a moisture content which depended on test frequency and stress intensity, crack growth rate increased steeply with further increases in moisture content. This rapid increase ceased at a higher moisture content which also depended on frequency and  $\Delta K$  level. Little further increase in crack growth rate was observed with increases in moisture content (upper plateau). It is worthy to note that both the Al-Cu-Mg alloy of Figure 67, top, and the 7075-type alloy of Figure 67, bottom, when tested at frequencies on the order of 60 to 100 Hz, exhibit their



THE EFFECT OF MOISTURE CONTENT AND FREQUENCY ON THE RATE OF FATIGUE CRACK GROWTH IN A AlCuMg ALLOY



THE EFFECT OF PARTIAL PRESSURE OF WATER VAPOR ON FATIGUE CRACK GROWTH IN A AlZnMg ALLOY AT ~ 57 Hz

Figure 67 Effects of Moisture Content on Fatigue Crack Growth of Aluminum Alloys (REF. 63).



respective moisture related growth rate transition over a relative humidity range of 2 to 10%, which corresponds to the low humidity environment considered in this study. Thus, at fast frequencies, greater variability in crack growth rate response in low humidity environment would be expected because of inability to precisely control humidity levels within the transition range. Either lowering frequency (Figure 67, top) or increasing moisture content beyond about 20% locates crack growth rate on the upper plateau, thereby reducing sensitivity of crack growth rate response to small changes in humidity.

#### 5.2.1 2XXX Alloys

In this investigation, no significant frequency effects were observed in high humidity environment (corresponds to crack growth behavior on upper plateau). At low humidity, a test frequency of 20 Hz produced significantly lower crack growth rates than did 2 Hz (Figure 68). Lines through data points on this figure were drawn to represent the upper plateau and onset of growth rate transition with decreasing moisture content. Sensitivity to frequency in low humidity environments indicates that water vapor partial pressures were sufficient to cause environmental effects. Faster crack growth with decreasing frequency in the transition regions is attributed to increase in available reaction time of water with fresh metal at slower frequency.

Statistical analysis confirmed an interaction between environment and temper. Greater divergence in growth rates between T86 and T31 tempers occurred at low humidity. As suggested by the  $\Delta K = 6 \text{ ksi}\sqrt{\text{in.}}$  curves of Figure 68, the magnitude of the disparity

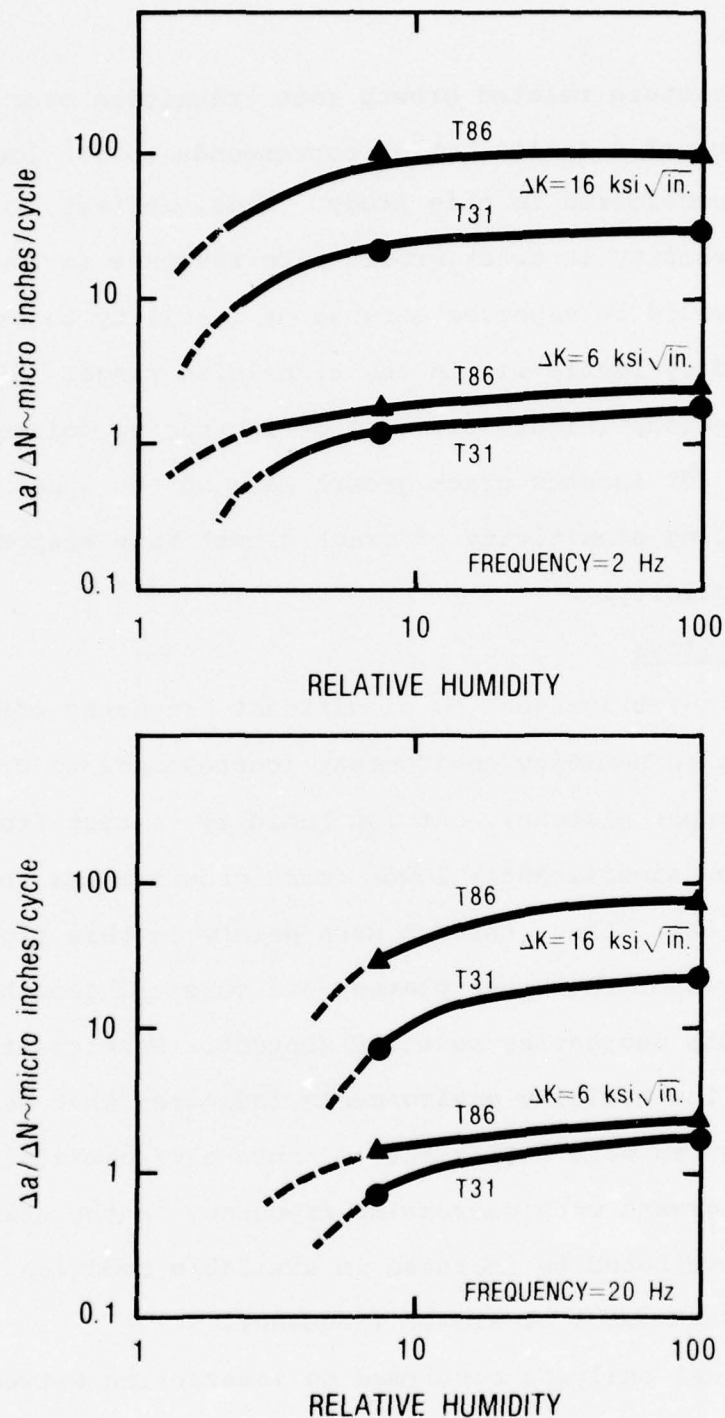


Figure 68 Effect of Frequency and Environment on Fatigue Crack Growth Rate of 2X24-T31 and T86 Tempers. Each Data Point Represents Averaged Growth Rate from Four Structures T31 (14, 15, 16, 17,) and T86 (18, 19, 20, 21,).

between T31 and T86 growth rates at low humidity can be influenced by frequency and its relationship to the moisture content transition.

Several investigations have suggested that the effectiveness of corrosion mechanisms operating at the tip of a propagating fatigue crack are related to the material's strength-ductility combination and the degree of material constraint (plane strain) in the near crack tip vicinity[28, 62, and 63]. In general, it has been shown that effectiveness of crack tip embrittling mechanisms are enhanced when material is in a highly constrained state (plane strain) and they are reduced with increasing  $\Delta K$  levels as the fracture mode transforms from one of plane strain to plane stress. Because strength and ductility are important in controlling the degree of material constraint at the crack tip, the better strength-ductility combination of the T31 temper renders this temper less susceptible to interaction with environment than the T86 temper at high and intermediate K levels. At low  $\Delta K$  where the influence of toughness is removed, both T86 and T31 tempers are subject to a high degree of material constraint (plane strain) and controlling environmental and mechanical fatigue components become similar. Therefore, growth rates for both tempers tend to converge.

#### 5.2.2 7XXX Alloys

An interaction between degree of precipitation and environment was noted for the alloy 7050 structures. Mean lives, averaged over 2 and 20 Hz, generally increased progressively with increasing degree of precipitation (Structure 27 to 28 to 1 to 5 to 7 to 6) when tested in either low or high humidity environment (Figure 63).

In the low humidity environment, the rate of increase in life was slight when progressing from Structure 27 (GP zones), to Structure 5 (S, S',  $\eta'$ ,  $\eta$ ). As precipitate size increased (Structure 5 to 7 to 6), life increased at a higher rate. The rate of increase in life when progressing from Structure 27 to 5 was higher in the high humidity environment. The lives of Structures 7 and 6 were both appreciably higher than life of Structure 5. As with 2XXX alloys, crack growth rate analysis indicated an increased level of environmental interaction with decreasing  $\Delta K$ , and growth rates converged at low  $\Delta K$  levels. The magnitude of the environmental interaction with growth rate does not appear to correlate with either yield strength or a measure of the ductility (e.g., UPE or NTS/YS). However, intermediate  $\Delta K$  results do correlate with past observations that resistance to stress-corrosion cracking of 7XXX alloys containing Cu generally increase with increasing degree of precipitation.

Frequency effects for the 7XXX-T6 and T76 alloys in low humidity air were lower in magnitude but generally similar to the direction noted for 2024-T31 in low humidity. The higher frequency, 20 Hz, gave somewhat lower crack propagation rates. This can be explained on the premise that the greater crack tip velocity at the higher frequency allows the mechanical component of fatigue to outpace the environmental interaction mechanism. At 2 Hz with lower resultant crack tip velocity, additional time is available per cycle for environment interaction to take place.



An opposite effect in high humidity air was noted for the 7XXX-T6 and T76 alloys. The 2 Hz crack propagation rates were consistently lower than 20 Hz rates. It is hypothesized that the reversed effect of frequency is related to the "critical frequency effect" observed when testing in hostile environments by Bucci[69] on a titanium alloy and others[70 and 71] on steel alloys. These investigators all observed that when testing their particular alloy-environment combination at stress intensity levels below  $K_{Isc}^*$  (a threshold stress intensity below which a crack will not grow by stress corrosion when subject to a sustained load), a "critical" frequency is achieved where the interaction of cyclic loading and environment on crack growth rate is maximized. At frequencies above "critical" the frequency-environment interaction follows the previously postulated pattern. However, at cyclic loading rates less than "critical," the fatigue environment interaction is suppressed. For the limiting case of zero frequency (sustained load test), environmental effects must be nonexistent for stress intensities below  $K_{Isc}^*$ .

Factors that control the critical frequency are related to the particular environment/strength-ductility combinations of the metal, the  $K_{Isc}$  level, and the kinetics of the crack tip-environment interaction. Crack growth kinetics may include blunting of

---

\* $K_{Isc}$  values in the T-L orientation of 25 and 29 ksi $\sqrt{\text{in.}}$  for 7075-T651 and 7050-T73651 plate, respectively, have been reported[72]. For both materials in plate form,  $K_{Isc}$  is quite close to their respective  $K_{Ic}$  levels.

the crack tip by chemical erosion and/or buildup of residue of corrosion by-product on the fracture surfaces, thereby increasing crack closure forces[49]. The latter two mechanisms would tend to retard crack growth with a slower rate of cyclic loading (slower crack velocity). Kinetics of the environmental interaction with crack growth of the 7050 alloys aged under other conditions are apparently different enough to alter the "critical" rate of loading.

Ideally, the evaluation of alloy fatigue crack propagation performance should be carried out at the critical frequency (worst case). For this reason, a further understanding of the nature and mechanisms of frequency-environment interaction of aluminum alloy is recommended (refer to section 7 on Future Work).

### 5.3 Relationship Between Mechanical Properties and Fatigue Crack Propagation Performance

Mean predicted propagation life (averaged for both humidity levels and test frequencies at  $\Delta K = 6$  to  $15 \text{ ksi}\sqrt{\text{in.}}$ ) are plotted versus transverse monotonic yield strength and log unit propagation energy (UPE), a fracture toughness index, in Figures 69 and 65, respectively. Values for the 2X24 alloys with low and high Mn were averaged.

Considering 2XXX alloys initially, propagation life did not correlate well with yield strength, although mean life of alloy 2024 decreased linearly as strength increased progressively from T31, T36, T81, to T86 tempers. Life of sheet in the nonstandard T8X temper, however, was substantially below that of sheet in the T36 temper, although yield strengths were comparable. In addition,

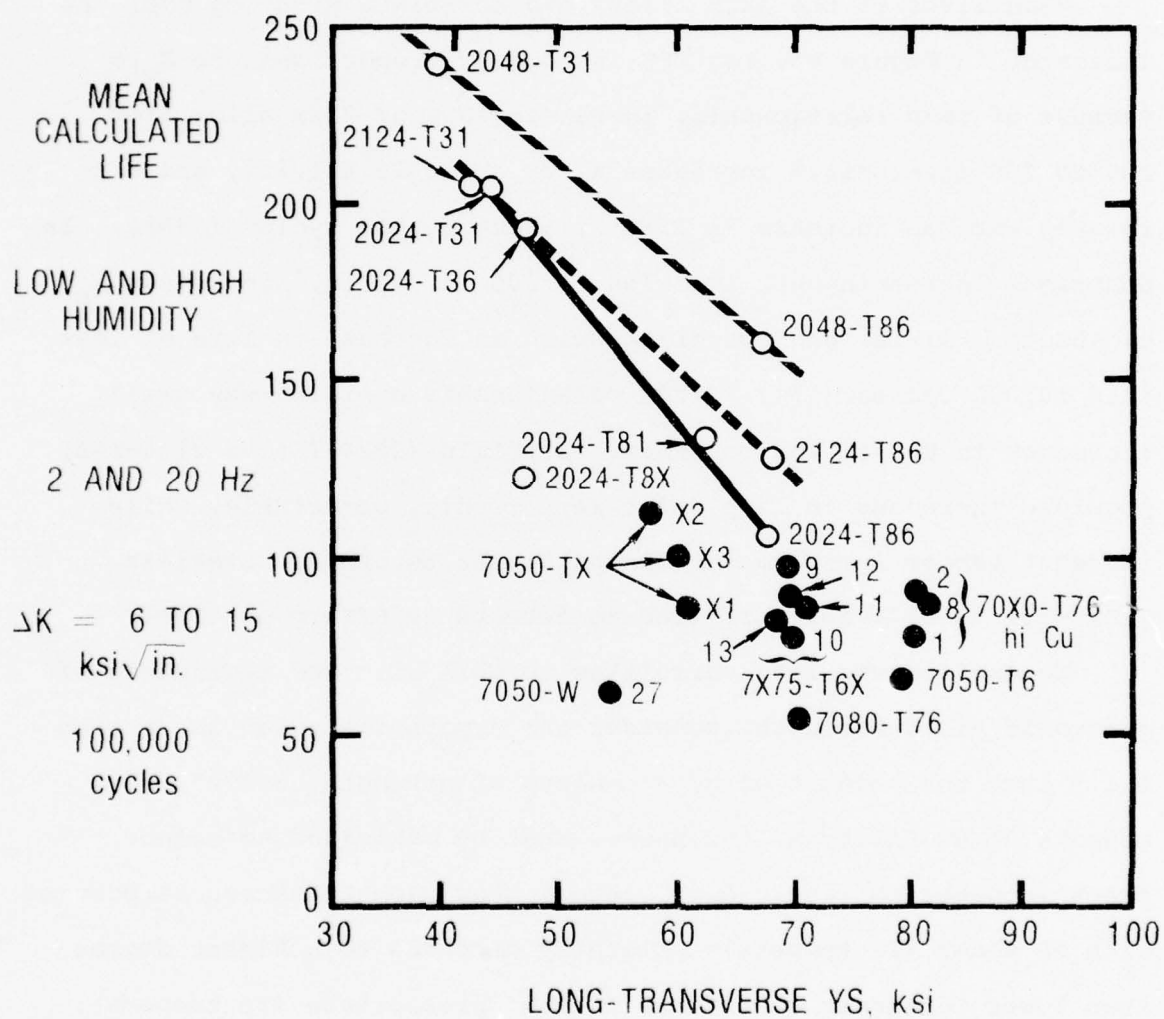


Figure 69 Yield Strength Vs. Fatigue Crack Propagation Performance of 2XXX and 7XXX Alloy Sheet.

mean lives of 2048 were superior to lives of 2024 while 2124-T86 was superior to that of 2024-T86.

Mean lives of the 2XXX alloys did correlate with log UPE. As indicated in Figure 65, log UPE is roughly proportional to  $K_c$ .† Because of this relationship, increasing UPE of 2XXX alloy from 100 to 200 in.-lb/in.<sup>2</sup> increases  $K_c$  by about 15 ksi√in., and correlates with an increase in life of about 30,000 cycles (~30%). In contrast, increasing UPE from 700 to 800 in.-lb/in.<sup>2</sup> increases  $K_c$  by about 3 ksi√in. and correlates with an increase in life of less than 10,000 cycles (~5%). This relationship explains why small increases in UPE of low toughness materials (2024-T86 vs 2124-T86) provided increases in life which were readily detectable, while somewhat larger increases in UPE of higher toughness materials (2024-T31 vs 2124-T31) provided no detectable effect on life.

To explain why life correlates so well with UPE regardless of monotonic yield strength, consider the hypothesis posed in section 5.1.5 that the product of  $\sigma$ , a measure of strength, and  $\epsilon^*$ , a measure of ductility or toughness, must be maximized to reduce crack propagation rate. Also, recall that high toughness structures with GP zones (T3 tempers) cyclically hardened to a higher degree than lower toughness structures with  $S'$  precipitate (T8 tempers). Increases of cyclic strength and toughness may be related to increases in  $\sigma$  and  $\epsilon^*$ , respectively, in the crack growth rate relationship. These observations strongly indicate that mean life

---

†Obtained by replotting data for 0.063 inch panels in Figure 19 of Reference [73].



of 2XXX alloys correlate well with log UPE because toughness,  $\epsilon^*$ , and strength at the crack tip,  $\sigma$ , increase simultaneously.

In 7XXX alloys, no pattern relating mean life to either monotonic yield strength (Figure 65) or to log UPE (Figures 63 and 69) was detected. The lack of correlation of crack propagation performance with monotonic strength was discussed previously in section 5.1.5.1. Absence of correlation of log UPE with mean life of 7XXX alloys suggests that other factors override (cancel) a possible correlation involving UPE, e.g.,  $\sigma$  and  $\epsilon^*$  may not increase simultaneously. Moreover, effects of environment on strength-ductility relationship are a greater factor in 7XXX alloys (compare Figure 67, top, with 67, bottom).

Therefore, lack of correlation between log UPE and mean life of 7XXX alloys may be due to major differences in sensitivity to moisture, to differences in rate of cyclic strain hardening, or to the smaller range in UPE evaluated.

Although mean life of 2XXX alloy correlated with log UPE (and probably with  $K_{IC}$ ), it should be emphasized that conclusions which attempt to quantify the role of fracture toughness on fatigue crack growth in this investigation apply to alloys tested in sheet gauge (nominal 1/16 inch thickness). The thickness interactions with non-plane-strain critical stress intensity,  $K_{IC}$ , has been reported previously[74]. Critical levels of fracture toughness,  $K_{IC}$ , developed for 7XXX and 2XXX alloys in 1/16 inch gauges lie well above  $22.5 \text{ ksi}\sqrt{\text{in.}}$ , the maximum cyclic stress intensity,  $K_{max}$ , at

$\Delta K = 15 \text{ ksi}/\text{in.}$ ,  $R = 1/3$ .\* For thick test sections where crack tip stress state is predominantly one of plane-strain, critical stress intensity levels (viz,  $K_{IC}$ , a fracture toughness lower bound) for high strength aluminum alloys approach highest values of  $K_{max}$  considered in this investigation. Thus, it would be expected that crack growth rate at high and intermediate  $\Delta K$  would show greater sensitivity to alloy fracture toughness with increasing test section thickness. In this investigation, thickness was controlled, so unnecessary confounding of microstructure's influence on fracture toughness versus fatigue resistance was removed. Therefore, qualitative interpretation of results of the investigation on the role of microstructure to fatigue crack growth resistance should apply over a much greater range of product thickness.

## 6. CONCLUSIONS

Table 16 to 18\*\* summarize the effects of microstructural and testing variants on fatigue crack propagation rate of high-strength, precipitation-hardenable aluminum alloys in sheet gauges (nominal 0.06 and 0.09 inch thickness). All were subjected to constant amplitude fatigue loading at a stress ratio of 1/3. Conclusions regarding interpretations of these effects were formulated by considering metallurgical, mechanical, and environmental influences. Validity of effects was established by visual comparison of  $da/dN$  vs  $\Delta K$  data, statistical and visual analysis of  $da/dN$  at discrete values of  $\Delta K$ , and statistical and visual analysis of calculated numbers of cycles to advance a crack a certain length (life)

---

\*  $K_{max} = \Delta K / (1-R) = 1.5 \Delta K$ , when  $R = 1/3$ .

\*\* Identical to Tables 1, 2, and 3; repeated for reader's convenience.

TABLE 16

SUMMARY OF MICROSTRUCTURAL EFFECTS ON FATIGUE CRACK PROPAGATION RATE (FCPR)  
7075 AND 7050 TYPE ALLOYS

Microstructural Variant	Low Humidity Air $\Delta K > 5 \text{ ksi}\sqrt{\text{in.}}$	High Humidity Air $\Delta K > 2 \text{ ksi}\sqrt{\text{in.}}$	Comments
Precipitate type and morphology by increasing degree of precipitation in 7050.	Increasing degree of precipitation decreased FCPR.	Larger effect than in low humidity.	With increased degree of precipitation, precipitate changed from GP to $\eta'$ to mixtures of S, S', $\eta$ , and $\eta'$ .
Cu Content 1% vs. 2.3%	High Cu gave slightly lower FCPR.	High Cu gave lower FCPR, $\Delta K > 5 \text{ ksi}\sqrt{\text{in.}}$	Low Cu gave lower FCPR $\Delta K < 4 \text{ ksi}\sqrt{\text{in.}}$ ; Confirmation of low $\Delta K$ result needed.
Volume % insoluble Constituent 0.5% vs. 1.2%	Low vol. % constituent gave lower FCPR $\Delta K > 15 \text{ ksi}\sqrt{\text{in.}}$	Low vol. % constituent gave lower FCPR $\Delta K > 15 \text{ ksi}\sqrt{\text{in.}}$	No effect when toughness already high by modifying Cr dispersoid.
$\text{Al}_{12}\text{Mg}_2\text{Cr}$ dispersoid size and distribution	Large, widely spaced dispersoids gave lower FCPR in 7075 $\Delta K > 15 \text{ ksi}\sqrt{\text{in.}}$	Large, widely spaced dispersoids gave lower FCPR $\Delta K > 15 \text{ ksi}\sqrt{\text{in.}}$	No effect in 7475 where toughness already high by reducing vol. % constituent.
Type of Dispersoid Zr, Mn, and Zr plus Mn	No effect.	No effect.	Varied in 7050 type alloy base.
Grain Size 5 to 65,000 grains/mm <sup>3</sup>	No effect.	No effect.	Varied in 7050 and 7075 type alloys.

TABLE 17

SUMMARY OF MICROSTRUCTURAL EFFECTS ON FATIGUE CRACK PROPAGATION RATE (FCPR)  
2024 TYPE ALLOYS

Microstructural Variant	Low Humidity Air $\Delta K > 5 \text{ ksi in.}$	High Humidity Air $\Delta K > 2 \text{ ksi/in.}$	Comments
Type of precipitate GP vs. S	GP zones gave lower FCPR. Disparity between FCPR of both precipitate types larger than in higher humidity.	GP zones gave lower FCPR when $\Delta K > 3 \text{ ksi/in.}$	With decreasing $\Delta K$ FCPR converge for both types of precipitate. No effect of precipitate when $\Delta K < 3 \text{ ksi/in.}$
Dislocation density 1% vs. 5% stretch after quenching.	1% Stretch gave lower FCPR $\Delta K > 15 \text{ ksi/in.}$	1% Stretch gave lower FCPR $\Delta K > 15 \text{ ksi/in.}$	Effect of stretch greater in T8 than in T3 temper.
Vol. % insoluble Constituent 1.4 vs. 2.28	Low Vol. % gave lower FCPR in T86 temper $\Delta K > 15 \text{ ksi/in.}$	Low vol. % gave lower FCPR in T86 temper $\Delta K > 15 \text{ ksi/in.}$	No effect in T31 temper.
Vol. % Mn dispersoid 1.1 vs. 2.6%	No effect.	No effect.	No tests at $\Delta K < 5 \text{ ksi/in.}$
Cu Content 3.25 vs. 4.25%	Low Cu gave lower FCPR in both T86 and T31 tempers.	Low Cu gave lower FCPR in both T86 and T31 tempers.	Only T31 tested $\Delta K < 5 \text{ ksi/in.}$ Additional tests needed to confirm and explain Cu effect.



TABLE 18

## SUMMARY OF EFFECTS OF TESTING VARIABLES ON FATIGUE CRACK PROPAGATION RATE (FCPR)

Testing Variant	2024-Type	7075-Type	7050-Type
Environment Low vs. high humidity air.	Low humidity air gave lower FCPR.	Low humidity air gave lower FCPR.	5% RH gave lower FCPR.
Frequency 2 vs. 20 Hz.	Little effect in high humidity air. 20 Hz gave lower FCPR in low humidity air.	Generally smaller effects than in 2024-T3L. 2 Hz gave lower FCPR than 20 Hz in high humidity and gave higher FCPR in low humidity.	2 Hz gave lower FCPR in high humidity in T76 temper.

The major conclusions are listed below:

1. Strength after cyclic loading, toughness or ductility, and resistance to environment are the three main material properties which influence fatigue crack propagation behavior of ingot metallurgy 2XXX and 7XXX aluminum alloys at  $\Delta K$  levels of about  $4 \text{ ksi}\sqrt{\text{in.}}$  and higher. Chemical composition, volume fraction, type, and morphology of strengthening precipitate and constituent particles along with dislocation density determine the magnitude of these properties.
2. Alloy 2024 in T3 tempers has superior fatigue crack propagation resistance compared to its resistance in T8 tempers because GP zones confer high ductility (toughness) and promote a high cyclic hardening rate while  $S'$  precipitates confer low ductility and promote a low cyclic strain hardening rate. The favorable strength-ductility combination of the T3 temper makes it less susceptible to acceleration of fatigue crack growth rate in the presence of moisture at high and intermediate levels of  $\Delta K$ , even at about 5% relative humidity.
3. Increasing toughness of 7075-T6 and 2024-T86 by decreasing volume fraction of insoluble constituent particles (7075 and 2024), modifying dispersoids (7075), and decreasing dislocation density (2024) decreases fatigue crack growth rate by increasing their limited ability to accommodate plastic strain before fracture. Increasing toughness of 7475-T6 by modifying dispersoids and of 2024 in T3 tempers by decreasing volume fraction of constituent particles or decreasing dislocation density has little or no effect because their ability to accommodate plastic strain is much higher.
4. The progressive improvement in fatigue crack propagation characteristics of 7050-type alloys (intermediate  $\Delta K$ ) as degree of precipitation increases from underaged to overaged and as Cu content increases from 1 to 2.3% arises from a progressive increase in resistance to degradation from moisture content. Lower Cu content offered improved fatigue crack growth resistance at  $\Delta K$  less than  $4 \text{ ksi}\sqrt{\text{in.}}$ . This latter result needs further verification.
5. Reduced Cu content (alloy 2048) provided improved fatigue crack propagation resistance over that of alloys 2124 and 2024. Benefit of low Cu at intermediate  $\Delta K$  is attributed to increased fracture toughness because of a reduction in  $\text{CuAl}_2$  and  $\text{Al}_2\text{CuMg}$  constituents. Benefit of lower Cu content at low  $\Delta K$  needs further verification and additional analysis to develop a rational hypothesis for this behavior.

6. The insensitivity of fatigue crack growth rate to microstructure in high humidity air at levels of  $\Delta K$  below about 3 ksi $\sqrt{\text{in.}}$  and the fractographic evidence of discontinuous growth suggests that properties of the solid solution (affected mainly by precipitation heat treatment practice) control the fatigue process of aluminum alloys under these conditions of high restraint in an aggressive environment.
7. Grain size from 5 to 65,000 grains per mm<sup>3</sup> had no effect on crack growth rate in peak and overaged 7XXX alloys.
8. Interaction of test frequency with environment was noted in 2XXX and some 7XXX alloys. The largest effects of frequency for 2XXX alloys were noted in low humidity environment where crack growth rate was increased by decreasing frequency from 20 to 2 Hz. Faster crack growth with decreasing frequency was attributed to increase in available reaction time of water with fresh metal. For some 7XXX-T6 and T76, fatigue crack propagation rates in high humidity air decreased with frequency decrease. This was attributed to increased time at slower frequency for corrosion reactions to retard crack growth (e.g., blunting of crack tip by chemical erosion) for these alloys. Consequently, frequency and environmental effects must be considered when ranking alloys and tempers which do not exhibit gross differences in crack growth behavior.

The following conclusion is based on the work presented in Appendix A, Fatigue Crack Initiation Resistance:

Microstructural changes which improve resistance to fatigue crack propagation do not strongly affect resistance to fatigue crack initiation.

#### 7. RECOMMENDED FUTURE WORK

Metallurgical, mechanical, and environmental influences were considered in this work to formulate conclusions regarding the role of microstructure on fatigue crack propagation rate of high-strength 2XXX and 7XXX aluminum alloys.

The observation that grain size had no effect must be tempered with the realization that powder metallurgy (P/M) techniques can provide a grain size that is orders of magnitude finer than the smallest evaluated in this investigation. This ultrafine grain

size in P/M products may be at least part of the reason for the promising performance of 7XXX P/M alloys at low to intermediate regions of  $\Delta K$ [34]. Consequently, work with P/M alloys is recommended.

Interpretations regarding effects of insoluble constituent and dispersoid particles and of dislocation density are considered to be based on sufficient data, so no additional work is recommended.

Conclusions regarding interpretation of effects of precipitate structure and composition, and interaction with environment, however, are more tentative. Better understanding and added verification of possible effects on fatigue crack growth resistance by altering Cu content in 2XXX and 7XXX alloys is needed.

Because composition and precipitate had the largest effects, the additional work recommended is needed to provide information for alloy development of ingot metallurgy aluminum alloys with improved fatigue resistance.

Additional work including: (1) tests in other controlled environments (including inert), (2) strain controlled fatigue tests, (3) tests to measure ductility of cyclically deformed material, (4) crack closure measurements, (5) additional tests at low  $\Delta K$ , and (6) variable amplitude tests are needed. Items (1) through (4) would better define response of material properties, including interaction with environment, to cyclic loading and broaden knowledge of operating fatigue mechanisms. Additional low  $\Delta K$  tests would better establish the role of



microstructure at low  $\Delta K$  where the greatest portion of fatigue crack propagation life is spent in real structures.

Variable amplitude (spectrum loading) fatigue crack propagation tests are needed to better simulate in-service conditions. Moreover, these spectrum tests incorporate crack tip transient phenomena (viz, retardation) and offer the potential advantage of being a more sensitive indicator of the role of microstructure than the constant amplitude test[75].

#### ACKNOWLEDGMENT

Strain control fatigue tests and their related interpretation to fatigue crack propagation results of this investigation were provided by D. A. Mauney. His participation in technical discussions pertinent to this investigation is gratefully acknowledged.

The consultation of R. F. Kohm on statistical methods for analysis of data and assistance provided by R. C. Malcom in assimilation and display of the large quantity of experimental data generated by this investigation are also gratefully acknowledged.

#### REFERENCES

1. G. T. Hahn and R. Simon, "Metallurgical Control of Fatigue Crack Growth in High Strength Aluminum Alloys," Air Force Materials Laboratory Report TR-72-48, May 1972.
2. J. C. Grosskreutz, "Fatigue Mechanisms and the Development of Fatigue-Resistant Materials," Air Force Materials Laboratory Report TR-70-55, May 1970.
3. C. E. Feltner and P. Beardmore, "Strengthening Mechanisms in Fatigue," American Society for Testing Materials, STP 467, p 71, 1969.
4. J. C. Grosskreutz, "Strengthening and Fracture in Fatigue (Approaches for Achieving High Fatigue Strength)," Met. Trans., 3, p 1255, May 1972.
5. Larry H. Glassman and Arthur J. McEvily, Jr., "Effects of Constituent Particles on the Notch-Sensitivity and Fatigue-Crack-Propagation Characteristics of Aluminum-Zinc-Magnesium Alloys," NASA Technical Note, April 1962.
6. J. C. Grosskreutz and G. G. Shaw, "Mechanisms of Fatigue in 1100-O and 2024-T4 Aluminum," Air Force Materials Research Laboratory Report TR-65-127, July 1965.
7. J. C. Grosskreutz and G. G. Shaw, "Mechanisms of Fatigue in 7075-T6 Aluminum," Air Force Materials Laboratories Report TR-66-96, May 1966.
8. J. Schijve and P. deRijk, "The Fatigue Crack Propagation in 2024-T3 Alclad Sheet Materials from Seven Different Manufacturers," National Aero- and Astronautical Research Institute, NLR M. 2162, May 1966.
9. D. Broek, "The Effect of Intermetallic Particles on Fatigue Crack Propagation in Aluminum Alloys," Fracture 1969, (Proceed. 2nd Int. Conf. Fracture, Brighton, 1969), p 754, Chapman and Hall Ltd., London.
10. J. C. Grosskreutz, G. G. Shaw, and D. K. Benson, "The Effect of Inclusion Size and Distribution on 2024-T4 Aluminum," Air Force Materials Laboratory, Report TR-69-121, June 1969.
11. B. K. Park, V. Greenhut, G. Luetjering, and S. Weissman, "Dependence of Fatigue Life and Flow Stress on the Microstructure of Precipitation-Hardened Al-Cu Alloys," Air Force Materials Laboratory Report TR-70-195.

12. "Mechanism of Fatigue Enhancement in Selected High-Strength Aluminum Alloys," Progress Report, Naval Air Development Center, Report No. NADC-MA-7171, 10 December 1971.
13. S. M. El-Soudani and R. M. Pelloux, "Influence of Inclusion Content on Fatigue Crack Propagation in Aluminum Alloys," Met. Trans., 4, p 519, February 1973.
14. R. K. Ham and M. L. Wayman, "The Fatigue and Tensile Fracture of TD-Nickel," Trans. Met. Soc. AIME, 239, p 721, 1967.
15. G. Lutjering, H. Doker, and D. Munz, "Microstructure and Fatigue Behavior of Al-Alloys," The Microstructure and Design of Alloys, (Proceed. 3rd Int. Conf. Strength of Metals and Alloys, 1, Cambridge, England, p 427, August 1973).
16. A. R. Rosenfield, C. W. Price, C. J. Martin, D. S. Thompson, R. E. Zinkham, "Research on Synthesis of High-Strength Aluminum Alloys," Part I, The Relationship Between Microstructure and Mechanical Properties in Aluminum Alloys, AFML TR-74-129, December 1974.
17. L. P. Karjalainen, "The Effect of Grain Size on the Fatigue of an Al-Mg Alloy," Scripta Met., 7, p 43, 1973.
18. D. S. Thompson and R. E. Zinkham, "Program to Improve the Fracture Toughness and Fatigue Resistance of Aluminum Sheet and Plate for Aircraft Applications," AFML-TR-73-247, Vol I (September 1973), Vol II (September 1974).
19. D. Broek and C. Q. Bowles, "The Effect of Precipitate Size on Crack Propagation and Fracture of an Al-Cu-Mg Alloy," Jour. Inst. of Metals, 99, p 255, August 1971.
20. M. V. Hyatt, "Program to Improve the Fracture Toughness and Fatigue Resistance of Aluminum Sheet and Plate for Airframe Applications," AFML-TR-73-224, September 1973.
21. F. G. Osterman, Tech. Report AFML-TR-71-121, 1971.
22. C. M. Hudson and S. K. Seward, "A Literature Review and Inventory of the Effects of Environment on the Fatigue Behavior of Metals," Engineering Fracture Mechanics, Vol 8, No. 2, 1976.
23. M. Holt and J. G. Kaufman, "Indices of Fracture Characteristics of Aluminum Alloys Under Different Types of Loading," Current Engineering Practice, Vol 16, No. 3, 1973.

24. W. F. Brown and J. Srawley, "Plane Strain Crack Toughness Testing of High-Strength Metallic Materials," ASTM, STP 410, 1966.
25. S. M. El-Soudani and R. M. Pelloux, "A Comparative Analysis of Automated and Manual Measurements of Volume Fraction of Inclusions in Aluminum Alloy Rolled Sheets," Metallography, 6, p 37-64, 1973.
26. O. L. Davies (Editor), Design and Analysis of Industrial Experiments, Hafner Publishing Co., 1971.
27. J. H. Weber and R. W. Hertzberg, "Influence of Grain Orientation on Fatigue Crack Propagation," Met. Trans., 2, p 3498, December 1971.
28. J. A. Feeney, J. C. McMillan, and R. P. Wei, "Environmental Fatigue Crack Propagation of Aluminum Alloys at Low Stress Intensity Levels," Met. Trans., 1, p 1741, June 1970.
29. J. E. Vrugink, "Use of the Microprobe in Fracture Analysis," Met. Eng. Quart., 14, p 3, August 1974.
30. R. J. Selines and R. M. Pelloux, "Effect of Cyclic Stress Wave Form on Corrosion Fatigue Crack Propagation in Al-Zn-Mg Alloys," Met. Trans., 3, p 2525, 1972.
31. C. Laird in Ultrafine Grain Metals, Proceedings of 16th Sagamore Army Materials Research Conferenc, August 19-22, 1969, Syracuse University Press, J. Burke and V. Weiss, Editors.
32. A. W. Thompson and W. A. Backofen, "The Effect of Grain Size on Fatigue," Acta Met., Vol 19, p 597, 1971.
33. J. C. Grosskreutz and G. G. Shaw, "Fine Grain Structure Adjacent to Fatigue Cracks," Acta Met., Vol 20, p 523, April 1972.
34. W. L. Otto, "Metallurgical Factors Controlling Structure in High-Strength Aluminum P/M Wrought Products," AFML-TR-76-60, May 1976.
35. M. V. Hyatt and W. E. Quist, "The Effects of Zinc/Magnesium Ratio and Copper Content on the Fatigue Properties of Al-Zn-Mg-Cu Alloys," Symposium on the Achievement of High Fatigue Resistance in Metal Alloys, June 1969.
36. P. Lukas, M. Klesnil, and R. Fiedler, "Plastic Zone Around the Propagating Fatigue Crack," Phil. Mag., 20, No. 166, p 799, October 1969.



37. M. A. Williams and G. G. Smith, "Dislocation Structures Near a Propagating Fatigue Crack in an Al-1/2% Mg Alloy," *Acta Met.*, 18, p 1035, September 1970.
38. Tsugio Ogura and Seiichi Karashima, "Studies on the Structure Developed Around Fatigue Cracks of Aluminum Using a High Voltage Electron Microscope," Trans. Japan. Inst. Metals, 15, p 324, 1974.
39. R. J. H. Wanhill, "Fractography of Fatigue Crack Propagation in 2024-T3 and 7075-T6 Aluminum Alloys Tested in Air and Vacuum," NLR Report TR-74094-U, April 1974.
40. S. Karashima, H. Oikawa, and T. Ogura, "Studies on Sub-Structures Around a Fatigue Crack in Fcc Metals and Alloys," Trans. Japan. Inst. Metals, 9, p 205, 1968.
41. T. Ogura and S. Karashima, "Substructure Formation Around Fatigue Cracks and Its Role in the Propagation of Fatigue Cracks in Aluminum," Trans. Japan. Inst. Metals, 6, p 428, November 1972.
42. R. M. Pelloux, "Review of Theories and Laws of Fatigue Crack Propagation," Proceedings of the Air Force Conference on Fatigue and Fracture of Aircraft Structures and Metals, AFFDL-TR-70-144.
43. J. R. Rice, "The Mechanics of Crack Tip Deformation and Extension by Fatigue," ASTM, STP 415, 1967.
44. F. Endogen, "Crack Propagation Theories," Fracture, An Advanced Treatise, Vol II, Academic Press, New York, 1968.
45. J. P. Gallagher, "Fatigue Crack Growth Rate Laws Accounting for Stress Ratio Effects," ASTM E24.04.04 Task Group Report, Philadelphia, October 1974.
46. P. C. Paris, "The Fracture Mechanics Approach to Fatigue," Proceedings 10th Sagamore Army Materials Research Conference, Syracuse University Press, New York, p 107, 1964.
47. T. H. Sanders, D. A. Mauney, and J. T. Staley, "Strain Control Fatigue as a Tool to Interpret Fatigue Initiation of Aluminum Alloys," presented at 10th Annual International Symposium on Material Science, Fundamental Aspects of Structural Alloy Design, Seattle, Washington, September 1975.
48. S. Majumdar and J. Morrow, "Correlation Between Fatigue Crack Propagation and Low Cycle Fatigue Properties," Univ. of Ill., T. & A.M. Report #364, 1973.

49. W. Elber, "The Significance of Fatigue Crack Closure," ASTM STP 486, 1971.
50. R. G. Weber and A. J. McEvily, Fracture, Proceedings of the 2nd International Conference on Fracture, Brighton, p 414, 1969.
51. R. J. Donahue, H. McI. Clark, P. Atanmo, R. Kumble, and A. J. McEvily, "Crack Opening Displacement and the Rate of Fatigue Crack Growth," Int. Jour. of Fracture Mechanics, Vol 8, p 209, 1972.
52. G. A. Miller and J. F. Throop, "Optimum Fatigue Crack Resistance," Presented to ASTM E9 Committee at ASTM Annual National Meeting, Atlantic City, 1969.
53. J. Weertman, "Theory of Fatigue Crack Growth Based on BCS Crack Theory with Work Hardening," Int. Jour. of Fracture, 0, p 125, 1973.
54. J. Weertman, "Rate of Growth of Fatigue Crack Calculated from the Theory of Infinitesimal Dislocation Distributed on a Plane," Int. J. of Fracture, 2, p 460, 1966.
55. T. Endo and J. Morrow, "Cyclic Stress-Strain and Fatigue Behavior of Representative Aircraft Metals," J. of Materials, 4, p 1959, 1969.
56. D. A. Mauney, Alcoa Laboratories, privata communication explaining procedure similar to Reference 47.
57. P. J. E. Forsyth, Acta Met., Vol 11, p 703, 1963.
58. C. A. Stubbington and P. J. E. Forsyth, J. Institute of Metals, Vol 90, p 347, 1961-2.
59. R. W. Hertzberg and W. J. Mills, "On the Character of Fatigue Surface Micromorphology in the Ultra-low Growth Rate Regime," to be published ASTM, STP 600.
60. C. D. Beachem and D. A. Meyn, ASTM, STP 436, p 59, 1968.
61. J. A. Santner and M. E. Fine, Met. Trans., 7A, p 583, 1976.
62. A. J. McEvily and R. P. Wei, "Fracture Mechanics and Corrosion Fatigue," Corrosion Fatigue, Proceedings of the University of Connecticut Conference, p 381, June 1971.
63. R. P. Wei, "Some Aspects of Environment Enhanced Fatigue Crack Growth," Engineering Fracture Mechanics, Vol 1, No. 4, p 633, 1970.

64. F. J. Bradshaw and C. Wheeler, "The Effects of Environment on Fatigue Crack Growth in Aluminum and Some Aluminum Alloys," Applied Materials Research, Vol 5, p 112, 1966.
65. A. Hartman, F. J. Jacobs, A. Nederveen, and R. DeRijk. NRL TNM 2182, 1967.
66. F. J. Bradshaw and C. Wheeler, RAE, TR 68041, 1968.
67. M. J. Harden and M. A. Wright, "Mechanisms of Atmospheric Interaction with the Fatigue of Metals," NASA CR-116, 1968.
68. H. Shaw, S. E. Podlaser, and I. R. Kramer, "Effect of Vacuum on the Fatigue Life of Aluminum," Acta Met., Vol 14, No. 3, p 341, 1966.
69. R. J. Bucci, "Environment Enhanced Fatigue and Stress-Corrosion Cracking of a Titanium Alloy plus a Simple Model for the Assessment of Environmental Influence on Fatigue Behavior," Ph.D. Dissertation, Lehigh University, 1970.
70. J. P. Gallagher, "Corrosion Fatigue Crack Growth Behavior Above and Below  $K_{Isc}$ ," NRL Report 7064, Naval Research Laboratory, Washington, D.C., May 1970.
71. J. P. Gallagher and R. P. Wei, "Corrosion Fatigue Crack Propagation Behavior in Steels," Corrosion Fatigue, Proceedings of the University of Connecticut Conference, p 409, June 1971.
72. Damage Tolerant Design Handbook, "A Compilation of Fracture and Crack Growth Data for High-Strength Aluminum Alloys," Air Force Materials Laboratory, Air Force Flight Dynamic Laboratory, December 1972.
73. J. G. Kaufman and M. Holt, "Fracture Characteristics of Aluminum Alloys," Alcoa Research Laboratories Technical Paper No. 18, 1965.
74. G. R. Irwin, "Fracture Mode Transition for a Crack Transversing a Plate," Trans. ASME, Vol 82, Series D, p 417, 1960.
75. R. J. Bucci, "Spectrum Loading - A Useful Tool to Screen the Role of Microstructure in Fatigue Crack Growth Resistance of Metal Alloys," Presented at Tenth National Fracture Mechanics Symposium, Philadelphia, August 23, 1976.

## APPENDIX A

### FATIGUE CRACK INITIATION RESISTANCE\*

#### 1. Introduction

The microstructural effects on fatigue crack propagation resistance, previously described, give no indication of the effect on fatigue crack initiation resistance. Because of this, the following evaluation was performed to insure that any of the 25 microstructural variants evaluated would not seriously detract from crack initiation resistance.

The pursuit of any program on fatigue crack initiation resistance requires several criteria to be specified:

1. Definition of fatigue crack initiation
2. Realistic state of stress
3. Economical method of crack detection

The technology in the area of nucleation and growth of small cracks (crack initiation) has not developed to the state of linear elastic fracture mechanics. For this reason, conducting a laboratory test that will result in data usable in all engineering structural configurations is not possible at this time. Because of this, the crack initiation test criteria are specified to approximate the conditions under which the material is expected to be used.

#### 2. Procedure

Fatigue crack initiation resistance was evaluated by using the compact tension keyhole specimen shown in Figure A-1. This

---

\*This portion of the investigation was conducted and written by D. A. Mauney, Engineering Properties and Design Division, Alcoa Laboratories.



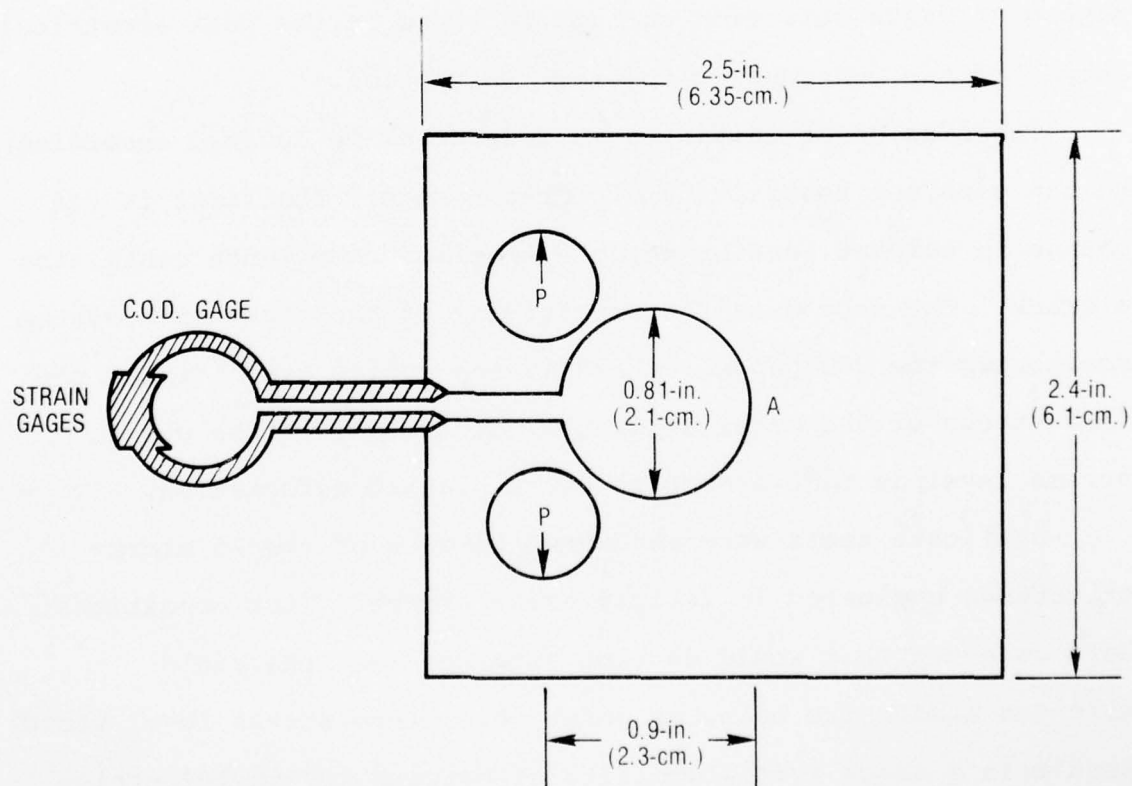


Figure A-1 Compact Tension Keyhole Specimen For Fatigue Crack Initiation Testing.

specimen is loaded cyclically at points "P" and crack initiation occurs from the inside hole surface near point "A." The crack opening displacement (COD) gauge allows an electronic means of crack detection. At a constant load amplitude, the peak COD will increase as a crack initiates at point "A."

The advantage of using the compact tension keyhole specimen in this evaluation is that its stress state is representative of many aircraft sheet applications. Examples of these would be mild stress concentrators in rivet holes, weight reduction holes, and sheet metal bends. This specimen also provides an economical method of crack detection through increase in the peak electrical output of the COD gauge with crack initiation.

The size of an initiated fatigue crack is defined according to the combined sensitivity of three things. The first is the change in compact tension keyhole specimen compliance containing a crack. The second is the sensitivity of the electronic system monitoring the COD gauge. Third is the cyclic stability of the flow stress of the material in the notch root, if the cyclic stress level is high enough to cause plastic deformation.

Duplicate tests were conducted on each of the 25 microstructures evaluated in fatigue crack growth. Test conditions were selected that would develop stresses near the yield strength inside the hole, at point "A." This stress level would result in a crack initiation life of between  $10^4$  to  $10^5$  cycles and would be the same for comparison of as many microstructures as possible. These conditions were chosen to approximate a

damaging part of a fighter spectrum, as well as permitting completion of all tests within the time allotted. As a result of the degree of plasticity in the notch root at the selected high stress levels, elastic-plastic finite element methods were used to accurately select specimen cyclic loads. Specimens were cycled at a stress ratio near zero ( $R = 0.1$ , ratio of minimum stress to maximum stress) with a sine wave loading function at 25 Hz. All testing was conducted on a CGS closed loop electrohydraulic testing machine in laboratory air at  $50 \pm 10$  percent relative humidity.

The experimentally determined initiated crack depth was an average of 0.060 inch with a maximum crack depth of 0.150 inch. The limit switch capability on the CGS machine was used to discontinue the test when crack initiation occurred. This long and variable detectable crack length is not of real concern. The primary reason is because of the high stress intensity level that occurs on a very small crack when nucleated in this specimen at the stress levels being used. In fact, a crack less than 0.001 inch deep would propagate to the average or maximum detected depth in fewer than 1% of the total cycles of the test. Part of the variability in crack size detection is thought to be a result of lack of consistent compliance. Factors which affect compliance are sheet thickness, degree of bow in the specimens, and differences in cyclic strain hardening or softening.

### 3. Results

The results of the fatigue tests are presented in Table A-1. Significance of the results was determined assuming log normal

TABLE A-1

## FATIGUE CRACK INITIATION TEST RESULTS

Structure Number	Alloy	Maximum Stress, ksi	Cycles to Initiation		Mean Cycles To Initiation
			First Test	Second Test	
1	7050-T76	60	34240	36090	35165
2	7050+Mn-T76	60	43610	111110	77360
3	X7080(HiCu)-T76	60	27130	25440	26285
4	X7080-T76	60	57900	14550	36225
5	7050-TX1	44	74290	48770	61530
6	7050-TX2	44	79730	45900	62815
7	7050-TX3	44	16170	22350	33195
8	X7080(HiCu)-T76(Lg.g.s.)	60	32770	33620	33195
9	7075-T61	60	27970	38910	33440
10	7075-T6	60	47050	182640	114845
11	7475-T61	60	267200	79220	173210
12	7475-T6	60	42150	43060	42605
13	7075-T61(Lg.g.s.)	60	74640	104030	89335
14	2024(HiMn)-T31	42	81450	149800	115625
15	2124(HiMn)-T31	42	64000	95750	79875
16	2024(LoMn)-T31	42	97300	110400	103850
17	2124(LoMn)-T31	42	76050	80210	78130
18	2024(HiMn)-T86	60	38520	31410	34965
19	2124(HiMn)-T86	60	42590	39340	40965
20	2024(LoMn)-T86	60	35030	28780	31905
21	2124(LoMn)-T86	60	34950	37770	36360
22	2024(LoMn)-T36	42	463530	572160	517845
23	2024(LoMn)-T81	60	19730	22600	21165
24	2048-T31	42	67500	77050	72275
25	2048-T86	60	43010	47350	45180

NOTE: (Lg.g.s.) - indicates large grain size.



distribution in life and using Yates algorithm for the full factorial modules and two sample "t" tests assuming nonequality of sample variance in all other modules. Comparisons were only made for structures tested at the same stress level. At a 95% confidence level there were no significant results except for the difference between 2024-T31 and T36. Mean life of the T36 temper structure was significantly longer. Results that were statistically significant at the 75% confidence level were generally either not practically significant, were in conflict with published results, or had such high scatter that validity of conclusions drawn from such a small amount of data was suspect.

#### 4. Conclusions

By using duplicate specimens designed to simulate the stress state of many aircraft sheet applications, effects of microstructure on resistance to fatigue crack initiation were generally not significant at the 95% confidence level. To verify the sole exception, additional replicate tests, plus replicate tests at other stress levels, would be required to confirm with a high confidence level whether microstructure had an effect. At this time, however, microstructural changes which improve resistance to fatigue crack propagation do not generally appear to strongly affect resistance to fatigue crack initiation.

## APPENDIX B

### EFFECTS OF MICROSTRUCTURE ON TOUGHNESS

#### 1. 2XXX

Aging practice and percent stretch affected strength and toughness of the 2XXX alloys (Figures 38 and 39). Alloy 2024 in the T31, T36, T81, and T86 tempers provided a continuous distribution with strength progressively increasing and both UPE (unit crack propagation energy in the tear test) and NTS/YS (ratio of notch tensile strength to yield strength) progressively decreasing. Toughness of 2024 overaged to the T36 temper strength level (T8X), however, was similar to that of the higher strength 2024-T86.

In contrast, decreasing Fe and Si levels to eliminate the insoluble  $\text{Al}_{12}(\text{Fe,Mn})_3\text{Si}$  and to reduce the amount of insoluble  $\text{Al}_7\text{Cu}_2\text{Fe}$  and  $\text{Mg}_2\text{Si}$  (reduce volume percent from 2.2 to 1.4) increased toughness (2024 versus 2124) without affecting strength.

By reducing the Cu level from 4.25 to 3.25 percent while maintaining the low Fe and Si contents found in alloy 2124, i.e., alloy 2048 (volume percent constituent 0.5), toughness increased greatly while yield strength decreased only slightly. This increase in toughness over 2124 is attributed to a lower volume fraction of the Cu-containing intermetallics,  $\text{Al}_2\text{CuMg}$  and  $\text{CuAl}_2$ .

The volume fraction of dispersoid had little effect. Effects of volume percent (2.6 vs 1.1) of  $\text{Al}_{20}\text{Cu}_2\text{Mn}_3$  dispersoid on toughness can be determined in 2024 and 2124 in the T31 and T86 tempers by comparing the high and low Mn versions of these alloy-temper combinations (Figures 38 and 39). This comparison shows that an

increase in Mn from 0.40 to 0.80 (calculated increase in volume percent of 1.1 to 2.6  $\text{Al}_{20}\text{Cu}_2\text{Mn}_3$  dispersoid) did not significantly affect the combination of strength and toughness in these alloys.

## 2. 7XXX

Significant changes in UPE and NTS/YS of the 7XXX alloys were also obtained by modifying the structure (Figures 36 and 37). For example, UPE and NTS/YS of 7075-type alloys were increased significantly by controlling certain microstructural features. By decreasing Fe and Si content to reduce the volume fraction of insoluble constituent particles, toughness of 7075, as measured by UPE and NTS/YS, was significantly increased (7475-T6 vs 7075-T6). Still further increases in toughness were obtained by coalescing the  $\text{Al}_{12}\text{Mg}_2\text{Cr}$  dispersoid to increase interparticle spacing (T6 vs T61). This combination of controlling purity and dispersoid morphology, i.e., patented Alcoa process,\* provided the highest combination of strength and toughness, 7475-T61 (Structure 11).

In addition to these modifications to increase toughness, Structure 13, 7075-T61, provided a surprisingly higher toughness structure than the twelvefold smaller grain size 7075-T61, Structure 9. These two grain structures are shown in Figures 14 and 10. In fact, this combination of grain size and dispersoid size developed a higher toughness than the 7475-T6 material containing small  $\text{Al}_{12}\text{Mg}_2\text{Cr}$  dispersoids.

The structural features controlling the toughness of the Cr-free 7XXX alloys are difficult to evaluate since the yield strengths

\*U.S. Patent 3791880, February 12, 1974

are quite dissimilar in some instances. However, it is interesting to note that 7050-T76 sheet containing both Mn and Zr dispersoids developed a higher toughness than 7050 with only the  $Zr_3Al$  dispersoid. Caution should be exercised, however, in concluding that this behavior is typical because the  $Al_2CuMg$  particles in the 7050 may have contributed to the lower toughness in the Mn-free material.

### 3. Comparison with Commercial Material

To place the toughness of these materials in perspective with commercially established 2XXX and 7XXX alloys, UPE and NTS/YS values of these particular structures were compared to UPE and NTS/YS scatterbands normally found for commercially established alloys (Figures B-1 and B-2). As expected, the toughness of alloys 7075-T6 and 2024-T3X, T8X fall within their respective commercially established alloy scatterbands. The toughness of the remaining alloys in standard tempers are above these scatterbands in accord with the experimental program designed to produce alloys providing improved combinations of strength and toughness.

The toughness, measured by NTS/YS ratio, of the experimental temper 7050 alloy, Structures 5, 6, and 7, was considerably higher than that of conventionally precipitation heat treated 7XXX alloys; however, when compared on a yield strength basis, these structures fell within the scatterband shown in Figure B-2. Toughness of these structures based on UPE was somewhat lower than for conventional 7XXX, but within the upper part of the band of the 2XXX alloys (Figure B-1).



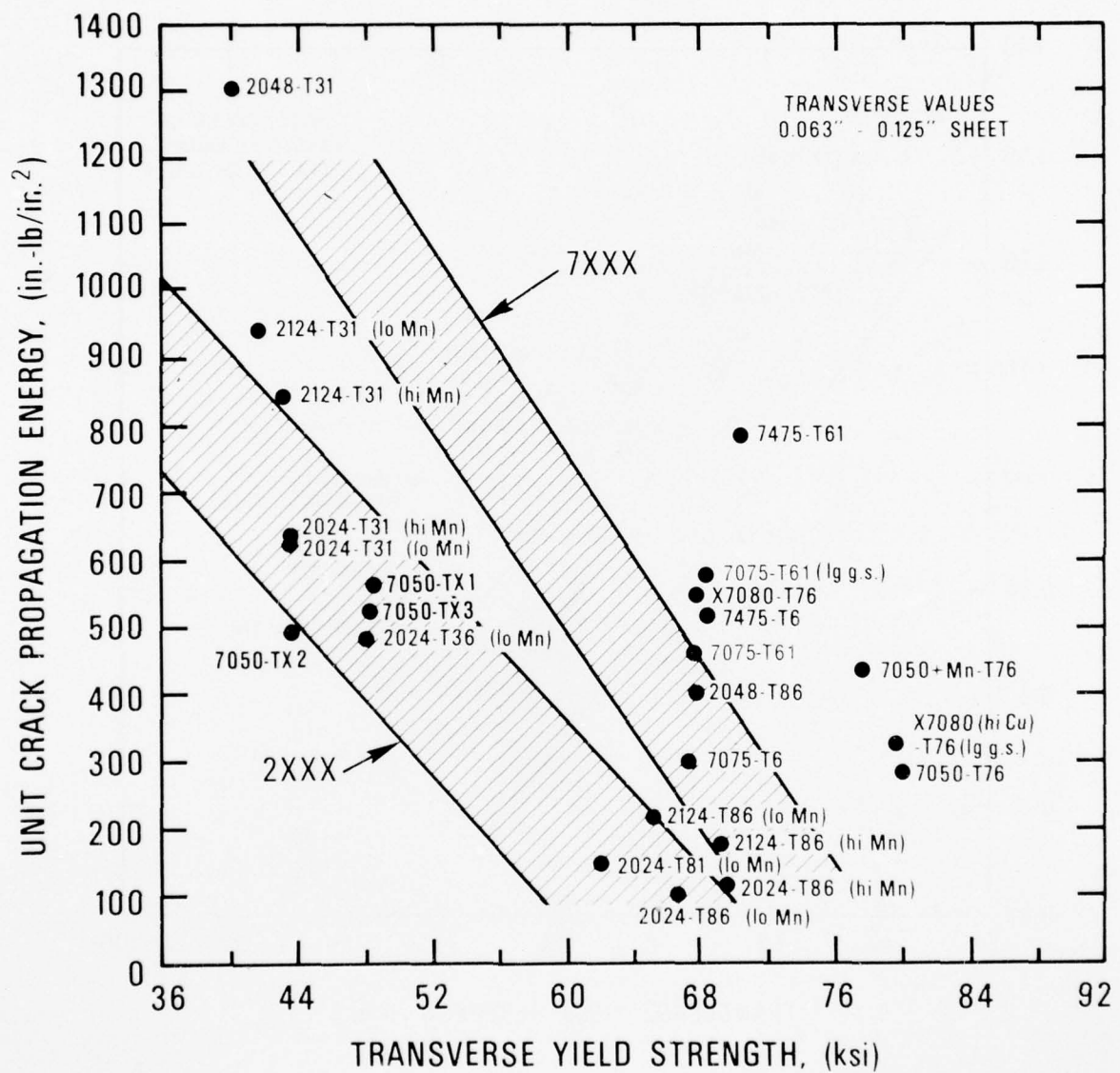


Figure B-1 Comparison of the Toughness of the 25 2XXX and 7XXX Alloys with Commercially Established Al Alloys. Toughness Measured by Unit Crack Propagation Energy.

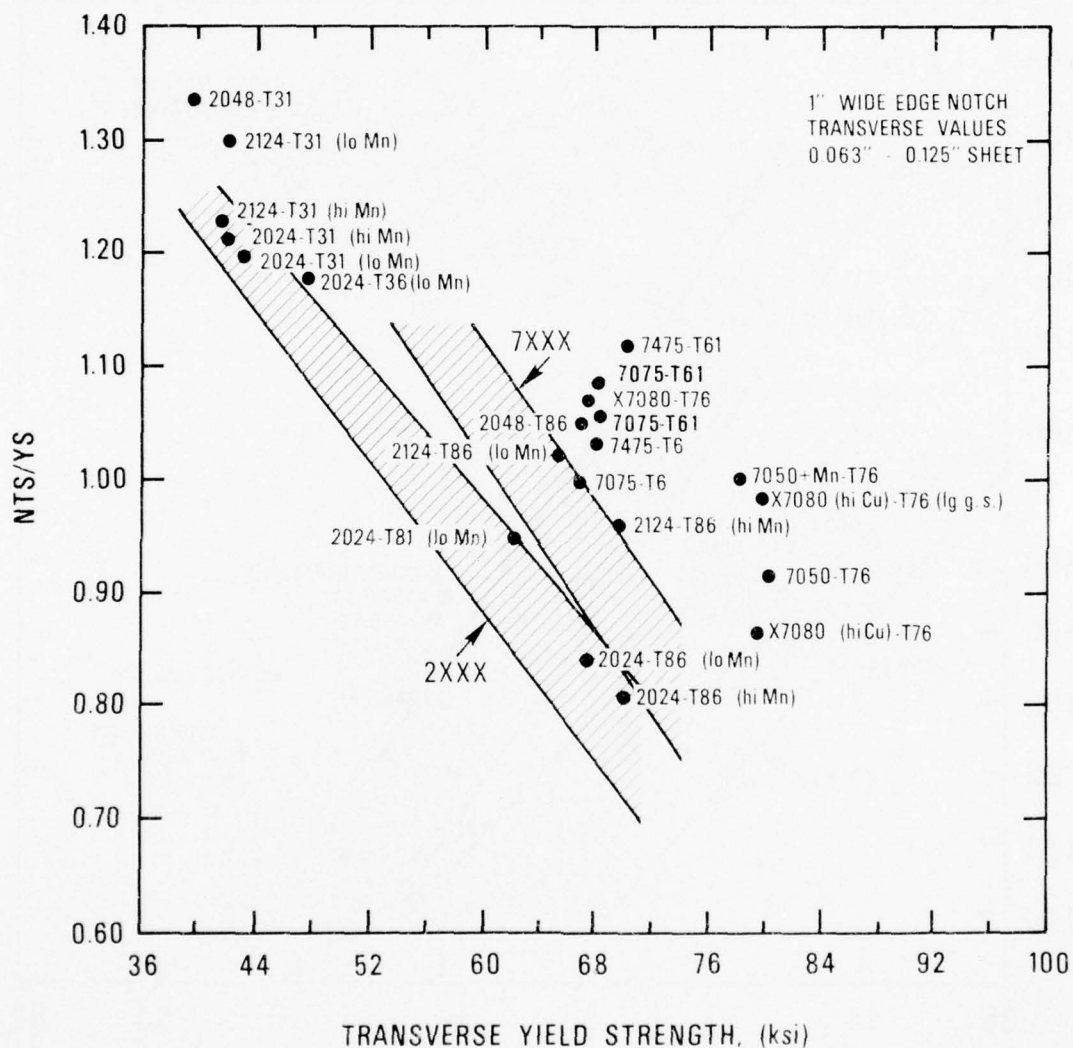


Figure B-2 Comparison of the Notch Toughness of the 25 2XXX and 7XXX Alloys with Commercially Established Al Alloys.

APPENDIX C

INTERMEDIATE  $\Delta K$ ,  $\Delta a/\Delta N$  vs  $\Delta K$  PLOTS

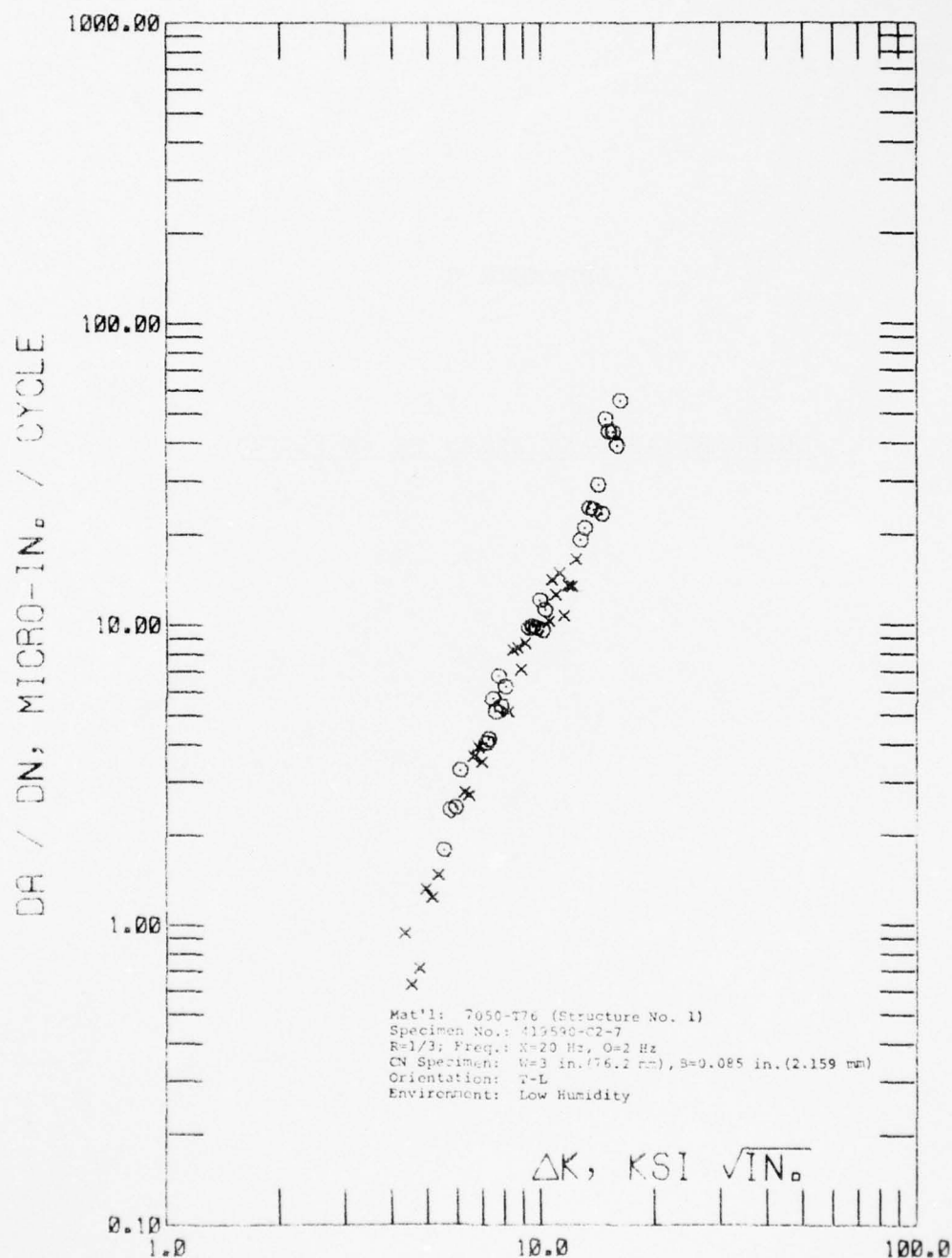


Figure C-1 Cyclic Stress Intensity Range,  $\Delta K$ , Vs. Cyclic Fatigue Crack Growth Rate,  $\Delta a / \Delta N$ , of Structure No. 1

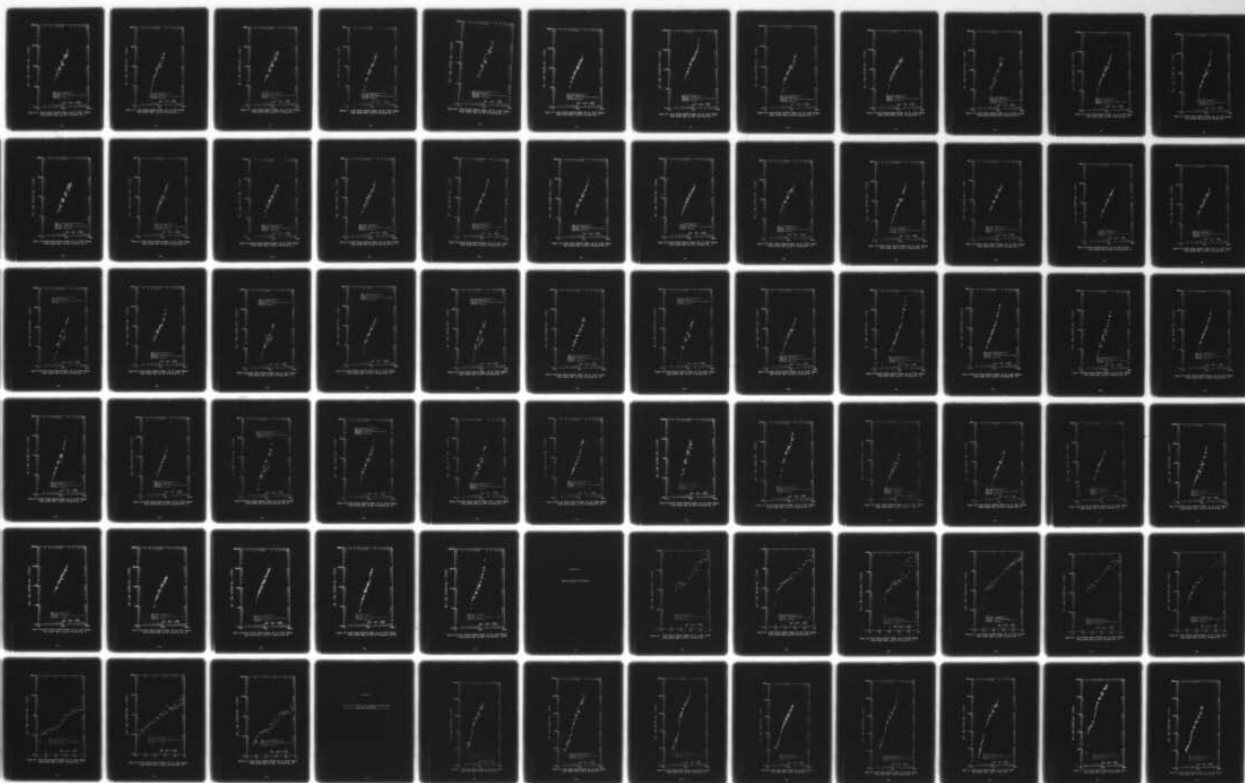


AD-A037 156

ALUMINUM CO OF AMERICA ALCOA CENTER PA ALCOA LABS F/G 11/6  
EFFECTS OF MICROSTRUCTURE ON FATIGUE CRACK GROWTH OF HIGH-STRENGTH (U)  
AUG 76 W G TRUCKNER, J T STALEY, R J BUCCI F33615-74-C-5079  
56-76-AF5 AFML-TR-76-169 NL

UNCLASSIFIED

3 OF 3  
AD  
A037156



END

DATE  
FILMED  
4-77

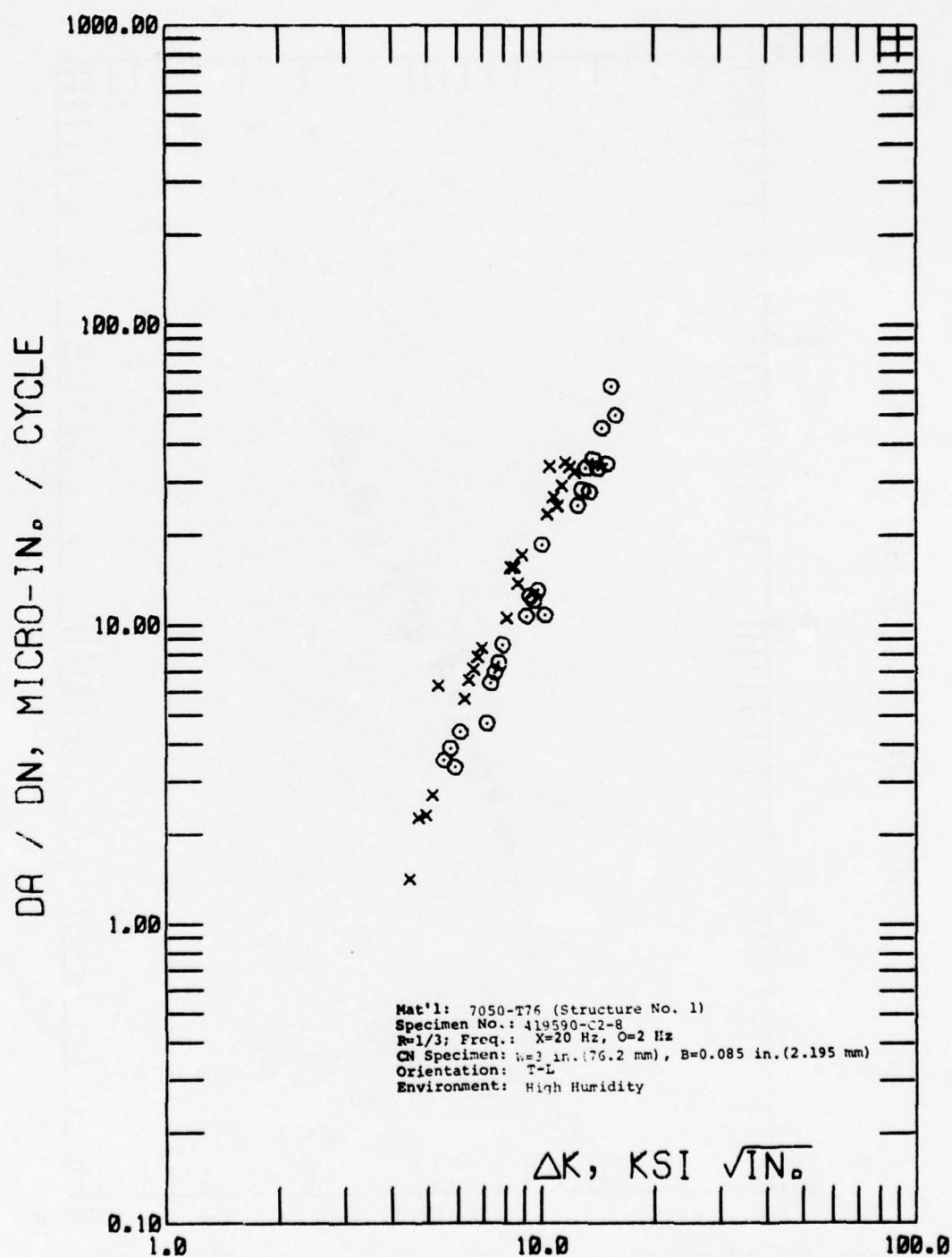


Figure C-2 Cyclic Stress Intensity Range,  $\Delta K$ , Vs. Cyclic Fatigue Crack Growth Rate,  $\Delta a / \Delta N$ , of Structure No. 1

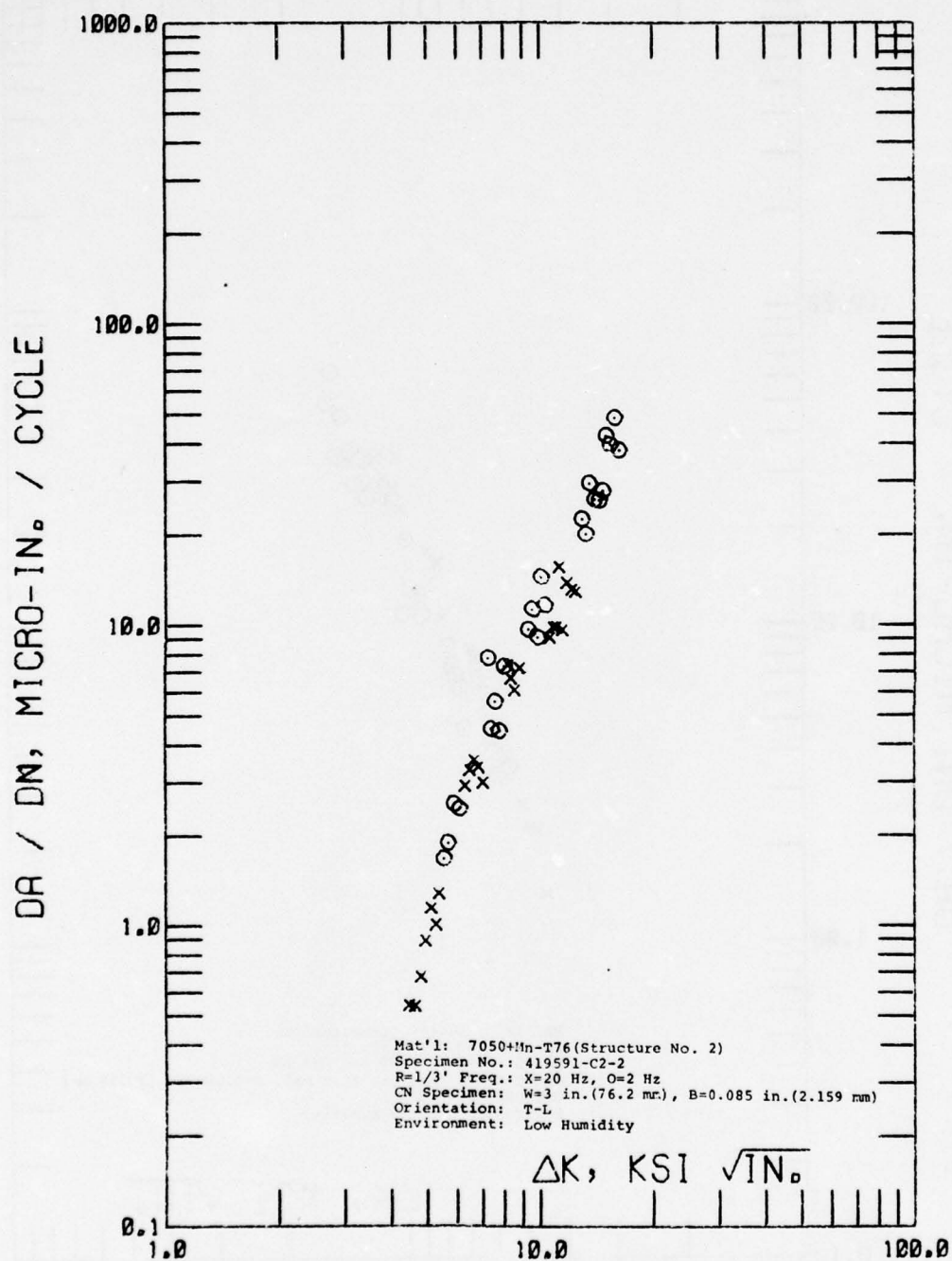


Figure C-3 Cyclic Stress Intensity Range,  $\Delta K$ , Vs. Cyclic Fatigue Crack Growth Rate,  $\Delta a / \Delta N$ , of Structure No. 2

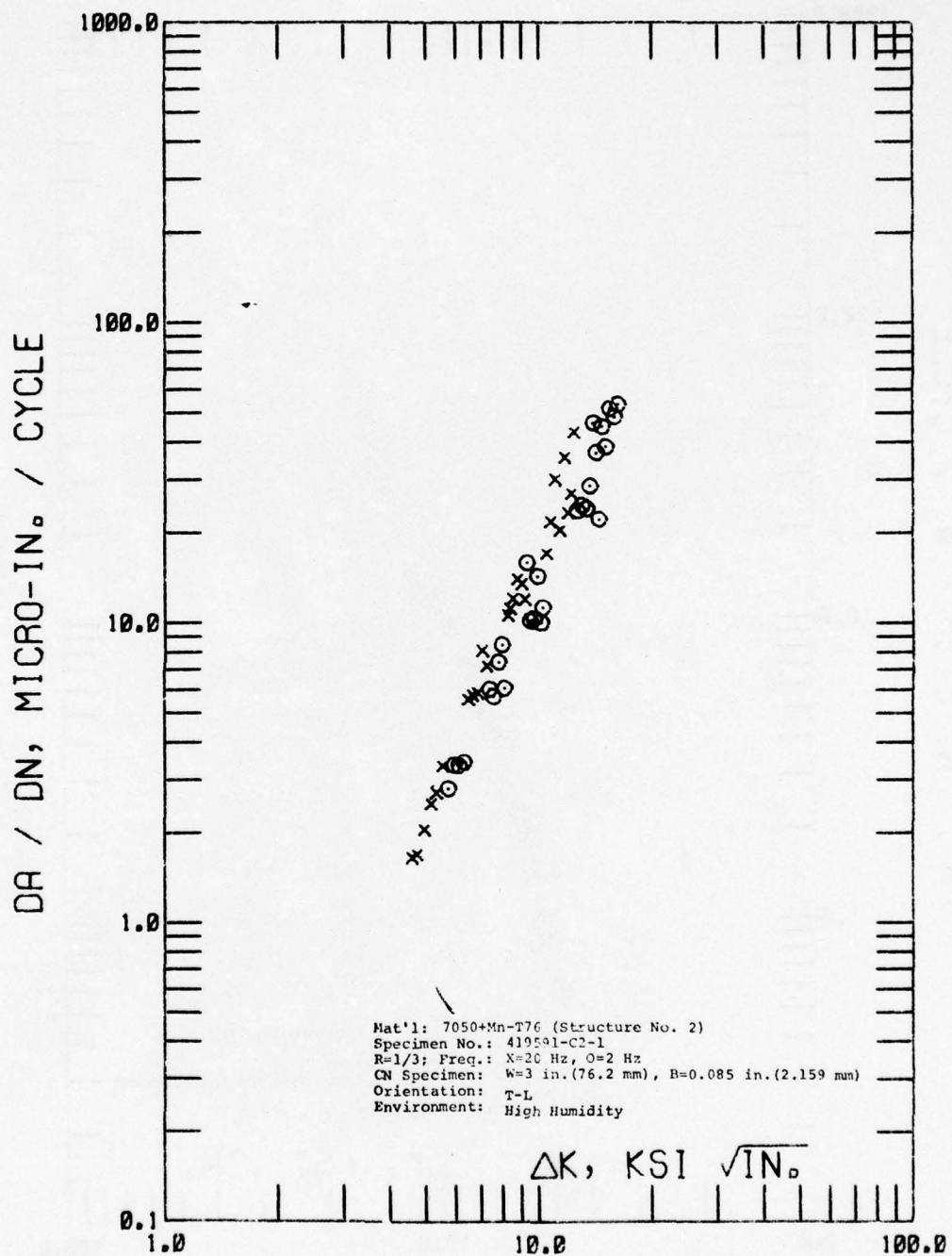


Figure C-4 Cyclic Stress Intensity Range,  $\Delta K$ , Vs. Cyclic Fatigue Crack Growth Rate,  $\Delta a / \Delta N$ , of Structure No. 2



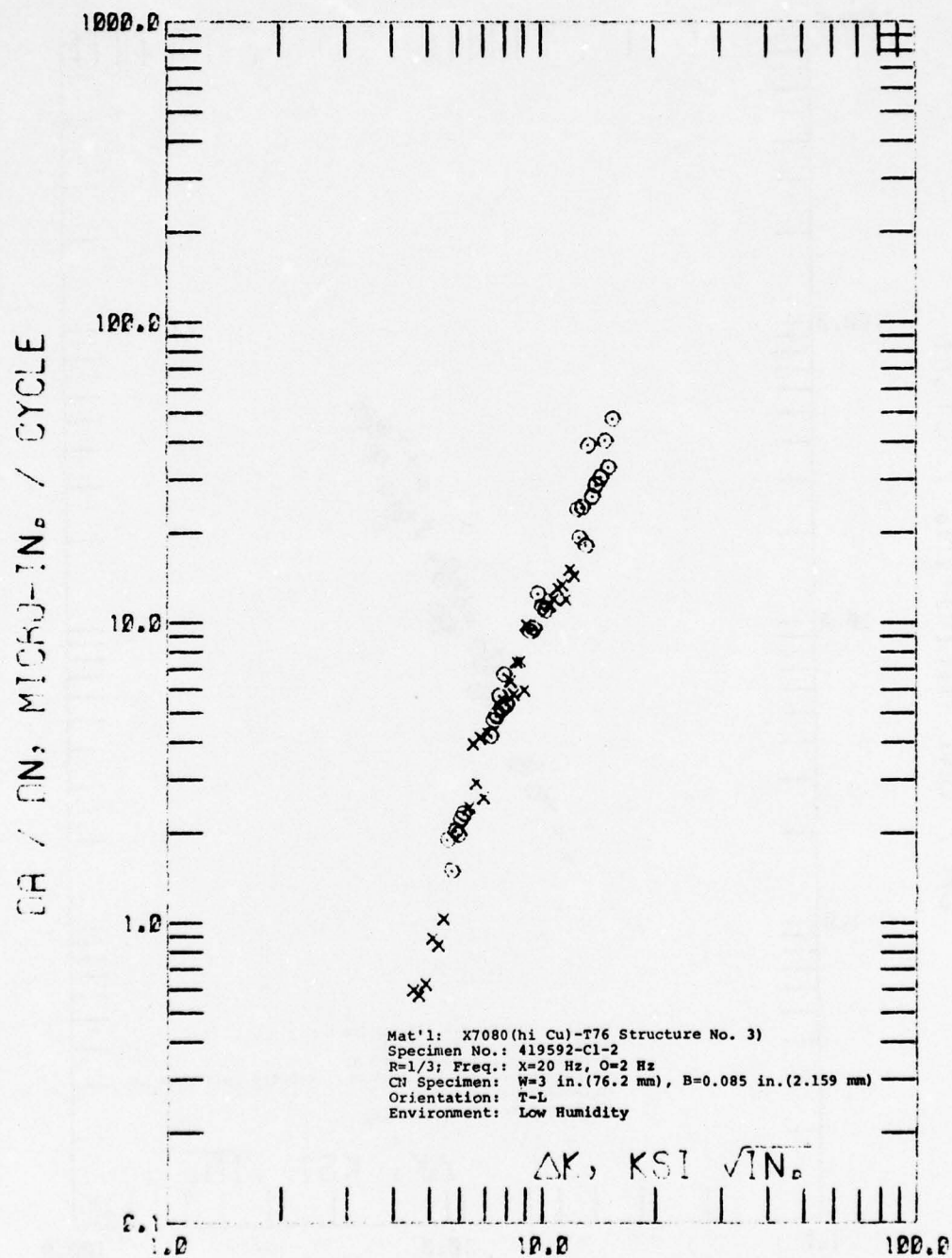


Figure C-5 Cyclic Stress Intensity Range,  $\Delta K$ , Vs. Cyclic Fatigue Crack Growth Rate,  $\Delta a / \Delta N$ , of Structure No. 3

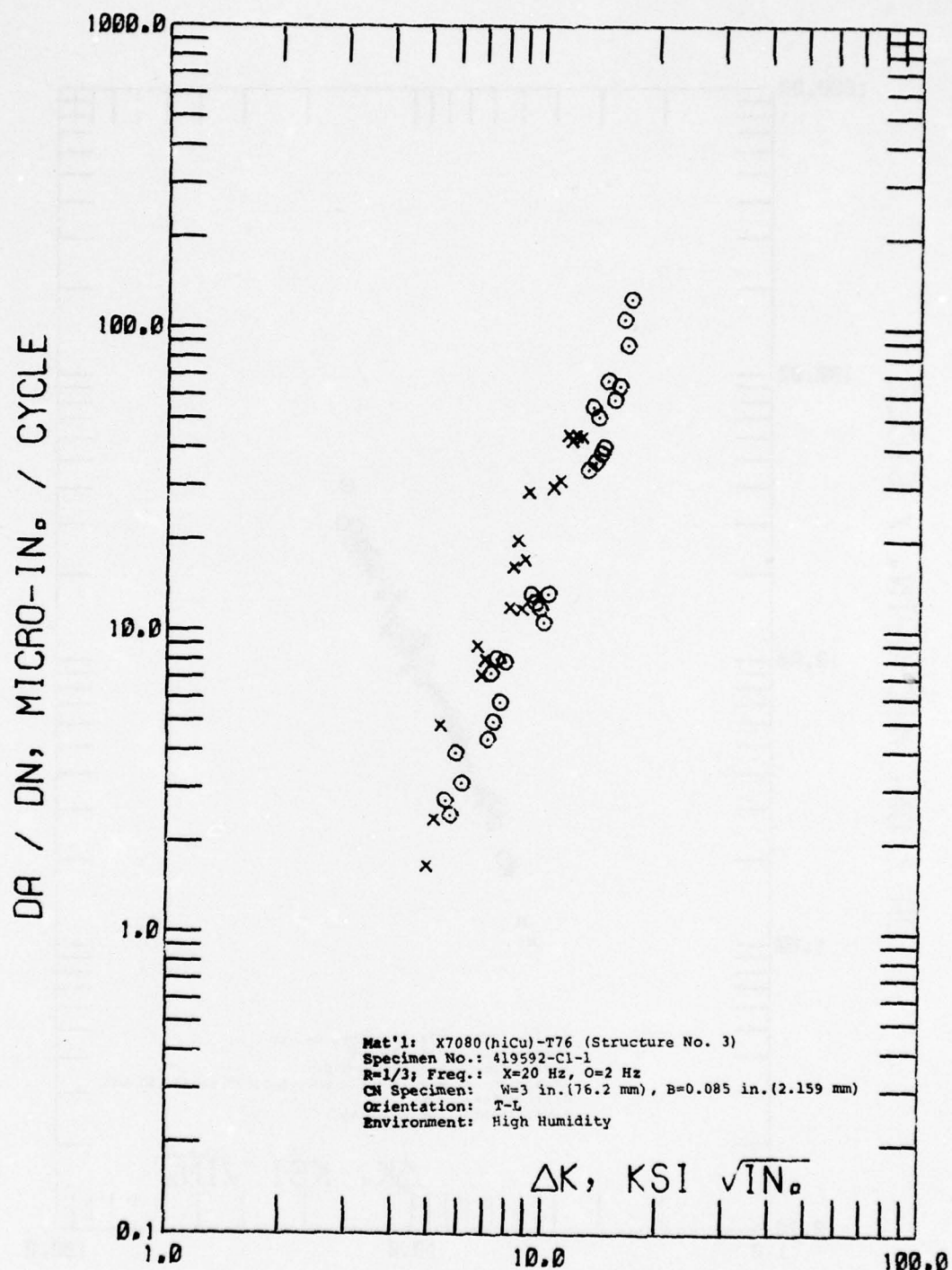


Figure C-6 Cyclic Stress Intensity Range,  $\Delta K$ , Vs. Cyclic Fatigue Crack Growth Rate,  $\Delta a / \Delta N$ , of Structure No. 3

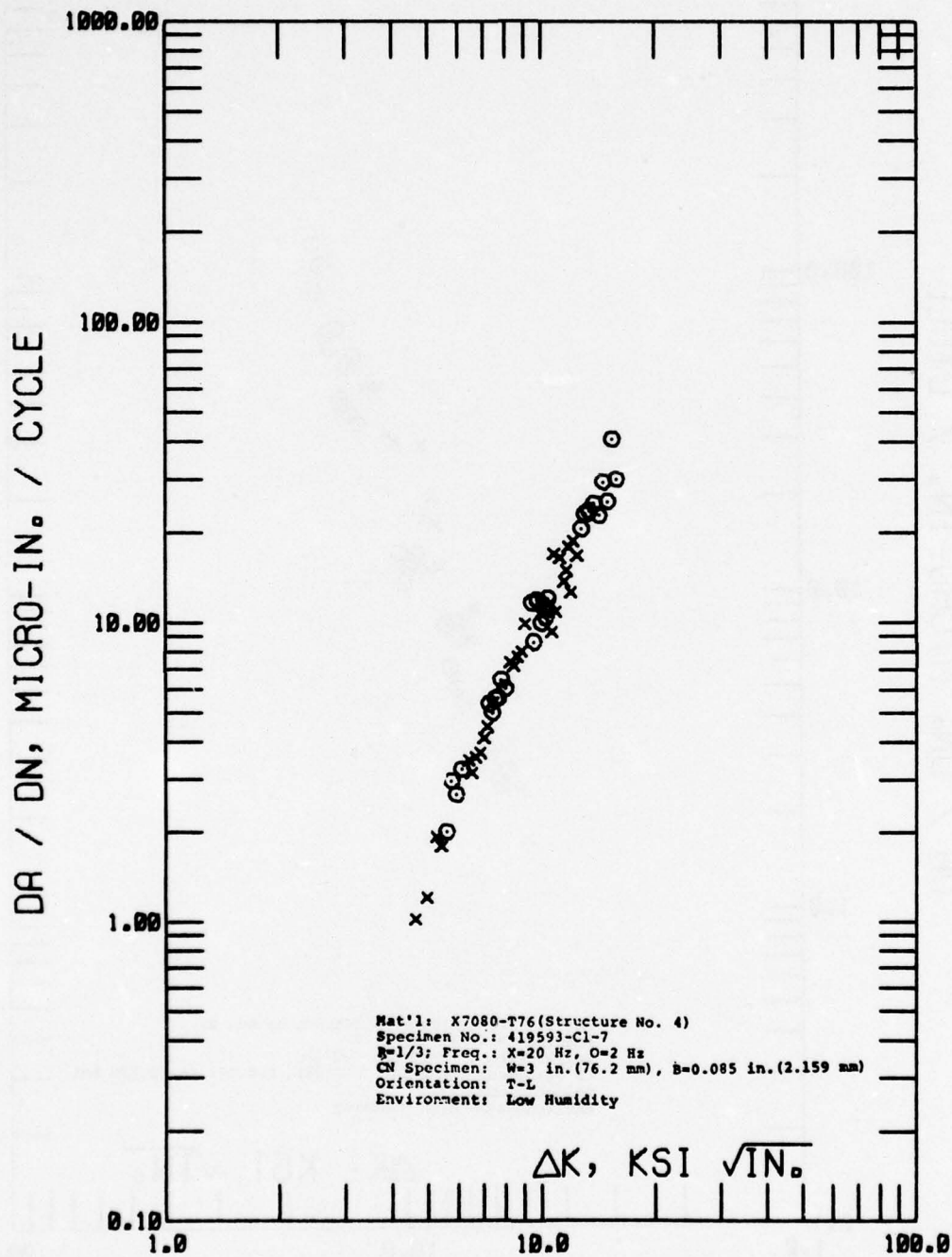


Figure C-7 Cyclic Stress Intensity Range,  $\Delta K$ , Vs. Cyclic Fatigue Crack Growth Rate,  $\Delta a/\Delta N$ , of Structure No. 4

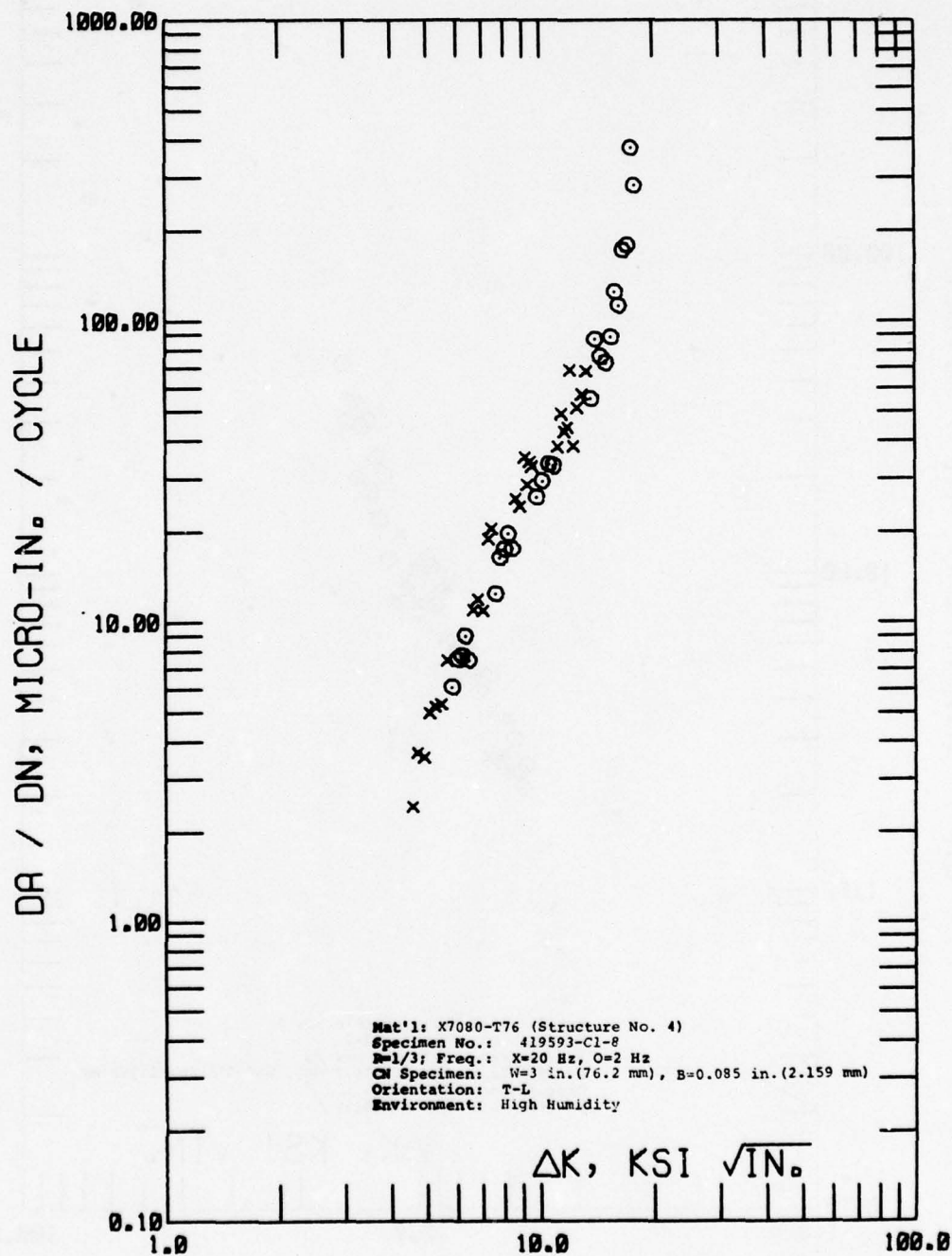


Figure C-8 Cyclic Stress Intensity Range,  $\Delta K$ , Vs. Cyclic Fatigue Crack Growth Rate,  $\Delta a/\Delta N$ , of Structure No. 4



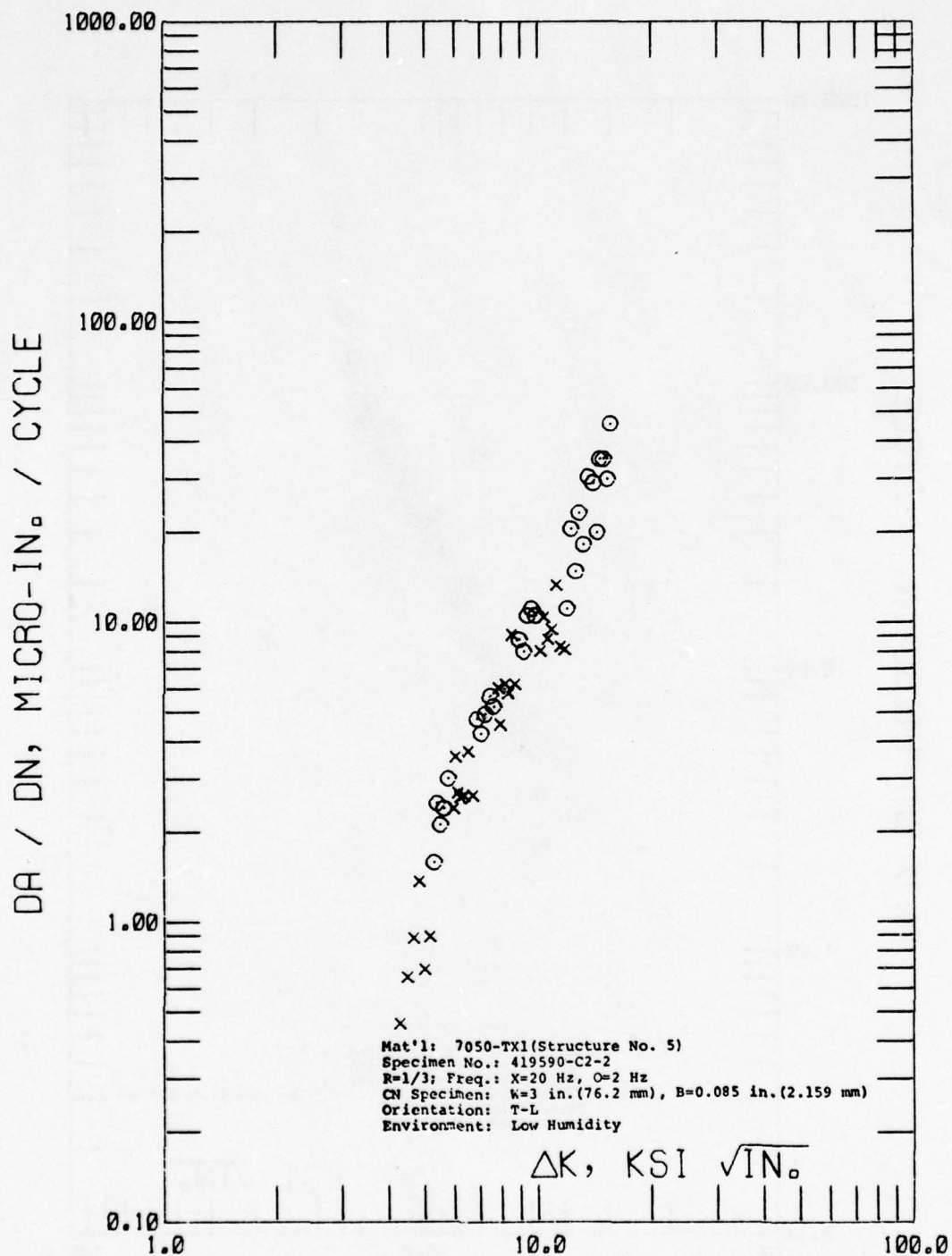


Figure C-9 Cyclic Stress Intensity Range,  $\Delta K$ , Vs. Cyclic Fatigue Crack Growth Rate  $\Delta a / \Delta N$ , of Structure No. 5

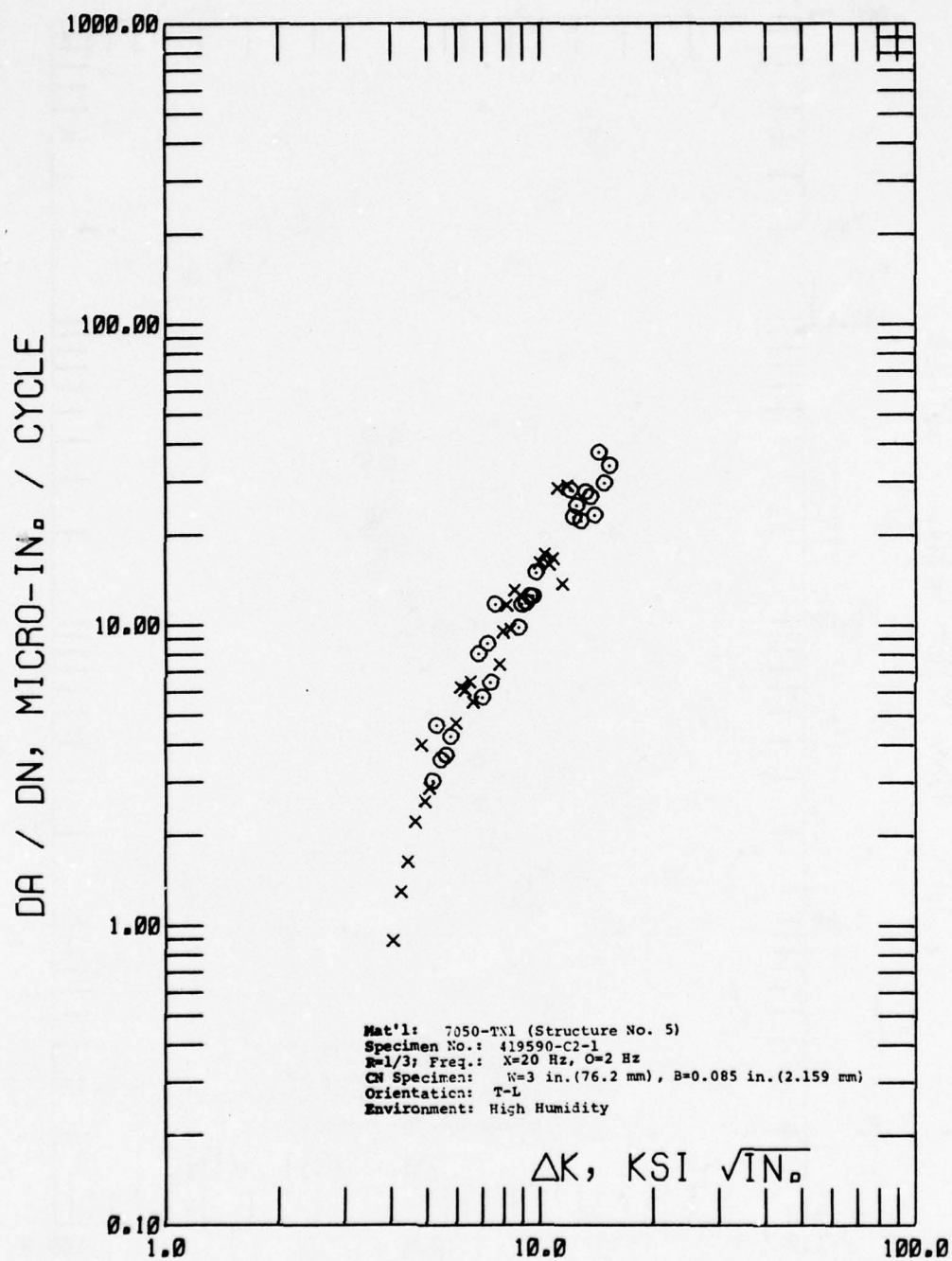


Figure C-10 Cyclic Stress Intensity Range,  $\Delta K$ , Vs. Cyclic Fatigue Crack Growth Rate,  $\Delta a / \Delta N$ , of Structure No. 5

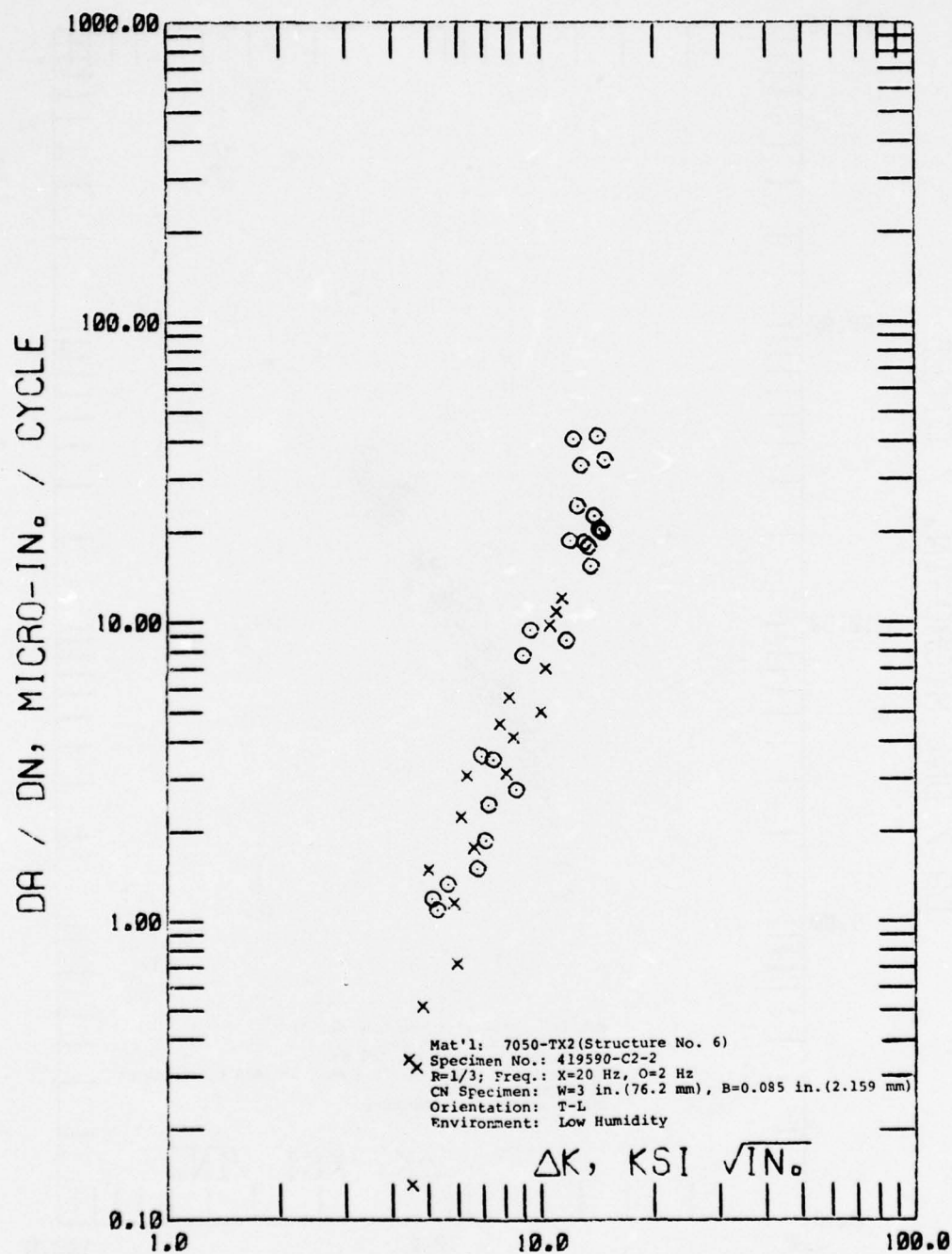


Figure C-11 Cyclic Stress Intensity Range,  $\Delta K$ , Vs. Cyclic Fatigue Crack Growth Rate  $\Delta a / \Delta N$ , of Structure No. 6

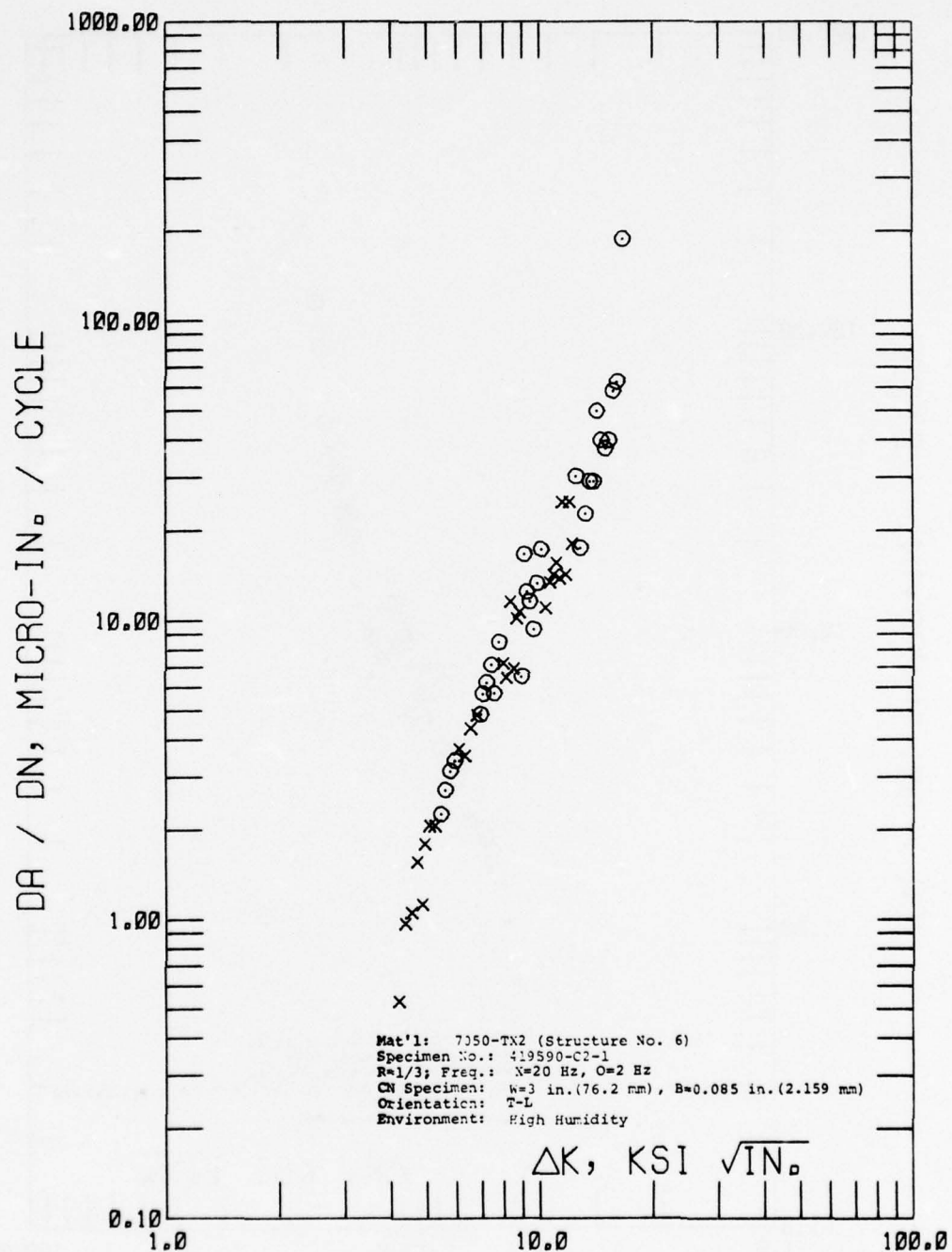


Figure C-12 Cyclic Stress Intensity Range,  $\Delta K$ , Vs. Cyclic Fatigue Crack Growth Rate,  $\Delta a / \Delta N$ , of Structure No. 6



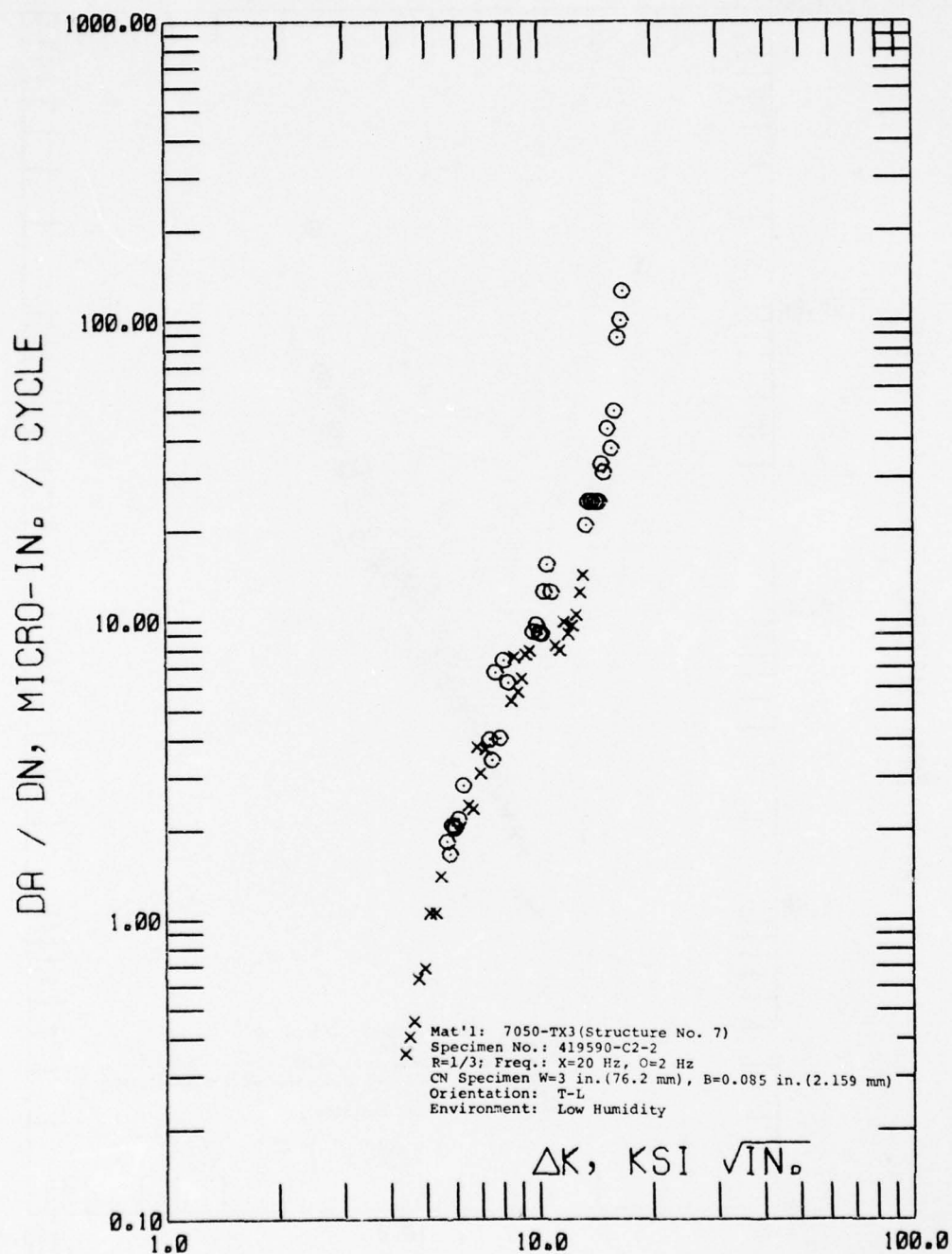


Figure C-13 Cyclic Stress Intensity Range,  $\Delta K$ , Vs. Cyclic Fatigue Crack Growth Rate  $\Delta a / \Delta N$ , of Structure No. 7

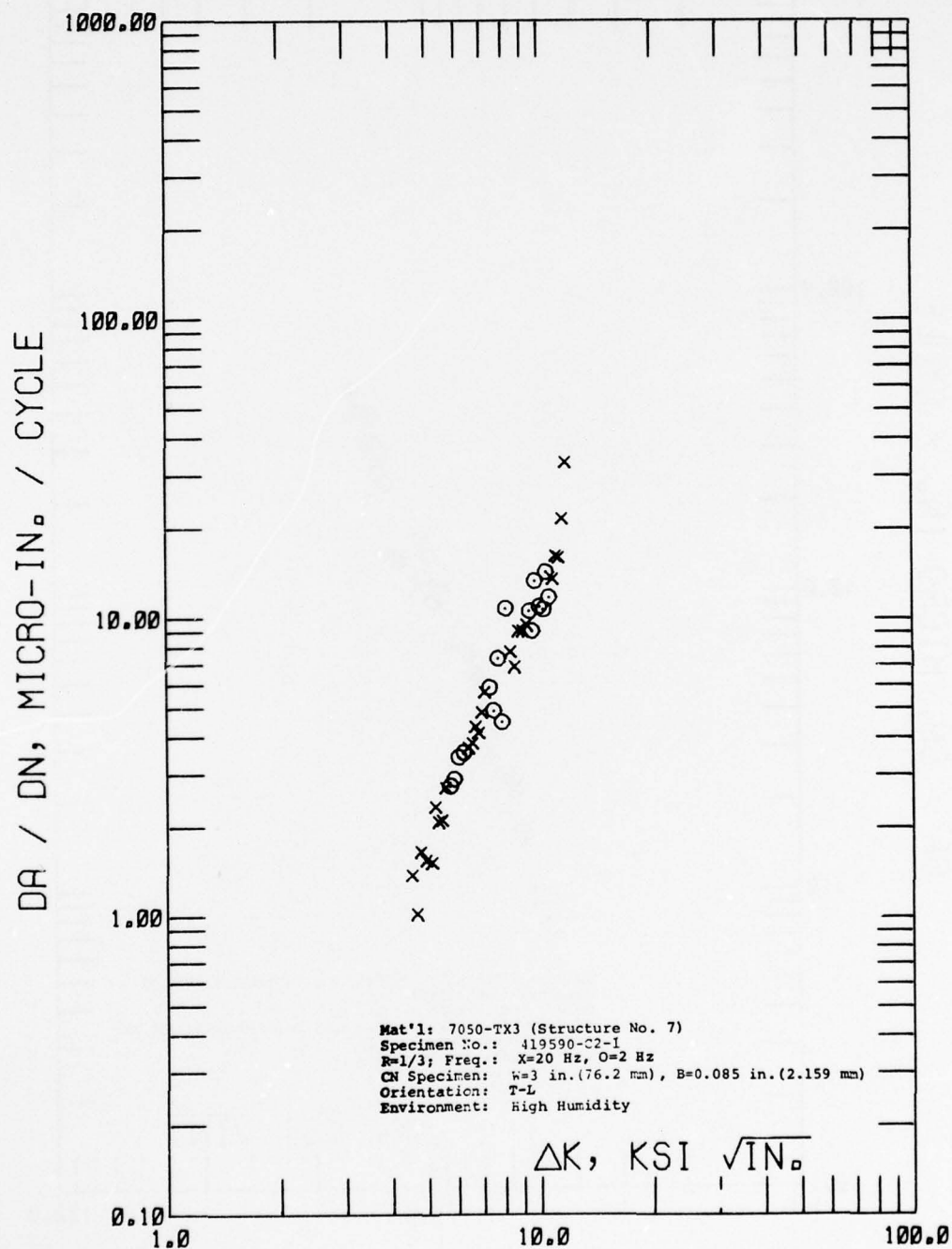


Figure C-14 Cyclic Stress Intensity Range,  $\Delta K$ , Vs. Cyclic Fatigue Crack Growth Rate,  $\Delta a/\Delta N$ , of Structure No. 7

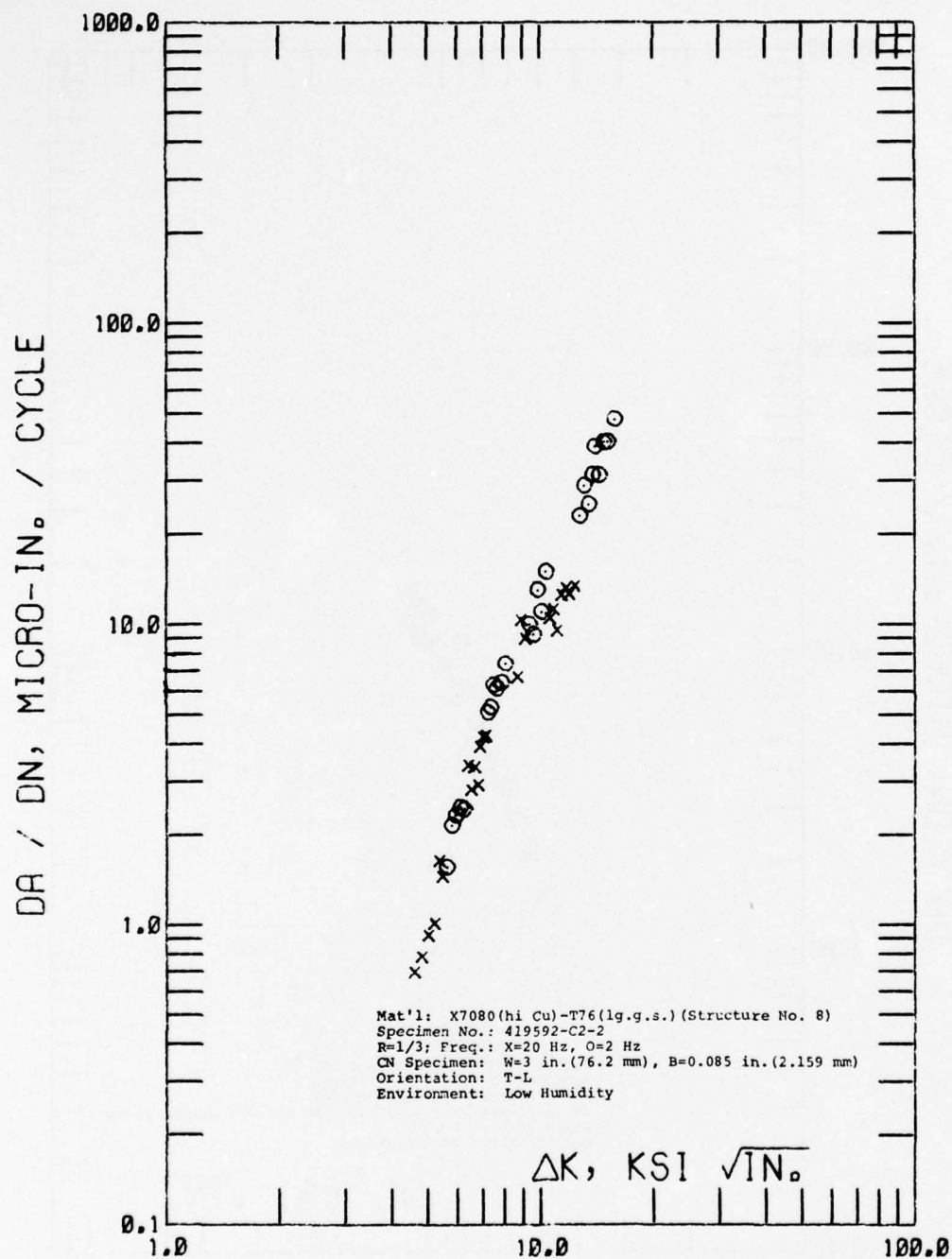


Figure C-15 Cyclic Stress Intensity Range,  $\Delta K$ , Vs. Cyclic Fatigue Crack Growth Rate,  $\Delta a / \Delta N$ , of Structure No. 8

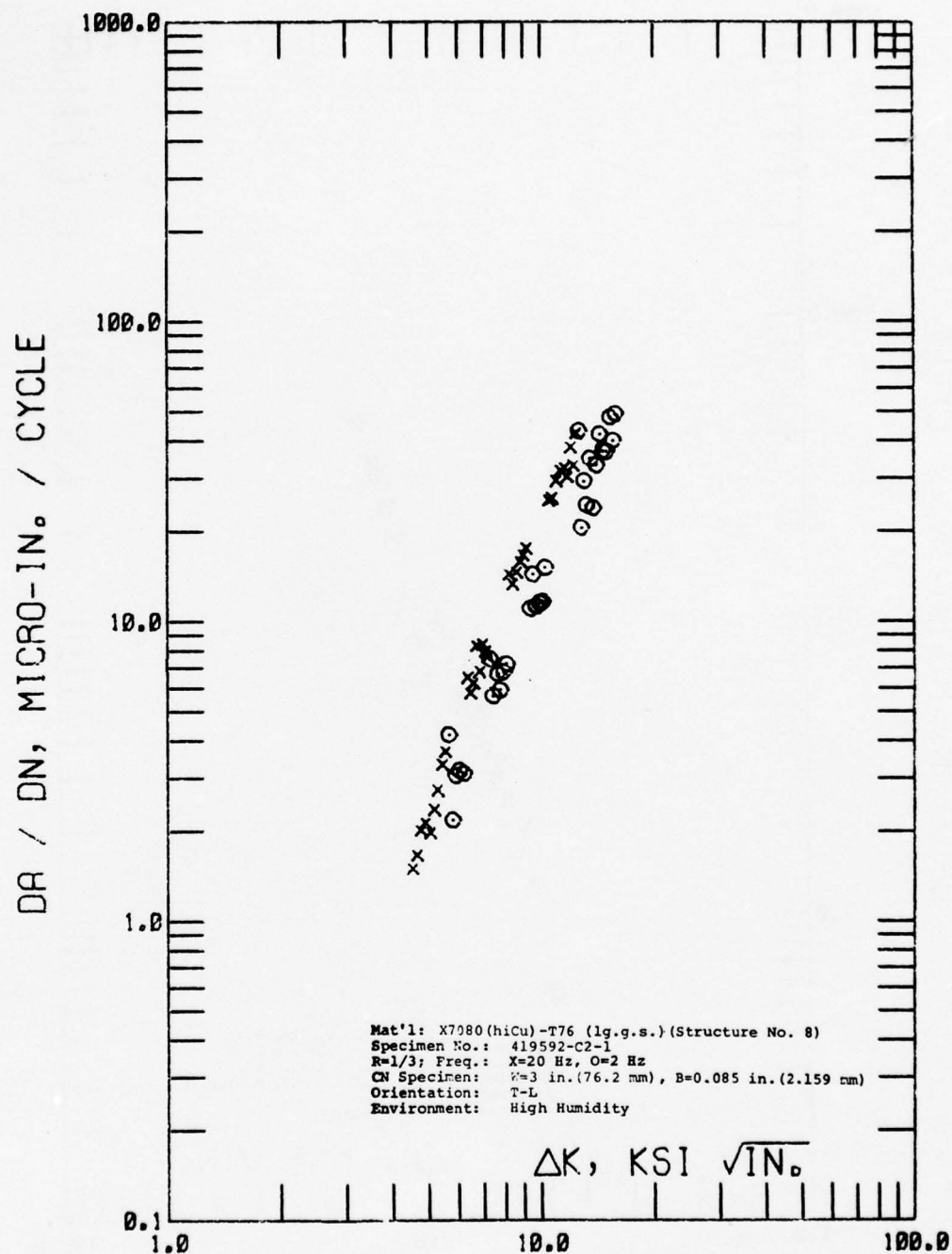


Figure C-16 Cyclic Stress Intensity Range,  $\Delta K$ , Vs. Cyclic Fatigue Crack Growth Rate,  $\Delta a / \Delta N$ , of Structure No. 8.



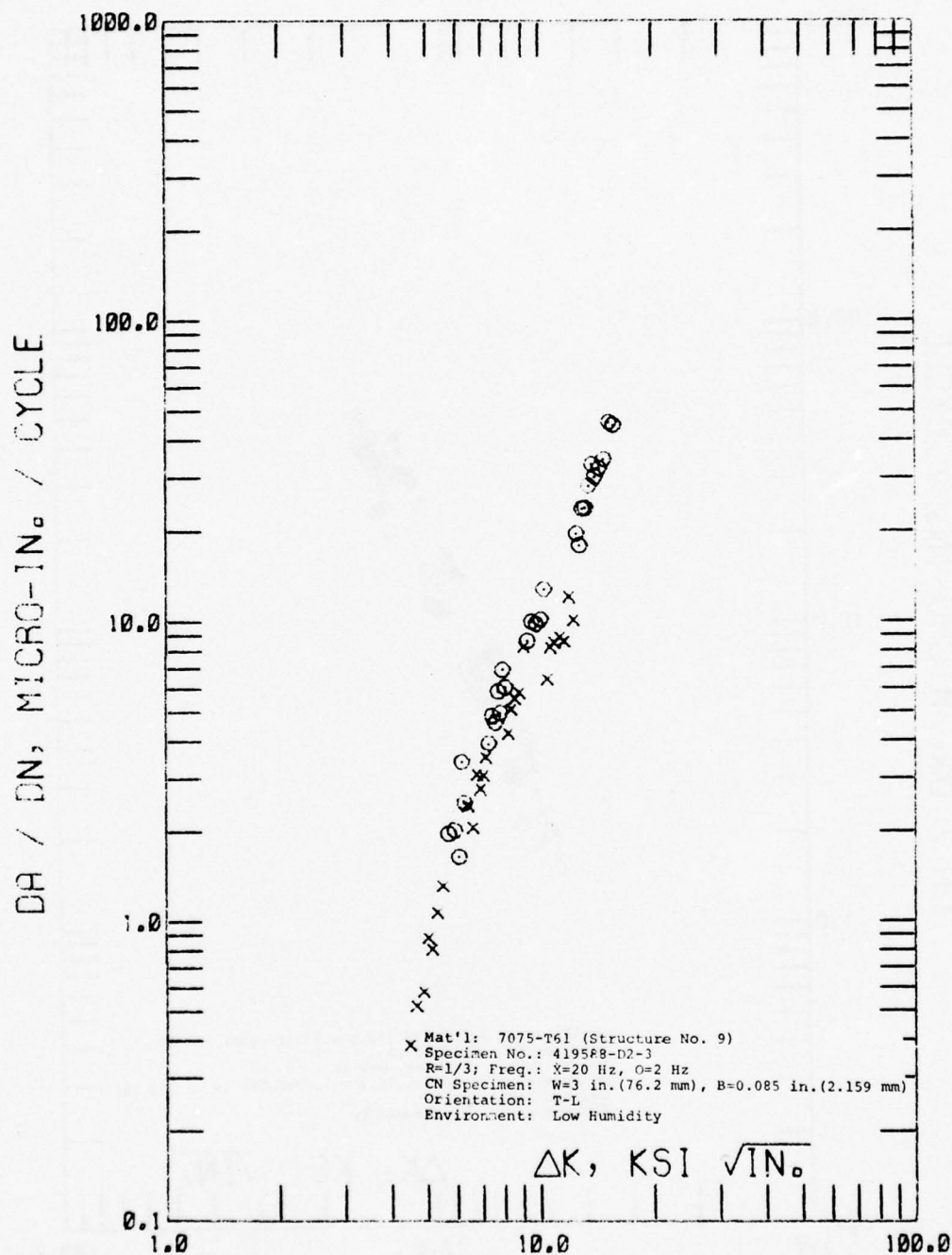


Figure C-17 Cyclic Stress Intensity Range,  $\Delta K$ , Vs. Cyclic Fatigue Crack Growth Rate,  $\Delta a / \Delta N$ , of Structure No. 9

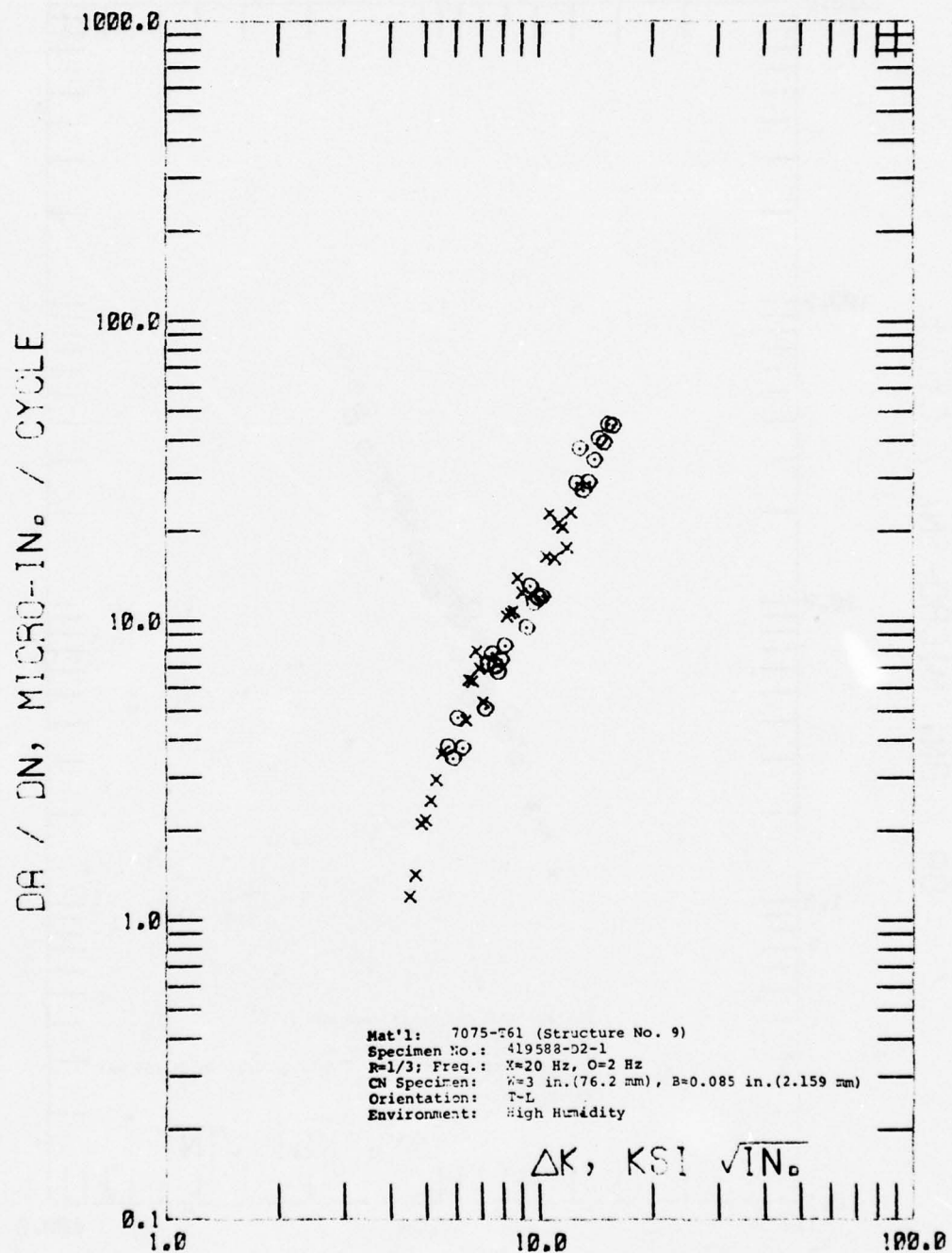


Figure C-18 Cyclic Stress Intensity Range,  $\Delta K$ , Vs. Cyclic Fatigue Crack Growth Rate,  $\Delta a / \Delta N$ , of Structure No. 9

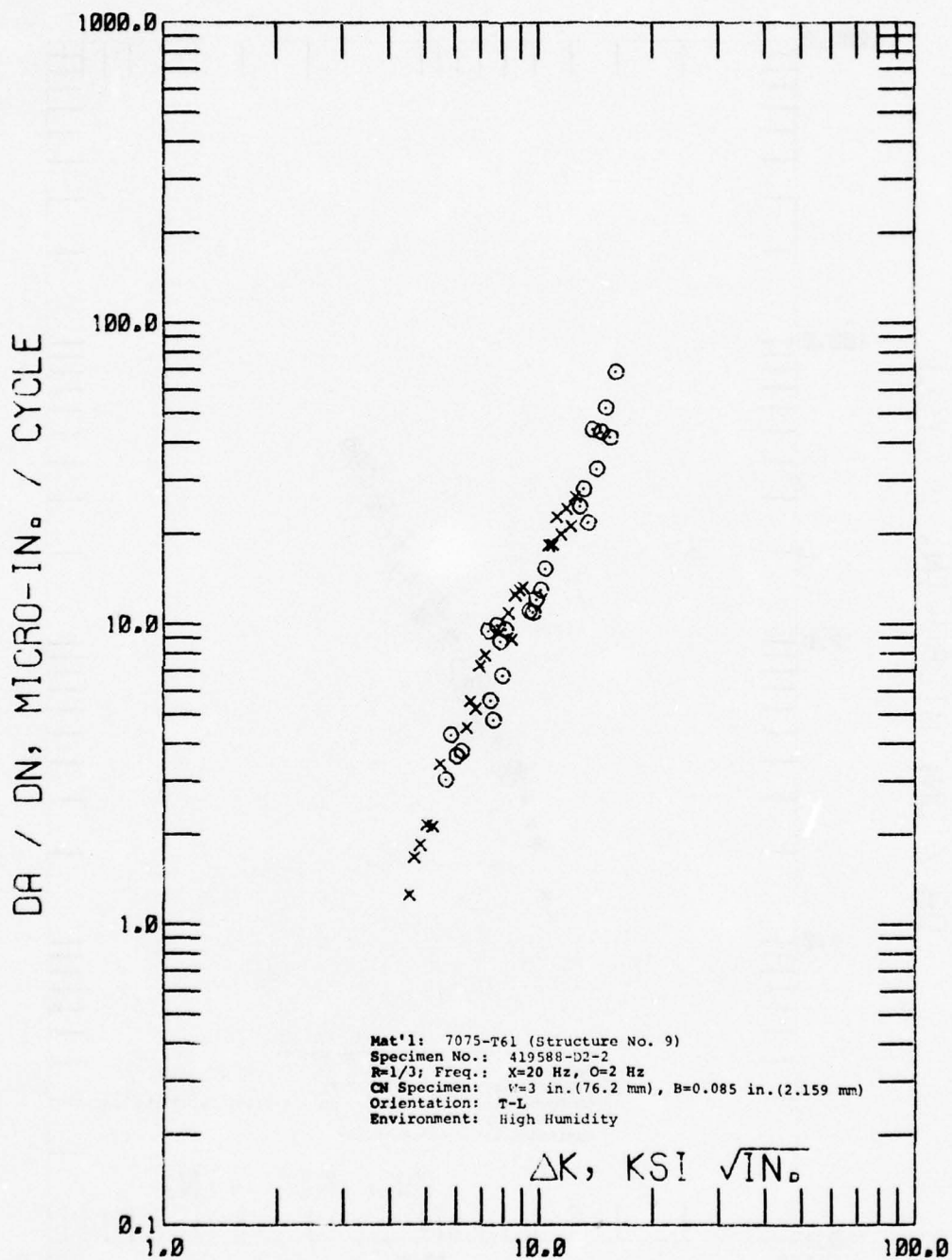


Figure C-19 Cyclic Stress Intensity Range,  $\Delta K$ , Vs. Cyclic Fatigue Crack Growth Rate  $\Delta a / \Delta N$ , of Structure No. 9

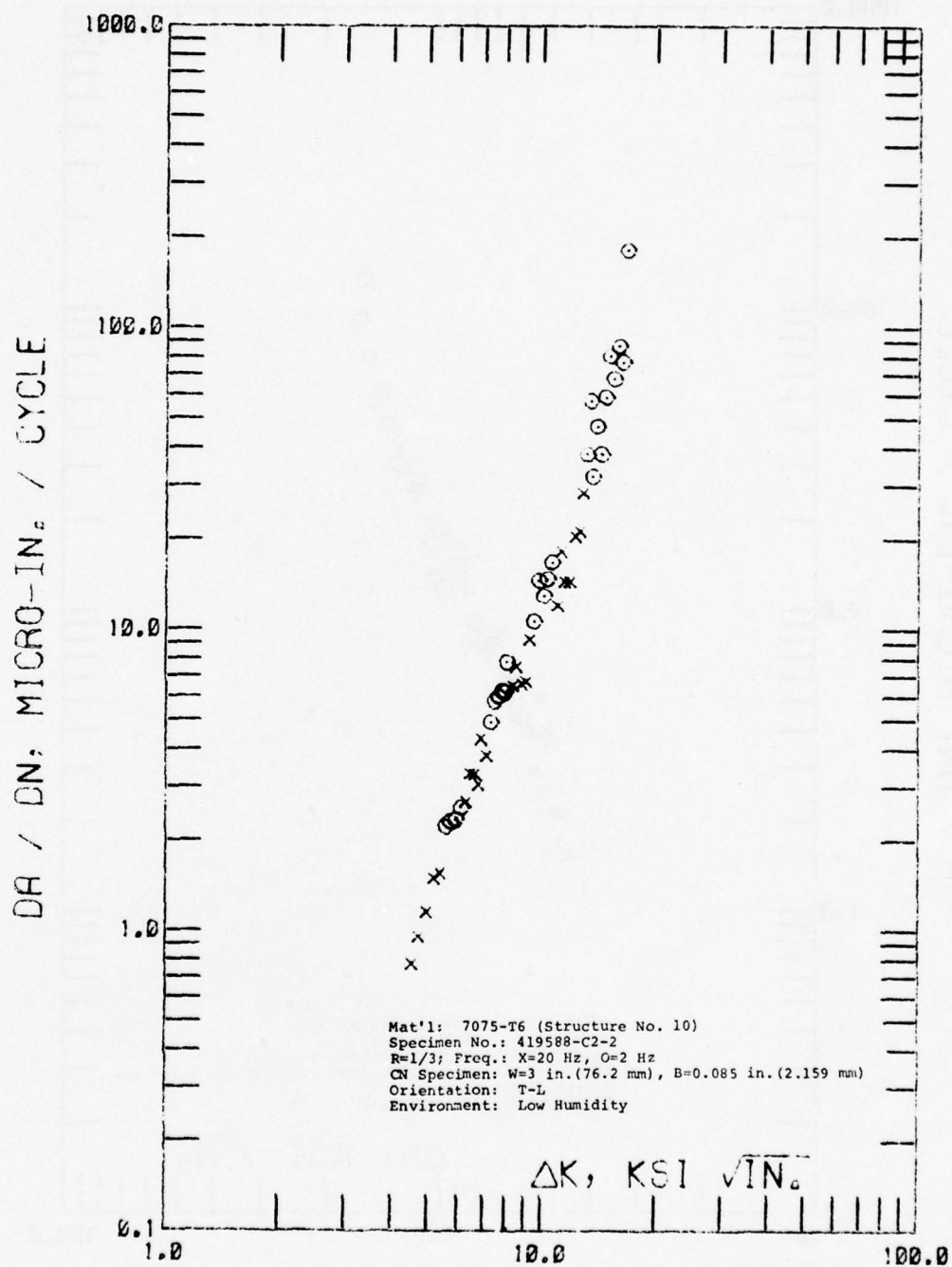


Figure C-20 Cyclic Stress Intensity Range,  $\Delta K$ , Vs. Cyclic Fatigue Crack Growth Rate,  $\Delta a / \Delta N$ , of Structure No. 10



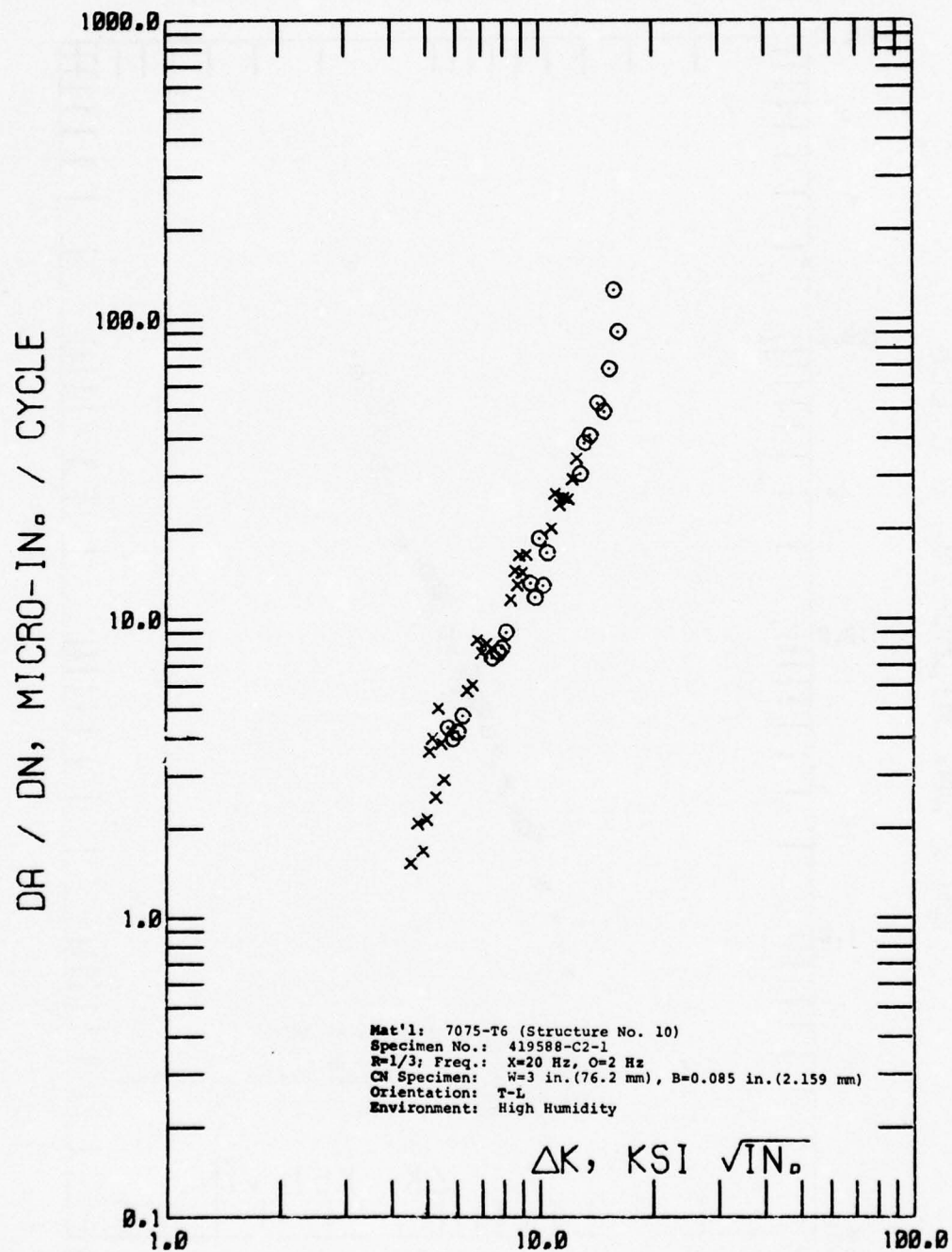


Figure C-21 Cyclic Stress Intensity Range,  $\Delta K$ , Vs. Cyclic Fatigue Crack Growth Rate,  $\Delta a / \Delta N$ , of Structure No. 10

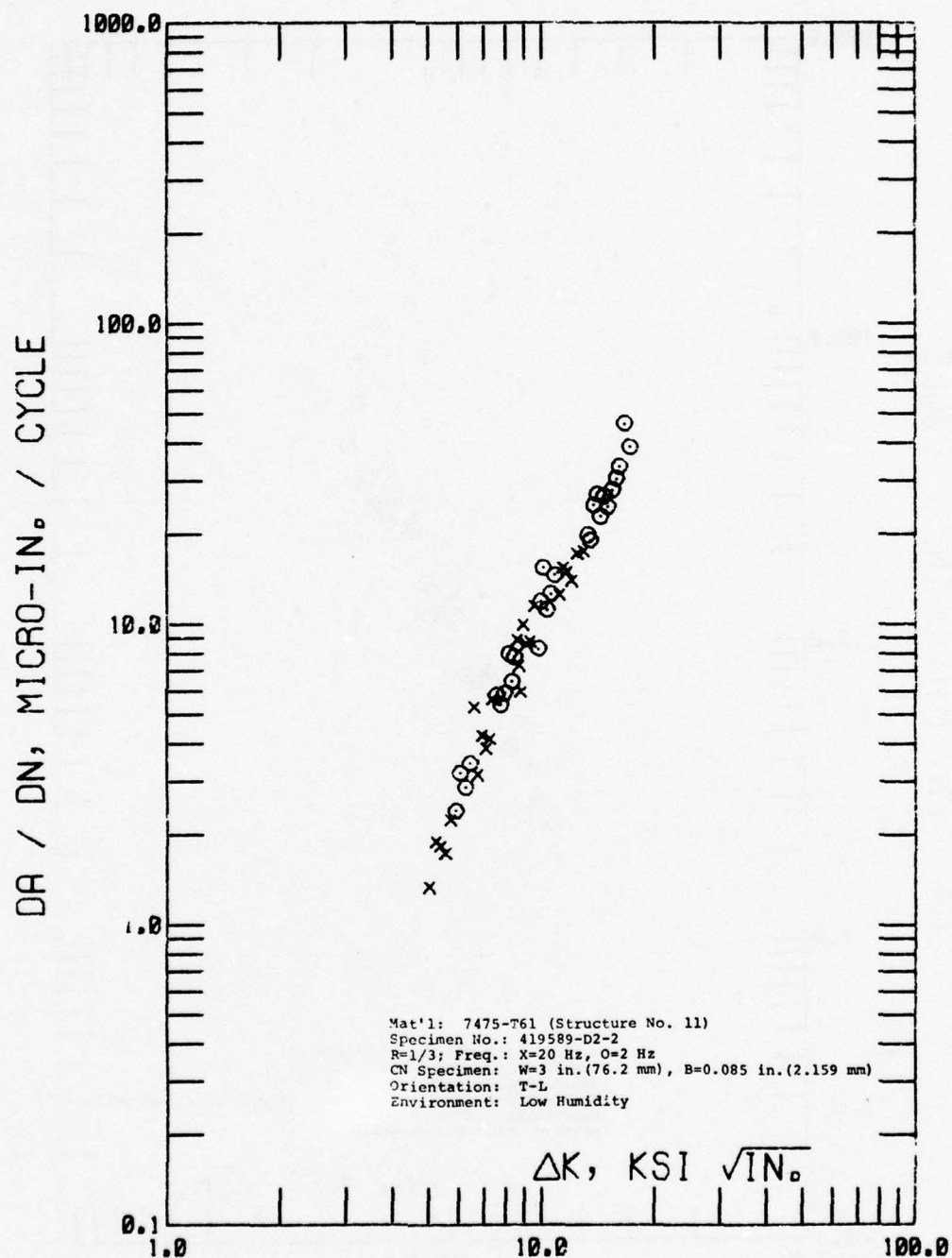


Figure C-22 Cyclic Stress Intensity Range,  $\Delta K$ , Vs. Cyclic Fatigue Crack Growth Rate,  $\Delta a / \Delta N$ , of Structure No. 11

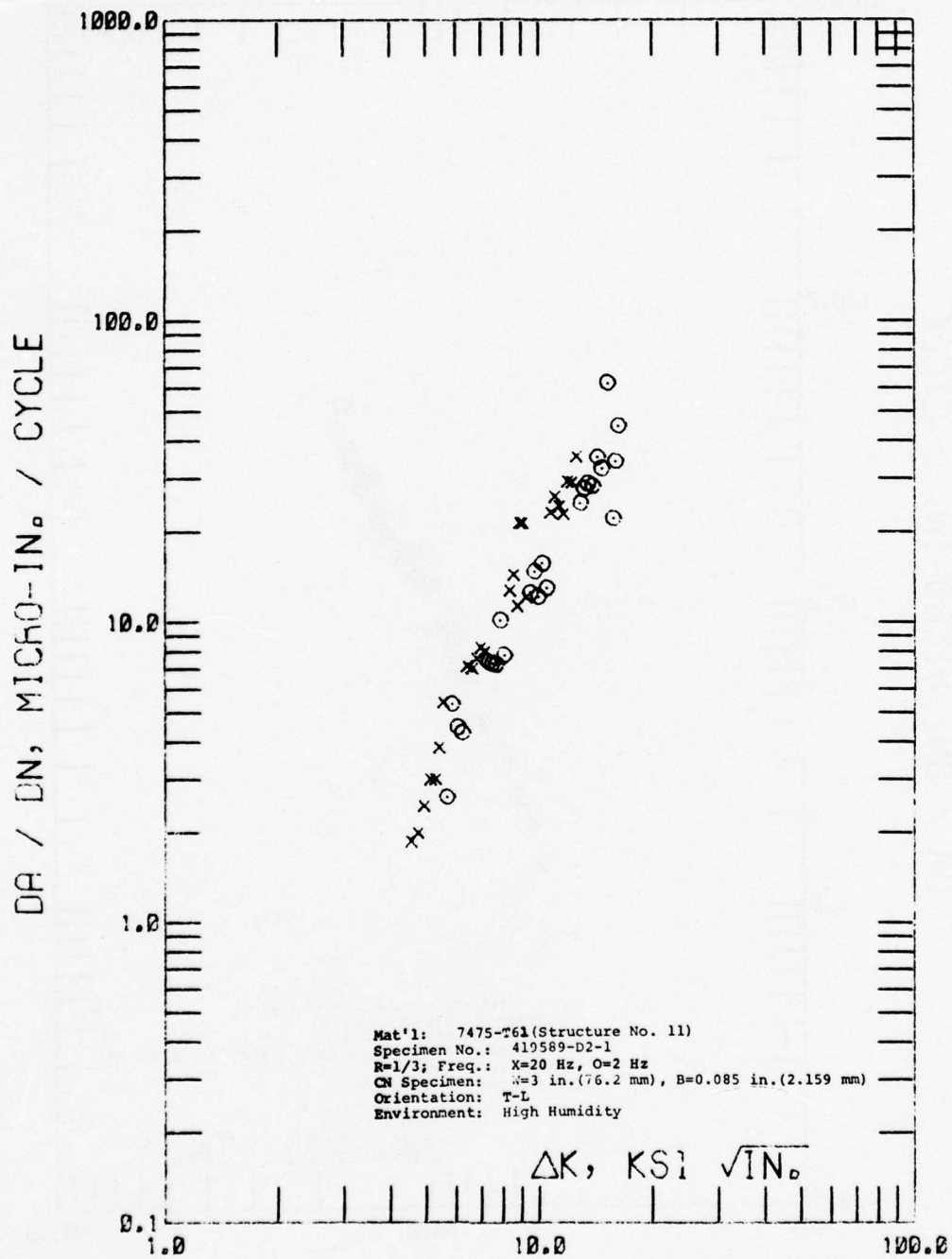


Figure C-23 Cyclic Stress Intensity Range,  $\Delta K$ , Vs. Cyclic Fatigue Crack Growth Rate  $\Delta a / \Delta N$ , of Structure No. 11

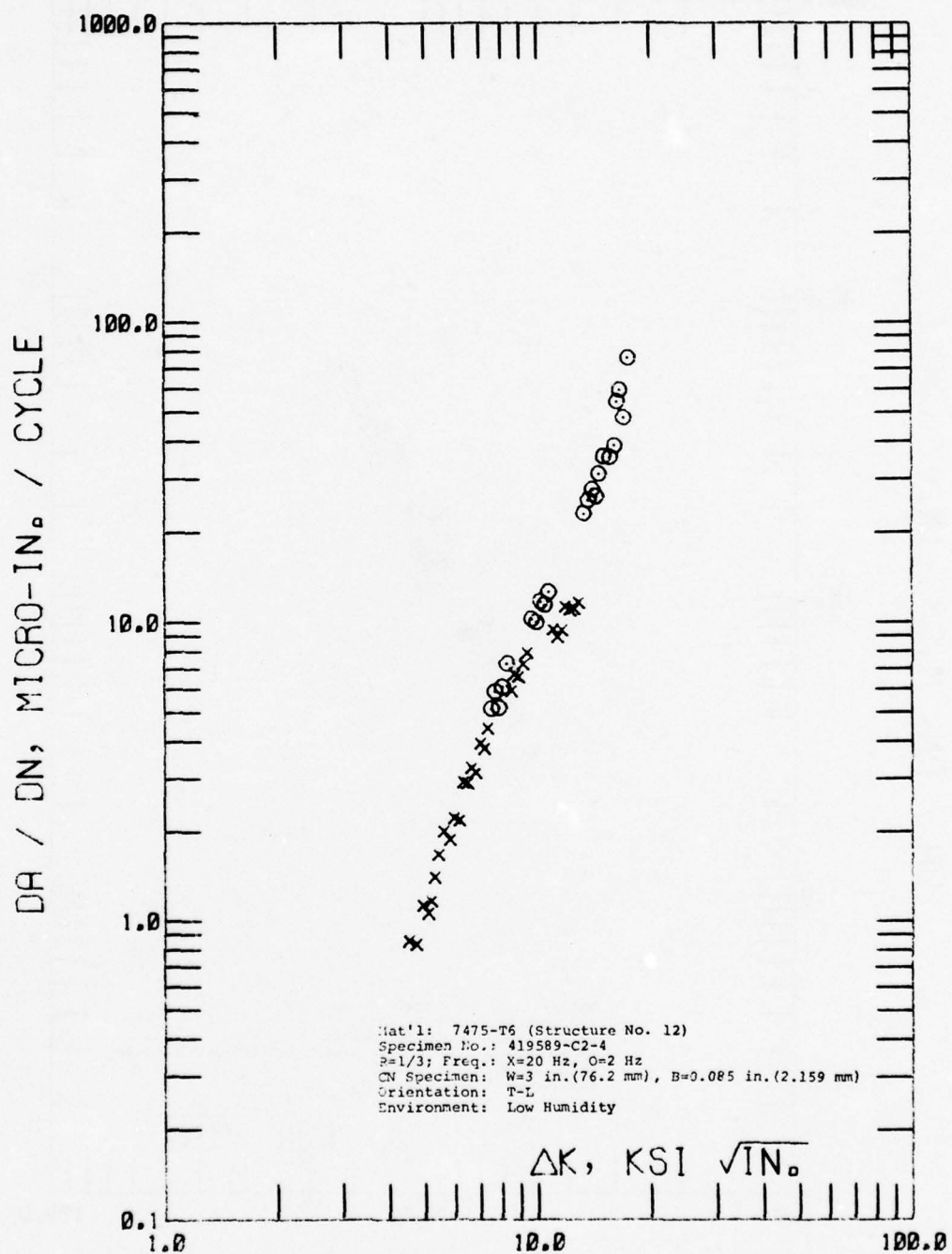


Figure C-24 Cyclic Stress Intensity Range,  $\Delta K$ , Vs. Cyclic Fatigue Crack Growth Rate,  $\Delta a/\Delta N$ , of Structure No. 12



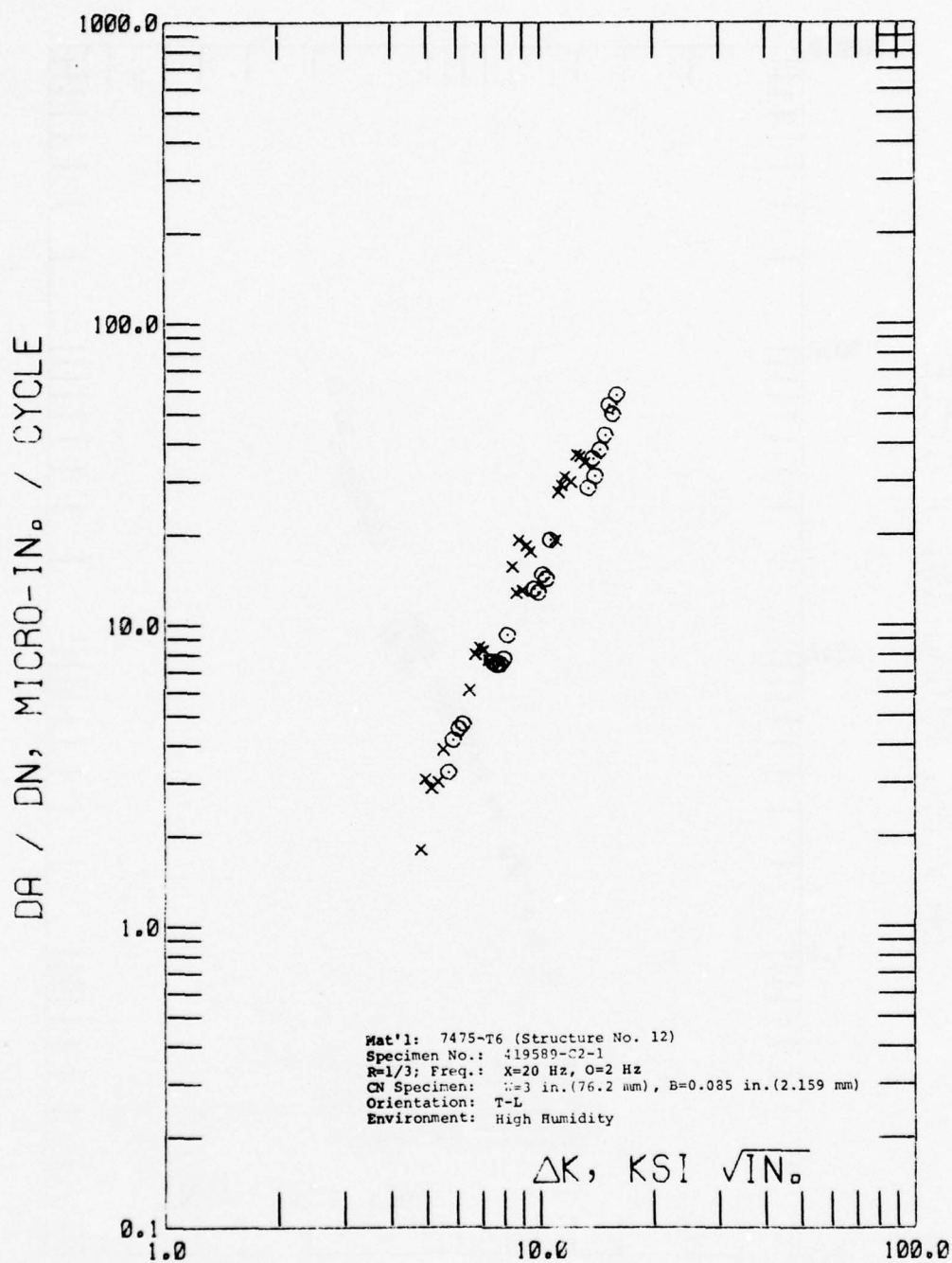


Figure C-25 Cyclic Stress Intensity Range,  $\Delta K$ , Vs. Cyclic Fatigue Crack Growth Rate,  $\Delta a / \Delta N$ , of Structure No. 12

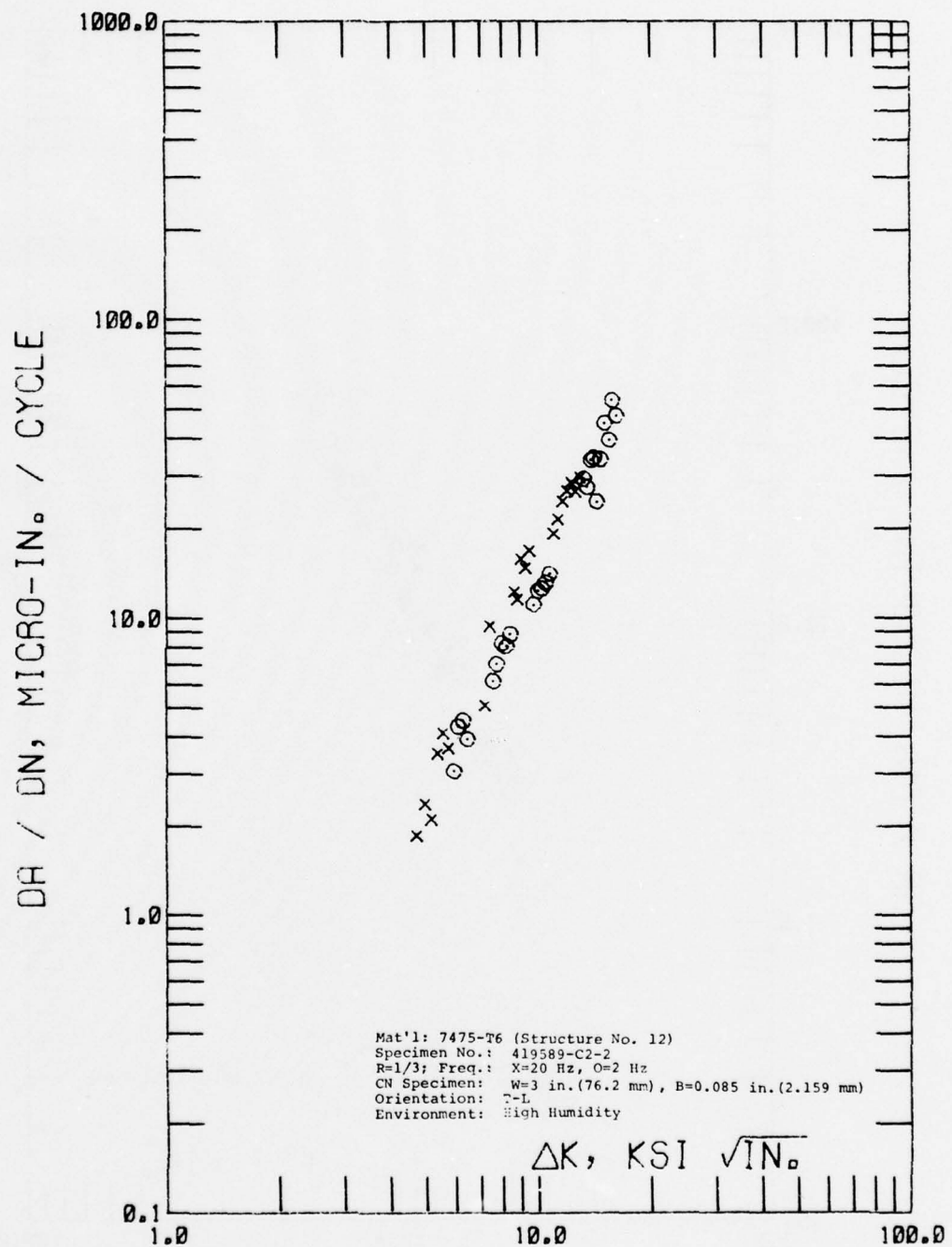


Figure C-26 Stress Intensity Range,  $\Delta K$ , Vs. Cyclic Fatigue Crack Growth Rate,  $\Delta a/\Delta N$ , of Structure No. 12

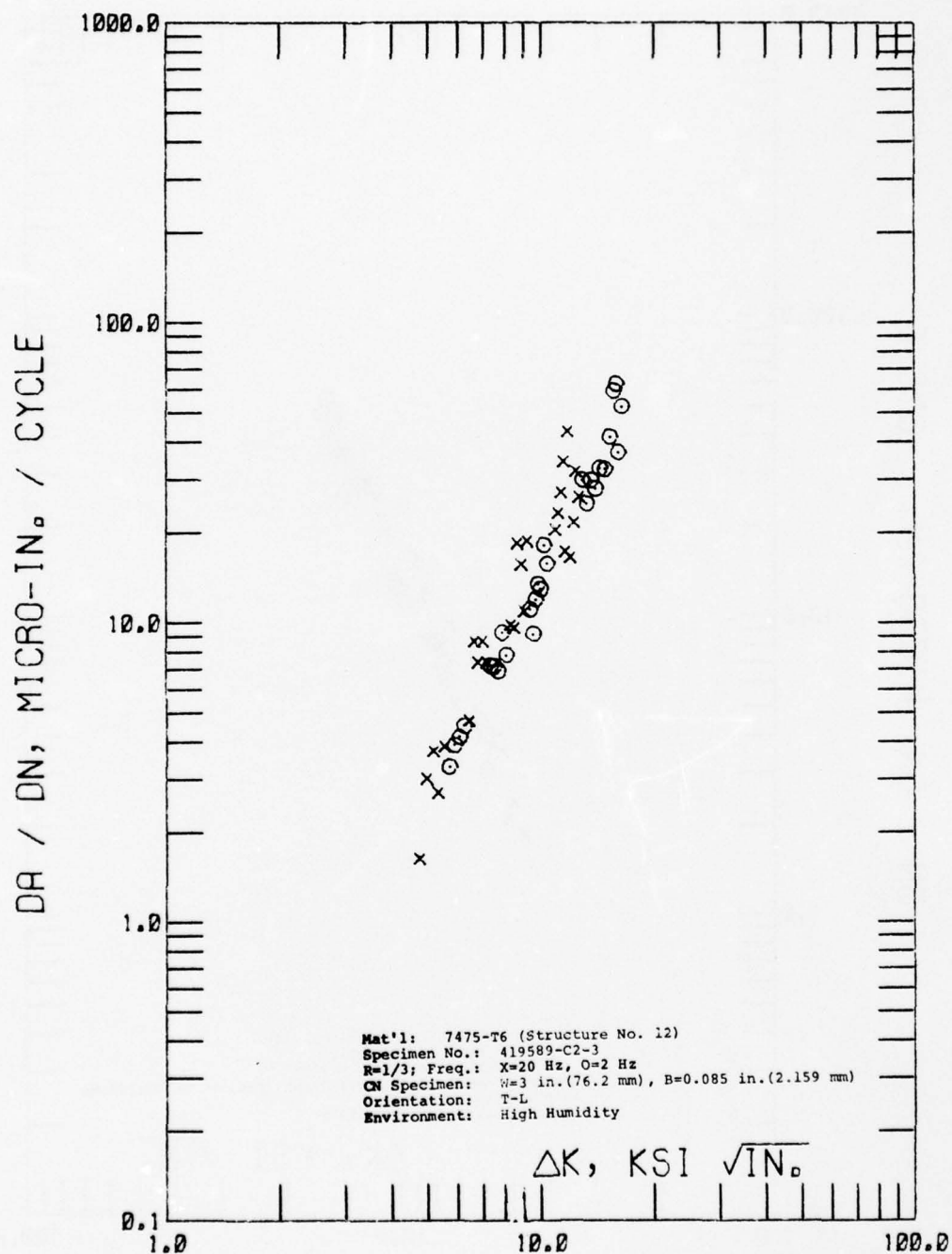


Figure C-27 Cyclic Stress Intensity Range,  $\Delta K$ , Vs. Cyclic Fatigue Crack Growth Rate,  $\Delta a / \Delta N$ , of Structure No. 12

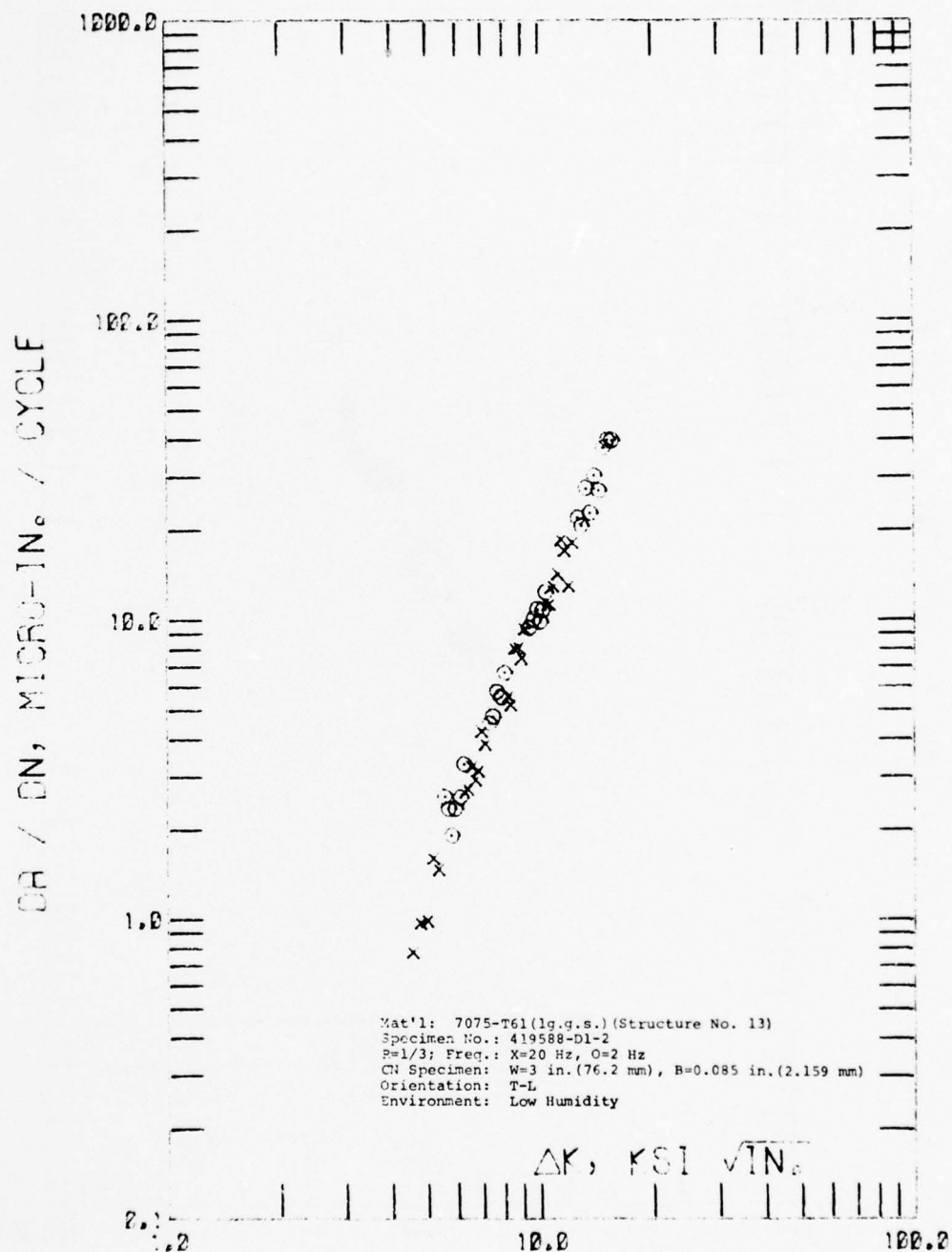


Figure C-28 Cyclic Stress Intensity Range,  $\Delta K$ , Vs. Cyclic Fatigue Crack Growth Rate,  $\Delta a / \Delta N$ , of Structure No. 13



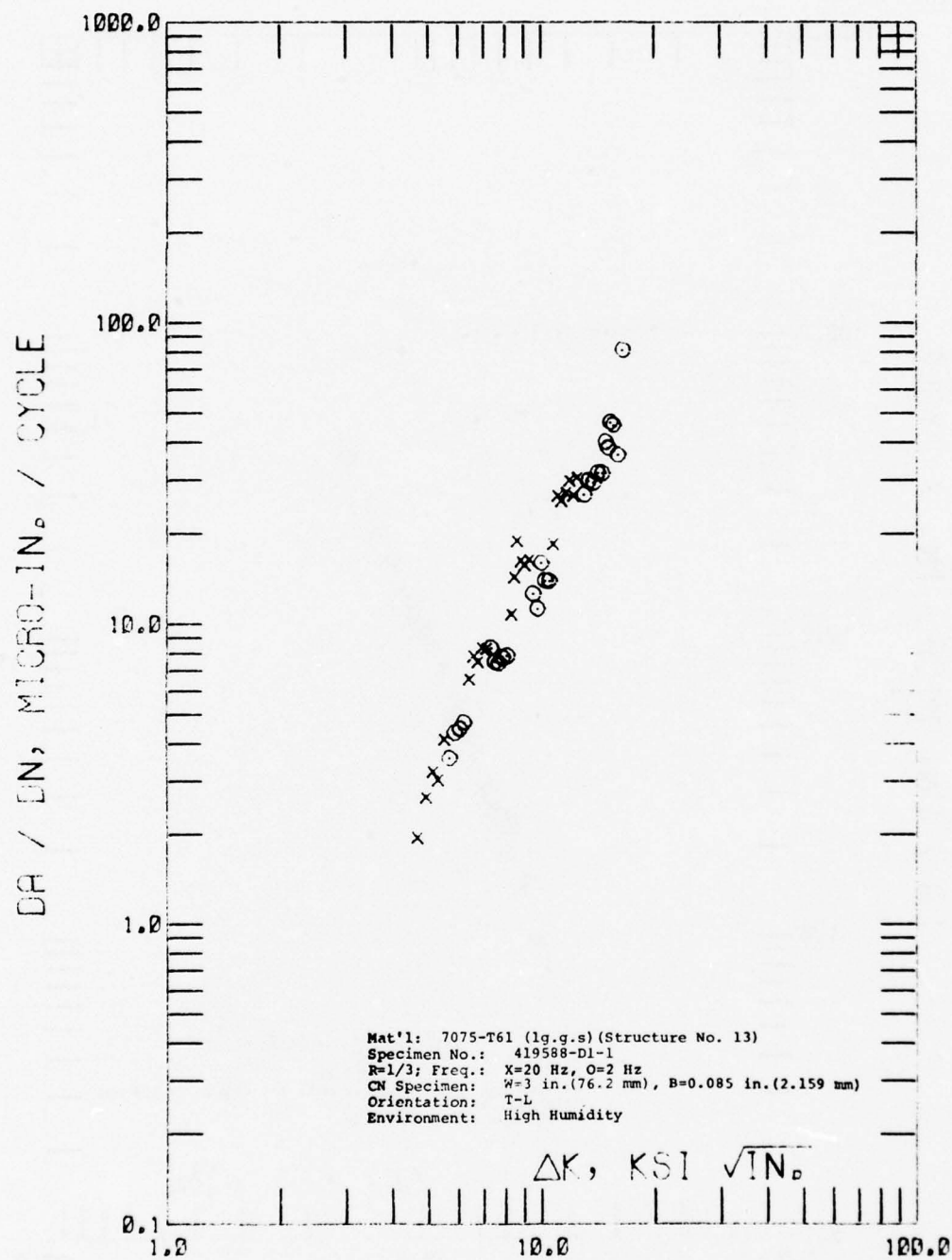


Figure C-29 Cyclic Stress Intensity Range,  $\Delta K$ , Vs. Cyclic Fatigue Crack Growth Rate,  $\Delta a / \Delta N$ , of Structure No. 13

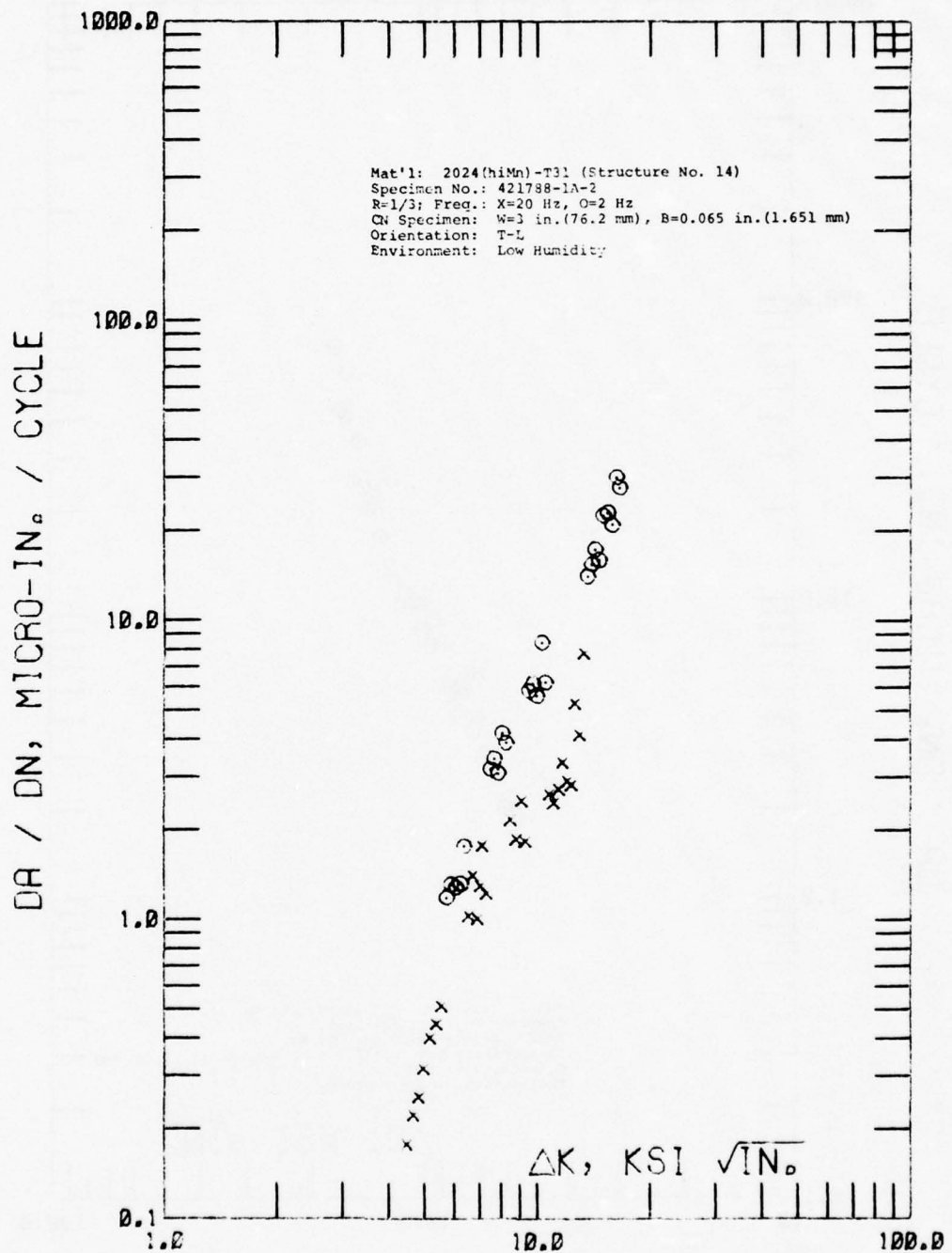


Figure C-30 Cyclic Stress Intensity Range,  $\Delta K$ , Vs. Cyclic Fatigue Crack Growth Rate  $\Delta a/\Delta N$ , of Structure No. 14

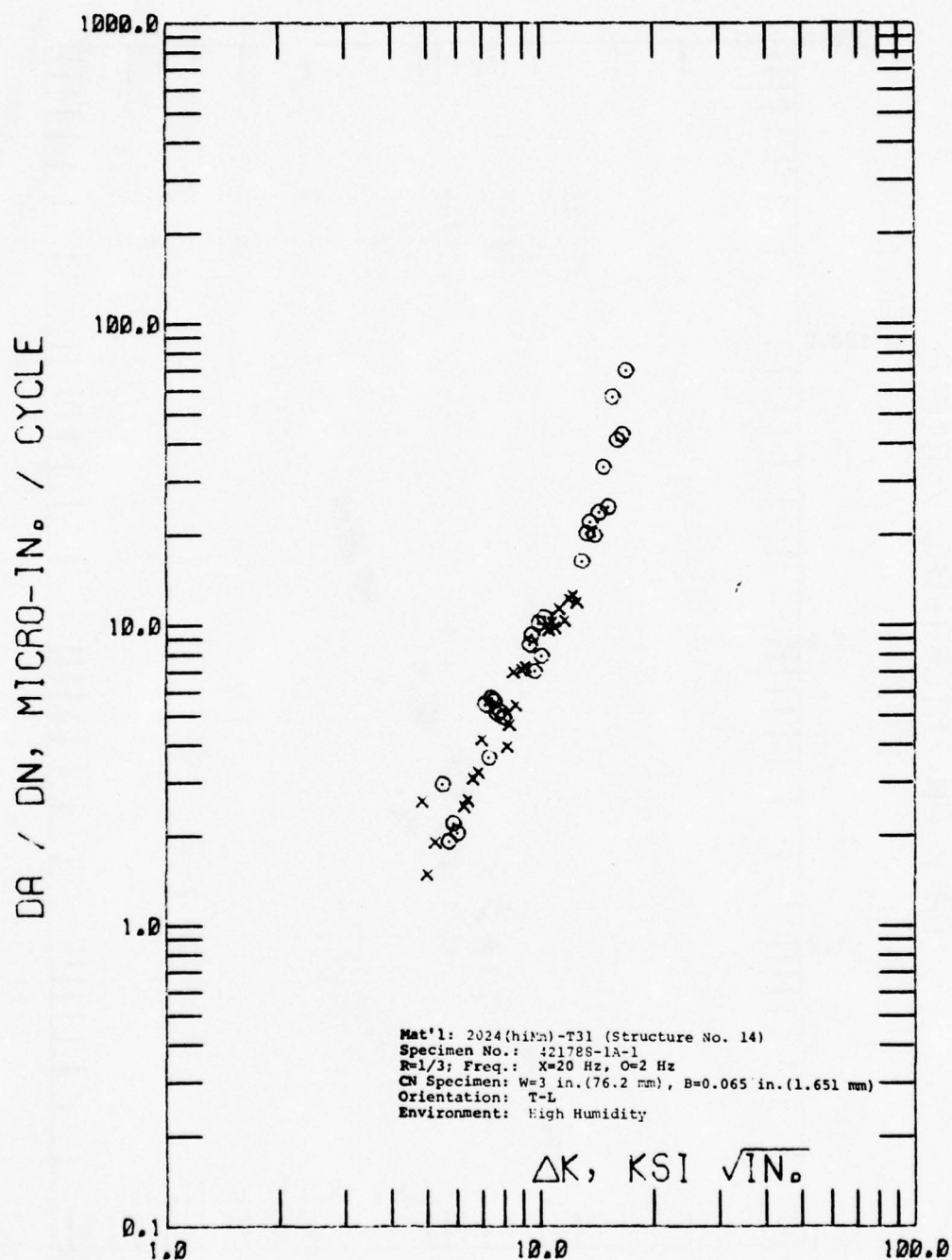


Figure C-31 Cyclic Stress Intensity Range,  $\Delta K$ , Vs. Cyclic Fatigue Crack Growth Rate,  $\Delta a / \Delta N$ , of Structure No. 14

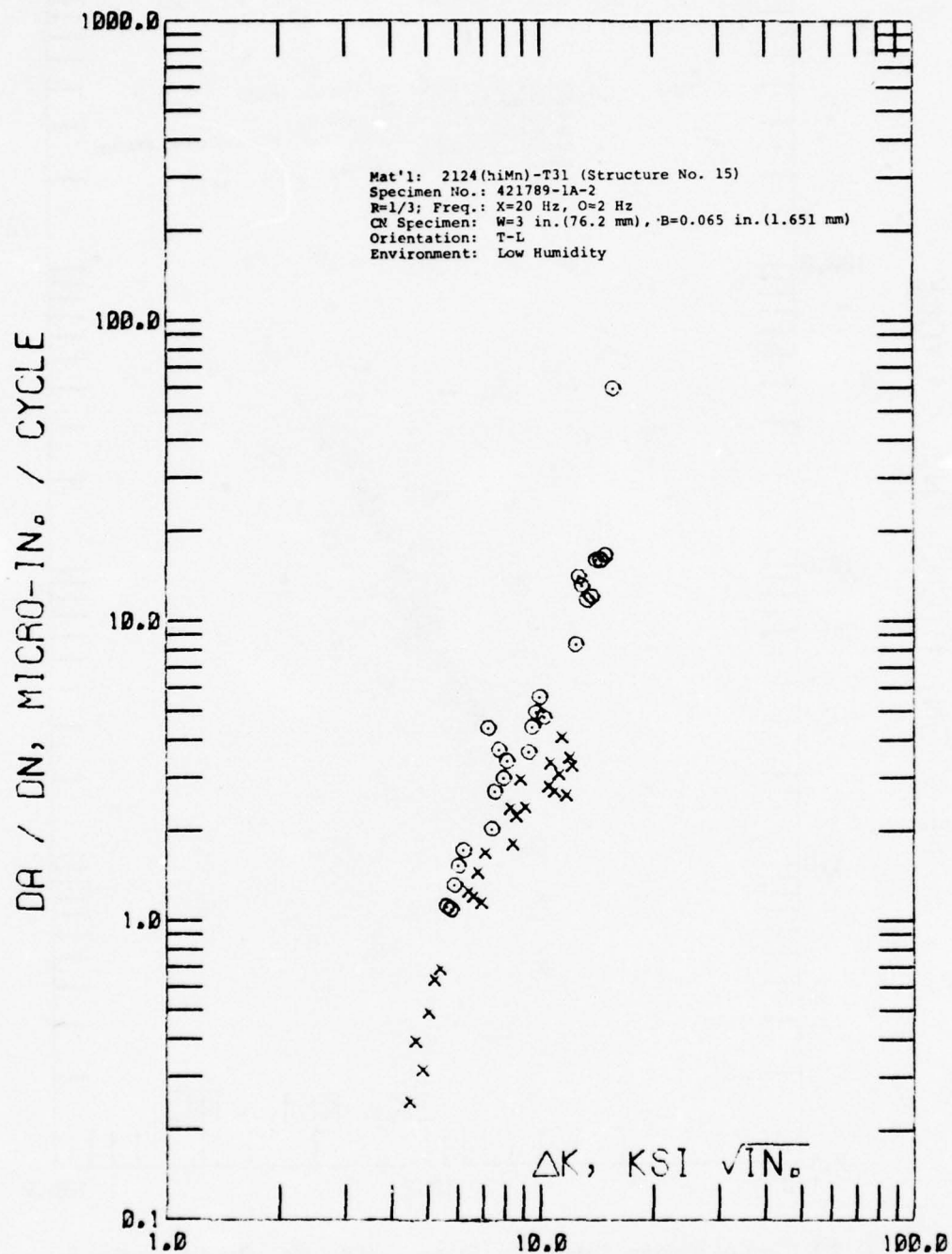


Figure C-32 Cyclic Stress Intensity Range,  $\Delta K$ , Vs. Cyclic Fatigue Crack Growth Rate,  $\Delta a / \Delta N$ , of Structure No. 15



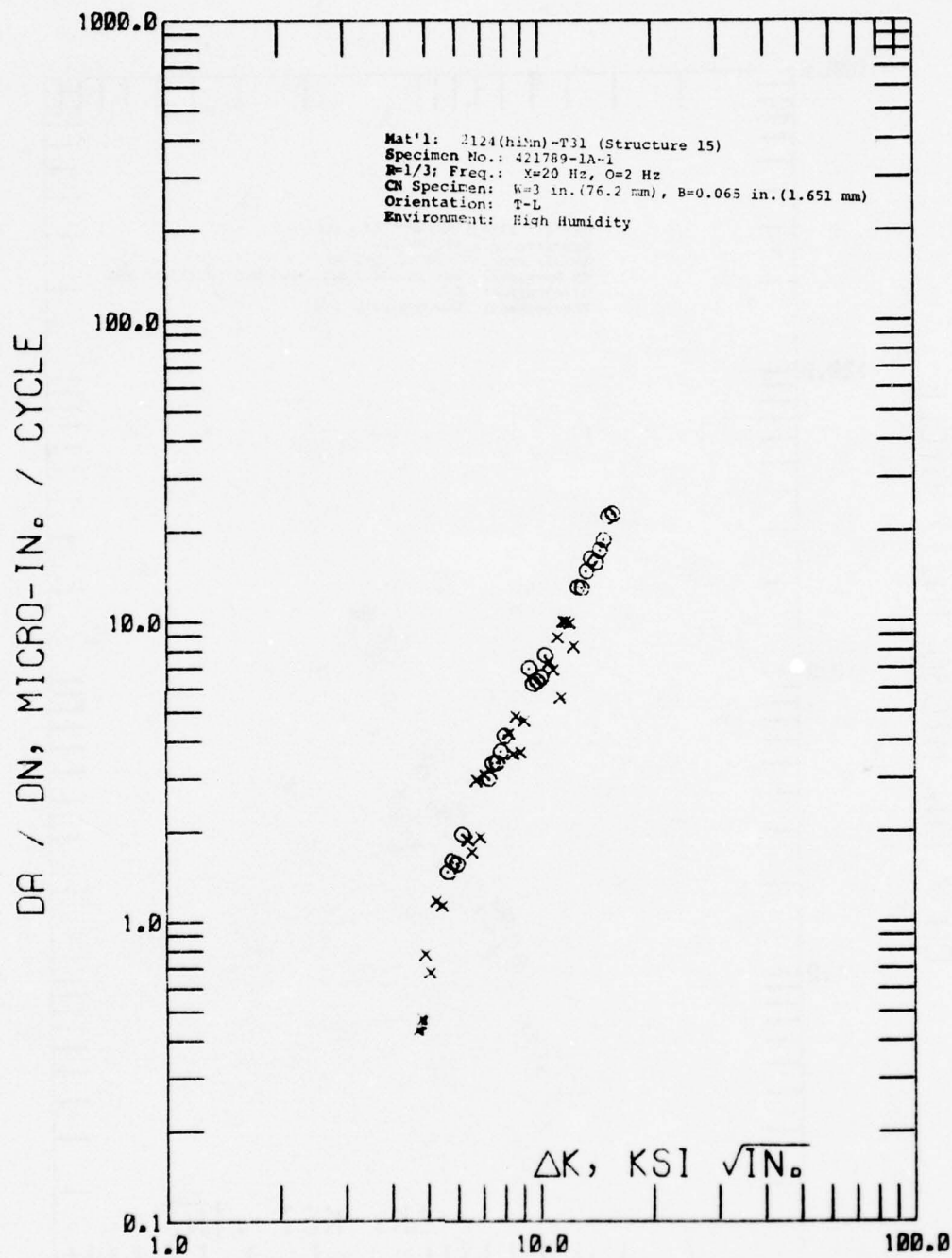


Figure C-33 Cyclic Stress Intensity Range,  $\Delta K$ , Vs. Cyclic Fatigue Crack Growth Rate,  $\Delta a / \Delta N$ , of Structure No. 15

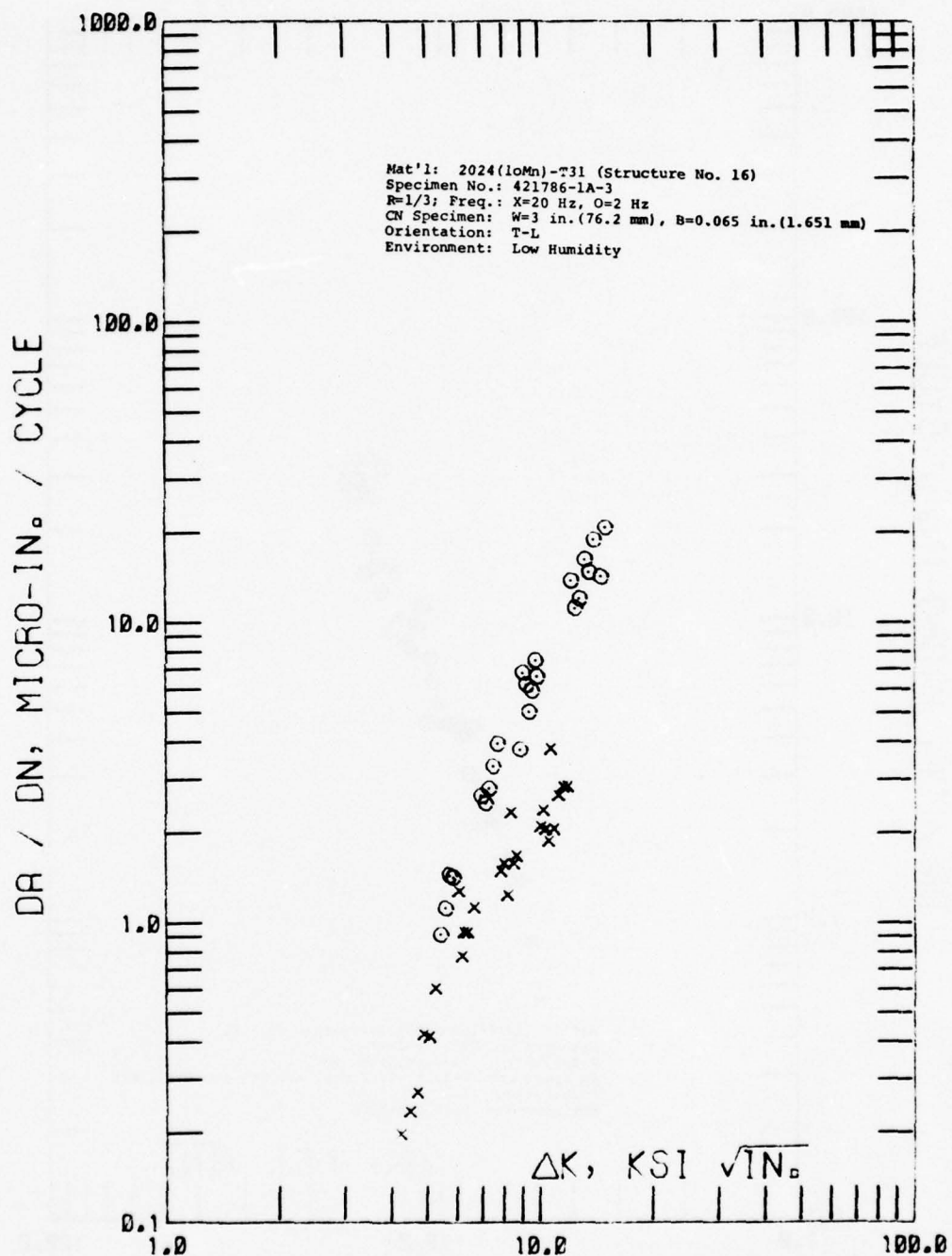


Figure C-34 Cyclic Stress Intensity Range,  $\Delta K$ , Vs. Cyclic Fatigue Crack Growth Rate,  $\Delta a / \Delta N$ , of Structure No. 16

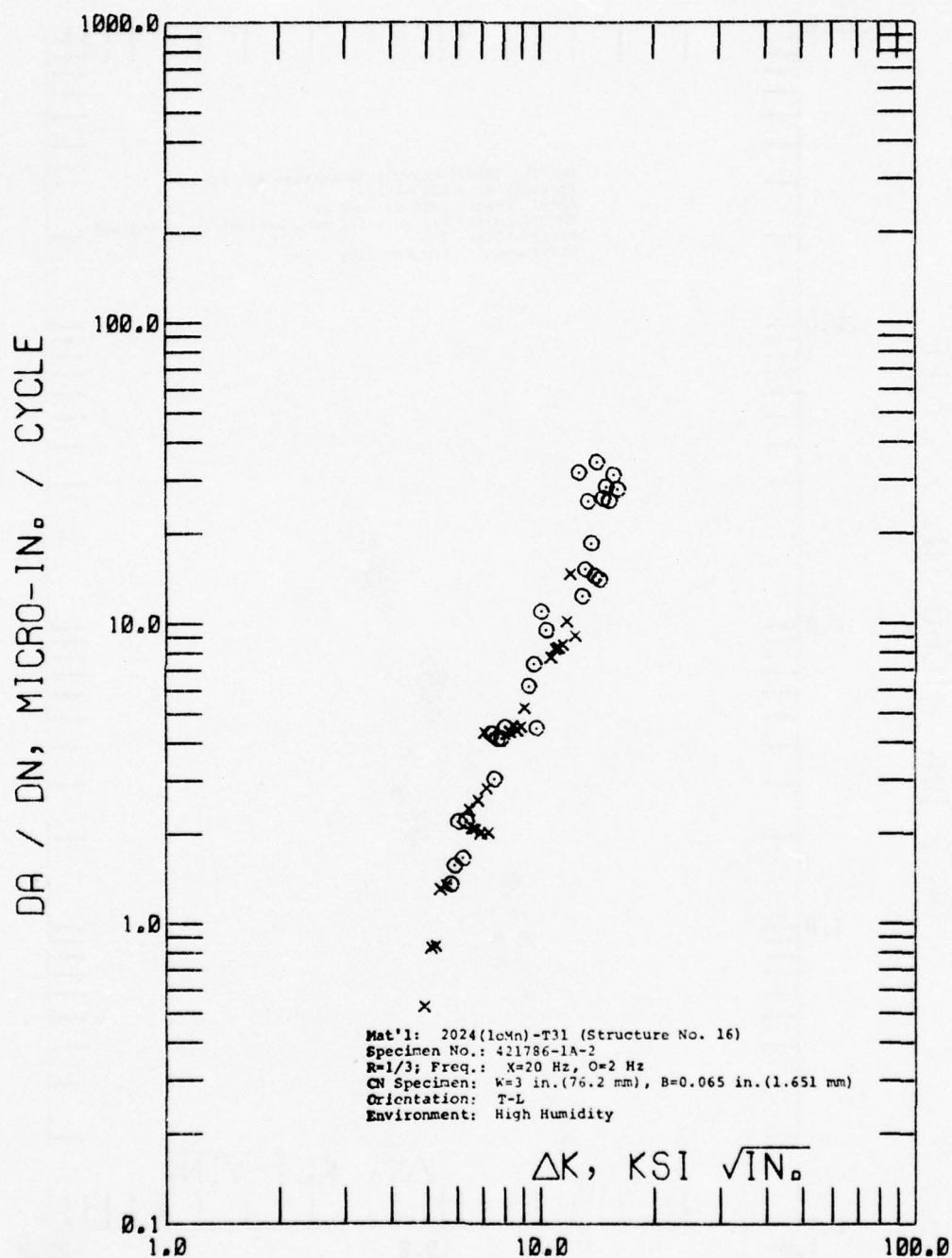


Figure C-35 Cyclic Stress Intensity Range,  $\Delta K$ , Vs. Cyclic Fatigue Crack Growth Rate,  $\Delta a / \Delta N$ , of Structure No. 16

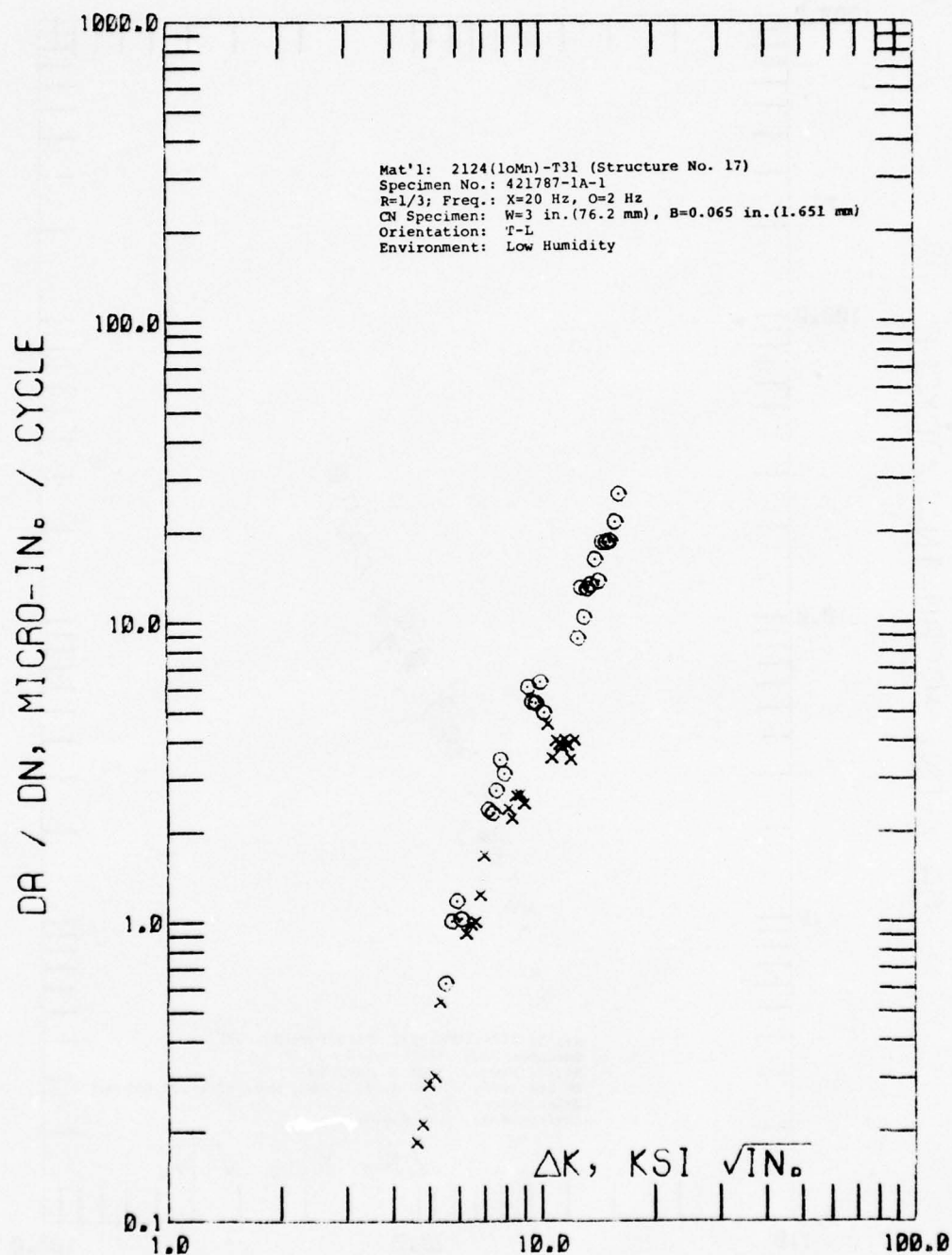


Figure C-36 Cyclic Stress Intensity Range,  $\Delta K$ , Vs. Cyclic Fatigue Crack Growth Rate,  $\Delta a/\Delta N$ , of Structure No. 17



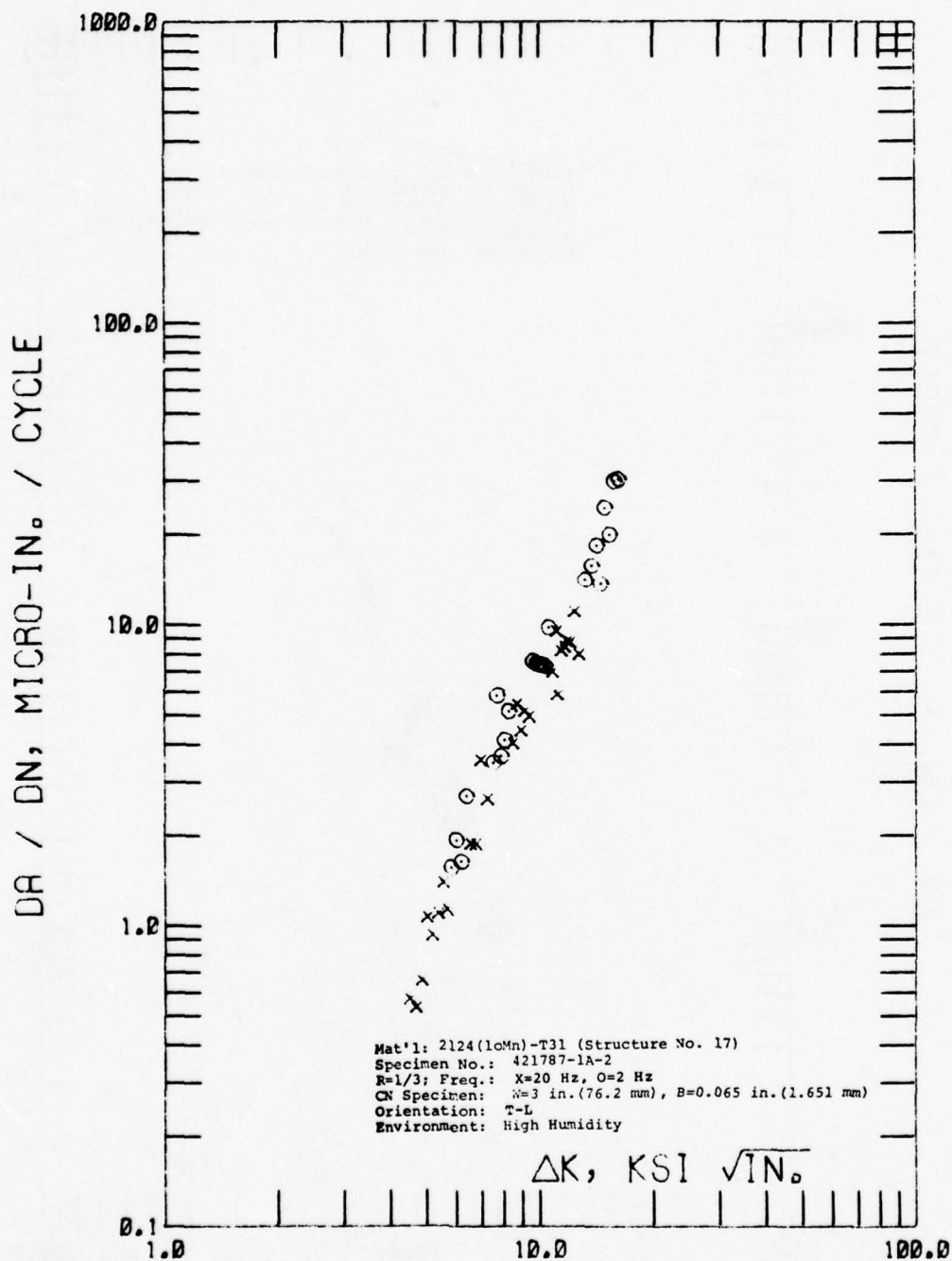


Figure C-37 Cyclic Stress Intensity Range,  $\Delta K$ , Vs. Cyclic Fatigue Crack Growth Rate,  $\Delta a / \Delta N$ , of Structure No. 17

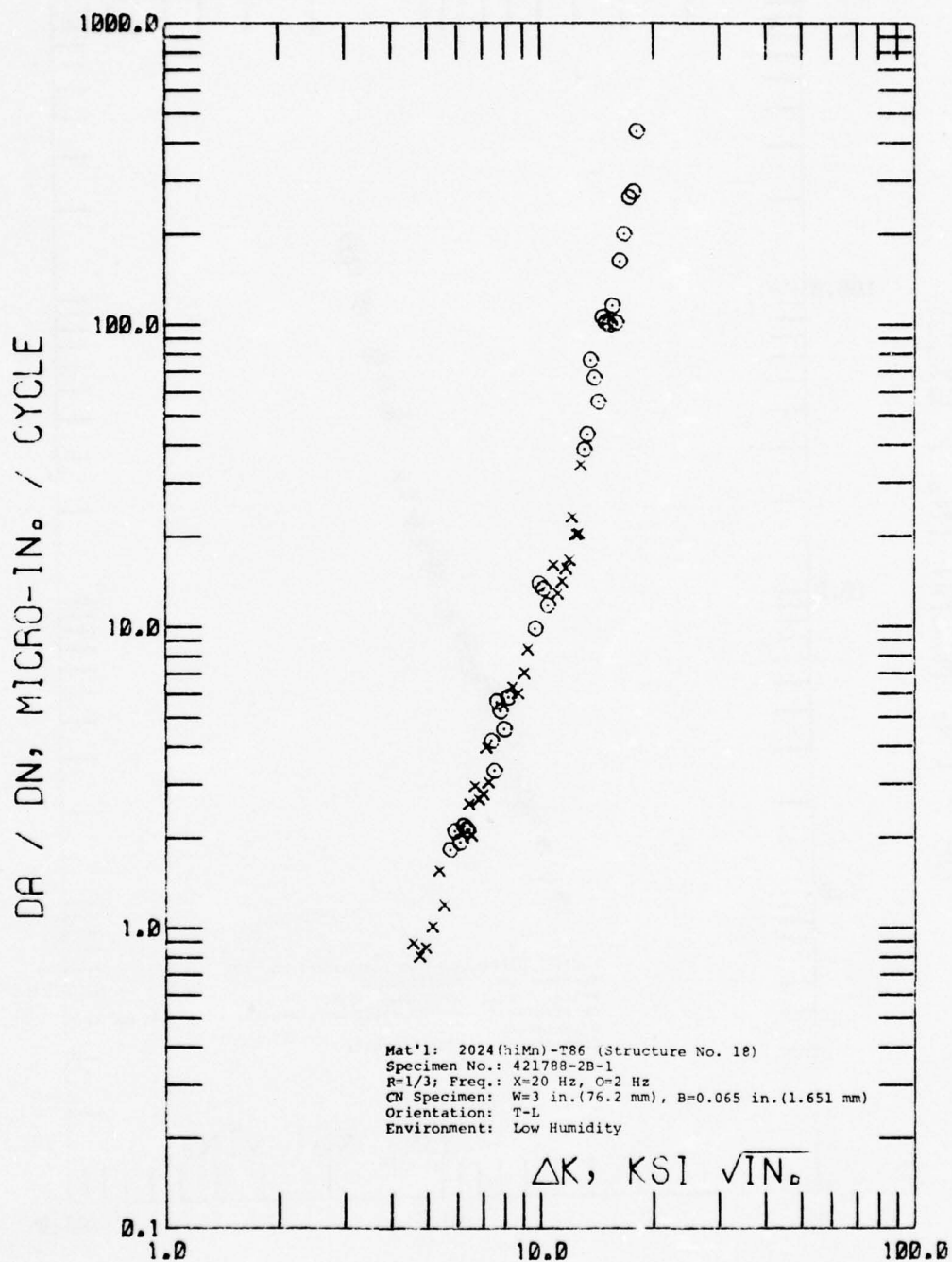


Figure C-38 Cyclic Stress Intensity Range,  $\Delta K$ , Vs. Cyclic Fatigue Crack Growth Rate,  $\Delta a / \Delta N$ , of Structure No. 18

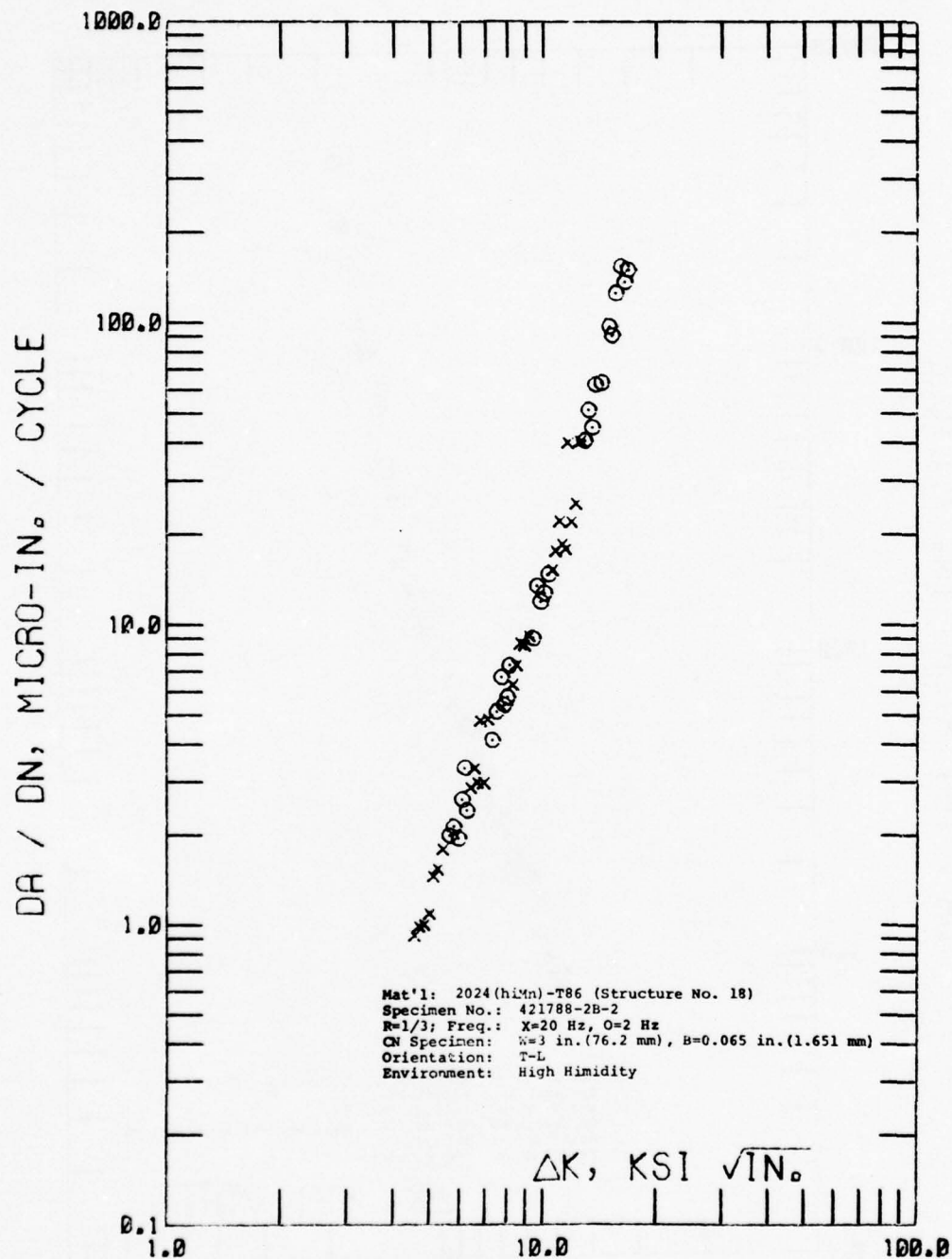


Figure C-39 Cyclic Stress Intensity Range,  $\Delta K$ , Vs. Cyclic Fatigue Crack Growth Rate,  $\Delta a / \Delta N$ , of Structure No. 18.

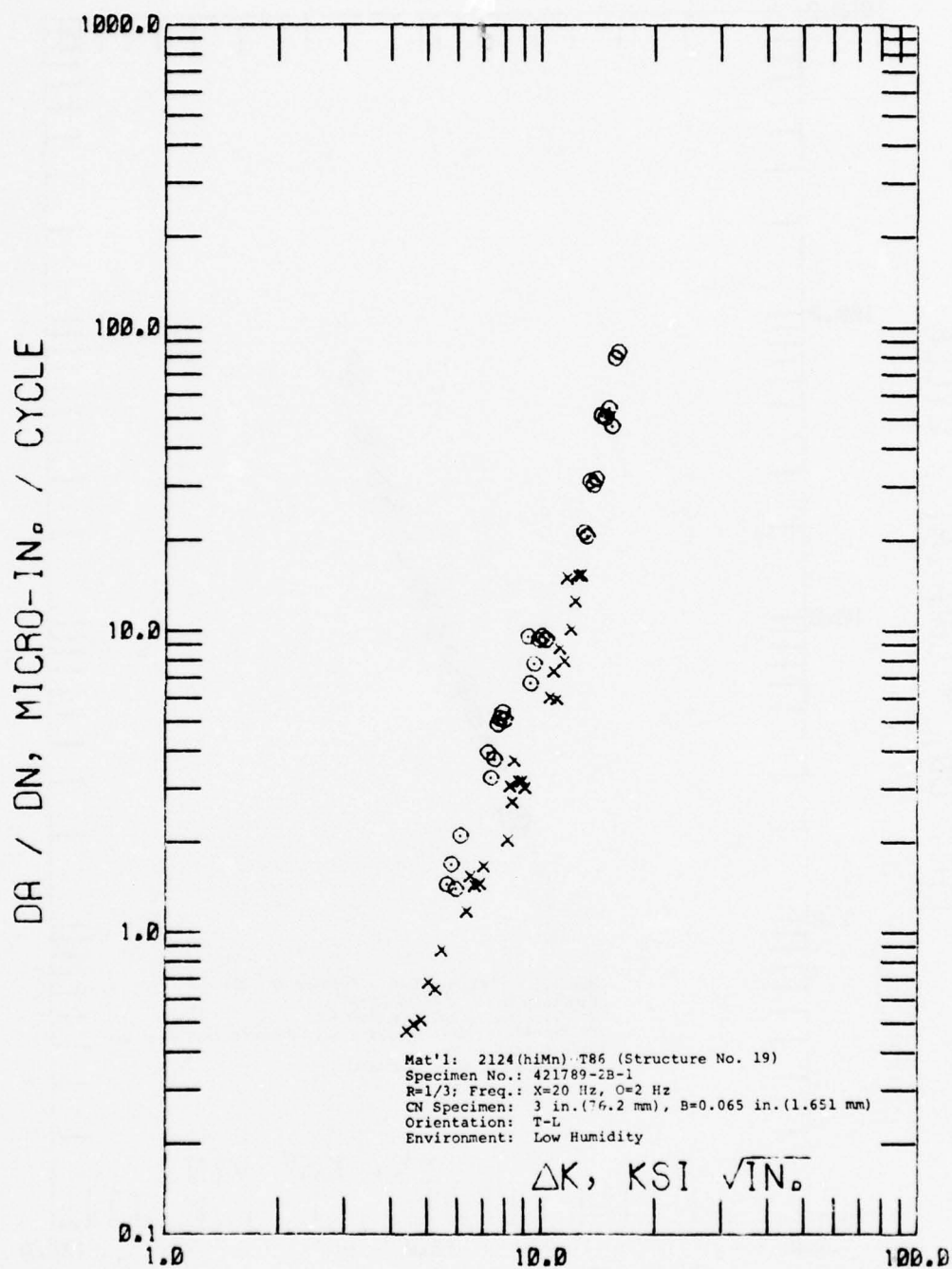


Figure C-40 Cyclic Stress Intensity Range,  $\Delta K$ , Vs. Cyclic Fatigue Crack Growth Rate,  $\Delta a / \Delta N$ , of Structure No. 19



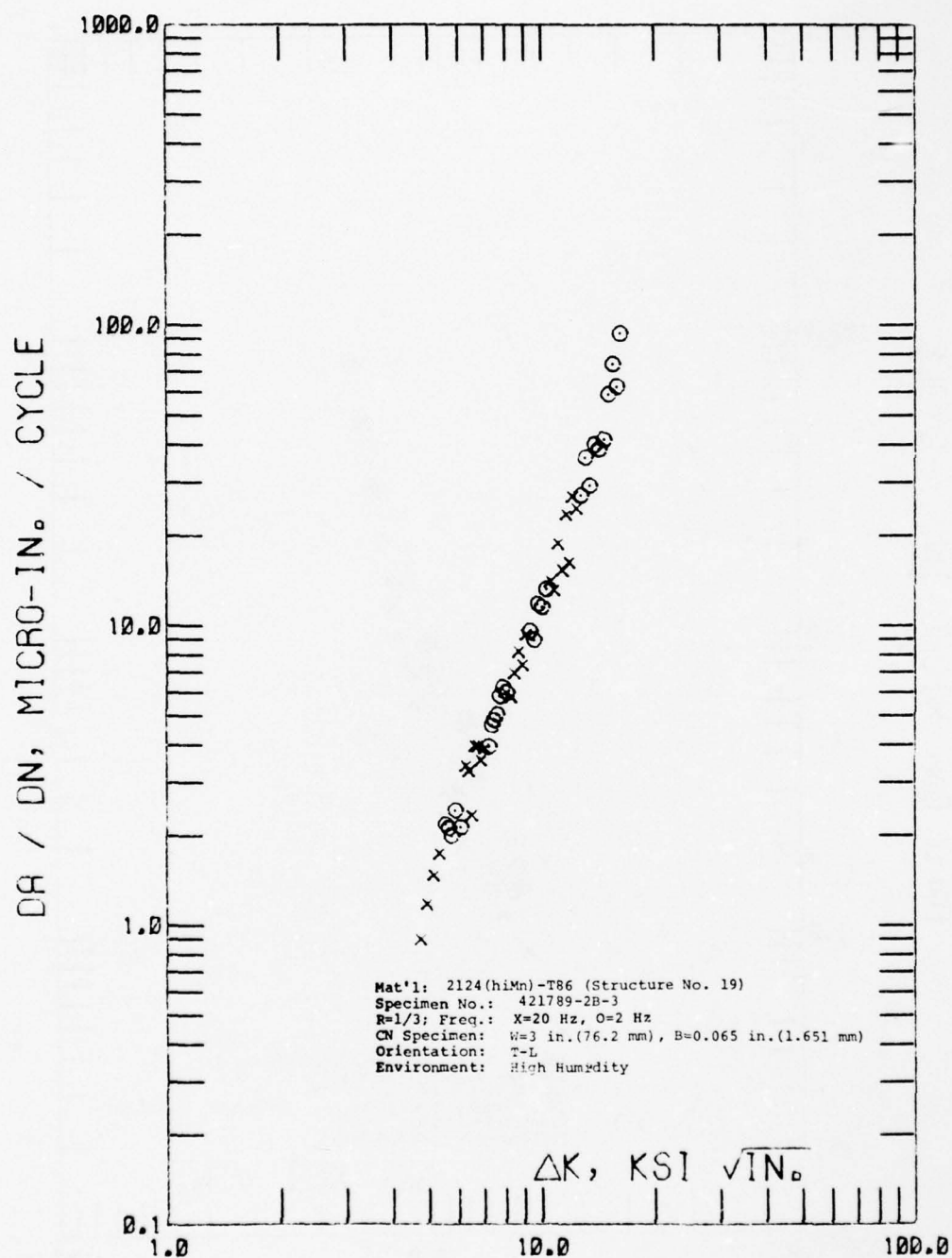


Figure C-41 Cyclic Stress Intensity Range,  $\Delta K$ , Vs. Cyclic Fatigue Crack Growth Rate,  $\Delta a / \Delta N$ , of Structure No. 19

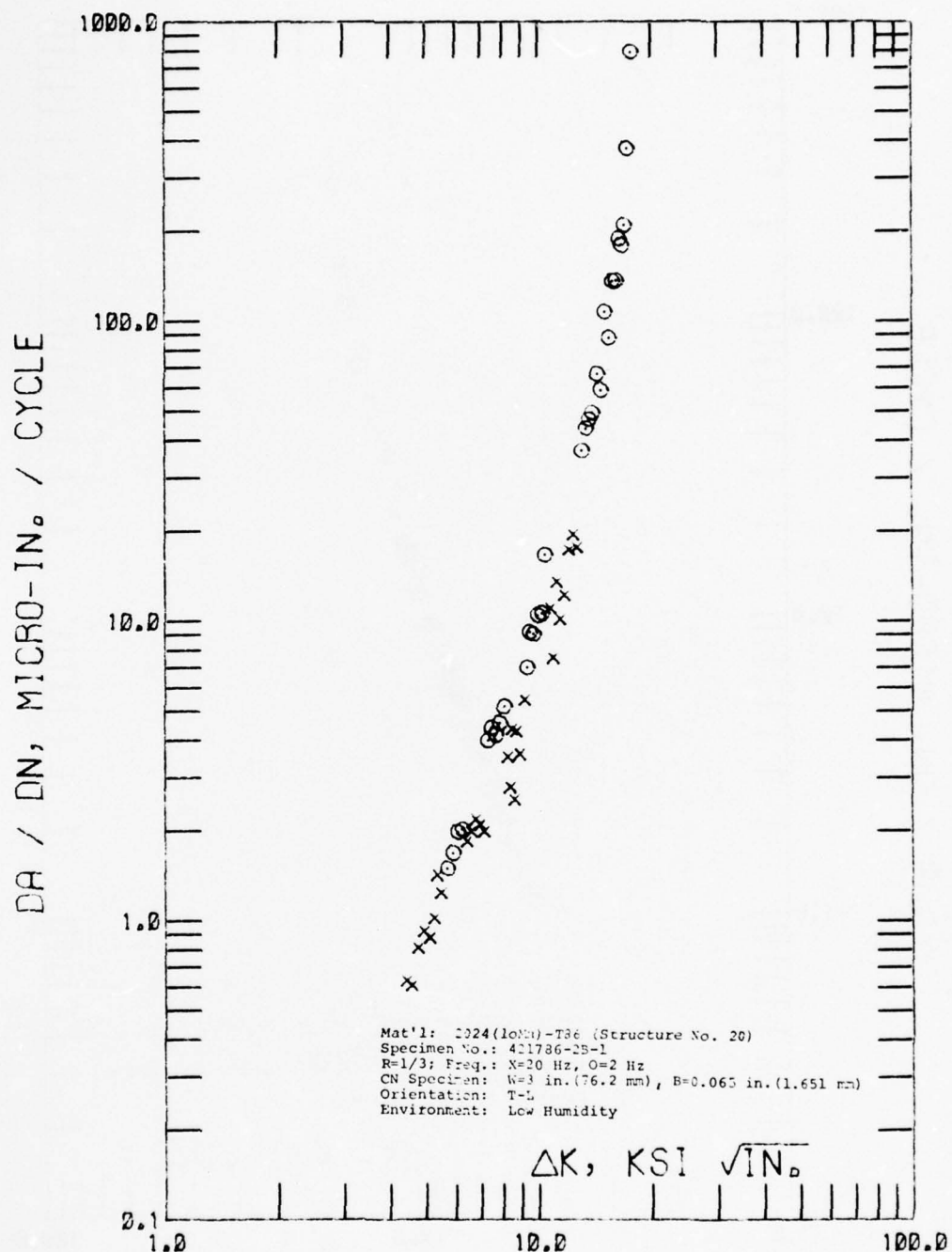


Figure C-42 Cyclic Stress Intensity Range,  $\Delta K$ , Vs. Cyclic Fatigue Crack Growth Rate  $\Delta a/\Delta N$ , of Structure No. 20

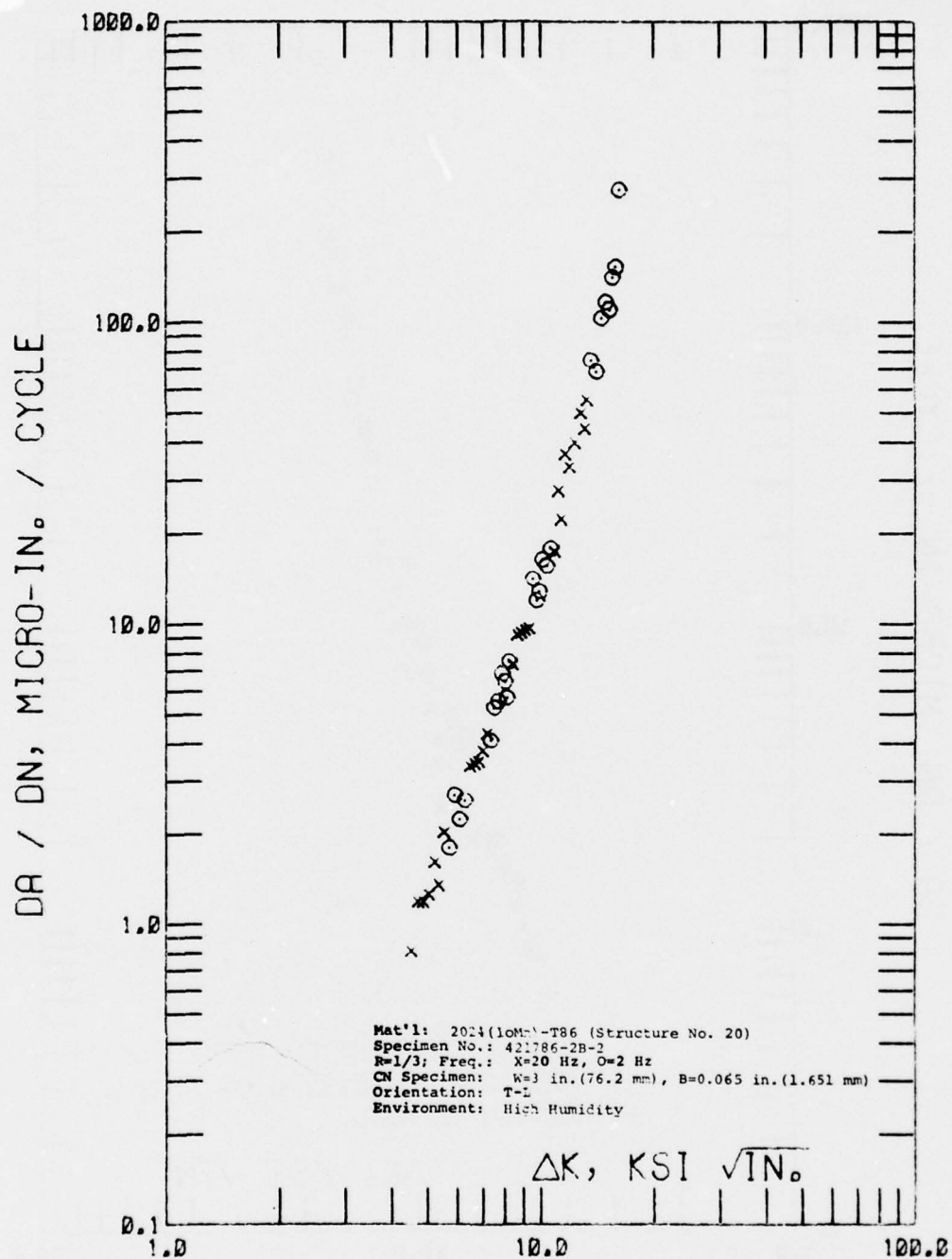


Figure C-43 Cyclic Stress Intensity Range,  $\Delta K$ , Vs. Cyclic Fatigue Crack Growth Rate,  $\Delta a / \Delta N$ , of Structure No. 20

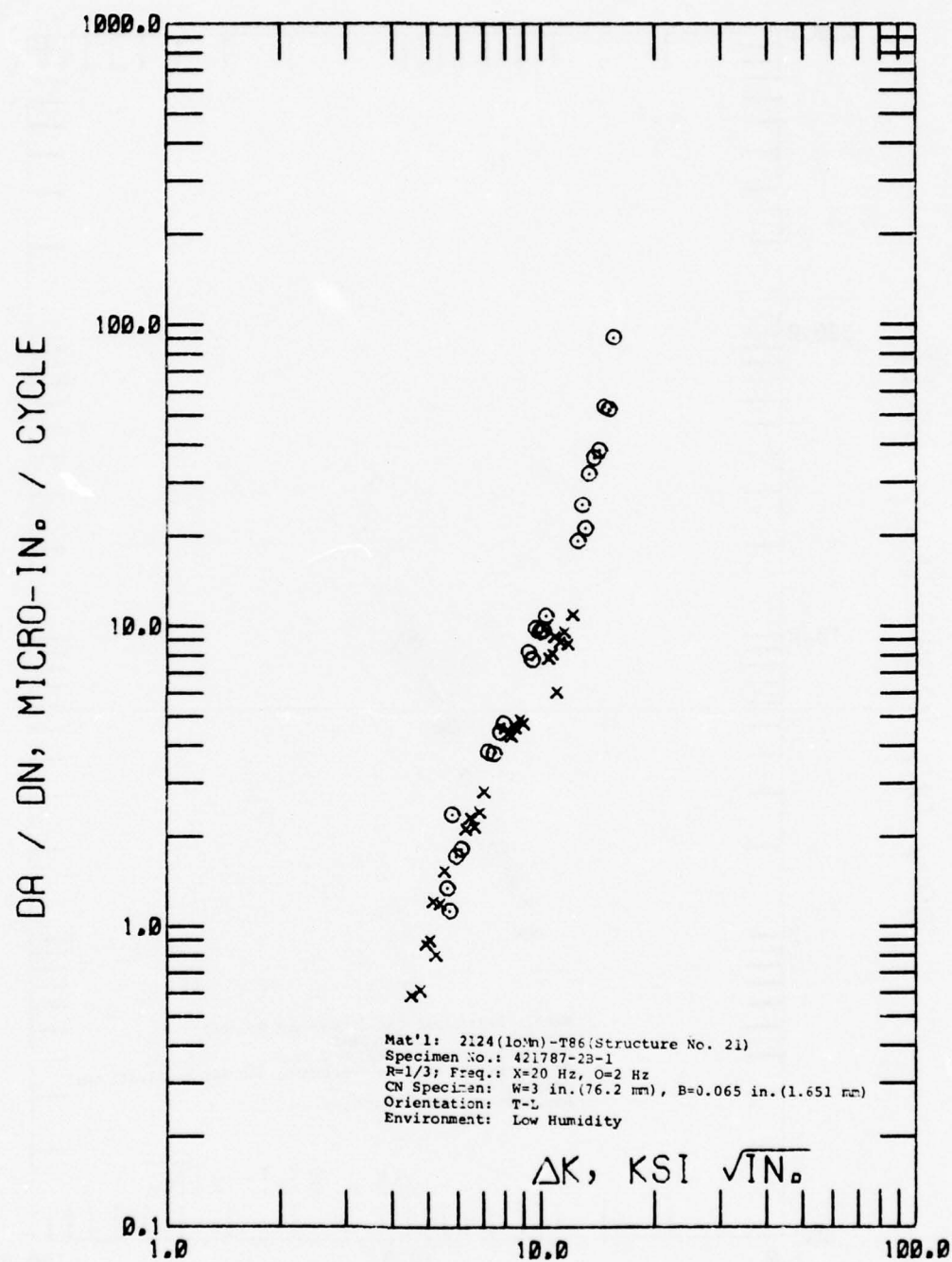


Figure C-44 Cyclic Stress Intensity Range,  $\Delta K$ , Vs. Cyclic Fatigue Crack Growth Rate,  $\Delta a / \Delta N$ , of Structure No. 21



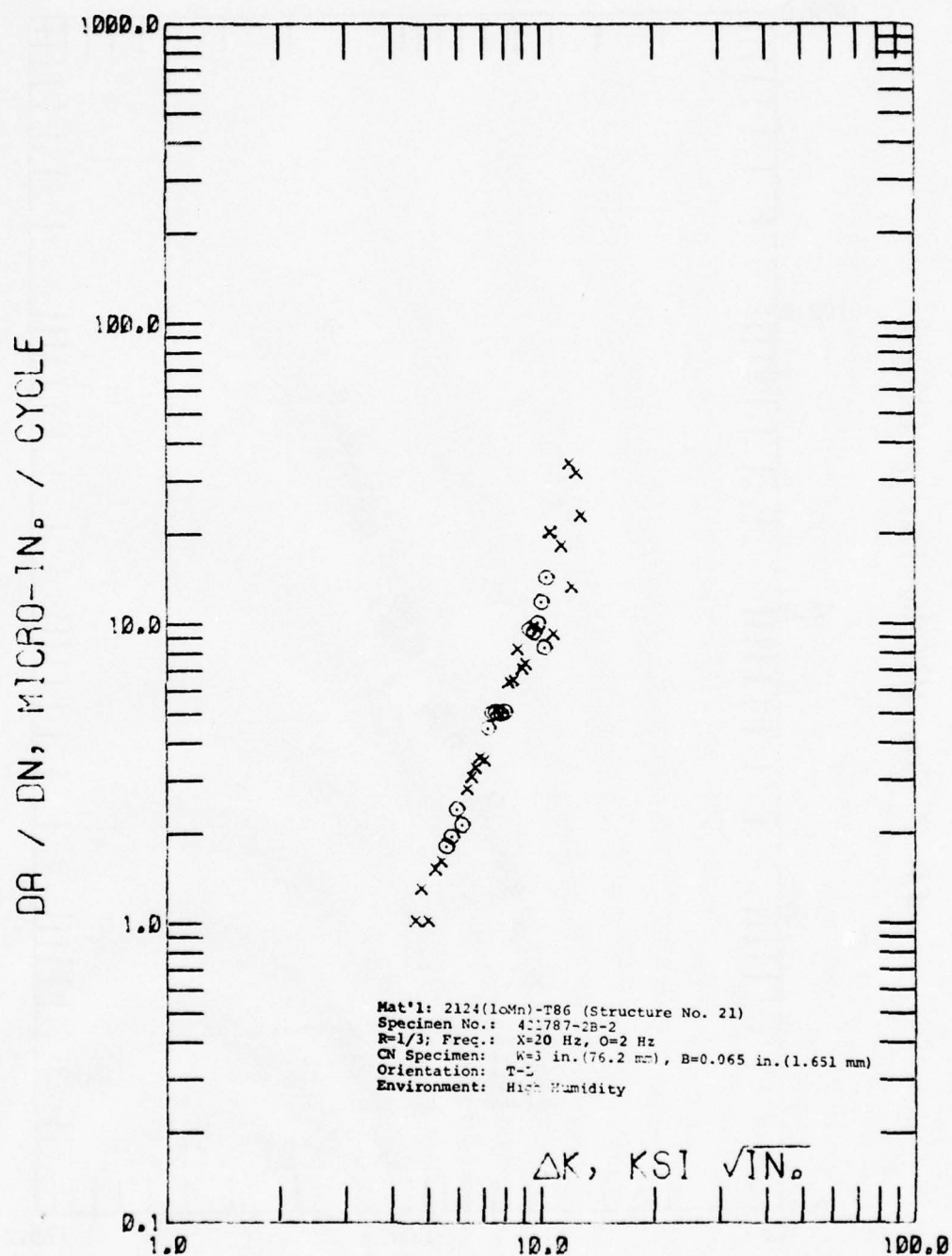


Figure C-45 Cyclic Stress Intensity Range,  $\Delta K$ , Vs. Cyclic Fatigue Crack Growth Rate,  $\Delta a / \Delta N$ , of Structure No. 21

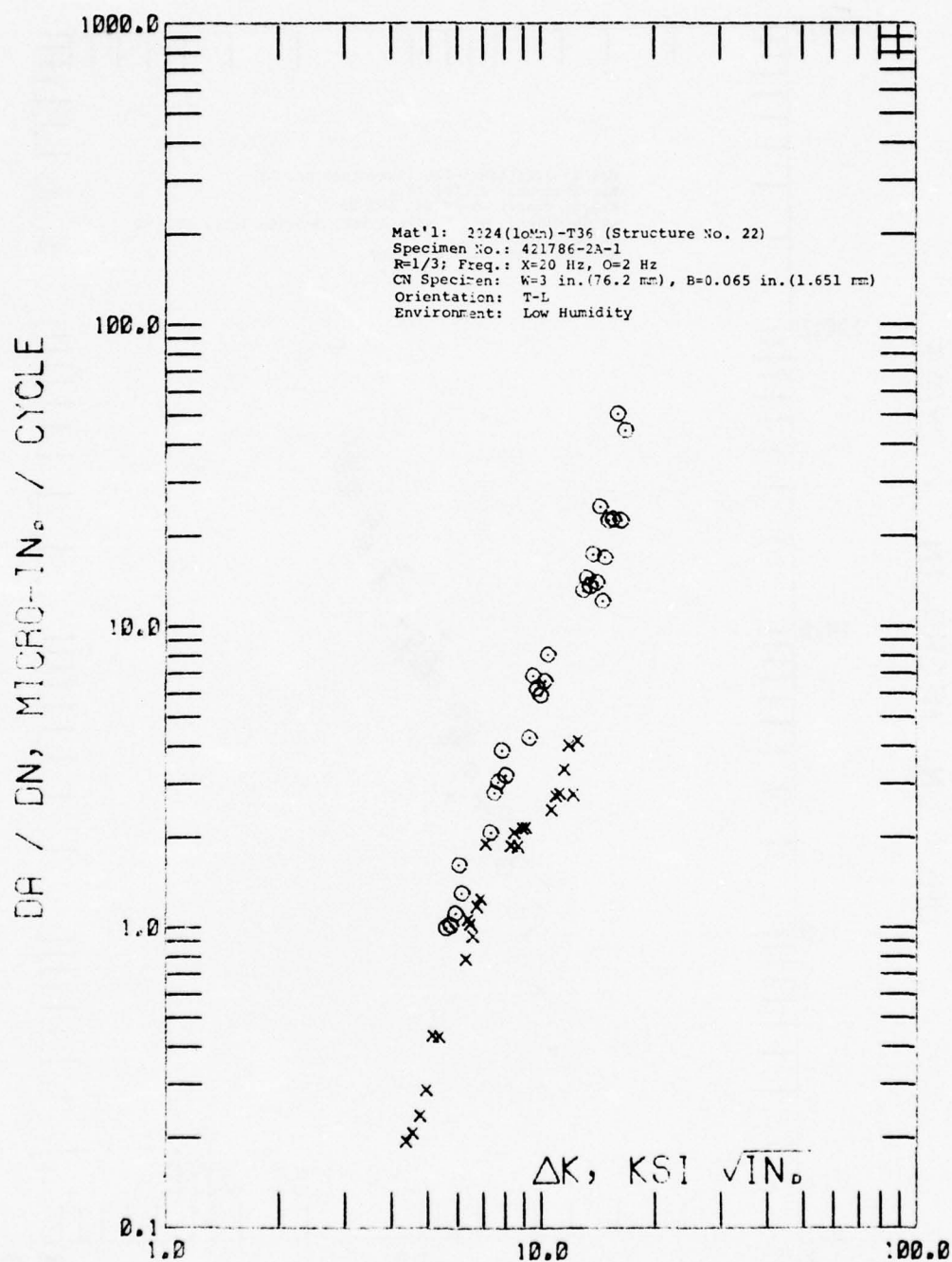


Figure C-46 Cyclic Stress Intensity Range,  $\Delta K$ , Vs. Cyclic Fatigue Crack Growth Rate  $\Delta a/\Delta N$ , of Structure No. 22

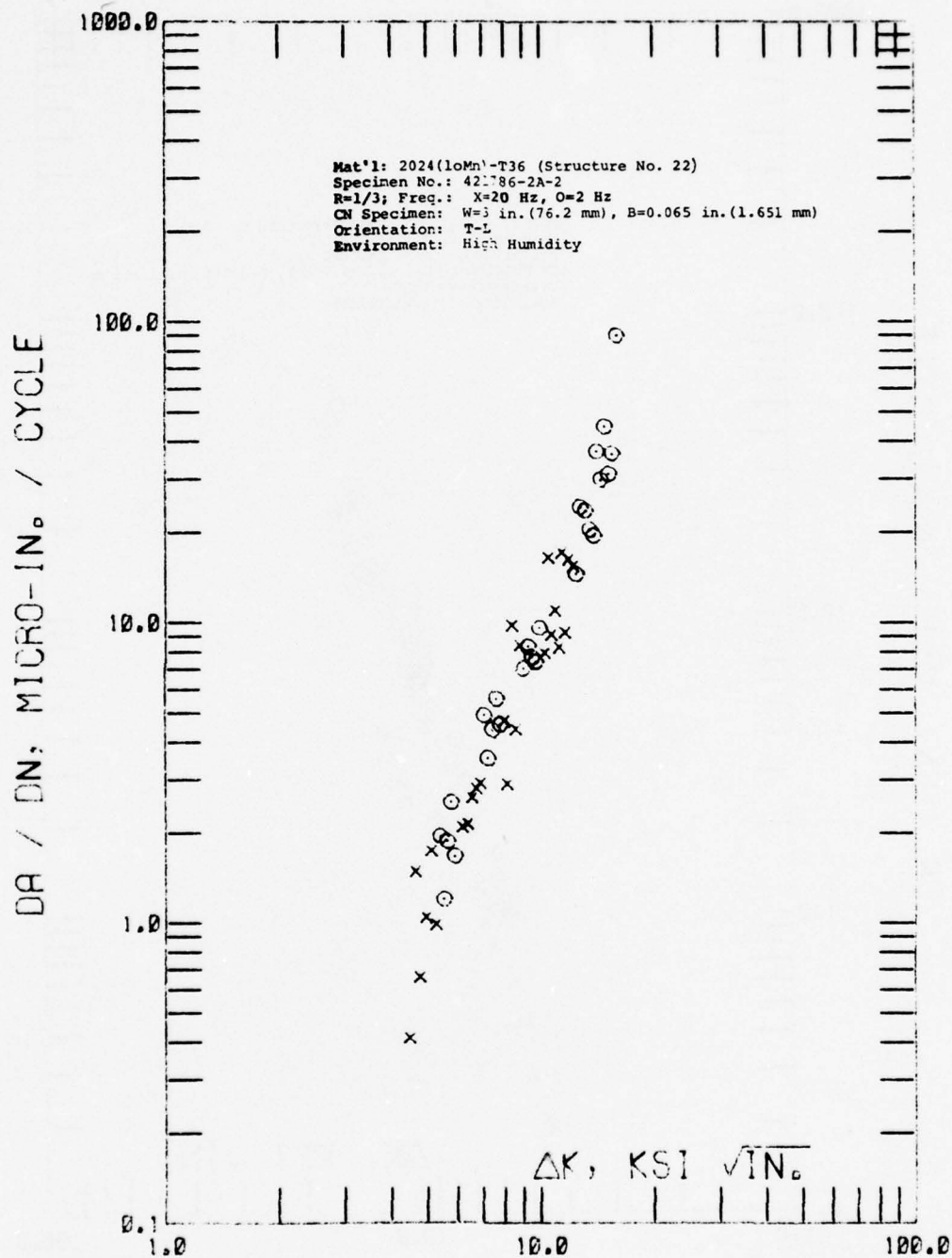


Figure C-47 Cyclic Stress Intensity Range,  $\Delta K$ , Vs. Cyclic Fatigue Crack Growth Rate,  $\Delta a / \Delta N$ , of Structure No. 22

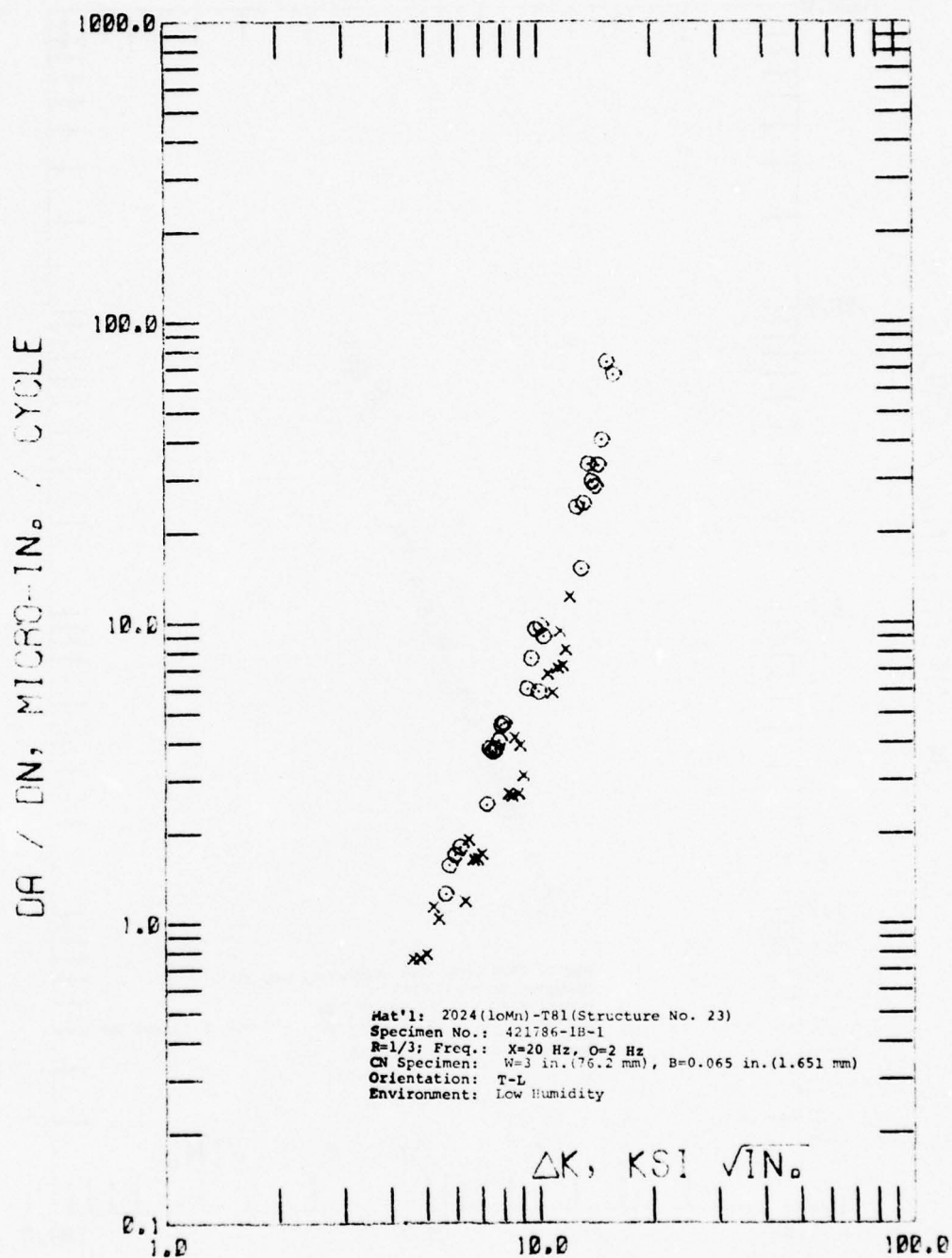


Figure C-48 Cyclic Stress Intensity Range,  $\Delta K$ , Vs. Cyclic Fatigue Crack Growth Rate,  $\Delta a / \Delta N$ , of Structure No. 23



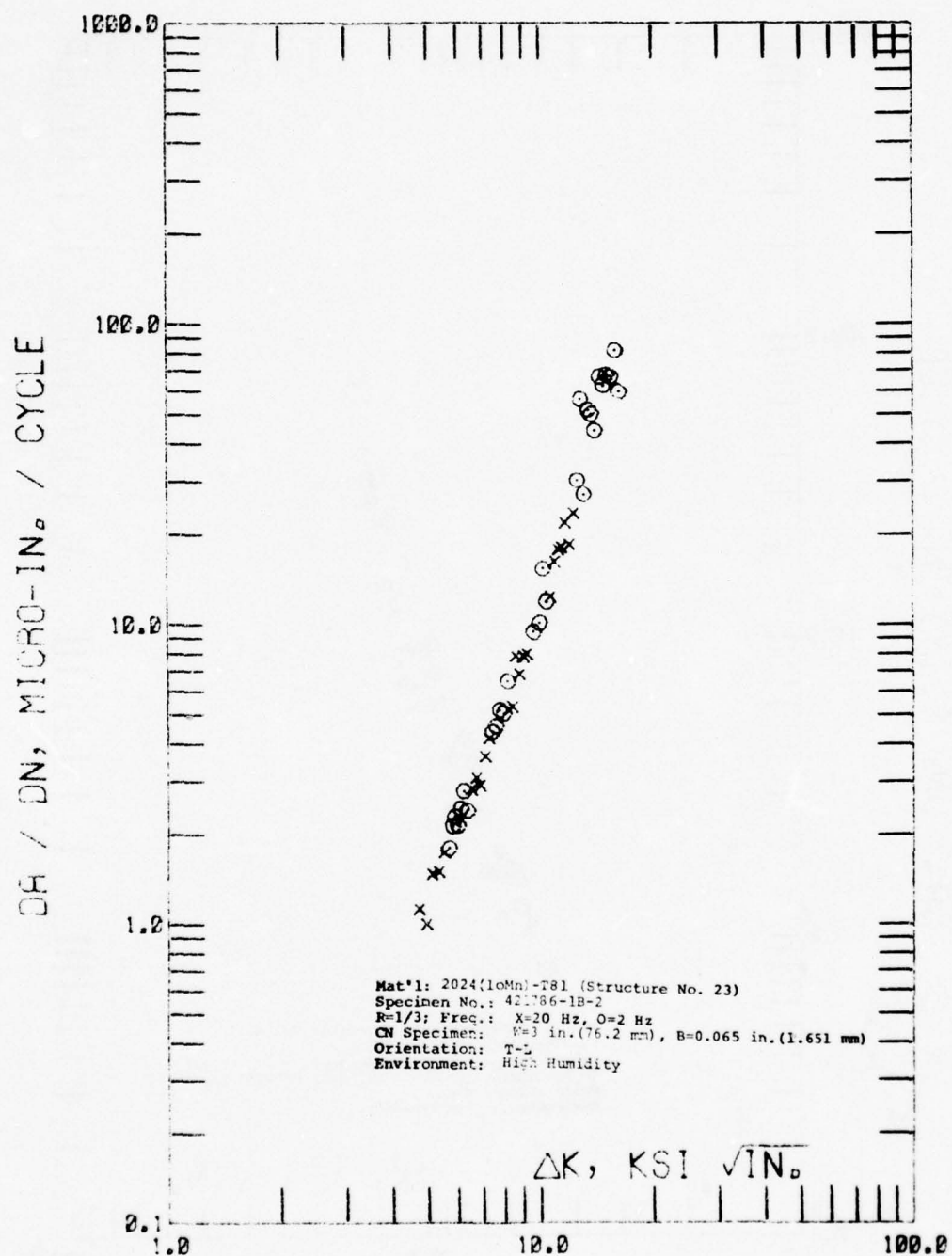


Figure C-49 Cyclic Stress Intensity Range,  $\Delta K$ , Vs. Cyclic Fatigue Crack Growth Rate,  $\Delta a / \Delta N$ , of Structure No. 23

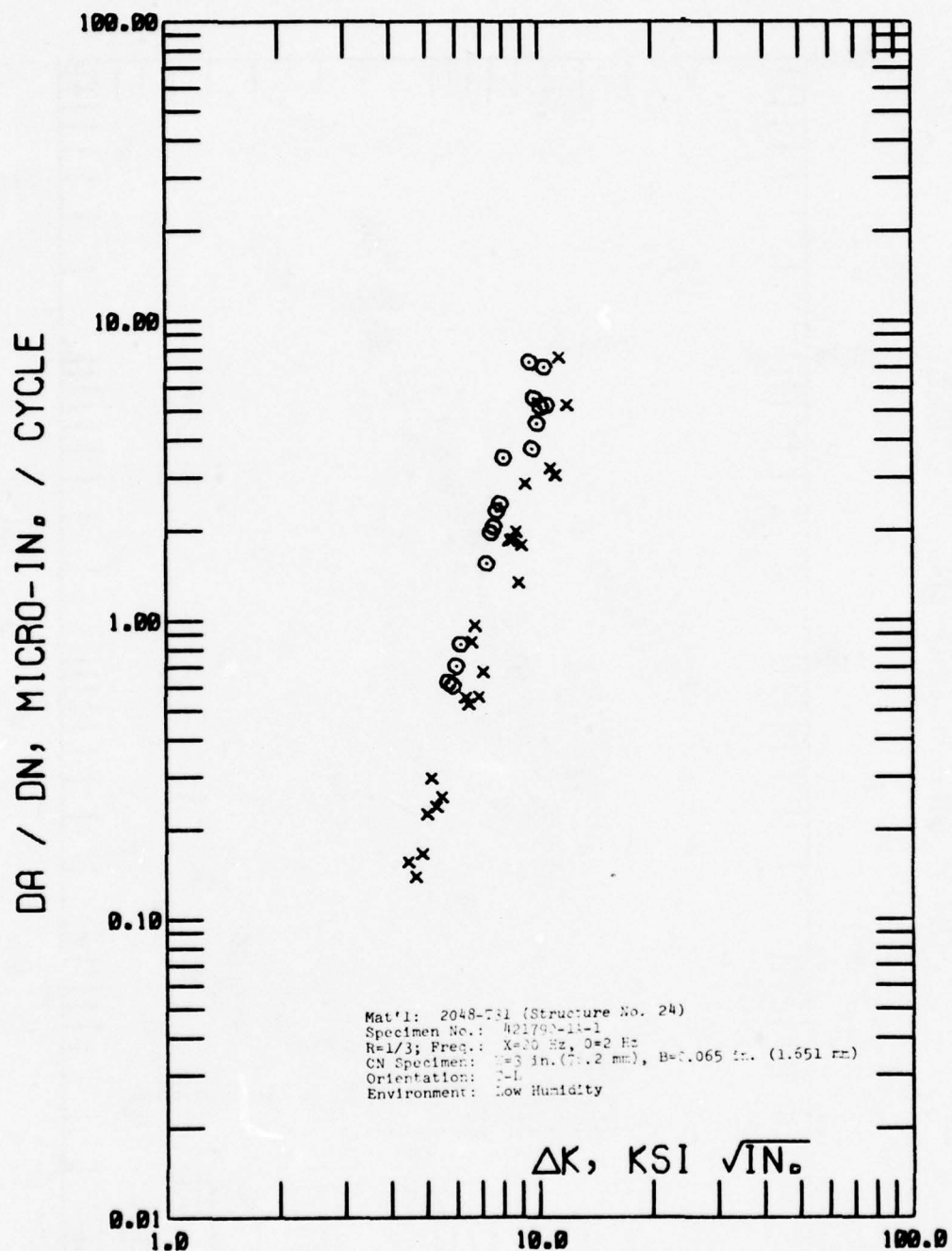


Figure C-50 Cyclic Stress Intensity Range,  $\Delta K$ , Vs. Cyclic Fatigue Crack Growth Rate,  $\Delta a/\Delta N$ , of Structure No. 24

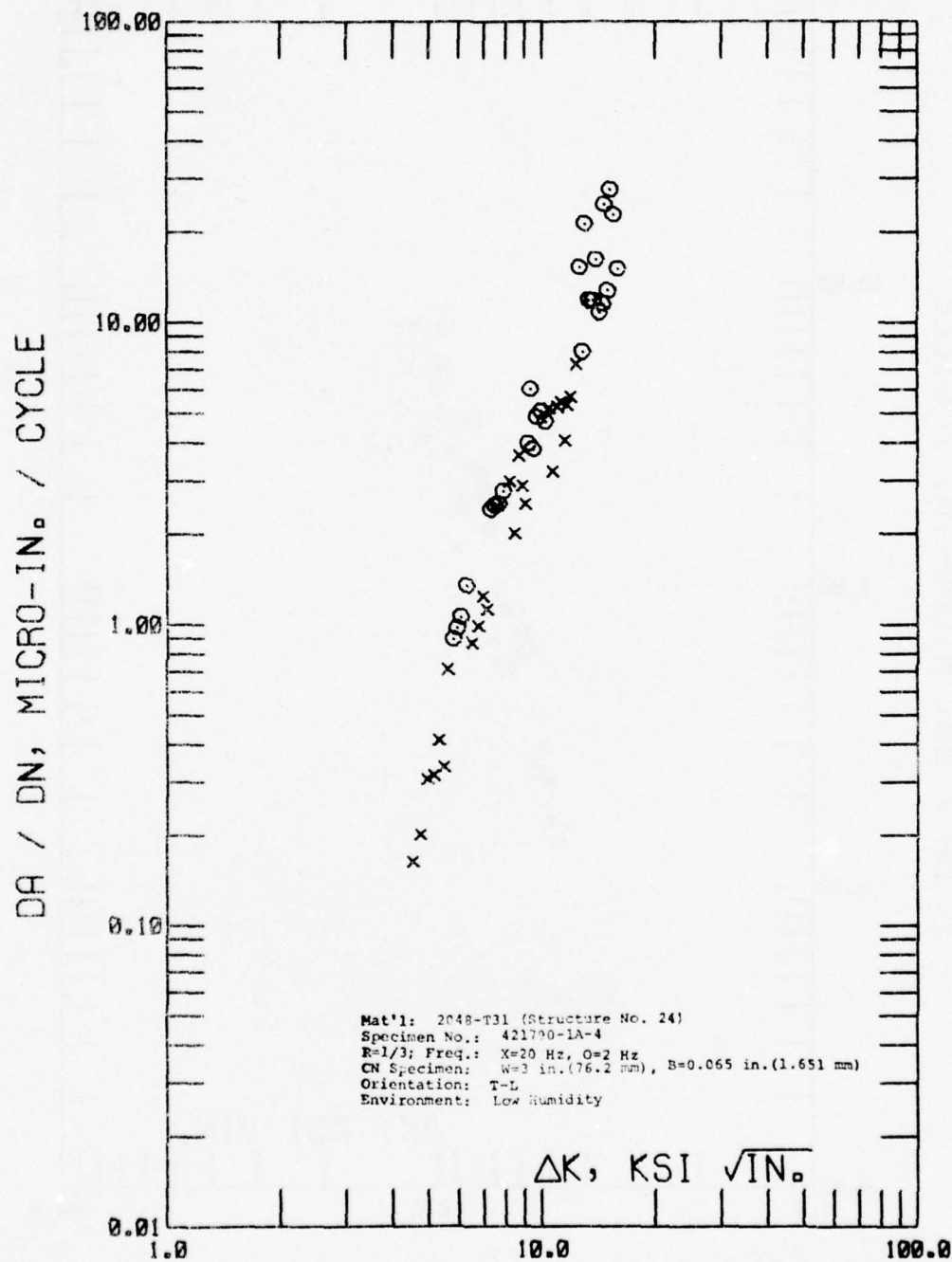


Figure C-51 Cyclic Stress Intensity Range,  $\Delta K$ , Vs. Cyclic Fatigue Crack Growth Rate,  $\Delta a / \Delta N$ , of Structure No. 24

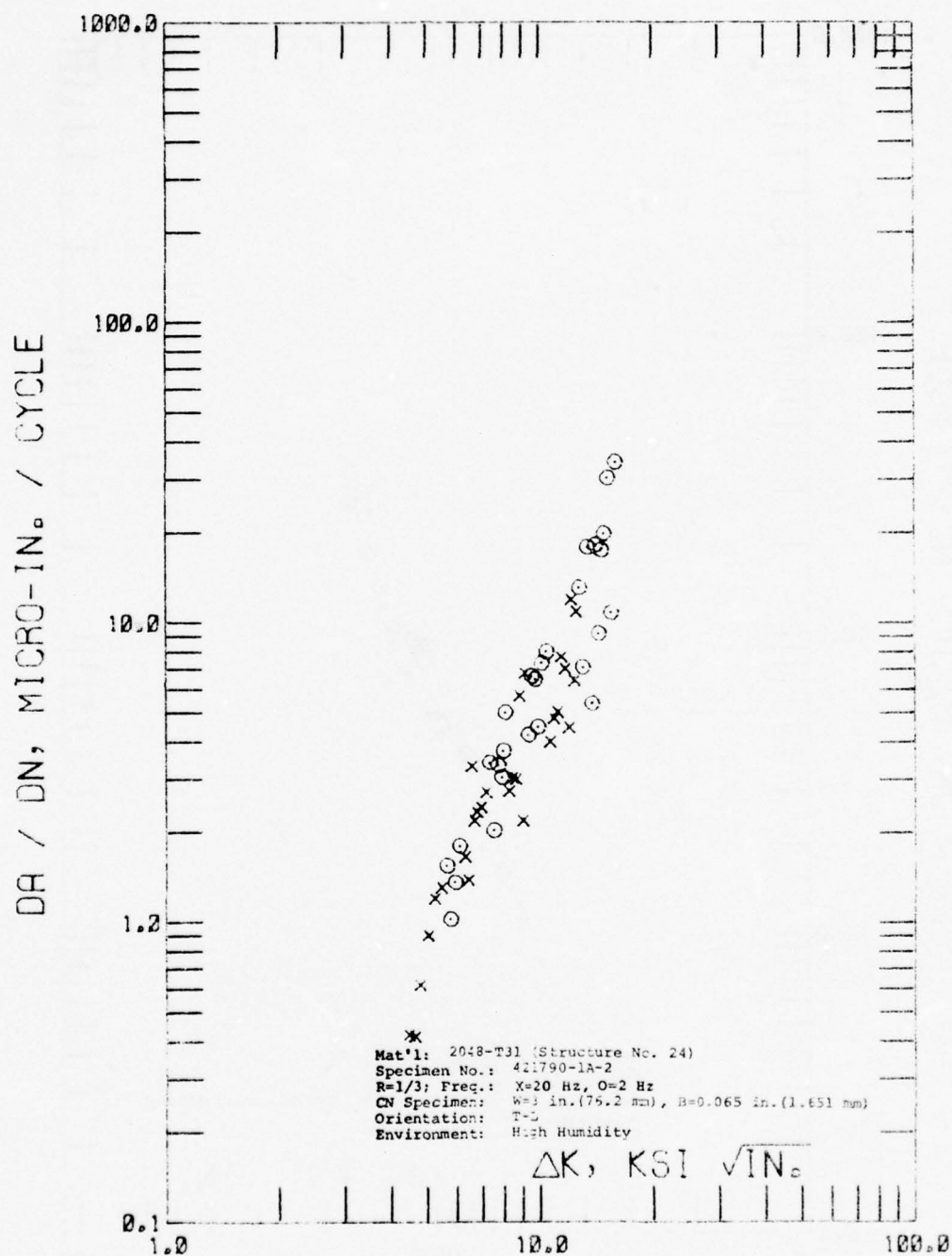


Figure C-52 Cyclic Stress Intensity Range,  $\Delta K$ , Vs. Cyclic Fatigue Crack Growth Rate,  $\Delta a / \Delta N$ , of Structure No. 24



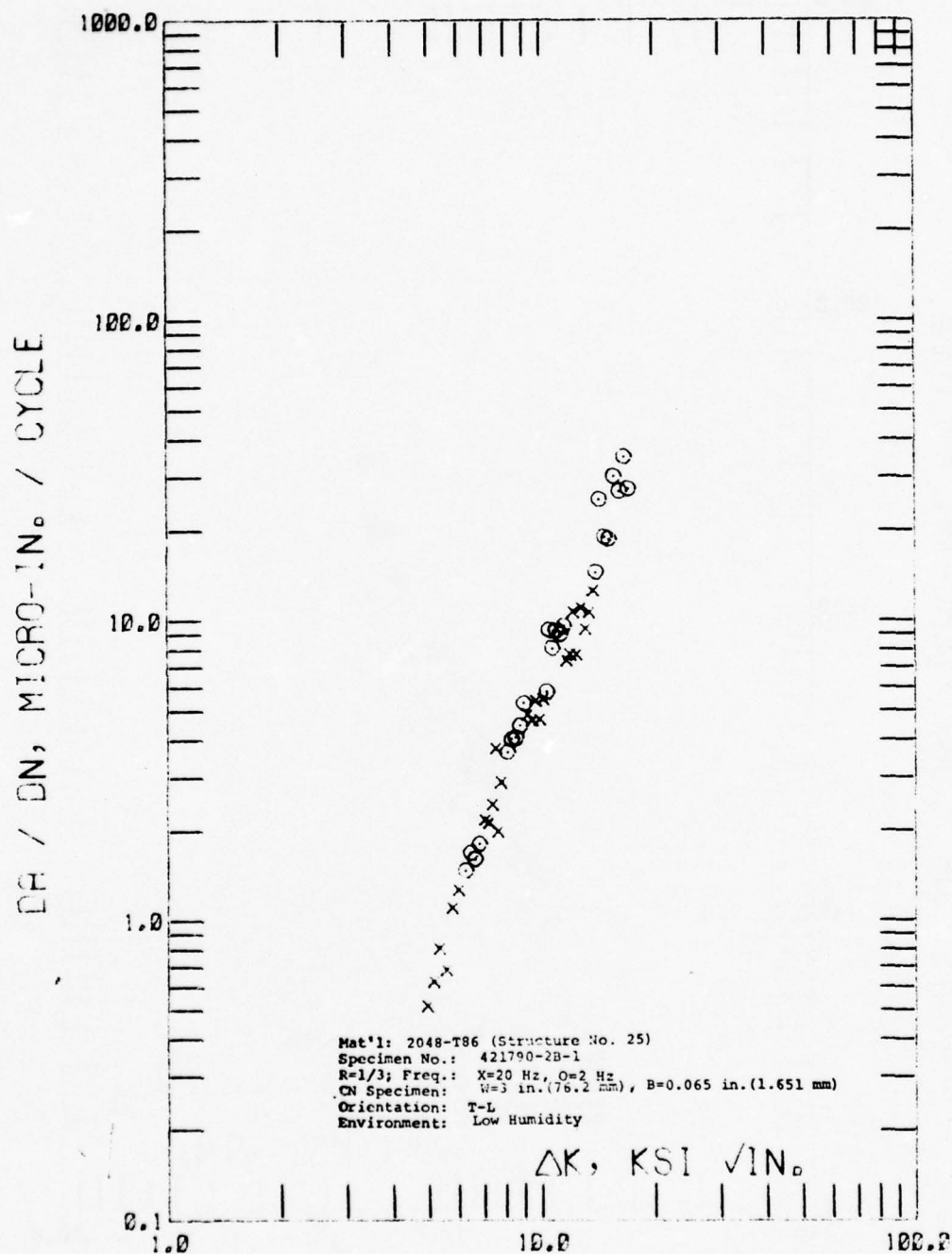


Figure C-53 Cyclic Stress Intensity Range,  $\Delta K$ , Vs. Cyclic Fatigue Crack Growth Rate,  $\Delta a / \Delta N$ , of Structure No. 25

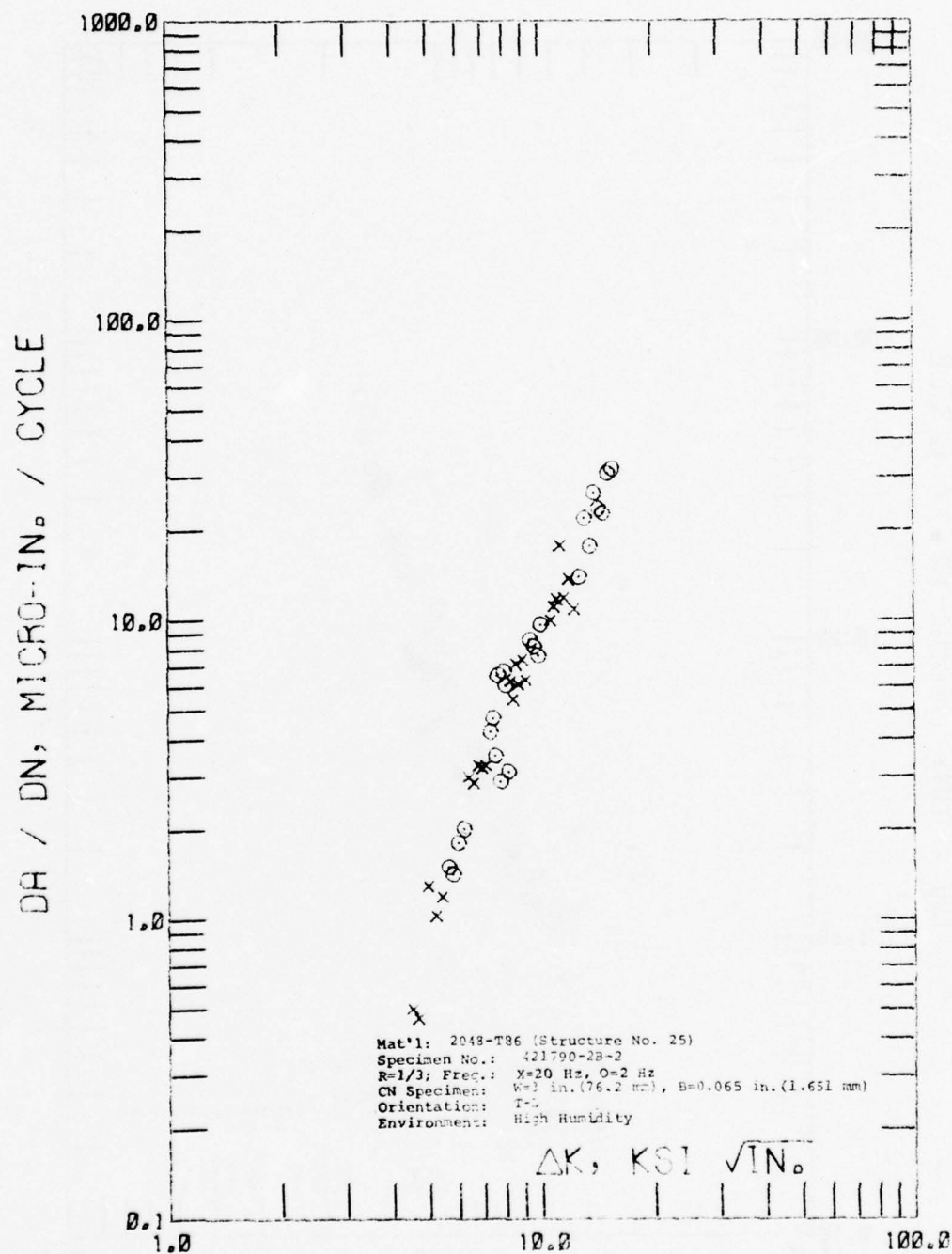


Figure C-54 Cyclic Stress Intensity Range,  $\Delta K$ , Vs. Cyclic Fatigue Crack Growth Rate,  $\Delta a / \Delta N$ , of Structure No. 25

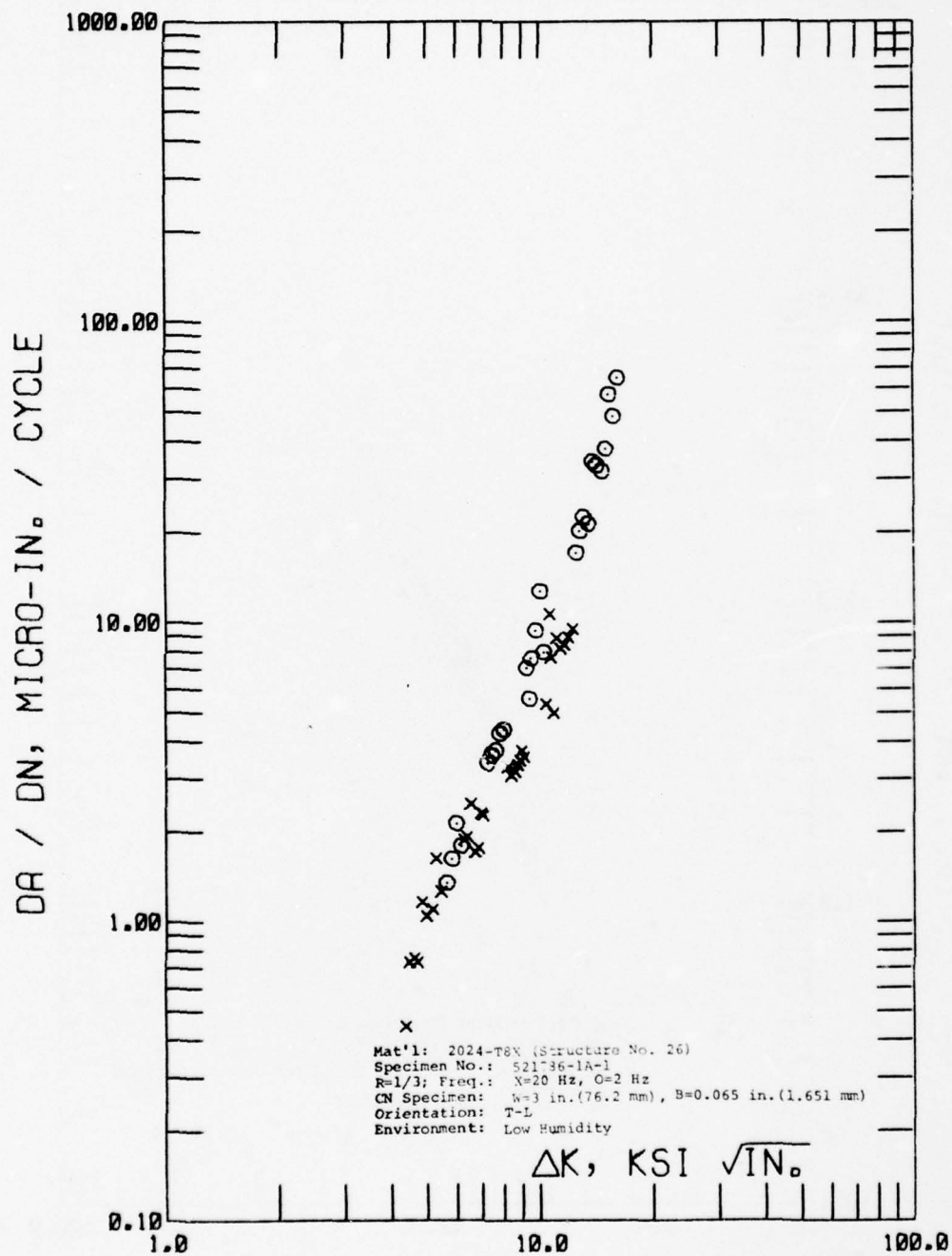


Figure C-55 Cyclic Stress Intensity Range,  $\Delta K$ , Vs. Cyclic Fatigue Crack Growth Rate,  $\Delta a / \Delta N$ , of Structure No. 26

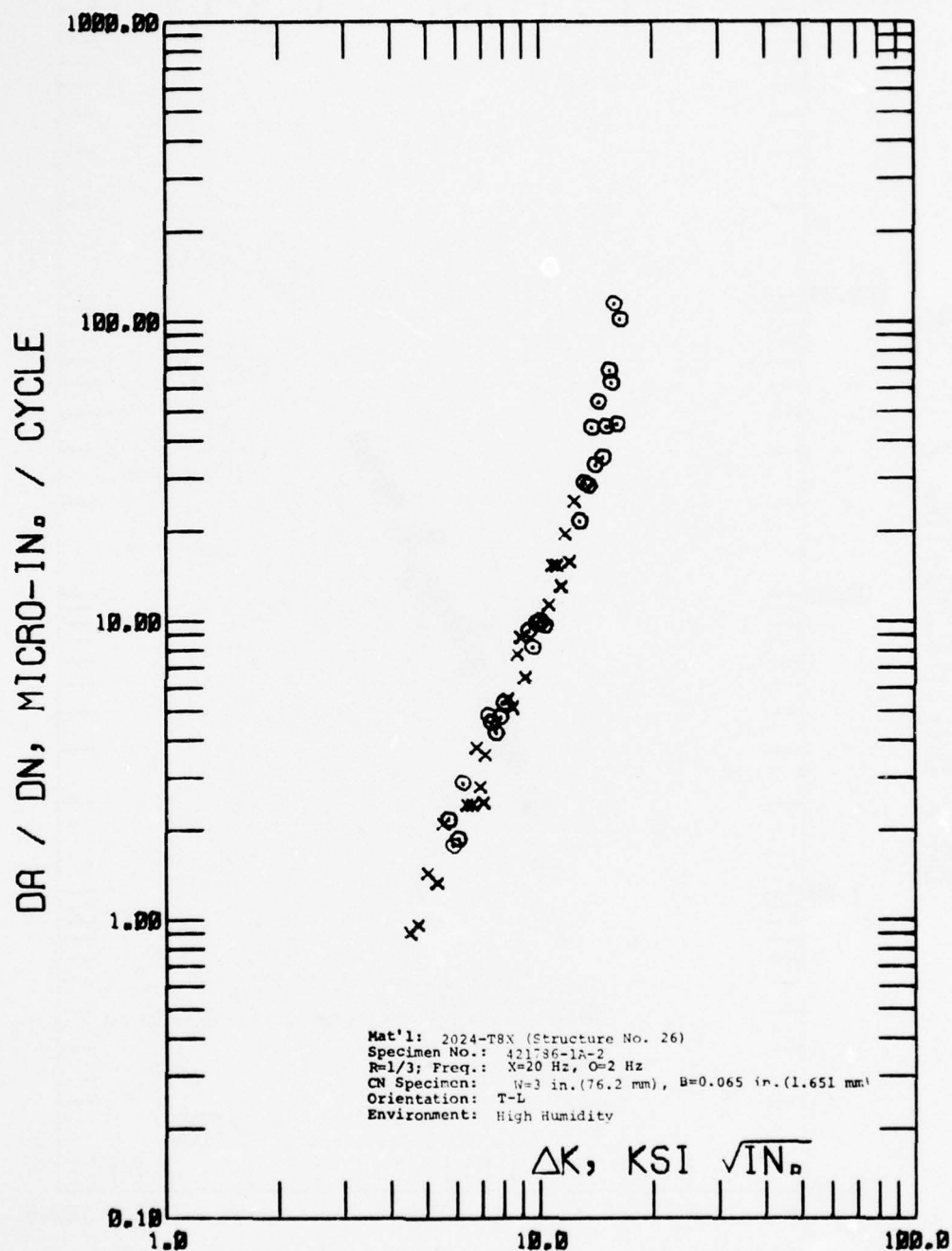


Figure C-56 Cyclic Stress Intensity Range,  $\Delta K$ , Vs. Cyclic Fatigue Crack Growth Rate,  $\Delta a / \Delta N$ , of Structure No. 26



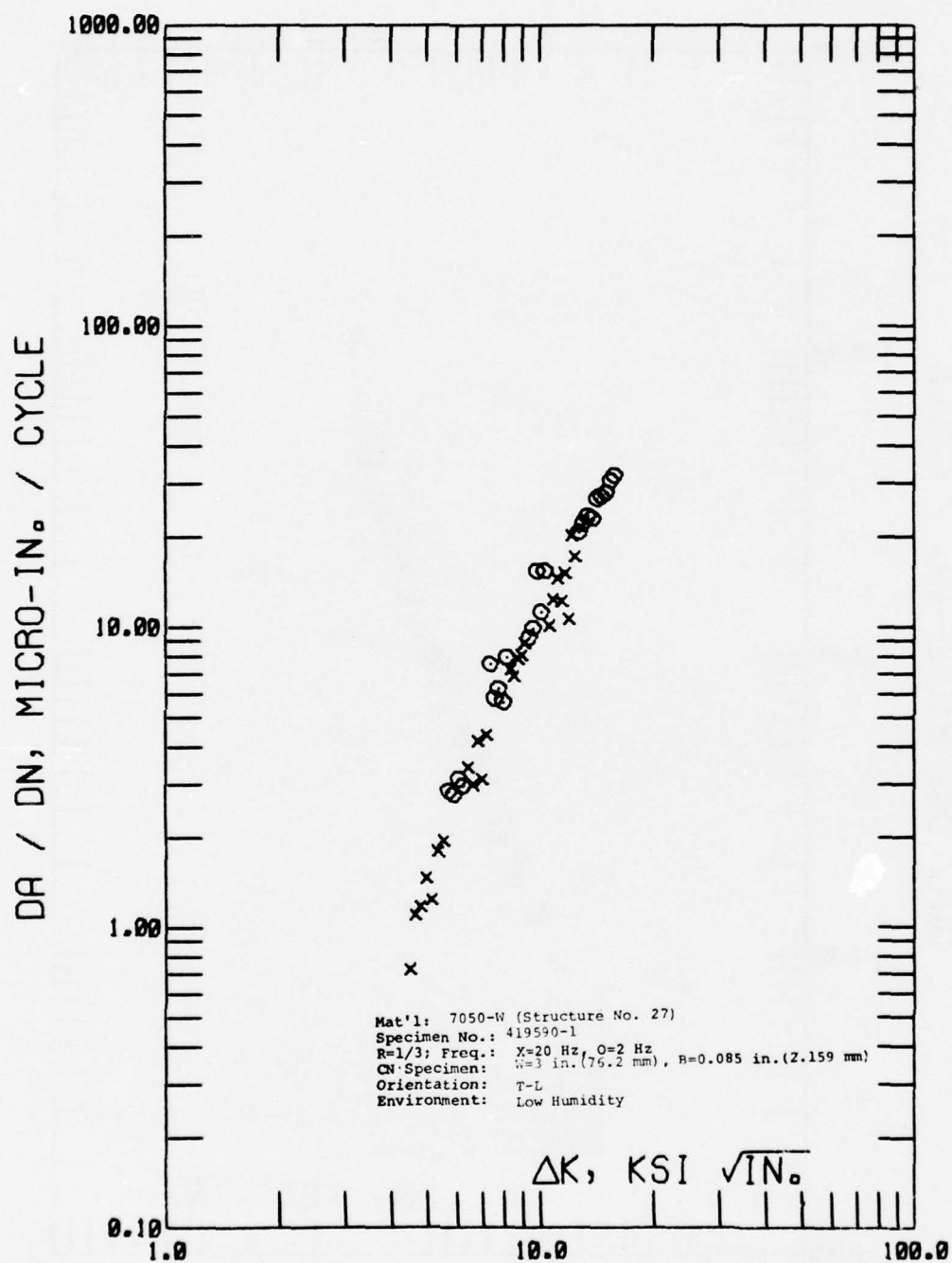


Figure C-57 Cyclic Stress Intensity Range,  $\Delta K$ , Vs. Cyclic Fatigue Crack Growth Rate,  $\Delta a / \Delta N$ , of Structure No. 27

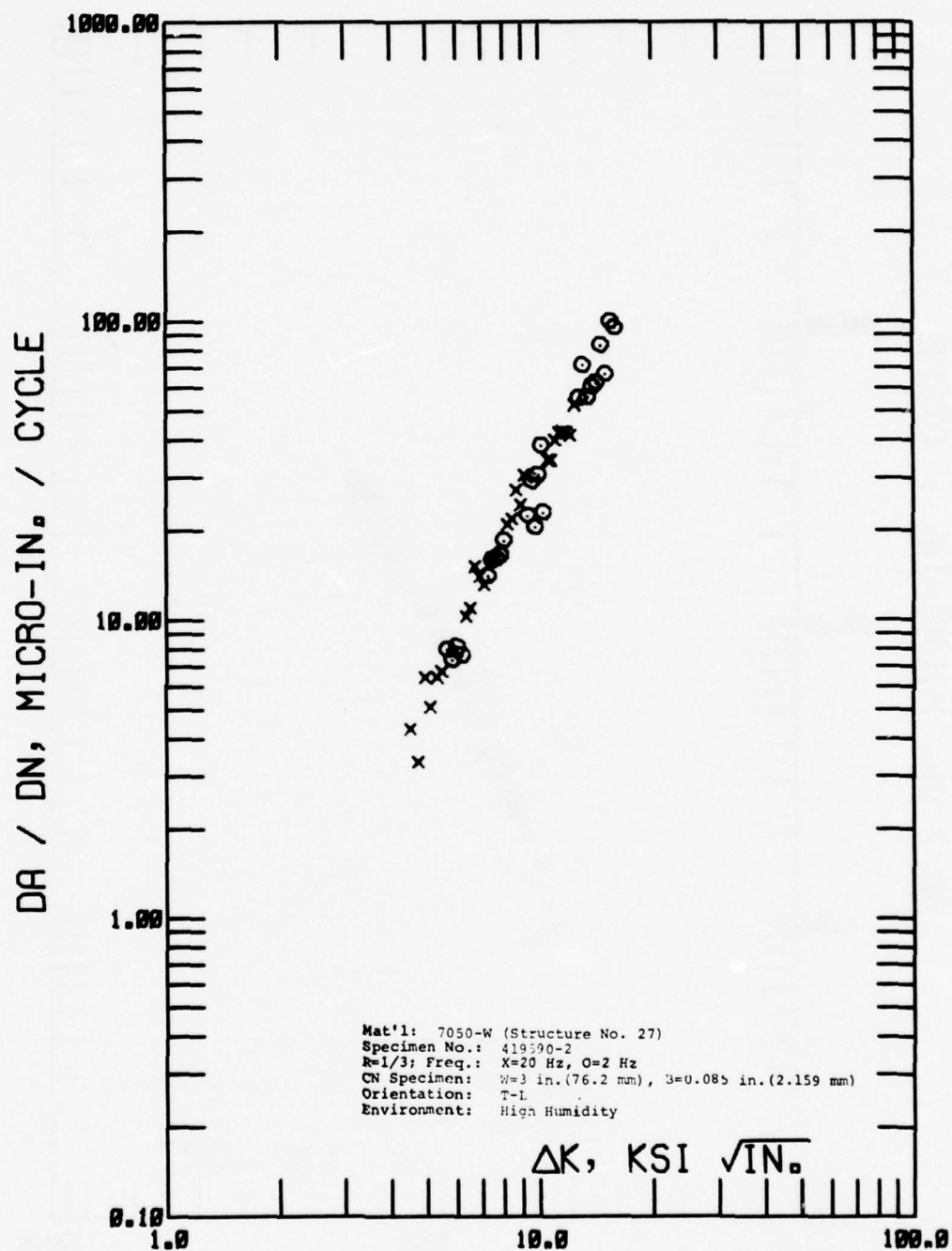


Figure C-58 Cyclic Stress Intensity Range,  $\Delta K$ , Vs. Cyclic Fatigue Crack Growth Rate,  $\Delta a / \Delta N$ , of Structure No. 27

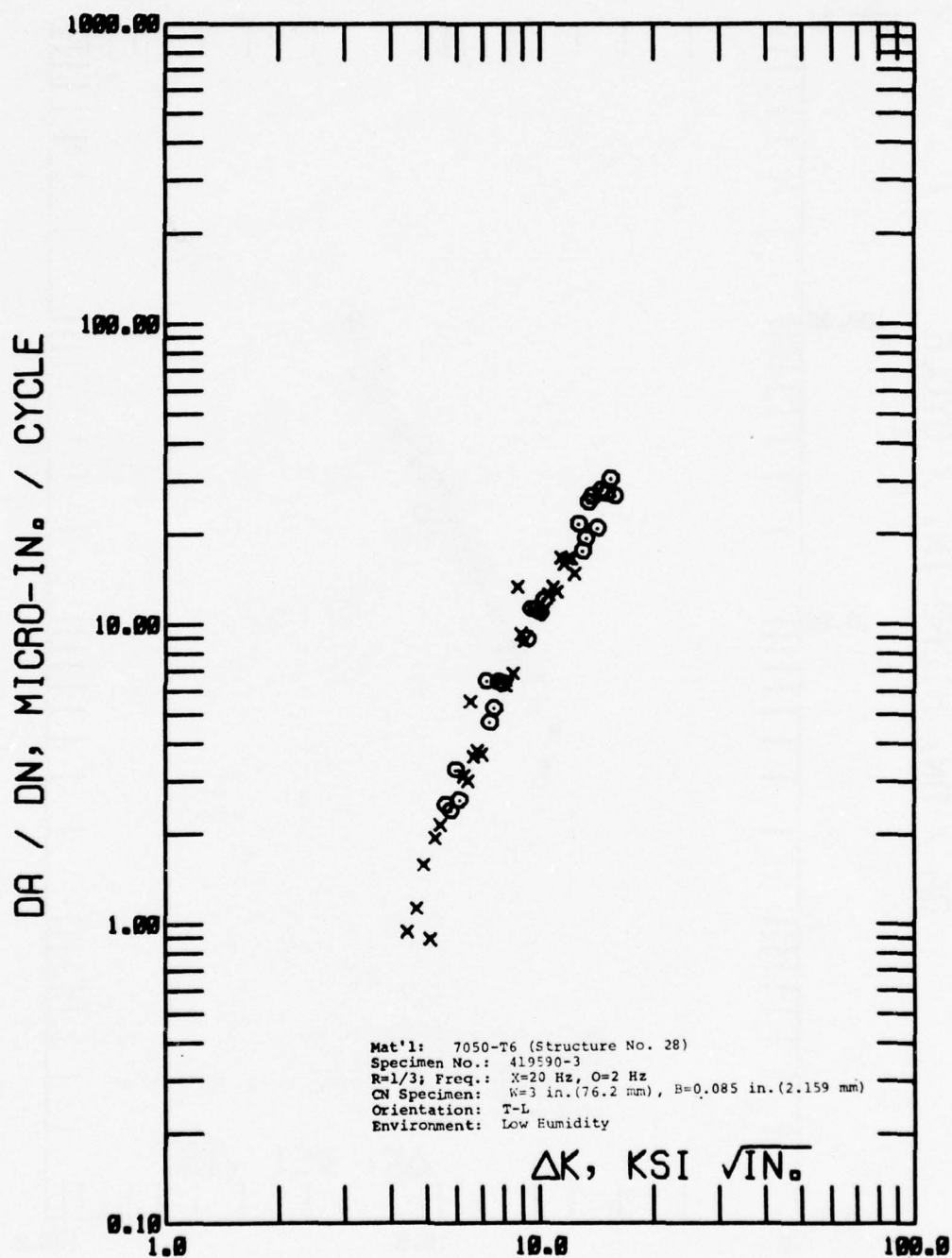


Figure C-59 Cyclic Stress Intensity Range,  $\Delta K$ , Vs. Cyclic Fatigue Crack Growth Rate,  $\Delta a / \Delta N$ , of Structure No. 28

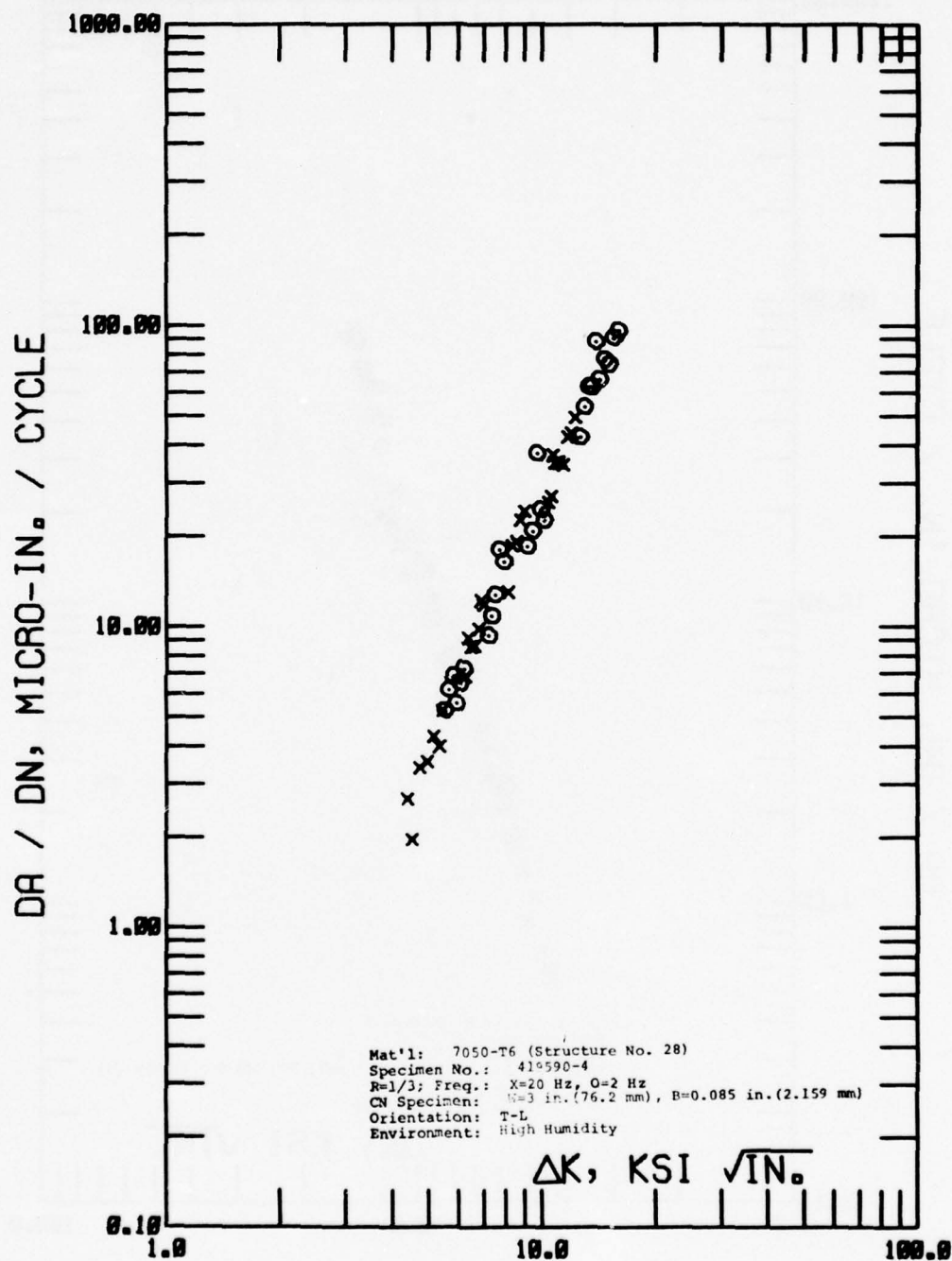


Figure C-60 Cyclic Stress Intensity Range,  $\Delta K$ , Vs. Cyclic Fatigue Crack Growth Rate,  $\Delta a / \Delta N$ , of Structure No. 28



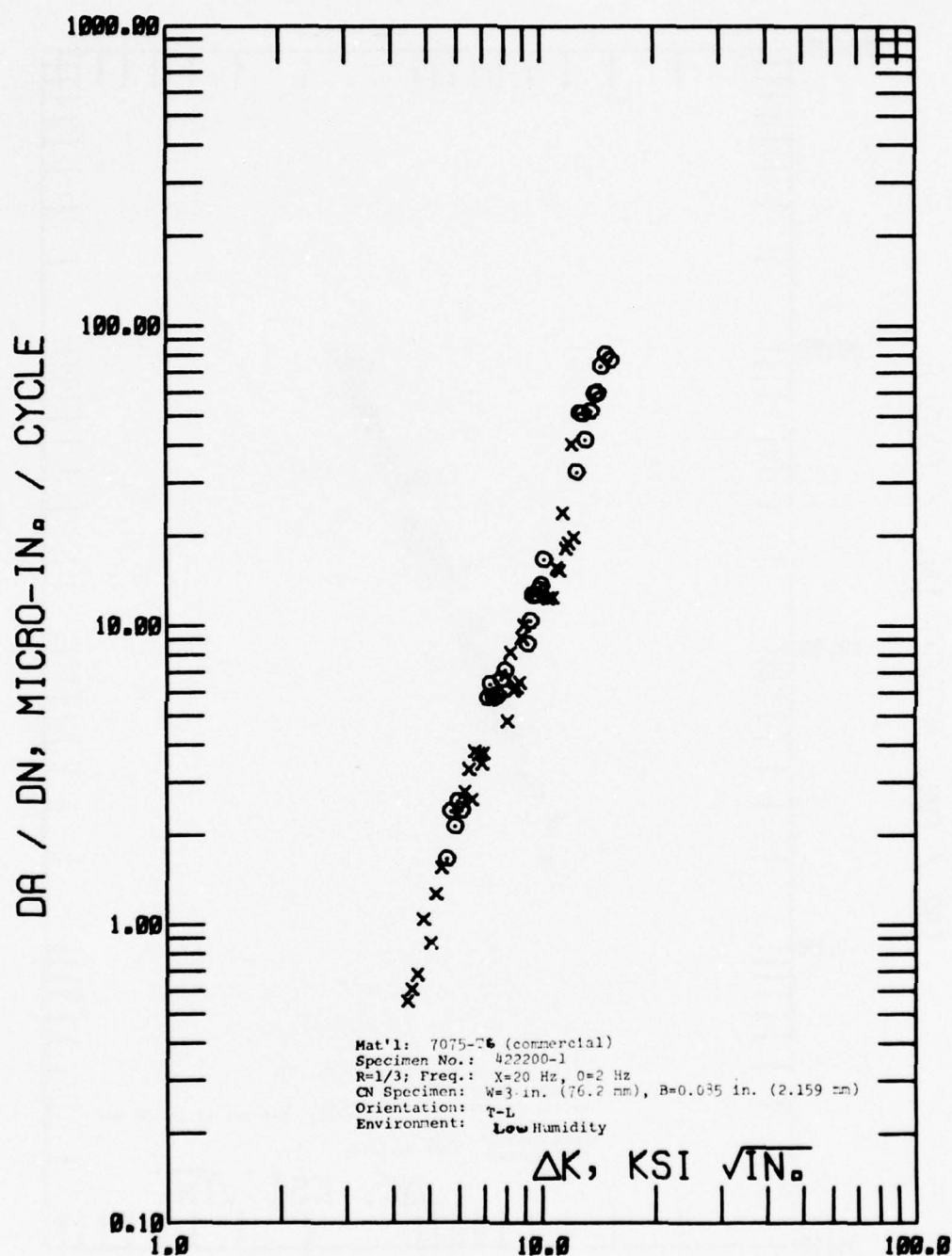


Figure C-61 Cyclic Stress Intensity Range,  $\Delta K$ , Vs. Cyclic Fatigue Crack Growth Rate,  $\Delta a/\Delta N$ , for Commercial 7075-T6

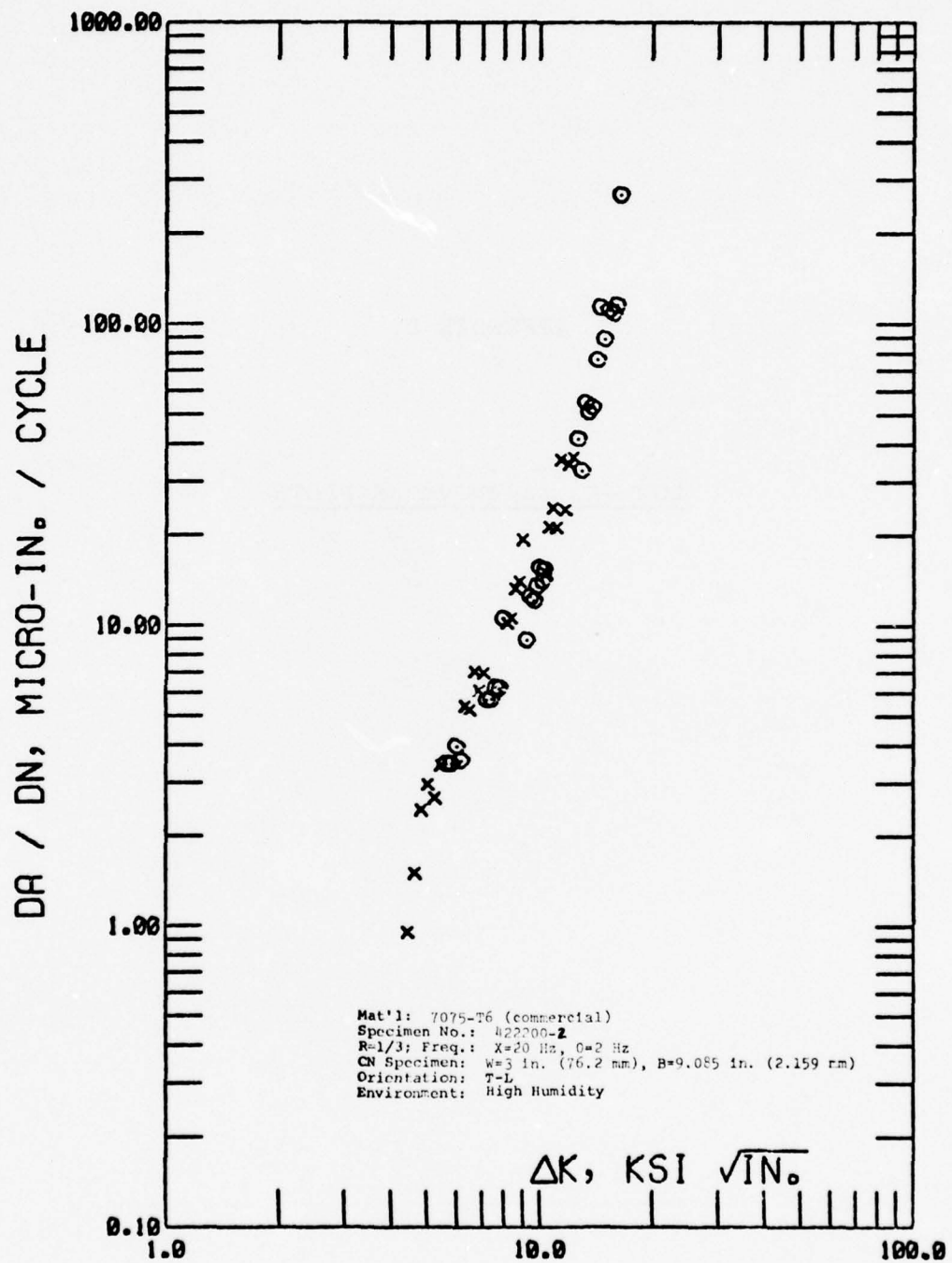


Figure C-62 Cyclic Stress Intensity Range,  $\Delta K$ , Vs. Cyclic Fatigue Crack Growth Rate,  $\Delta a / \Delta N$ , for Commercial 7075-T6

APPENDIX D

LOW  $\Delta K$ ,  $\Delta a/\Delta N$  vs  $\Delta K$  PLOTS

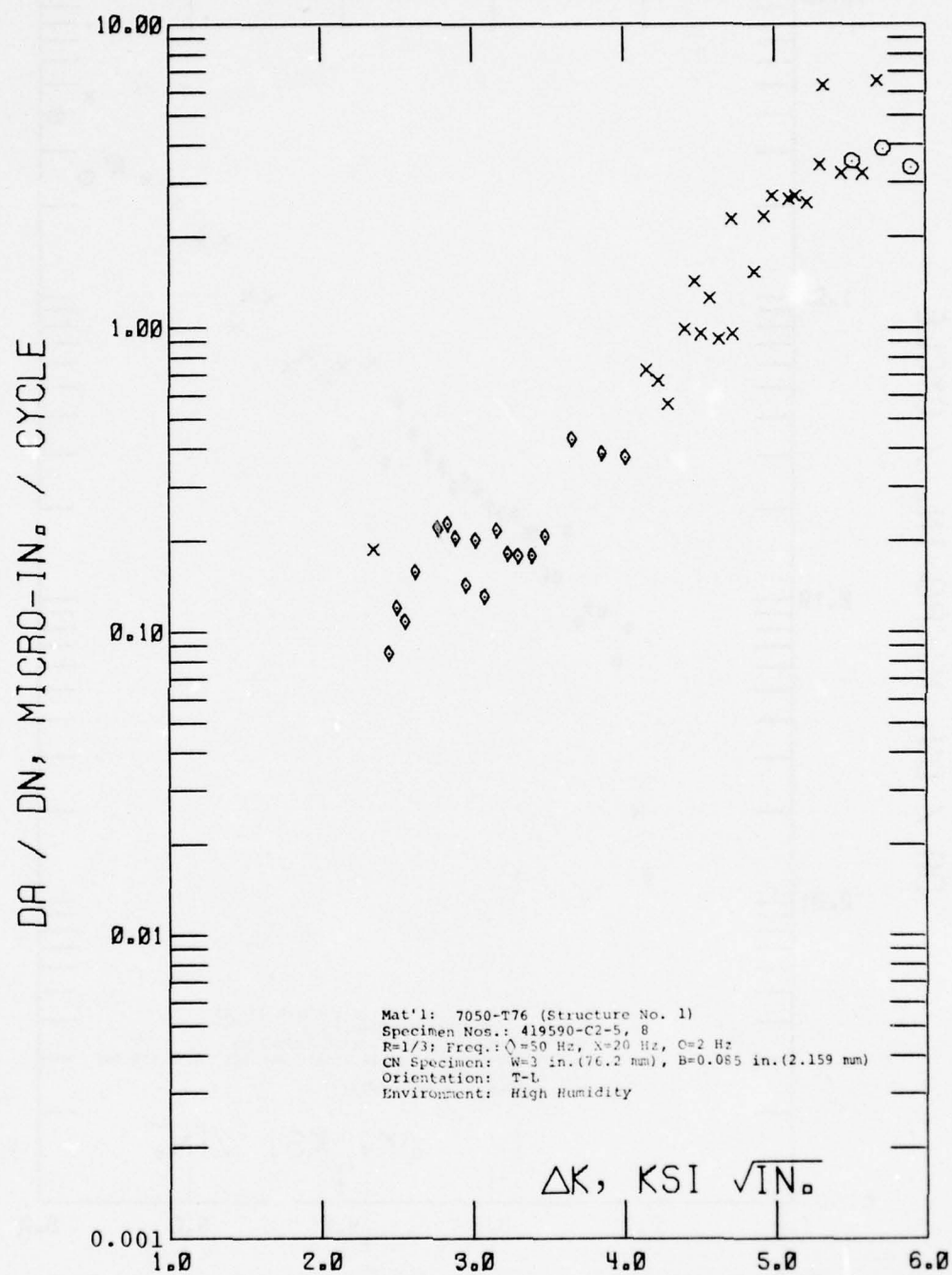


Figure D-1 Cyclic Stress Intensity Range,  $\Delta K$ , Vs. Cyclic Fatigue Crack Growth Rate,  $\Delta a / \Delta N$ , of Structure No. 1



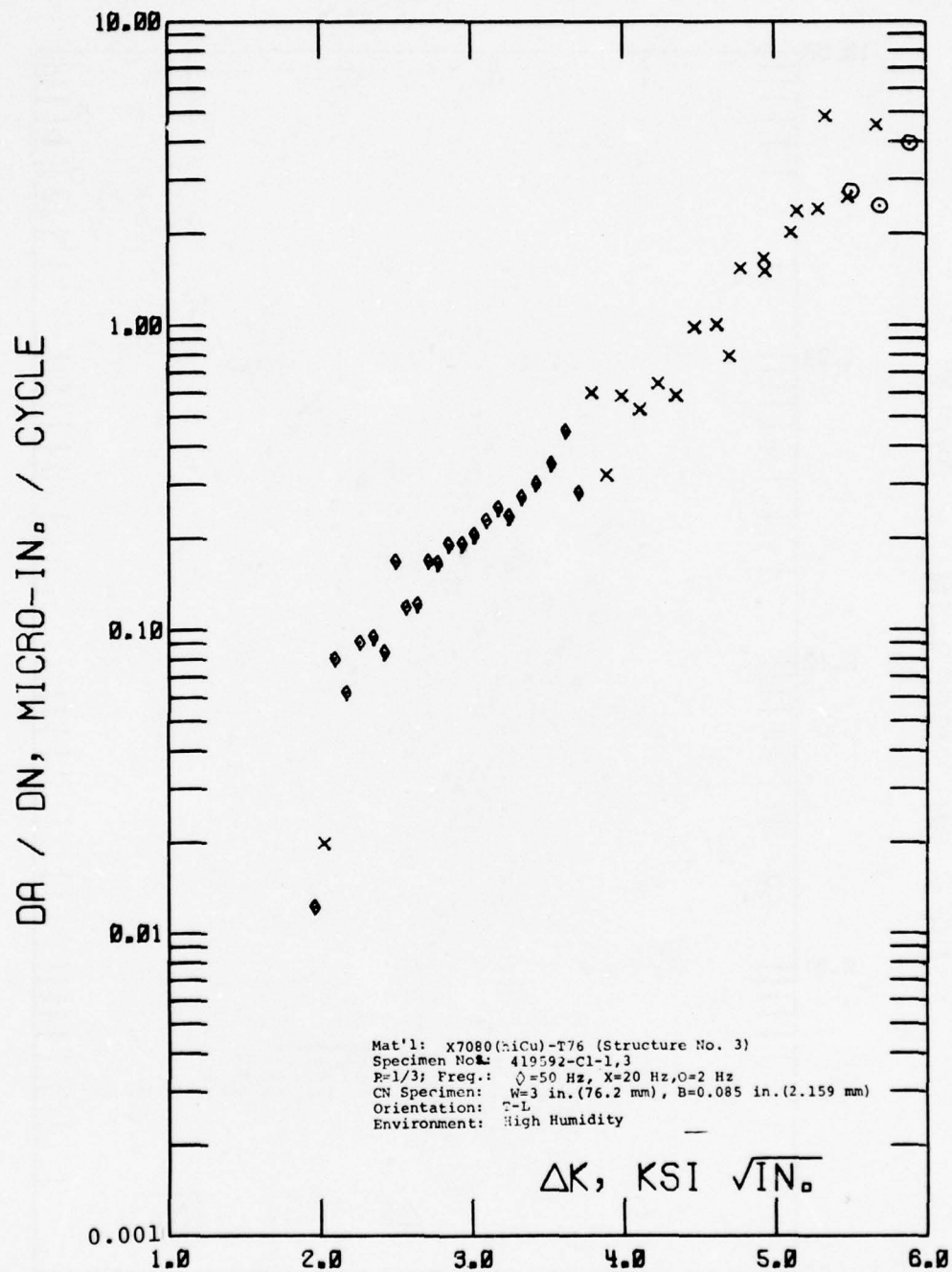


Figure D-2 Cyclic Stress Intensity Range,  $\Delta K$ , Vs. Cyclic Fatigue Crack Growth Rate,  $\Delta a / \Delta N$ , of Structure No. 3

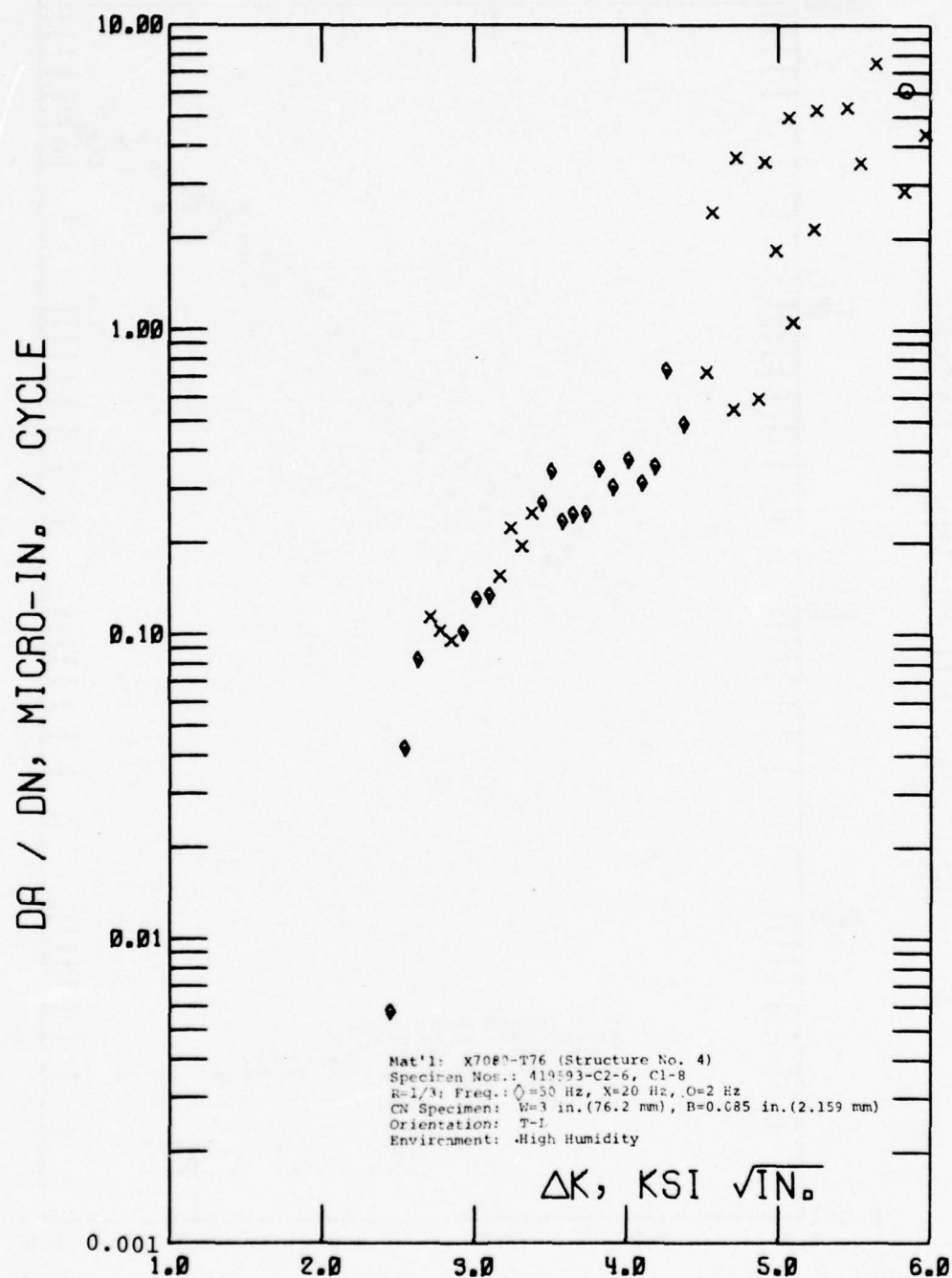


Figure D-3 Cyclic Stress Intensity Range,  $\Delta K$ , Vs. Cyclic Fatigue Crack Growth Rate,  $\Delta a / \Delta N$ , of Structure No. 4

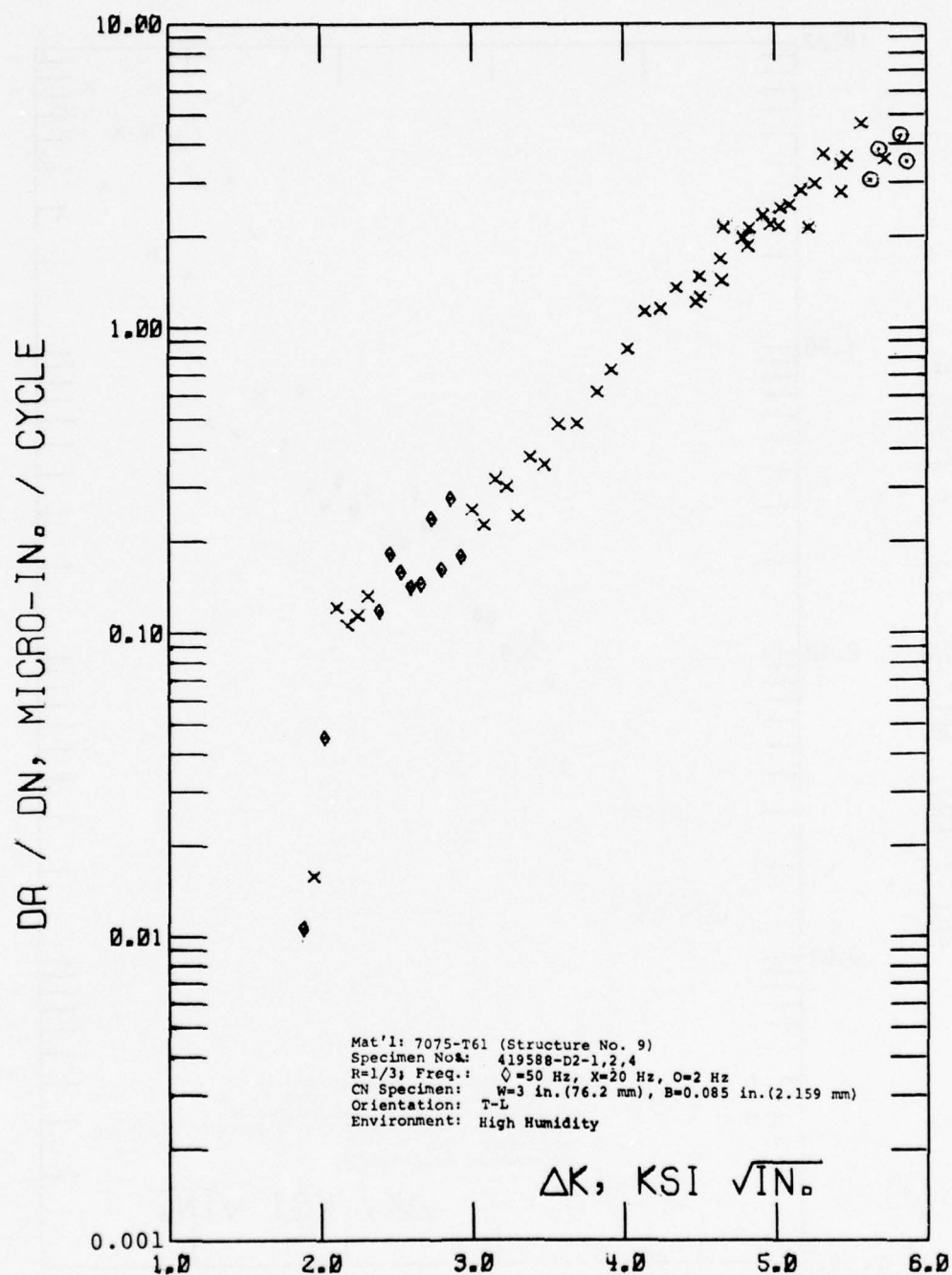


Figure D-4 Cyclic Stress Intensity Range,  $\Delta K$ , Vs. Cyclic Fatigue Crack Growth Rate,  $\Delta a / \Delta N$ , of Structure No. 9

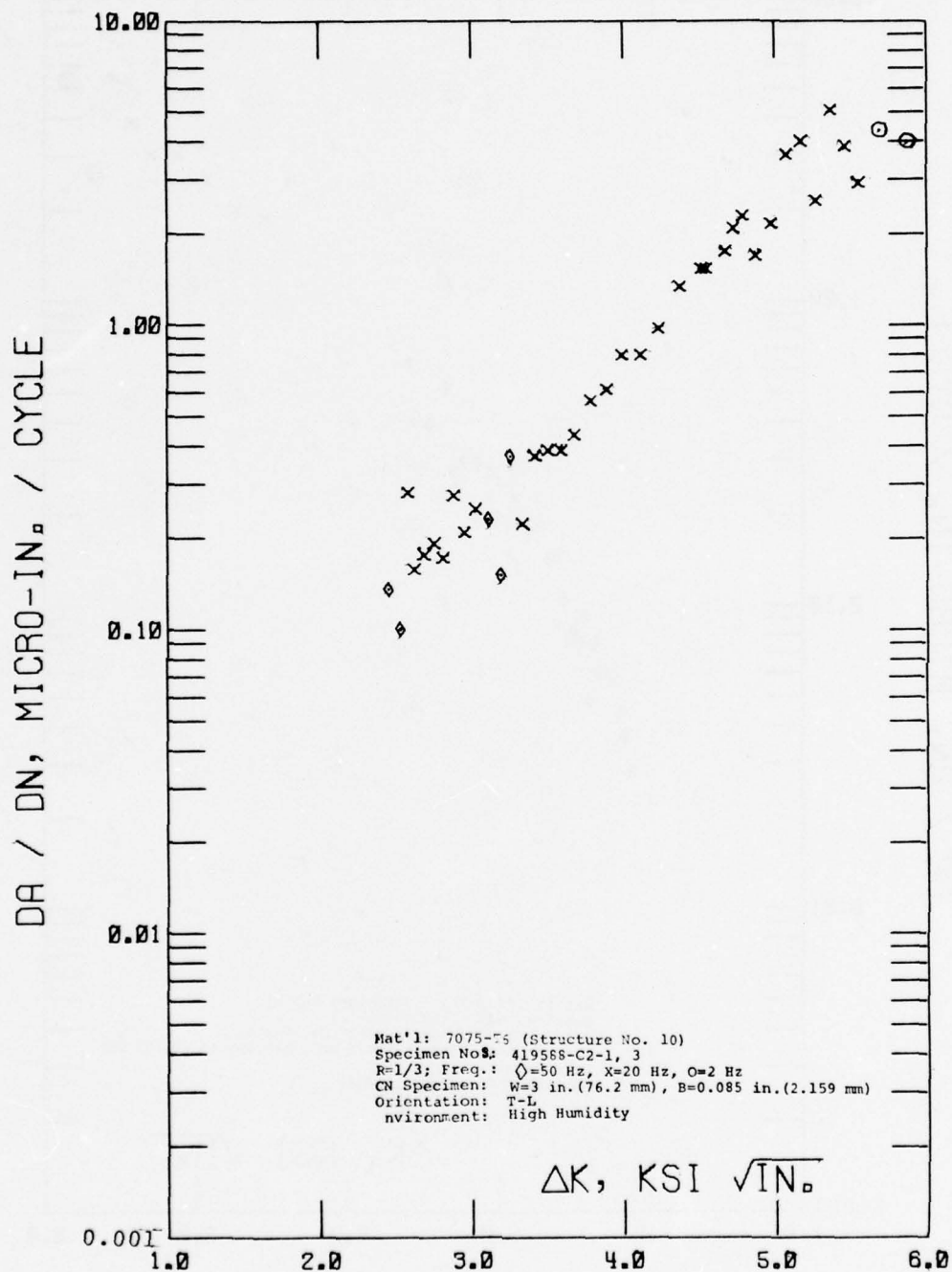


Figure D-5 Cyclic Stress Intensity Range,  $\Delta K$ , Vs. Cyclic Fatigue Crack Growth Rate  $\Delta a / \Delta N$ , of Structure No. 10



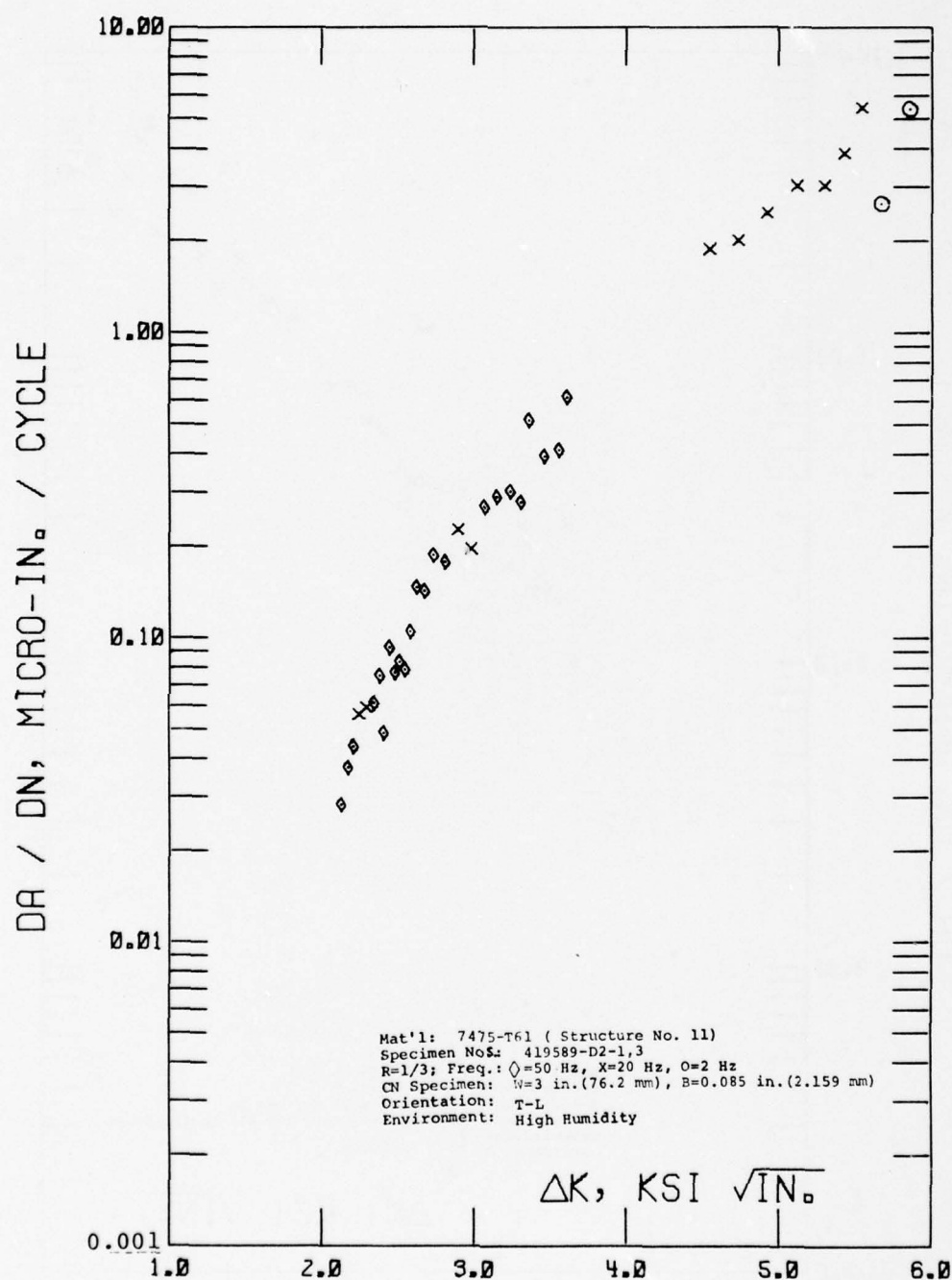


Figure D-6 Cyclic Stress Intensity Range,  $\Delta K$ , Vs. Cyclic Fatigue Crack Growth Rate,  $\Delta a / \Delta N$ , of Structure No. 11

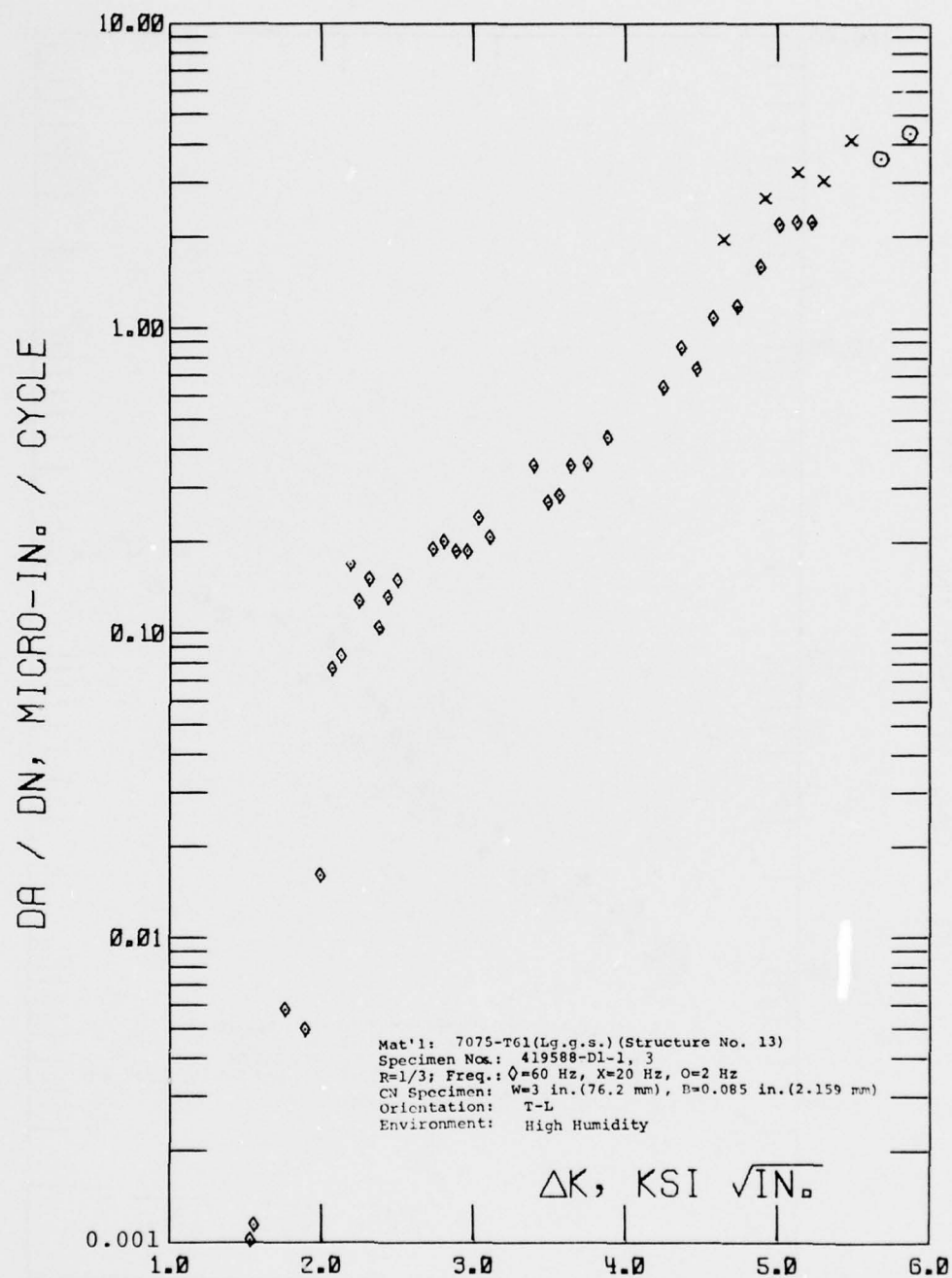


Figure D-7 Cyclic Stress Intensity Range,  $\Delta K$ , Vs. Cyclic Fatigue Crack Growth Rate,  $\Delta a / \Delta N$ , of Structure No. 13

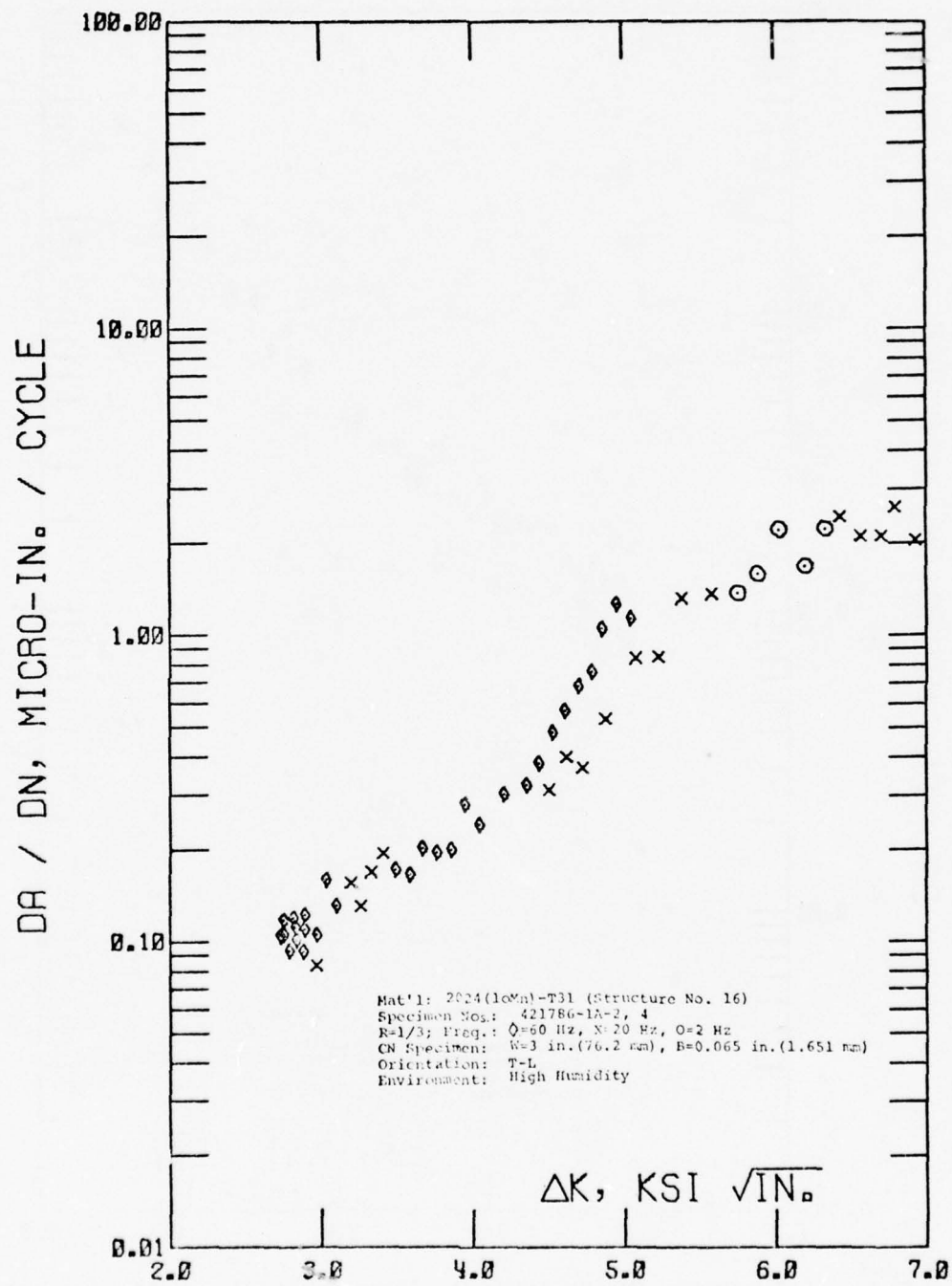


Figure D-8 Cyclic Stress Intensity Range,  $\Delta K$ , Vs. Cyclic Fatigue Crack Growth Rate,  $\Delta a / \Delta N$ , of Structure No. 16

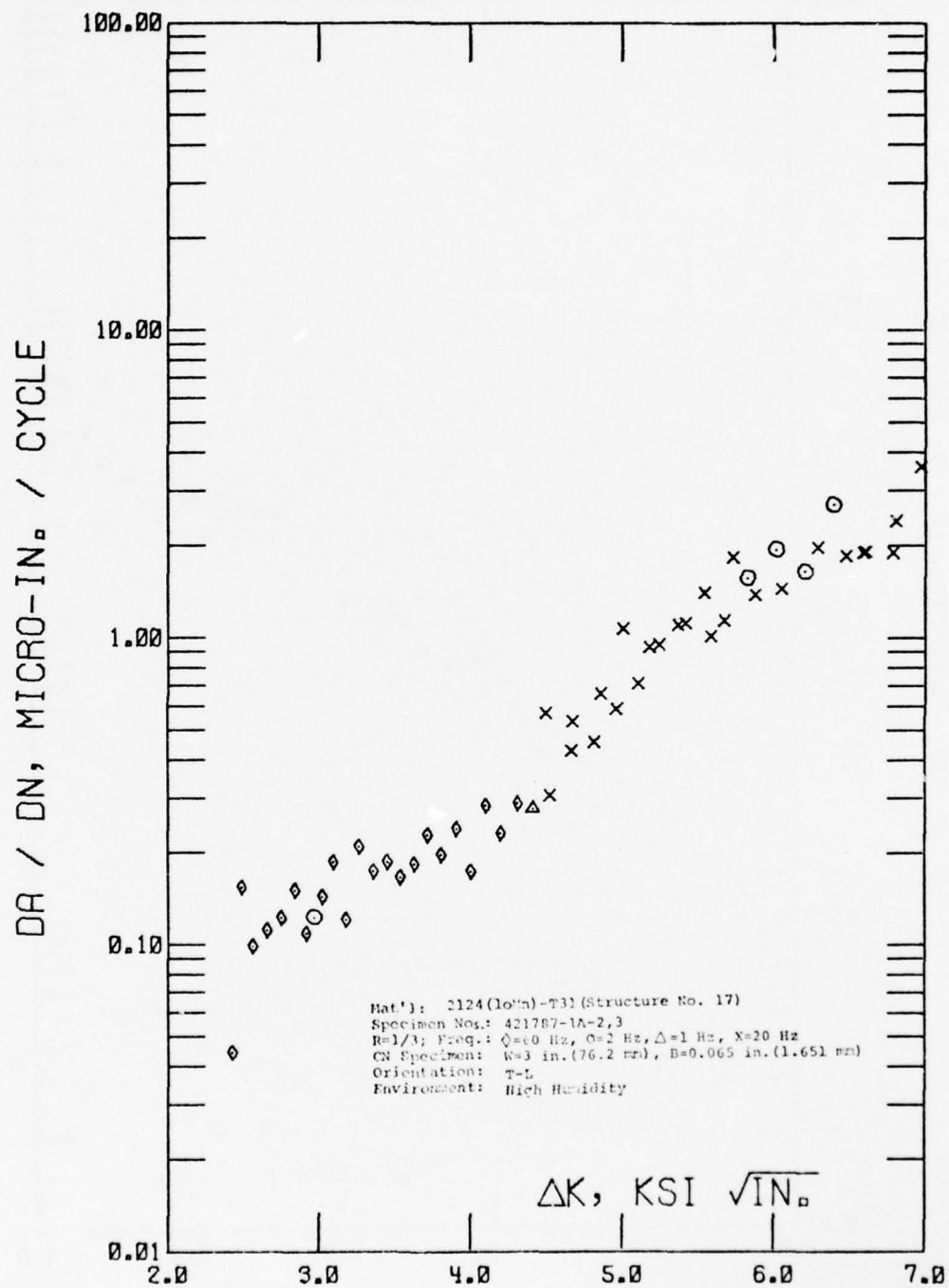


Figure D-9 Cyclic Stress Intensity Range,  $\Delta K$ , Vs. Cyclic Fatigue Crack Growth Rate,  $\Delta a / \Delta N$ , of Structure No. 17



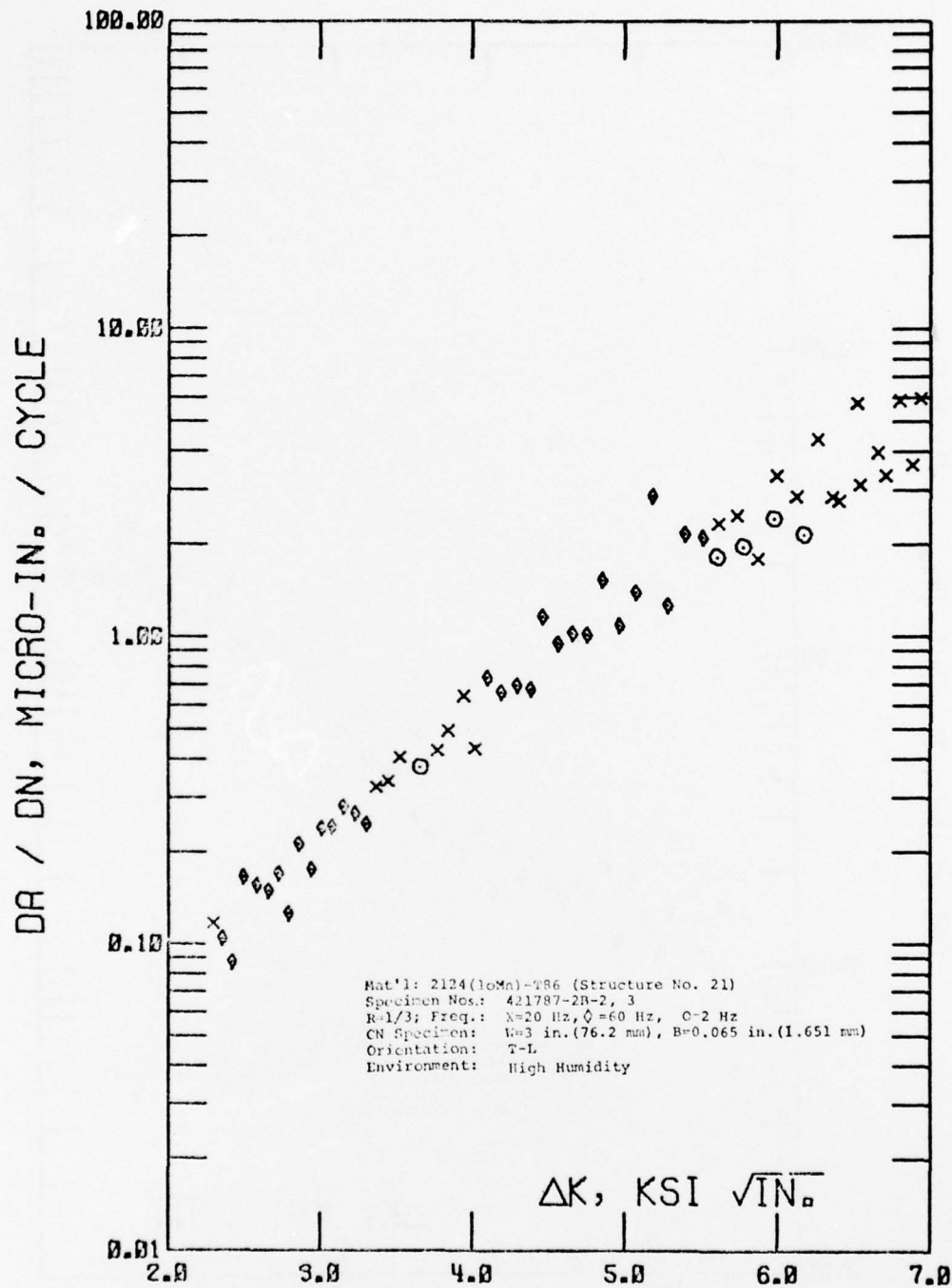


Figure D-10 Cyclic Stress Intensity Range,  $\Delta K$ , Vs. Cyclic Fatigue Crack Growth Rate,  $\Delta a / \Delta N$ , of Structure No. 21

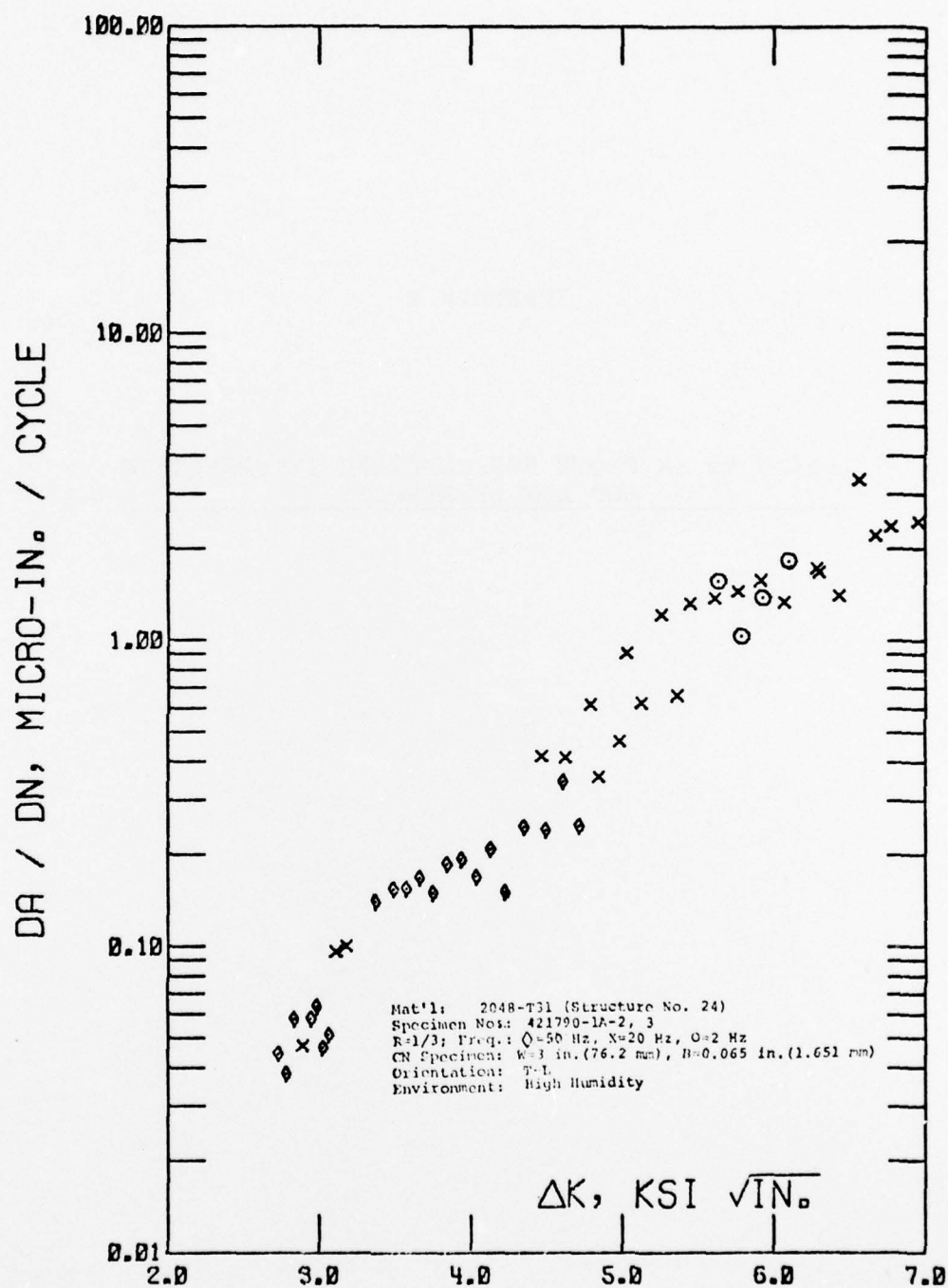


Figure D-11 Cyclic Stress Intensity Range,  $\Delta K$ , Vs. Cyclic Fatigue Crack Growth Rate,  $\Delta a / \Delta N$ , of Structure No. 24

APPENDIX E

$\Delta a/\Delta N$  vs  $\Delta K$  PLOTS FOR COMBINED INTERMEDIATE  
AND LOW  $\Delta K$  RESULTS

---

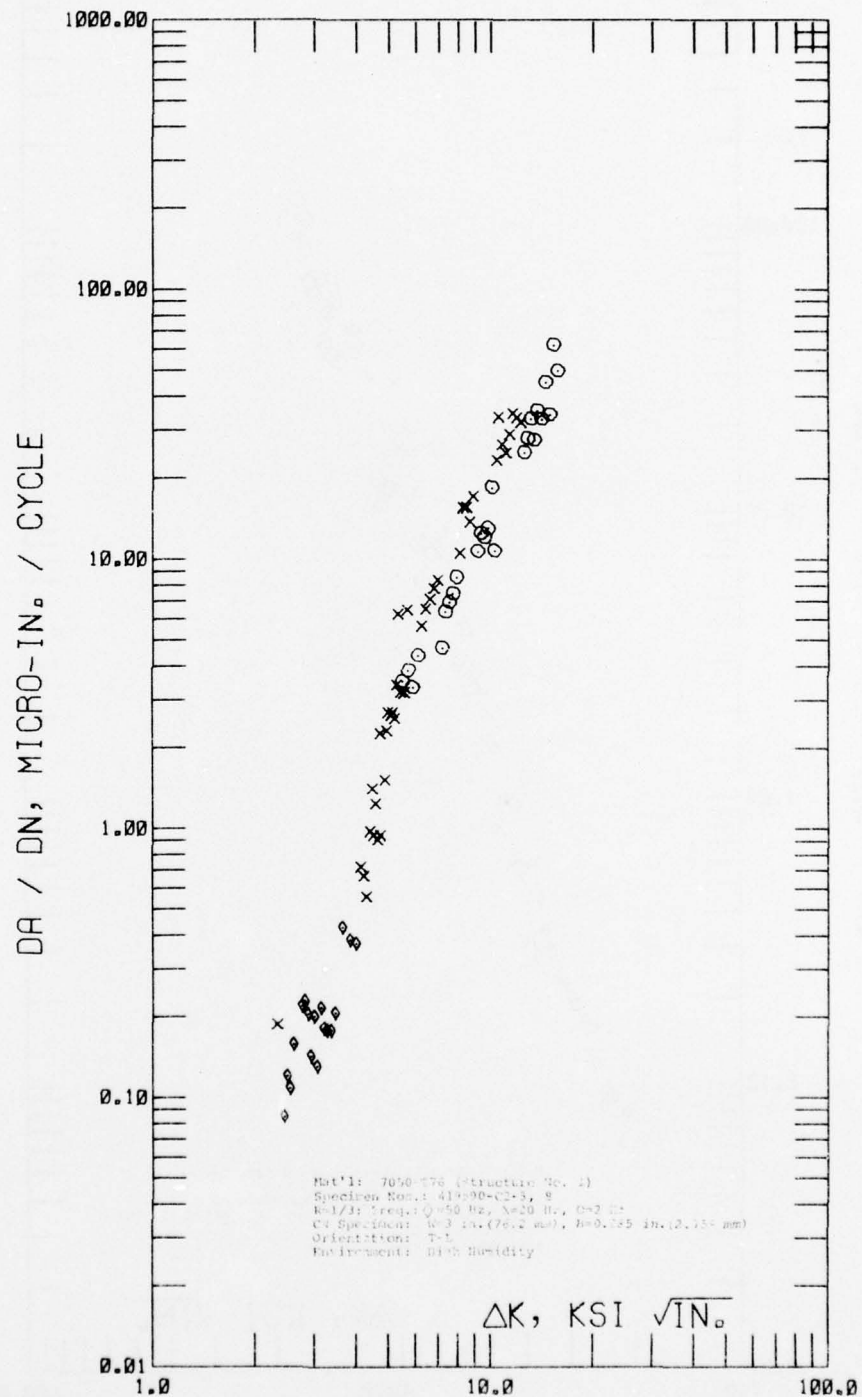


Figure E-1 Cyclic Stress Intensity Range,  $\Delta K$ , Vs. Cyclic Fatigue Crack Growth Rate,  $\Delta a / \Delta N$ , of Structure No. 1



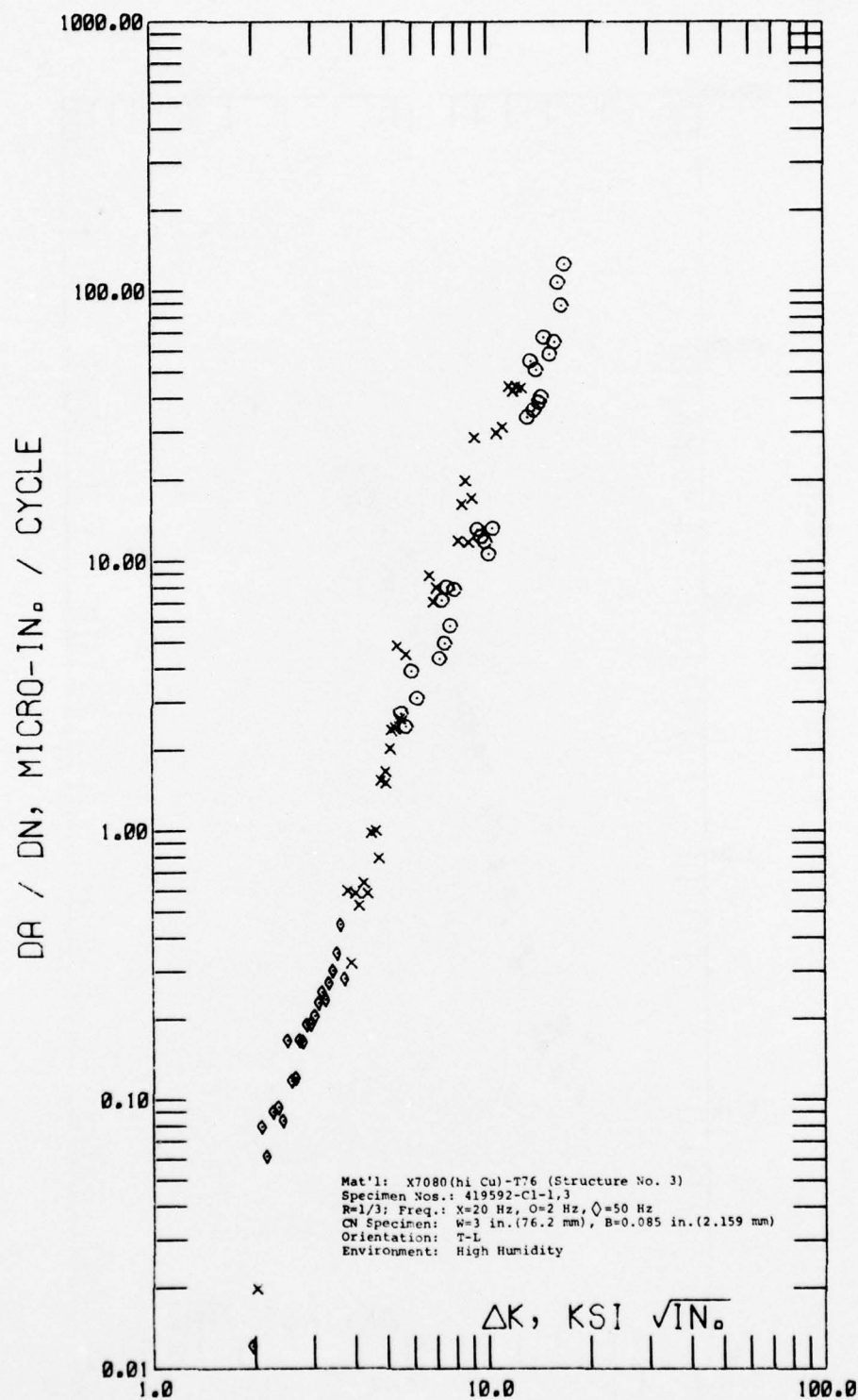


Figure E-2 Cyclic Stress Intensity Range,  $\Delta K$ , Vs. Cyclic Fatigue Crack Growth Rate  $\Delta a / \Delta N$ , of Structure No. 3

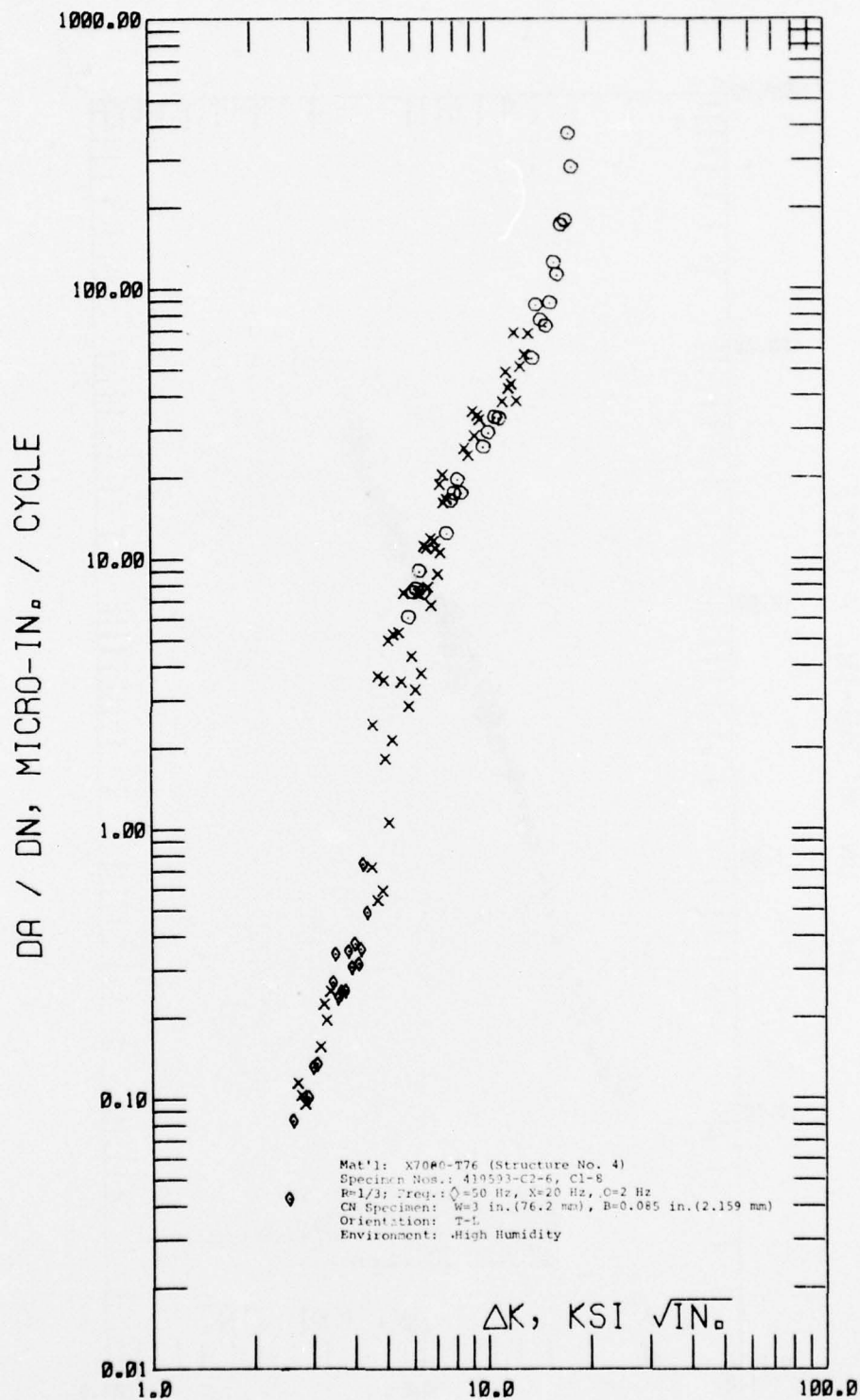


Figure E-3 Cyclic Stress Intensity Range,  $\Delta K$ , Vs. Cyclic Fatigue Crack Growth Rate,  $\Delta a / \Delta N$ , of Structure No. 4

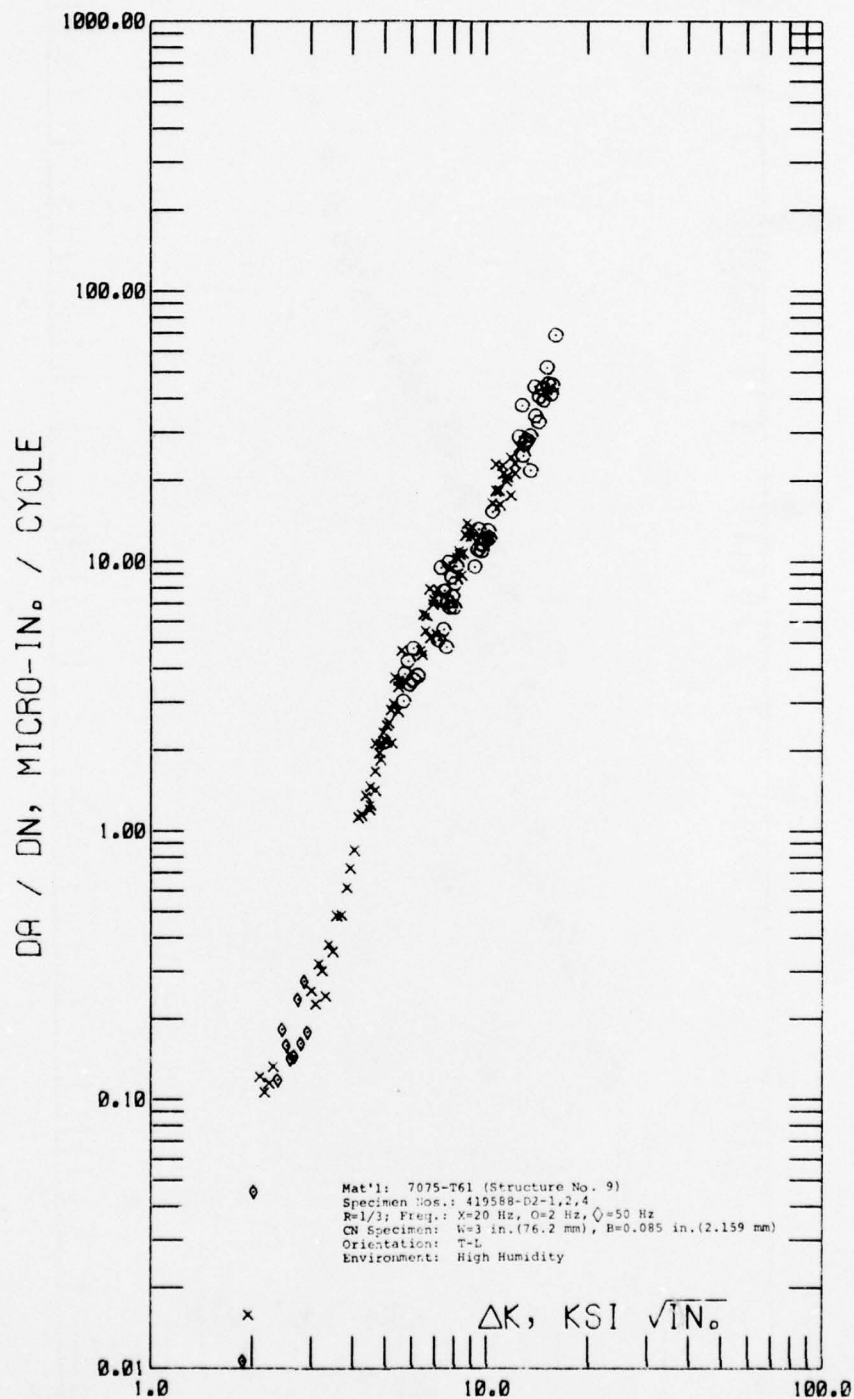


Figure E-4 Cyclic Stress Intensity Range,  $\Delta K$ , Vs. Cyclic Fatigue Crack Growth Rate,  $\Delta a / \Delta N$ , of Structure No. 9

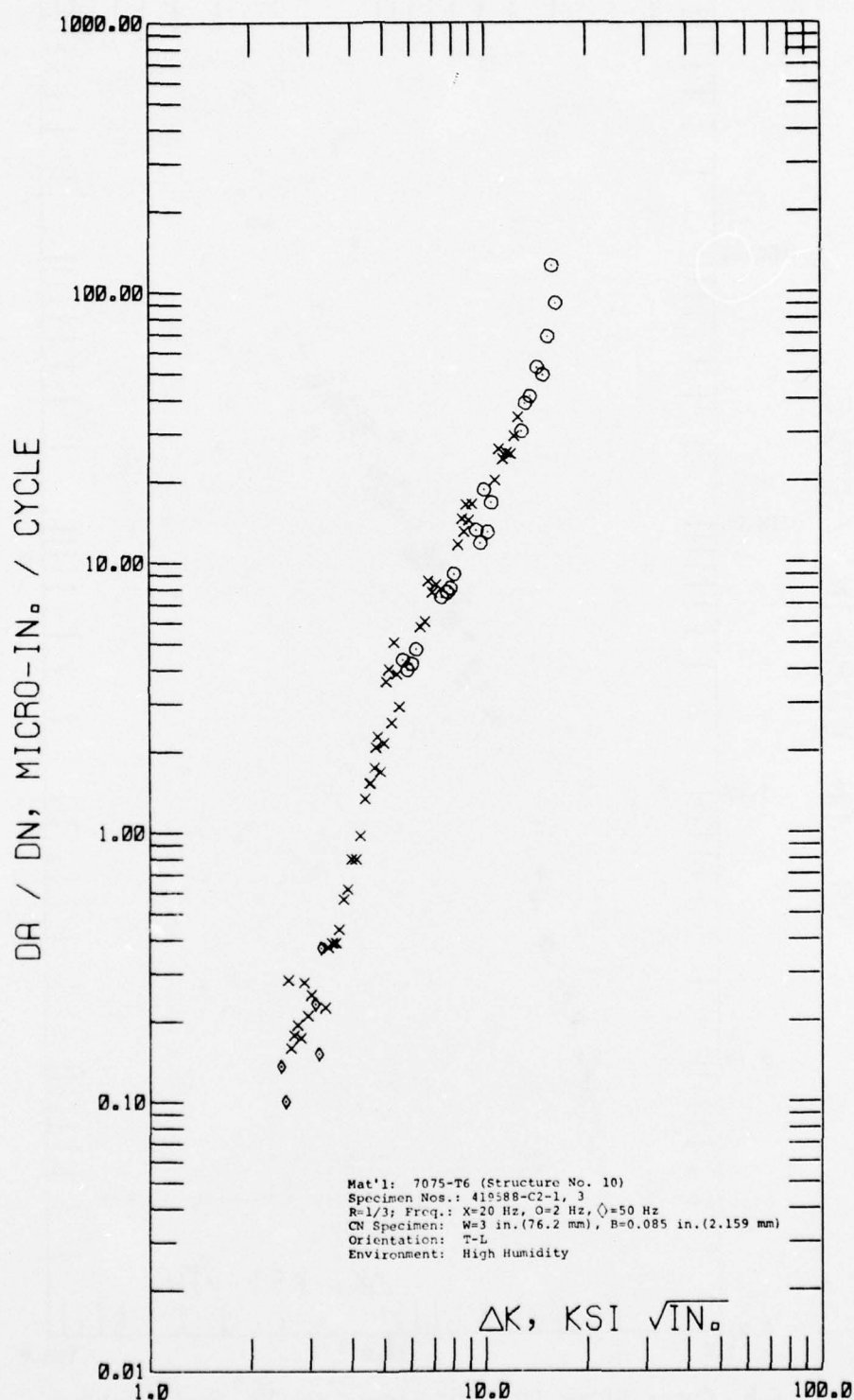


Figure E-5 Cyclic Stress Intensity Range,  $\Delta K$ , Vs. Cyclic Fatigue Crack Growth Rate  $\Delta a / \Delta N$ , of Structure No. 10



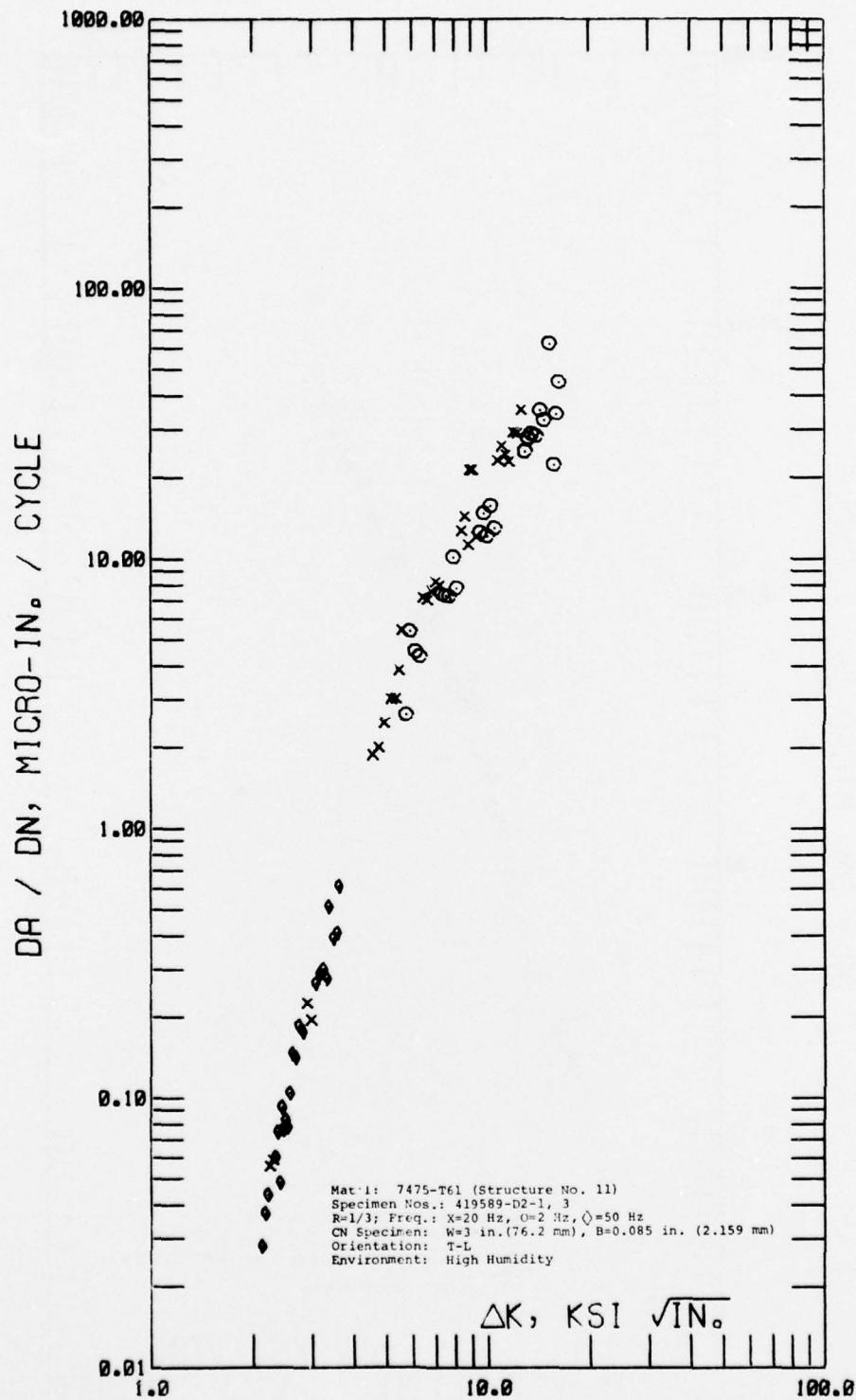


Figure E-6 Cyclic Stress Intensity Range,  $\Delta K$ , Vs. Cyclic Fatigue Crack Growth Rate,  $\Delta a / \Delta N$ , of Structure No. 11

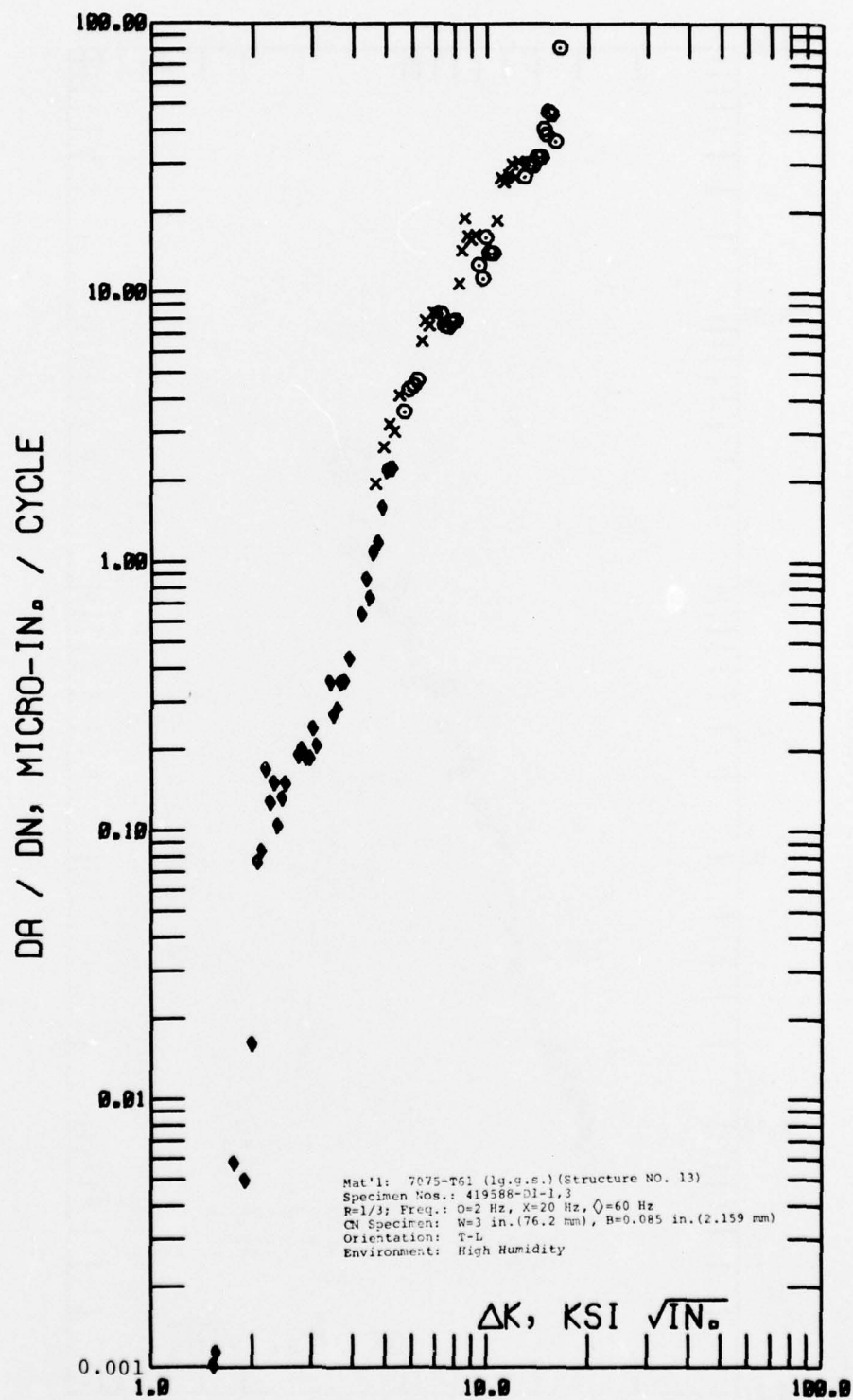


Figure E-7 Cyclic Stress Intensity Range,  $\Delta K$ , Vs. Cyclic Fatigue Crack Growth Rate,  $\Delta a / \Delta N$ , of Structure No. 13

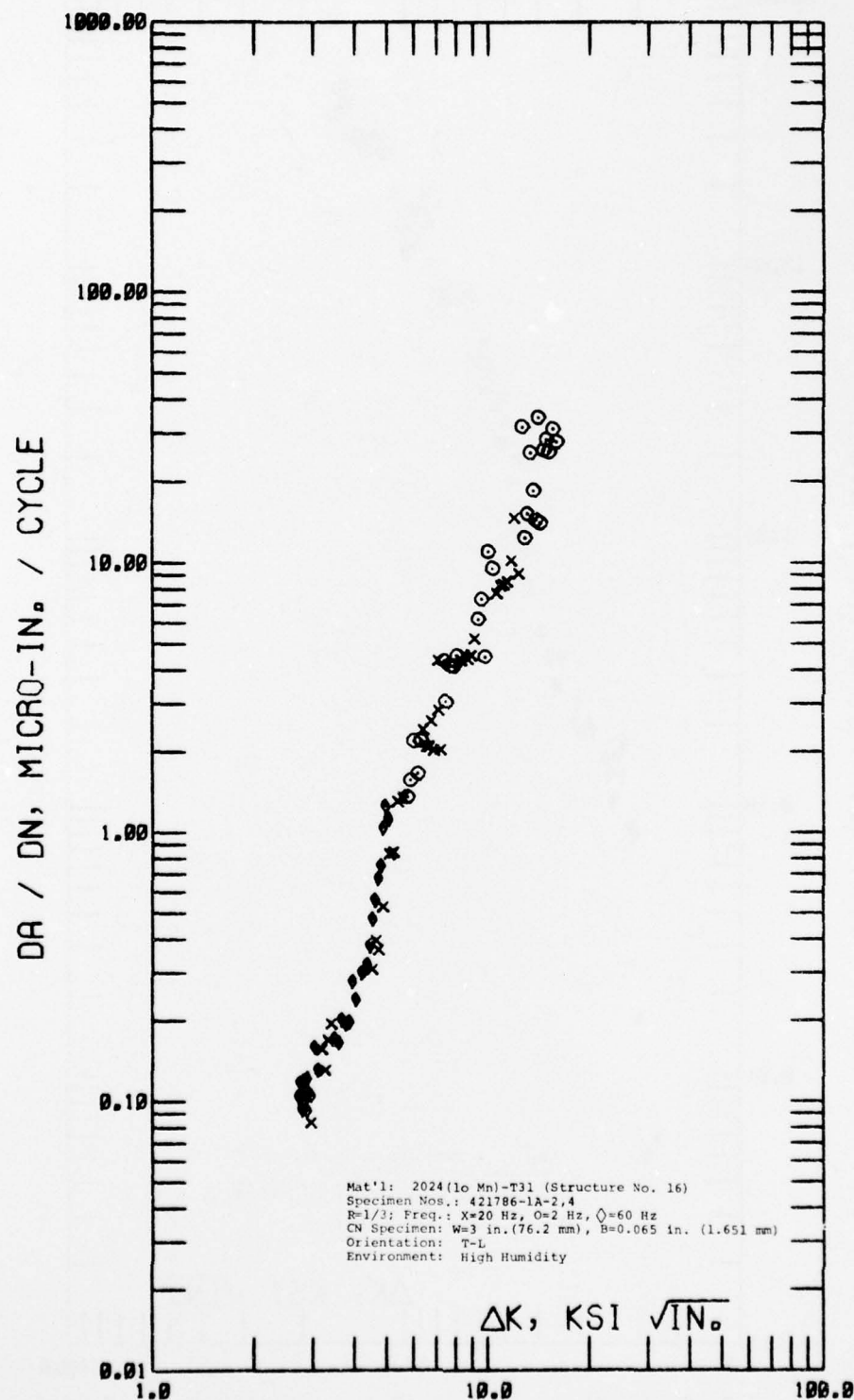


Figure E-8 Cyclic Stress Intensity Range,  $\Delta K$ , Vs. Cyclic Fatigue Crack Growth Rate,  $\Delta a / \Delta N$ , of Structure No. 16

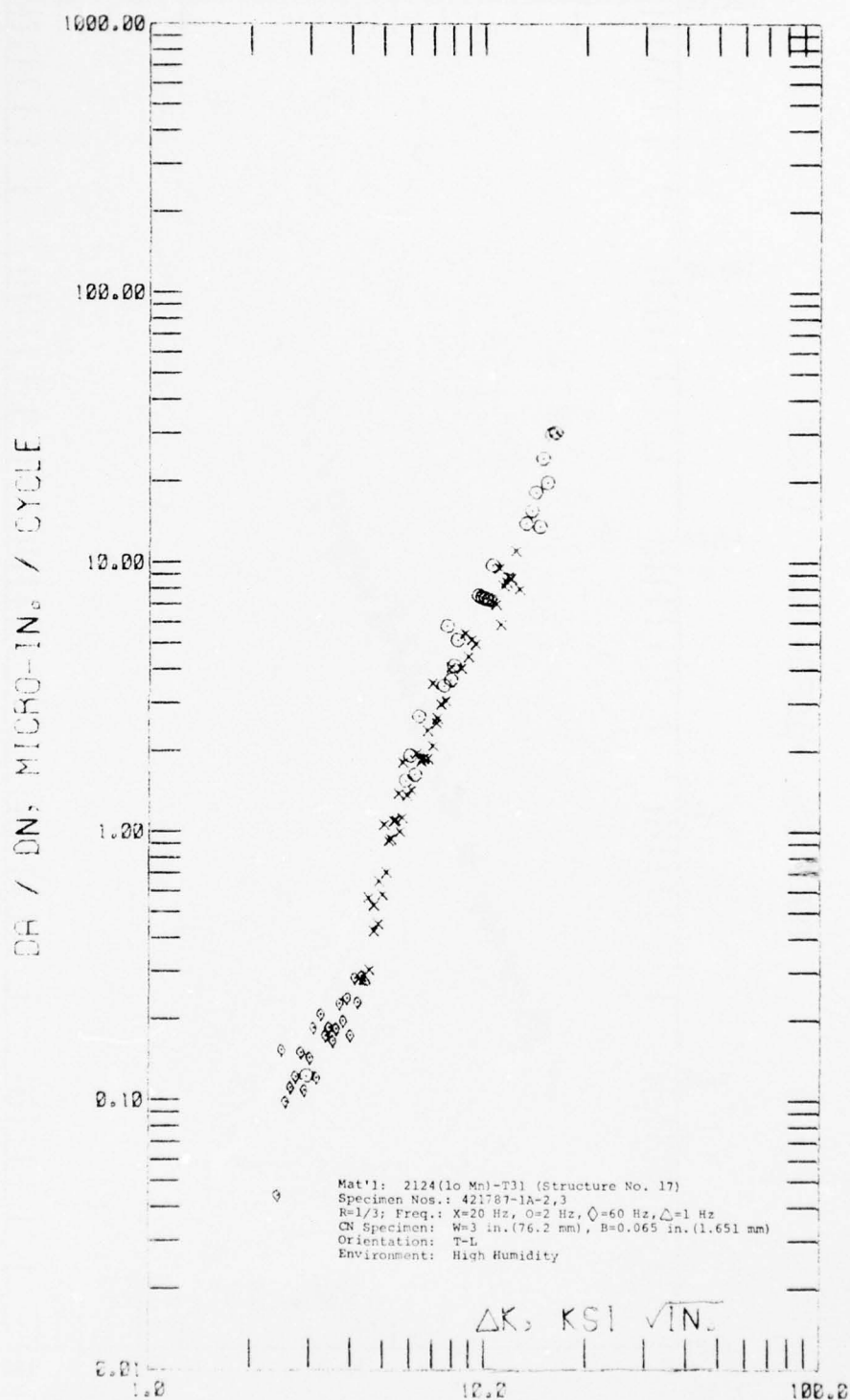


Figure E-9 Cyclic Stress Intensity Range,  $\Delta K$ , Vs. Cyclic Fatigue Crack Growth Rate,  $\Delta a / \Delta N$ , of Structure No. 17



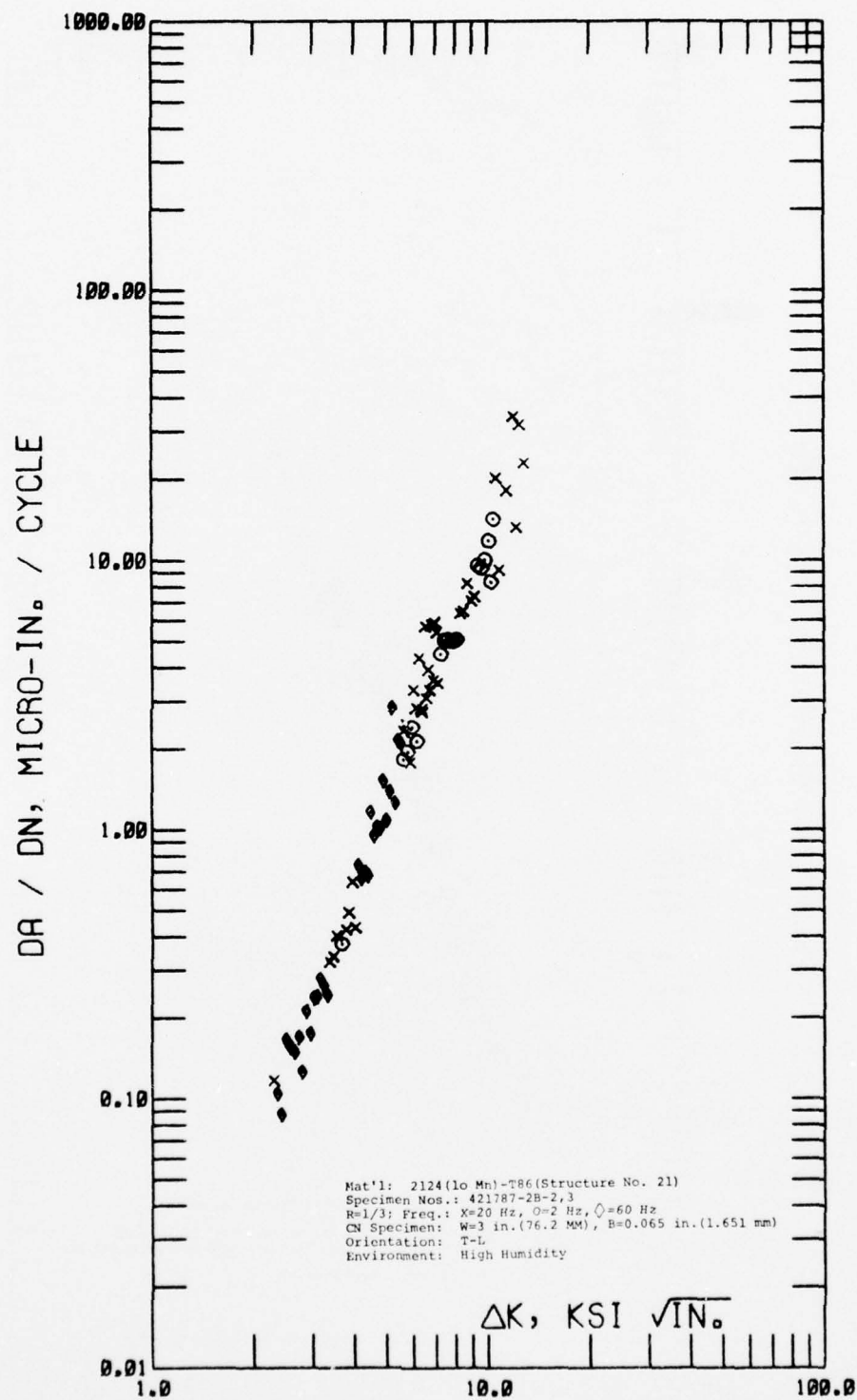


Figure E-10 Cyclic Stress Intensity Range,  $\Delta K$ , Vs. Cyclic Fatigue Crack Growth Rate  $\Delta a / \Delta N$ , of Structure No. 21

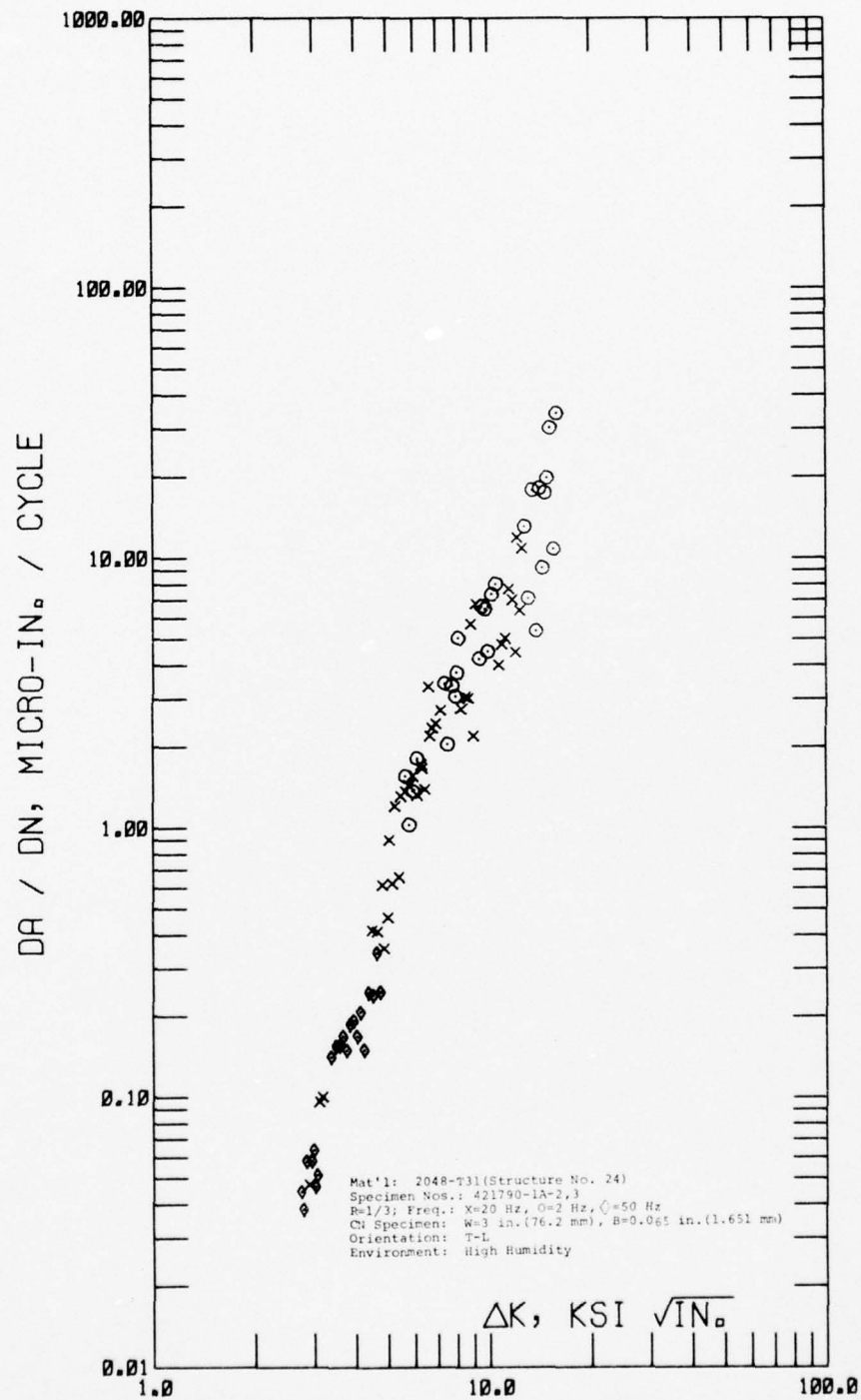


Figure E-11 Cyclic Stress Intensity Range,  $\Delta K$ , Vs. Cyclic Fatigue Crack Growth Rate,  $\Delta a / \Delta N$ , of Structure No. 24